

11-001
9932
p. 279

NASA Contractor Report 189106 - Vol -1

Stratified Charge Rotary Engine Critical Technology Enablement Volume I

C.E. Irion and R.E. Mount
Rotary Power International, Inc.
Wood-Ridge, New Jersey

(NASA-CR-189106-Vol-1) STRATIFIED
CHARGE ROTARY ENGINE CRITICAL
TECHNOLOGY ENABLEMENT, VOLUME 1
Final Report, Feb. 1990 - 1992
(Rotary Power International) 279 p

N94-34231

Unclas

G3/07 0009982

August 1992

Prepared for
Lewis Research Center
Under Contract NAS3-25945



National Aeronautics and
Space Administration

TABLE OF CONTENTS

1.0	Introduction	3
2.0	Executive Summary	7
3.0	Performance	21
3.1	Research Rig Engine/Critical Component Testing	23
3.2	New/Improved Computational Fluid Dynamics (CFD) Codes	47
4.0	Critical Technologies	95
4.1	Advanced Fuel Injection Systems	99
4.2	Reduced Friction/Improved Tribology/Sealing	151
4.3	Lightweight/Low Conductivity Parts	189
4.4	Catalytic Surfaces	201
4.5	Reference Engine Design	213
5.0	Airframe/Mission Model	243
6.0	Controls System Model	263
7.0	Turbomachinery	271
8.0	University Coordination	295
9.0	Conclusions and Recommendations	299
10.0	Listing of Appendices	303

1.0 INTRODUCTION

1.0 INTRODUCTION

A final report is provided for Contract NAS3-25945. The effort was conducted during the period of Feb 1990 through 1992. This contractual effort was the third phase in an overall consecutive contracts, multi-phase program (1983-1991) addressing Stratified Charge Rotary Engine technology enablement. The NASA long-range, overall program objectives are to establish the technology base for an advanced aircraft engine for the mid 1990's and beyond.

Phase III focused on critical technologies identified in the earlier phases while also further identifying and experimentally addressing the most critical technologies. The overall NASA effort has involved in-house efforts, small industry contracts and University grants in addition to the major industry effort with John Deere Technologies International, Inc. and earlier Curtiss-Wright Corporation.

As previously stated, NASA's objectives are to establish (through basic research) the technology base for a multi fuel, non-gasoline dependent, efficient general aviation aircraft engine. With this technology base, industry can then consider initiation of a full scale development and FAA certification program, thereby bringing the technology to the general aviation industry. Phases I, II and III are reviewed in Reference 1.

During Phase III, significant progress was achieved including:

- o Demonstration of 5 HP/CU IN (230 Kw/ℓ) power density
- o Demonstration of 0.375 Lbs/BHP-HR (228 Grs/Kw-HR) specific fuel consumption at cruise power using Jet-A fuel.
- o Correlation between experimental test results and advanced, high speed computational fluid dynamics.

During the contract, a business decision by Deere & Co. to terminate its involvement with rotary engines and focus on its core agricultural business forced a re-direction of the program and a reduction in scope. The technology advancement was thereby restricted to a degree since some configurations of rotor and rotor housing were defined but not tested. These factors are discussed more fully in Section 2.0.

Reference 1 "NASA's Rotary Engine Technology Enablement Program -- 1983 through 1991", E.A. Willis and J.J. McFadden, SAE 920311, Feb 24-28, 1992

2.0 EXECUTIVE SUMMARY

PRECEDING PAGE BLANK NOT FILMED

PAGE 4

2.0 EXECUTIVE SUMMARY

NASA Contract No. NAS3-25945, entitled "Stratified Charge Rotary Engine Critical Technology Enablement-Phase III" was a continuation of research work conducted in prior contracts NAS3-23056 and NAS3-24628 (Phases I and II, respectively).

As summarized in Figure No. 1, the NASA primary objectives for this effort are aimed at establishing a technology base through basic research which can ultimately lead to a new, advanced multi-fuel capability engine for the General Aviation industry.

During the Phase III effort, significant progress was achieved in the areas of power density and specific fuel consumption. These achievements are illustrated graphically over the 1988 to 1991 timeframe in Figure Nos. 2 and 3.

o Figure No. 2

Maximum power demonstration (with Jet-A fuel) at 400HP (300Kw) meeting the original goal of 5HP/cu. in. (230Kw/ℓ) and demonstrating long range potential. These tests were conducted with the 1007R single rotor research engine (200HP (150Kw) level) with appropriate correction to the twin rotor, 2013R engine basis.

o Figure No. 3

Brake specific fuel consumption (with Jet-A fuel) at 0.375 Lbs/BHP-Hr (228g/Kwh) at cruise conditions. These tests were conducted on the 1007R single rotor research engine with appropriate correction to the twin rotor, 2013R engine basis and, it should be noted that the testing related to BSFC was independent of testing for power output. That is, no one discrete configuration performed both power and BSFC achievements.

The original goal, based upon completion of the originally planned full Phase III program was 0.355 Lbs/BHP-Hr (216g/Kwh). With the decision by Deere and Company to terminate its involvement with rotary engines (September 1990), a re-planned program was directed by NASA for completion of testing in late 1991 vs. June 1992. In the redirected program, a goal of 0.375 Lbs/BHP-Hr (228g/Kwh) was established for 1991. This goal was achieved.

PRECEDING PAGE BLANK NOT FILMED

2.1 GENERAL BACKGROUND

Early studies directed by NASA Lewis Research Center identified the Stratified Charge Rotary Engine as the leading candidate for an advanced, non-aviation gasoline dependent general aviation engine for the mid-1990's and beyond time- frame, Reference 2. An industry-wide fuels conference conducted by NASA Lewis Research Center noted the ever-increasing limitations in the availability of high octane aviation fuels. An engine capable of operating with Jet-A fuel combined with low cost and high efficiency was deemed necessary. The Stratified Charge Rotary Engine can meet these requirements.

Figure No. 4 depicts the basic operating cycle for the Stratified Charge Rotary Engine, utilizing a pilot injector located in close proximity to a spark plug and a separate main injector.

Figure No. 5 presents an enlarged view of the basic injection-ignition geometry. The pilot injector provides a small quantity of fuel (less than 5% of the total fuel flow) and maintains a constant volume per stroke. A stoichiometric mixture is created at the spark plug-pilot injector region for spark ignitable conditions independent of fuel type. A wide variation in fuel flow as a function of load demand can then be introduced by the main injector into the pilot initiated combustion. This separation of main injector and pilot injector permits optimization of conditions in the light-off zone.

Figure No. 6 presents a general arrangement of a two rotor, Stratified Charge Rotary Aircraft Engine based upon the early NASA studies. This general configuration was used in studies conducted by Cessna and Beech under NASA Lewis Research Center's direction to investigate aircraft performance and operating cost characteristics.

2.2 PHASE I CONTRACT

The Phase I Contract NAS3-23056 was conducted during the period of 1983-1985 initially by Curtiss-Wright Corporation (through January 1984) and subsequently by the Rotary Engine Division of John Deere Technologies International, Inc.

During Phase I, a high performance single rotor research rig engine was designed, procured and check-out tested. The research rig engine was designed for 200BHP (150Kw) at speeds up to 9600RPM and peak internal pressures of up to 1400psi (9653kPa), Reference 3. Basic performance and multi-fuel operation was demonstrated.

2.3 PHASE II CONTRACT

The Phase II Contract NAS3-24628 utilized the research rig engine as a vehicle for examining component technologies. An advanced electronically controlled fuel injection system was procured and tested. Power output of 4.3HP/cu. in. (194Kw/ℓ)

was demonstrated exceeding the contract objectives of 4.0HP/cu. in. (180Kw/ℓ). Subsequently, a revised long range goal of 5HP/cu. in. (230Kw/ℓ) was established as an objective. A fuel consumption at cruise of 0.42 Lbs/BHP-HR (256 Grs/Kw-HR) was achieved on Jet-A, diesel and aviation gasoline fuels. During the Phase II effort, Computational Fluid Dynamics (CFD) studies were utilized extensively at John Deere Technologies International, Inc. and at NASA supporting contractors and grantees to guide the improved fuel economy thrust.

During the Phase II effort, discussions between NASA, JD TI, Inc. and Naval Air Development Center, Warminster, PA resulted in USN participation in the technology enablement efforts. This activity involved preparation of an engine performance model and design of a twin rotor core power section aimed at 250BHP (188Kw) at 66,000 Ft. (20km) altitude.

2.4 PHASE III CONTRACT

The Phase III Contract NAS3-25945 was awarded to JD TI, Inc. on 19 January 1990.

The program was comprised of five major tasks with appropriate sub-tasks. Figure No. 7 presents the Work Breakdown Structure.

A number of industry and university participants were involved in the overall program as reflected in Figure No. 8, Program Team.

The program addressed critical technology enablement in the areas of advanced, higher speed Computational Fluid Dynamics (CFD) analyses via three-dimensional combustion modeling; airframe mission modeling; design of a reference engine; friction reduction; improved tribology/sealing methods; control system modeling; lightweight/low conductivity parts; catalytic surfaces; advanced fuel injection and an extensive effort to define the turbomachinery system including the consideration of turbo-compounding.

As previously noted, with an announcement by Deere and Company in September 1990 of a desire to terminate its involvement with rotary engines, a re-directed program was outlined by NASA LeRC for October 1991 completion of testing (vs. the original contract end date of June 1992). Figure No. 9 presents the guidelines for the re-directed effort.

As outlined in the Section 1.0 Introduction, and in the initial portion of this summary, significant progress was achieved in the power density and efficiency regimes during the Phase III program. However, as noted, the power and BSFC capabilities have not been combined into a single, optimized configuration. Also, as a result of the program curtailment, some designs of rotor, rotor housing, porting variations, lightweight rotors and sealing/tribology were defined and procured but not tested. Further work would be required to conduct this optimization and to demonstrate overall performance (full range operability) in an engine suitable for aircraft

installation (i.e., twin rotor engine with appropriate accessories and controls including turbomachinery).

STRATIFIED CHARGE ROTARY ENGINE
CRITICAL TECHNOLOGY ENABLEMENT

NASA OBJECTIVES

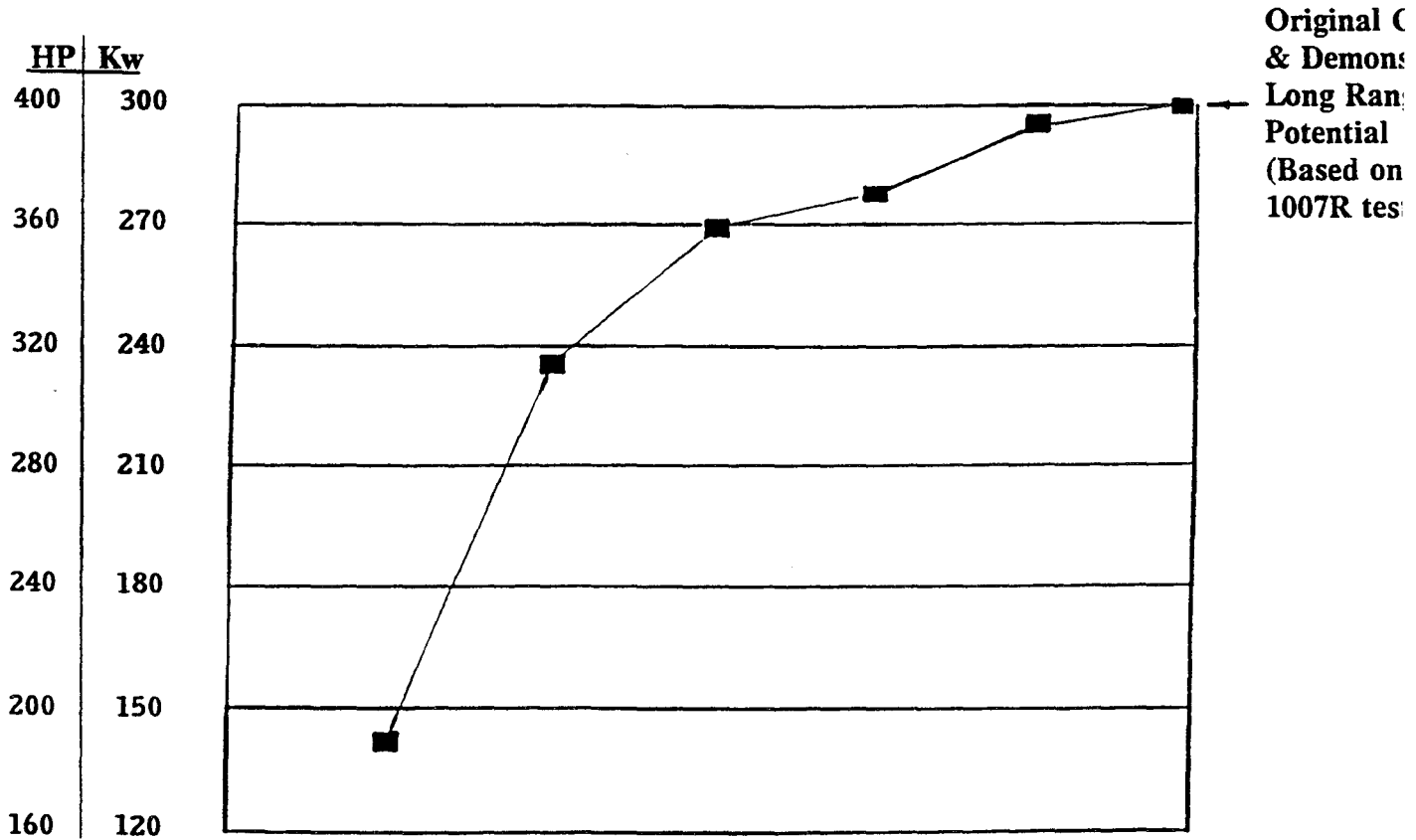
- o **MULTIFUEL CAPABILITY, INCLUDING CIVIL AND MILITARY JET FUEL AND DF-2**
- o **BRAKE SPECIFIC FUEL CONSUMPTION (BSFC) AT CRUISE OF 0.355 LBS/BHP-HR (216 GRS/Kw-HR)**
- o **POWER DENSITY OF 5 HP/CU. IN. (230 Kw/l)**
- o **TIME BETWEEN OVERHAULS (TBO) OF 2000 HOURS**
- o **ALTITUDE CAPABILITY: UP TO 33,000 FT. (10 KM) CRUISE**
- o **MODULAR DESIGN (FAMILY OF ENGINES CONCEPT)**
- o **MANUFACTURING COST COMPETITIVE WITH COMPARABLE RECIPROCATING ENGINES**

Figure No. 1

NASA SCRE CRITICAL TECHNOLOGY ENABLEMENT

MAXIMUM POWER

2013R SCORE 70 ENGINE



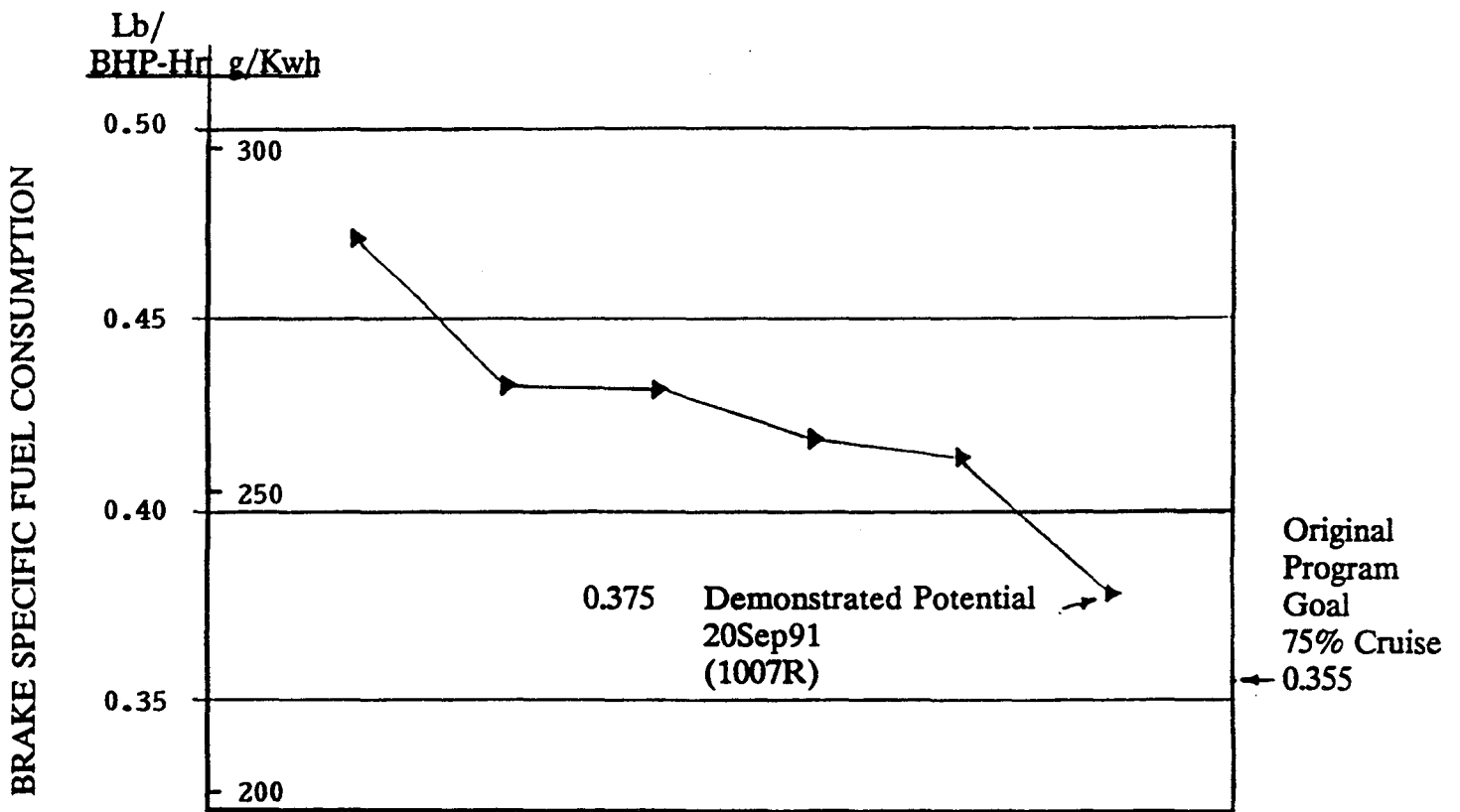
PROGRESS WITH TIME - 1988/1991

Figure No. 2

NASA SCORE CRITICAL TECHNOLOGY ENABLEMENT

BRAKE SPECIFIC FUEL CONSUMPTION

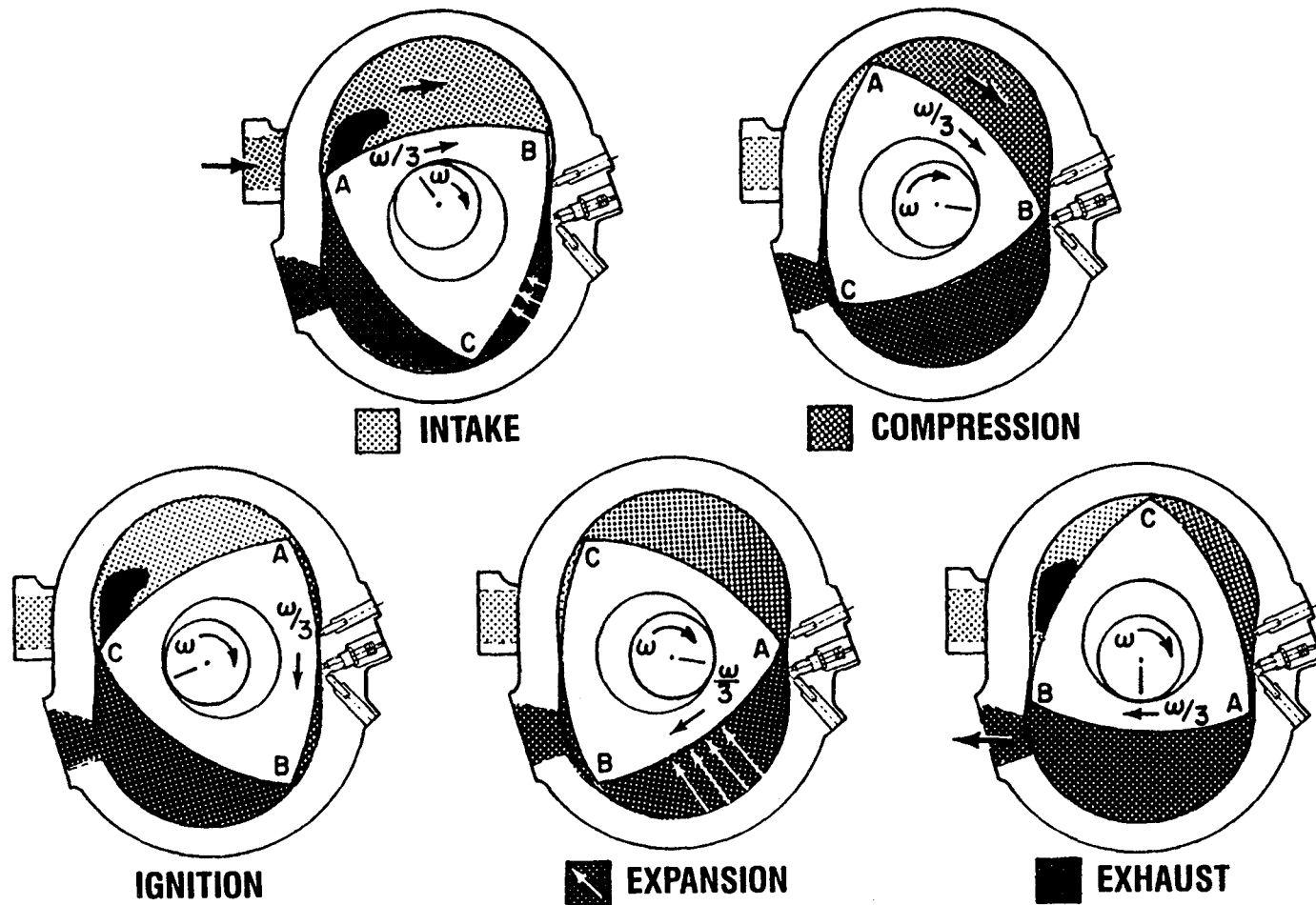
2013R SCORE 70 ENGINE



PROGRESS WITH TIME - 1988/1991

Figure No. 3

OPERATING CYCLE, STRATIFIED CHARGE ROTARY ENGINE



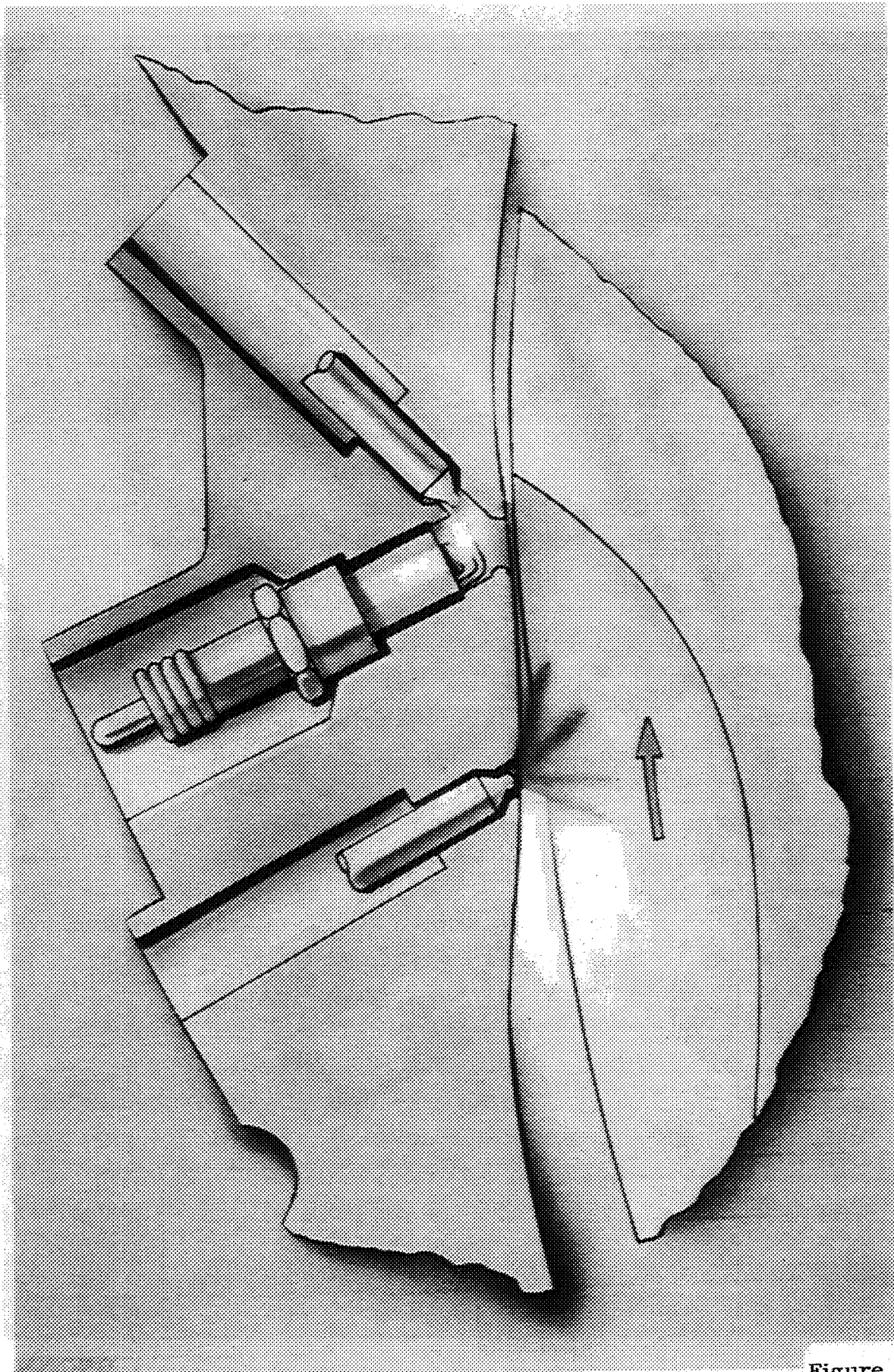
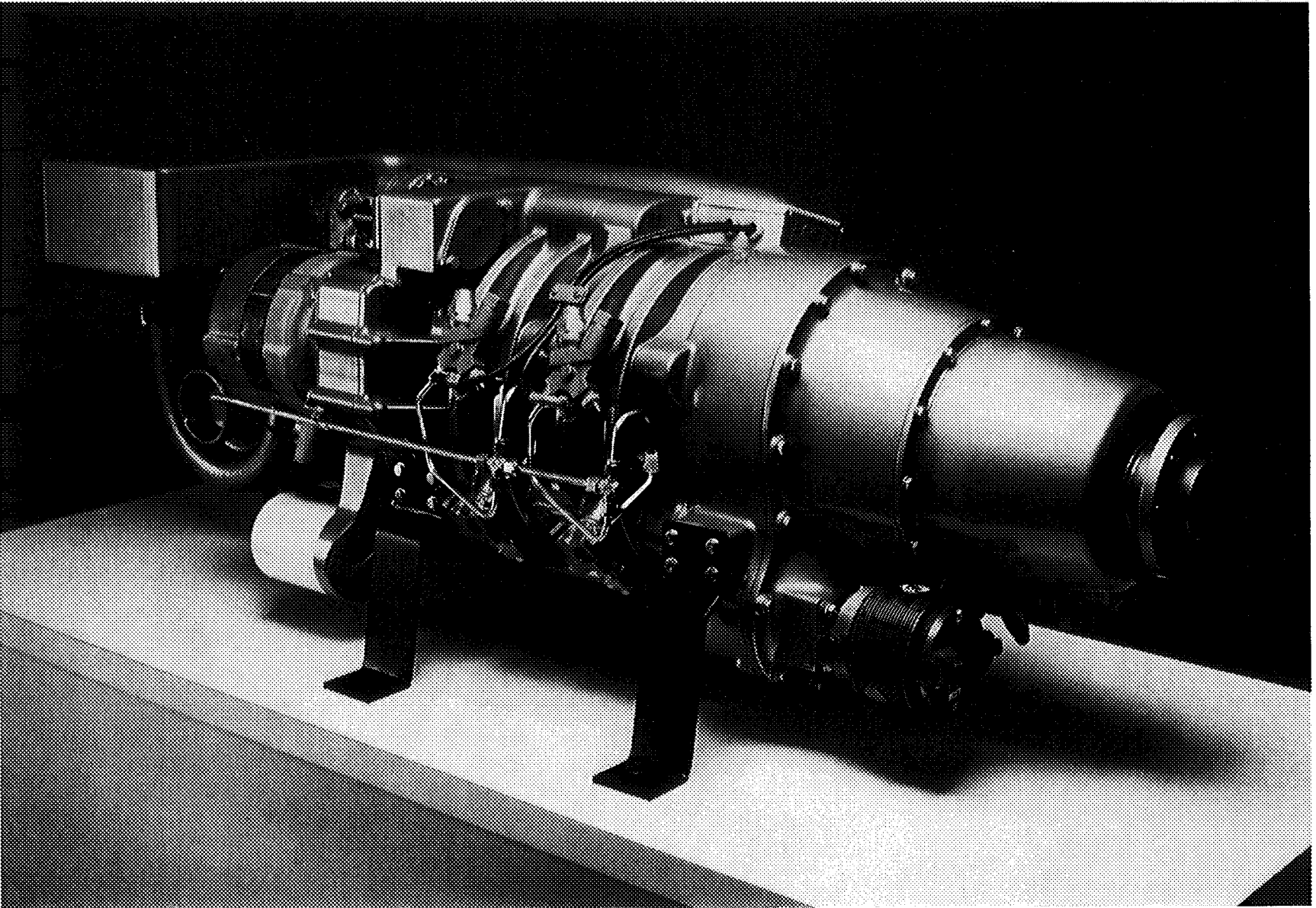


Figure No. 5



2013R AVIATION ENGINE

ORIGINAL PAGE IS
OF POOR QUALITY

STRATIFIED CHARGE ROTARY ENGINE CRITICAL TECHNOLOGY ENABLEMENT

WORK BREAKDOWN STRUCTURE

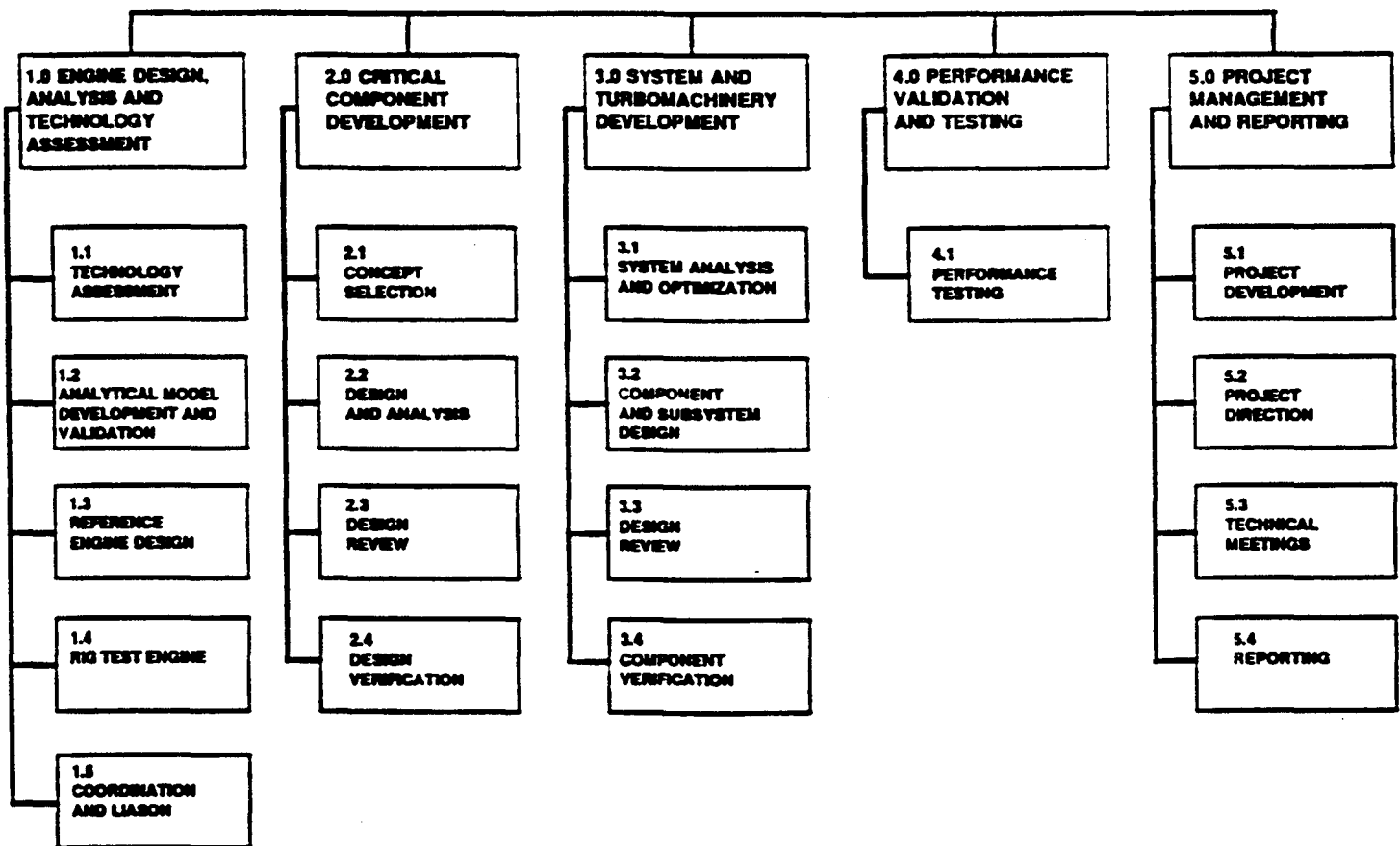
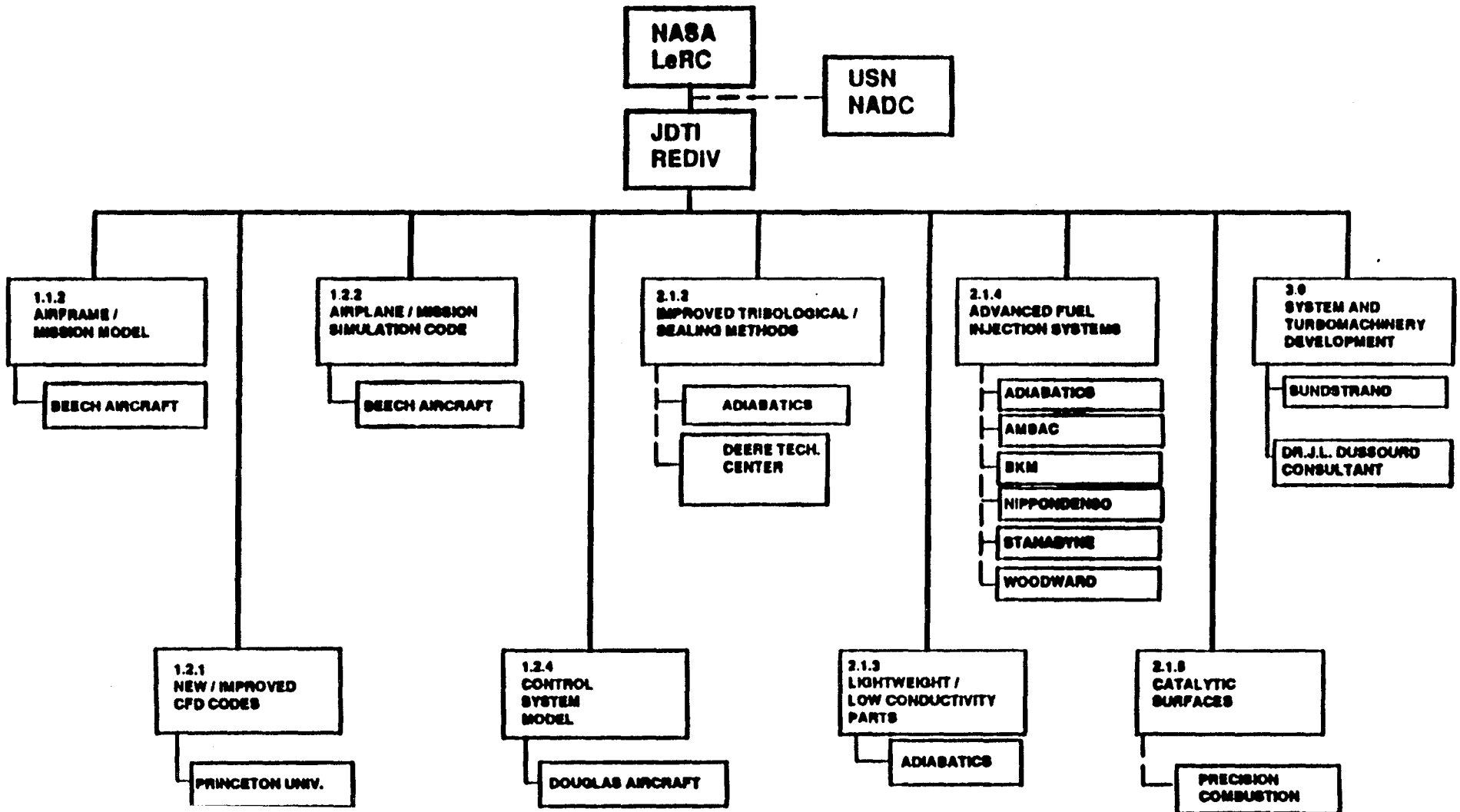


Figure No. 7

STRATIFIED CHARGE ROTARY ENGINE CRITICAL TECHNOLOGY ENABLEMENT

PROGRAM TEAM



STRATIFIED CHARGE ROTARY ENGINE
CRITICAL TECHNOLOGY ENABLEMENT

RE-DIRECTION OF CONTRACT NAS3-25945

GUIDELINES

- o **COMPLETE ALL TESTING BY OCTOBER 31, 1991 (LETTER REQUEST/NASA)**
- o **FOCUS ON BSFC (TARGET 0.375 LBS/BHP-HR (228G/KWH), 1991**
- o **CONTINUE COMBUSTION MODELING CFD WORK**
- o **CONTINUE SINGLE ROTOR RESEARCH RIG ENGINE TESTING**
- o **CONTINUE PERFORMANCE MODELING EFFORT**
- o **CONTINUE LIGHTWEIGHT ROTOR PROCUREMENT**
- o **CONTINUE SELECTED TRIBOLOGY/SEALING/REDUCED FRICTION EFFORTS**
- o **CONTINUE SBIR AND UNIVERSITY COORDINATION**
- o **TERMINATE ALL TURBOMACHINERY WORK**
- o **TERMINATE ALL CONTROLS SYSTEM MODELING WORK**
- o **MODIFIED/REDUCED FUEL INJECTION EFFORT**

Figure No. 9

3.0 PERFORMANCE

PRECEDING PAGE BLANK NOT FILMED

PAGE 20 PREVIOUSLY BLANK

3.1 NASA RESEARCH RIG ENGINE/CRITICAL COMPONENT TESTING

PRECEDING PAGE BLANK NOT FILMED

22

INTRODUCTION

The NASA 1007R Research Rig Engine provides an engine power section test bed for performance and critical component testing. The rig engine design simultaneously provides the capability to perform single rotor engine performance testing while retaining the capability of rapid engine configuration changes. A total of twelve separate rig engine builds were completed for the performance and combustion development portions of the NASA Phase III contract.

The NASA Rig Engine, described by the basic bill of material NJ11950, is comprised of a mainshaft assembly and rotor as the major rotating assemblies. The two end housings encapsulating the rotor housing and two end housing covers are equipped with mainshaft journal bearings to allow the sustained high load and high speed operation required in the rig engine program. A cross section of the rig engine is shown in Figure 1.

The rotor housing assembly includes the fuel delivery and ignition components. Fuel delivery to the combustion chamber is accomplished with two fuel injection nozzles, the main and pilot nozzles. The pilot nozzle, which shares a chamber with the single 12mm spark plug (ignitor), delivers approximately 5% of the total fuel flow at full load. By spraying the pilot fuel charge into the cavity shared with the ignitor fuel ignition is achieved. The ignited fuel then enters the main combustion chamber. The remaining 95% of the fuel flow is injected into the combustion chamber and rotor pocket by the main fuel injection nozzle. The ignited pilot fuel charge then ignites the main fuel charge. The base configuration of the rotor housing fuel injection nozzles, and rotor pocket at top center location are shown in Figure 2.

The rig engine core power section is augmented by a high speed gearbox (reference drawing LS34003) which drives the fuel injection system, and other engine accessories such as turbomachinery and oil metering systems. The fuel injection pump and turbomachinery configurations comprise an element of the power section performance development program.

Engine testing was performed primarily in test cell WX20-6, using an electric dynamometer for engine load and speed control. The engine and dynamometer are linked by a speed reduction gearbox due to dynamometer speed limitations. The driveline configuration is shown in Figure 3.

OBJECTIVE

The Research Rig Engine program focused on three primary goals set forth in the technical proposal:

1. To demonstrate a brake specific fuel consumption (bsfc) of 0.355 lbs/hp-hr (216 g/kwh) at optimum cruise condition above 50% maximum power. It should be noted that the redirection of the program as discussed in Section 2.0 Executive Summary resulted in a 1991 target of 0.375 lb./hp/hr (228 g/kwh). This target was demonstrated.
2. To demonstrate 200 brake horsepower (bhp) from the 0.7 liter displacement research rig, or a specific power of 5 horsepower per cubic inch. This was achieved.
3. To validate the Computational Fluid Dynamics (CFD) predictions for combustion development and reduction of engine bsfc. Validation and correlation of analytical with experimental results was achieved.

TECHNICAL APPROACH

Demonstrating the specific power of 5 horsepower per cubic inch with the research rig engine focused on the evaluation of fuel injection system and turbocharger configurations to achieve the desired power level.

The goal of achieving a bsfc of 0.375 lbs/hp-hr (228 g/kwh) and validating the CFD predictions were closely linked. Concepts for engine combustion development and reducing engine bsfc were derived from the CFD analysis. The CFD program was used to predict engine hardware modifications which would reduce engine bsfc by improving engine combustion characteristics. A series of discrete engine configuration modifications intended to reduce engine bsfc were then prepared. (Development of the engine configurations from the CFD code is described in the section titled New/Improved CFD Codes.) Rationale for the modifications were drawn both from the CFD predictions and from analysis of prior Phase II engine performance test results.

The engine configurations developed for demonstrating the power density goals and for reduction of engine bsfc were the following:

- o Power density demonstration
- o Dual orifice pilot
- o Dual ignitor rotor housing
- o Porting/timing rotor housing
- o Catalytic rotor
- o Leading rectangular pocket rotor
- o Leading standard pocket rotor
- o Dual pocket rotor

Numerous engine builds of different configuration engines were involved in the performance and combustion development testing of the NASA research engine. A tabulation of the key engine configuration components segregated by engine test concept is provided in Table I.

RESULTS

POWER DENSITY DEMONSTRATION

Demonstration of the power density goal of 5 hp /cu. in. (230 kw/ℓ) entailed two engine builds of the essentially standard rig engine configuration, and variation on engine accessories to meet the performance goal of 200 (150 kw) horsepower. Fuel injection pumps capable of operating at engine speeds up to 8500 rpm were defined and procured. Numerous high fuel flow capability fuel injection nozzles with non-shadowing fuel sprays were defined and procured. Turbochargers capable of providing the requisite airflows and withstanding turbine inlet temperatures exceeding 1800°F were prepared for the test.

The NASA rig engine demonstrated an observed power output of 197 (148 kw) horsepower at 8400 rpm. When adjusted for friction losses in the test cell speed reduction gearbox the engine output meets the NASA performance goal of 200 horsepower (150kw) from the 0.7 liter rig engine. The power output was obtained at 8400 rpm and an engine load of 227 (1.56 mPa) psi bmep. Engine combustion pressures did not exceed 1200 psi (8.27 mPa).

Further details of engine performance and hardware development are provided in Reference 1.

DUAL ORIFICE PILOT

The dual orifice pilot nozzle demonstrated perhaps the most significant bsfc performance gains of all the configurations tested. Reductions in engine bsfc of 4.3% observed at 4400 rpm were directly attributable to the dual orifice pilot modifications. Minimal hardware changes to the research rig engine design provided the observed performance improvement.

The dual orifice pilot nozzle and the attendant modifications to the pilot/ignitor cavity were tested in two engine builds, engine 0705-1 and engine 0704-10. The two engine configurations differed in significant features such as compression ratio and other performance related features. However, the performance improvements identified in both engines were of equal significance.

The dual orifice pilot engine 0705-1 demonstrated a reduction in observed brake specific fuel consumption of 4.3% at 4400 rpm. The best performance of the 7.5:1 compression ratio (CR) engine 0705-1 was at 5500 rpm. An observed bsfc of 0.422 lbs/hp-hr (257 g/kwh) was obtained at 98 brake horsepower (73.5 kw) and 5500 rpm. Detailed engine test performance results for Engine 0705-1 are provided in Reference 2.

Testing of the Dual Orifice Pilot in Engine 0705-1 encountered numerous difficulties in achieving hardware durability. The Dual Orifice Pilot demonstrated superior fuel ignition but suffered poor hardware durability in the first engine build 0705-1. The poor durability was due to high temperatures generated within the pilot-ignitor cavity. The high temperatures caused carboning of the fuel injection nozzle tips and severe erosion of the spark plug electrodes. Analysis of the nozzle durability problem and the development of a fuel system to improve Dual Orifice Pilot performance are provided in Reference 3. The changes developed were incorporated in the second Dual Orifice Pilot Engine 0704-10.

Engine 0704-10 demonstrated the reduction in engine bsfc achieved with a combination of performance related improvements and the dual orifice pilot nozzle. Engine 0704-10 with an 8.5:1 CR demonstrated an observed bsfc of 0.398 lbs/hp-hr (242 g/kwh) at 169 psi (1.164 mPa) bmep and 5500 rpm, or 95 horsepower (71kw). The bsfc performance of Engine 0704-10 meets the September 1991 bsfc goal of 0.375 lbs/hp-hr (228g/kwh) when adjusted for engine friction differences. An observed bsfc below 0.41 lbs/hp-hr (249 g/kwh) was demonstrated between 145 psi (0.999 mPa) and 180 psi (1.24 mPa) bmep at 6000 rpm, or 89-110 hp (67-83 kw). Further details of the engine test results are provided in Reference 4.

DUAL IGNITOR

The dual ignitor engine provided two ignition sources in the combustion chamber. A trailing, trochoid-surface mounted ignitor was incorporated to supplement the standard pilot ignitor. The engine was further modified to provide main nozzle light-off fuel sprays directing fuel to the trochoid ignitor.

The final configuration of the dual ignitor engine, tested in Engine 0704-8, allowed successful demonstration of a dominant trochoid ignitor combustion contribution. A 7.5% reduction in observed bsfc was provided by the trochoid ignitor at 130 psi bmep (0.896 mPa) and 6000 rpm, or 80 bhp (60kw). The best observed bsfc was 0.455 lbs/hp-hr (277 g/kwh) at 131 psi (0.902 mPa) bmep and 6000 rpm. Further discussion of the performance results for the four dual ignitor engines is provided in References 5 and 6.

Additional reductions in bsfc at higher loads were limited in the dual ignitor engine by the onset of combustion instability. Combustion analysis of engine operation with the dual igniter was undertaken to further examine the combustion instability phenomena observed. Three references discussed in the following paragraphs examine different aspects of the observed instability.

The first analysis effort focused on identifying the cause and the effect of the combustion instability observed in the dual igniter engine. The instability is attributed to auto ignition of the Jet-A fuel being burned. The auto ignition of the fuel is attributed to the rapid combustion pressure rise generated by the dual igniter engine configuration. Combustion cycle analysis indicated that the combustion instability and spikes did not detract from the

engine work output. The combustion instability and spikes were concluded to be detrimental primarily due to the high variability in engine output and peak combustion pressures generated. The rapid combustion pressure rise in particular appeared to affect the apex seal sealing effectiveness. The complete analysis is provided in Reference 7.

The second analysis effort compared the effectiveness of fuel lightoff for two configurations of trochoid mounted spark plugs; and the effect of increasing engine intake air temperatures on engine combustion. The analysis concluded that an electrode type spark plug resulted in far less cycle to cycle variability (indicated by misfires) than the surface gap type spark plug. The increased intake air temperature appears to have resulted in faster combustion, somewhat higher peak pressures and greater instability in the combustion pressure traces. The analysis is provided in further detail in Reference 8.

The third analysis examined in detail the effect of fuel octane rating on the combustion instability observed in the dual igniter engines. The combustion instability was effectively eliminated while operating on high octane fuel (gasoline). This demonstration appeared to confirm the hypothesis that auto ignition of the Jet A fuel was responsible for the combustion instability. Further discussion is provided in Reference 9.

PORTING/TIMING ENGINE

The Porting and Timing engine was designed to evaluate the effects of variable intake port flow area and variable intake opening and closing times on engine performance. The standard rotor housing and the variable porting/timing rotor housing are shown in Figure 4. Inserts (not shown) were designed for the Porting/Timing rotor housing which provided selective opening and closing times and port flow areas within the enlarged port areas evident in Figure 4. The rotor housing for Engine 0704-9 was originally intended to provide both variable intake and variable exhaust ports. However, errors in the rotor housing casting process prevented incorporating the variable exhaust ports. A salvage rework provided an exhaust port area enlarged by 33% compared to the standard exhaust port. The Porting/Timing rotor Housing shown in Figure 4 was completed after testing of Engine 0704-9.

The rotor housing tested in Engine 0704-9 provided three variations of intake flow areas and intake port opening/closing timings. The three intake port variants provided were the standard rig engine flow area and opening/closing timings, a 42% larger intake port with early opening and late closing, and a standard flow area with late opening and late closing timings.

All three variants were tested with the enlarged exhaust port described above. New intake and exhaust manifolds were provided to match the enlarged intake and exhaust flow areas.

Performance testing of the porting/timing Engine 0704-9 indicates that the standard intake port area and timing provides the lowest engine bsfc, and that a 3% reduction in bsfc was attributable to the enlarged exhaust port flow area. The Engine 0704-9 demonstrated an observed bsfc of 0.447 lbs/hp-hr (272 g/kwh) at 6000 rpm and 180 psi (1.24 mPa) bmep. The bsfc performance of the three intake ports appeared to converge at high engine loads.

The clear reduction in bsfc demonstrated in Engine 0704-9 indicates the need to further investigate the effects of intake and exhaust porting and timing. Comprehensive performance testing of the variable intake and exhaust port rotor housing is strongly recommended. More detailed discussion of the performance results of Engine 0704-9 are provided in Reference 10.

CATALYTIC ROTOR

The catalytic rotor engine test was intended to establish the potential for catalytic surfaces to improve combustion rates and improve engine operating efficiency. The catalytic coating is intended to promote combustion of fuel in close proximity to the rotor face and pocket. The catalytic coating, by promoting the oxidation process, is intended to reduce fuel ignition delay and promote combustion stability at lower temperatures than would be required for non-catalytic surfaces.

The catalytic coating is a proprietary coating developed and applied by Precision Combustion (reference SAE paper 890326). The catalytic coating was applied over a thermal barrier coating intended to increase the rotor surface temperature. The thermal barrier coating was tested in the NASA Phase II engine test program.

The catalytic rotor engine 0705-2 demonstrated a best observed bsfc of 0.427 lbs/hp-hr (260 g/Kwh) at 165 psi (1.137 mPa) bmep and 6000 rpm. Engine output is 100 bhp (75 kw) or 50% cruise power at the above speed and load.

A reduction in engine brake specific fuel consumption due to the catalytic coating applied to the rotor flank and pocket was not observed. The catalytic rotor engine performance was essentially identical to the thermal barrier rotor without the catalytic coating. Additional performance results are described in detail in Reference 11.

ROTOR COMBUSTION POCKET DEVELOPMENT

The CFD analysis produced four proposed variants of rotor combustion pocket shapes. The combustion pocket shape changes were predicted by CFD to increase gas recirculation within the rotor pocket during the compression and combustion phases of the engine cycle. Increased gas circulation was predicted to improve fuel-air mixing and to increase combustion rates.

The different pocket shapes proposed are shown in Figures 5 and 6. Figure 5 shows cross-sections of the standard pocket, the leading standard pocket, the leading re-entrant pocket and the leading rectangular pocket. The re-entrant pocket was not produced due to concerns for hardware durability from the formation of 'hot spots' at the thin cross-sectional areas created by the re-entrant shape. The leading rectangular pocket was a compromise design intended to emulate the characteristic behavior of a 'true' re-entrant pocket.

Figure 6 is a photograph of the four rotor pocket configurations which have been manufactured. Three of the pocket designs, the standard pocket, the leading standard pocket, and the leading rectangular pocket, were engine tested. The fourth, the dual pocket design, was not engine tested due to the foreshortening of the NASA contract effort.

Details of the hardware configurations and engine test results for the three combustion development rotor pockets are provided in the following sections.

LEADING RECTANGULAR POCKET ROTOR

The leading rectangular pocket rotor was predicted by CFD to increase gas recirculation and diffusivity and hence improve fuel and air mixing in the rotor pocket. Both the recirculation and diffusivity are to be driven by the squish flow from the trailing flank of the rotor. The rotor was modified to relocate the pocket to the leading flank of the rotor. The rotor pocket is roughly rectangular in shape as shown in Figure 5. To accommodate the relocated rotor pocket, an After Top Center (ATC) Main rotor housing was developed. The ATC Main housing featured relocated main and pilot fuel injectors and ignitor to correspond to the location of the leading rectangular rotor pocket when the engine is at top center. The location of the injectors and ignitors was derived from initial optimization studies using CFD. The 8.5:1 compression ratio Leading Rectangular (LR) pocket rotor and ATC Main rotor housing were tested in Engine 0707-1.

Performance of the LR pocket rotor demonstrated a slight penalty in observed bsfc but was limited in engine load capability by a pressure wave phenomena. An observed bsfc of 0.481 lbs/hp-hr (293 g/kwh) was demonstrated at 115 psi (0.792 mPa) bmep and 4400 rpm. This bsfc indicates a 1.5% increase compared to the 'standard' NASA rig engine configuration. Engine load capability was limited due to the presence of a pressure wave in the combustion chamber which generated conditions exceeding hardware design pressure limits.

Operating at 115 psi (0.792 mPa) bmep and 4400 rpm the combustion pressure in Engine 0707-1 was 44% higher than the comparable standard rig engine. A combustion pressure of 1600 psi (11.02 mPa) was observed at 6000 rpm and 112 psi (0.772 mPa) bmep. Detailed performance test results for the leading rectangular pocket rotor engine 0707-1 are provided in Reference 12.

The pressure wave phenomena was approximated using additional CFD analysis. The additional analysis indicates the pressure wave results from the rapid combustion generated by the leading rectangular pocket rotor. Further details of the analysis are provided in Reference 13. Additional study is required before final conclusions can be provided.

LEADING STANDARD POCKET ROTOR

The leading standard pocket rotor was predicted by CFD to increase diffusivity and hence fuel and air mixing in the rotor pocket. The diffusivity is predicted by CFD to be driven by the squish flow from the trailing flank of the rotor.

The leading standard pocket rotor provides a pocket shape identical to the standard rotor pocket relocated towards the leading flank. The leading standard pocket rotor was tested with the ATC Main rotor housing developed for use with the leading rectangular pocket rotor. The 8.5:1 compression ratio leading standard pocket rotor and ATC Main rotor housing were tested in Engine 0707-2.

The leading standard pocket rotor demonstrated an observed brake specific fuel consumption of 0.439 lbs/hp-hr (267 g/kwh) at 204 psi (1.405 mPa) bmep and 4400 rpm. A limited test duration of nine hours did not allow sufficient time for extensive performance optimization.

Performance of the leading standard rotor pocket indicated a 1.5% increase in observed bsfc relative to the standard location pocket rotor at 160 psi (1.102 mPa) bmep and 4400 rpm.

The leading standard pocket rotor engine 0707-2 demonstrated significant difficulty operating at speeds above 4400 rpm. A high frequency of engine misfire at engine speeds above 4400 rpm was encountered. The high rate of misfires prevented obtaining acceptable performance at speeds above 4400 rpm. An engine modification to reduce the misfire rate, such as the dual orifice pilot would appear to be required.

Additional details of performance tests of the leading standard pocket rotor engine 0707-2 are provided in Reference 14.

DUAL POCKET ROTOR (AND ROTOR HOUSING)

The dual pocket rotor design features two rotor pockets located symmetrically around the rotor flank center. The two pockets form separate combustion "chambers" for each of the trochoid lobes located on opposite sides of the rotor housing minor axis. Each pocket provides a separate main fuel injection nozzle and ignitor. The separate main fuel nozzles provide independent fuel injection timing and fuel flow for the two rotor pockets. The two rotor pockets are designed with equal displacements and yield an overall engine compression ratio of 8.4:1.

Two configurations of rotor housings were designed for use with the dual pocket rotor. The first design provided a single main fuel injection nozzle and trochoid surface mounted ignitor for each rotor pocket. The second, and preferred configuration, provides a separate pilot nozzle and pilot/ignitor cavity in addition to the main fuel injection nozzle for each rotor pocket. The pilot nozzle and ignitor cavity were added to address concerns regarding possible difficulties establishing stable fuel ignition and combustion in each pocket without the standard pilot ignition capability.

The dual pocket rotor and the first rotor housing with the main nozzle/ignitor configuration are available in machined hardware for testing. The second rotor housing featuring the pilot nozzle ignitor combination for fuel ignition is available in casting form but requires finish machining before testing could proceed.

CONCLUSIONS

1. The NASA single rotor rig engine demonstrated the power density of five horsepower per cubic inch (230 kw/ℓ), or 200 horsepower (150 kw) from 0.7 liter displacement, as set forth in the NASA Phase III technical proposal.
2. The NASA single rotor rig engine demonstrated the September 1991 brake specific fuel consumption goal (bsfc) of 0.375 lbs/hp-hr (228 g/kwr) when adjusted for engine friction differences. Achievement of the bsfc goal is based upon an observed bsfc of 0.398 lbs/hp-hr (242 g/kwr) at 169 psi (1.164 mPa) brake mean effective pressure (bmep) and 5500 rpm demonstrated in Engine 0704-10.
3. The NASA single rotor rig Engine 0704-10 demonstrated an observed bsfc below 0.41 lbs/hp-hr (249 g/kwr) between 145 psi (0.999 mPa) and 180 psi (1.240 mPa) bmep at 6000 rpm. An equivalent expression of this performance is an observed bsfc of 0.41 lbs/hp-hr or better between 45% and 55% cruise powers.
4. The configuration of Engine 0704-10 appears to provide the best near term configuration of the NASA rig engine. The significant features of Engine 0704-10 include the modified dual orifice pilot nozzle and pilot/ignitor cavity, an 8.4:1 compression ratio, and an enlarged exhaust port.
5. The dual orifice pilot nozzle configuration appears to provide the capability to extend the successful lean operating limit of the SCORE 70 engine.
6. The Nippondenso/Ambac type 9mm dual orifice pilot nozzles, used in Engine 0704-10, appear to provide superior performance and durability characteristics than the Stanadyne 5mm dual orifice pilot nozzles used in Engine 0705-1.
7. The dual ignitor engine configuration appears to require a redesign to overcome the combustion instability observed while operating on Jet A fuel. The redesign should address the load limitation encountered when operating with lightoff spray angles greater than 75 degrees. Spray angles greater than 75 degrees were required to obtain a trochoid ignitor combustion contribution. A complete reconfiguration to reverse lightoff spray direction and to relocate the trochoid ignitor correspondingly may be required. Additional CFD analysis may indicate the best development direction for the dual ignitor concept.
8. The leading rectangular pocket rotor appears to provide a significant increase in the engine combustion rate. Additional development is required to eliminate or mitigate the combustion pressure wave observed and to establish optimum engine configuration and performance.

9. The leading standard pocket rotor demonstrated a slight performance penalty relative to the standard rig engine during the limited amount of testing completed. Optimization of nozzle spray patterns and/or nozzle locations may be required to achieve the performance potential of the leading standard pocket rotor. Fuel lightoff performance problems at engine speeds above 4500 rpm must be addressed before further engine testing can fully explore the leading standard pocket rotor performance potential.

RECOMMENDATIONS

1. The NASA reference engine design should incorporate the major performance design features of the rig Engine 0704-10. The significant features include the modified pilot ignitor cavity, the 9mm pilot nozzle tips, an 8.4:1 compression ratio, and an enlarged exhaust port. Further performance testing is strongly recommended to examine engine performance at 7250 rpm and above, and to more clearly identify optimum engine F:A ratios, turbo-charger requirements, nozzle spray configurations, and fuel injection pump configuration.
2. The porting/timing engine configuration (reference decision number 12875NJ) should be tested. The effects of exhaust port opening and closing, and exhaust port flow area were demonstrated in Engine 0704-10 to be critical to engine performance. Test and analysis of the effects of exhaust port opening and closing, exhaust port flow area, and the interaction of these changes with the same variables of intake porting and timing, may provide additional performance improvements. Analysis and testing of intake plenum volumes and intake manifold tract lengths may be required to accommodate the broad range of engine speed operation encountered in this engine application.
3. Further development of the leading rectangular pocket rotor should work to eliminate the combustion pressure wave phenomena and to optimize the engine configuration. Modifications to the pressure relief slot appear to be required to prevent propagation of the combustion pressure to the trailing flank. Concepts which prevent this propagation should be analyzed and tested. Other alternatives include modifying the pocket to extend across the minor axis (by ramping the pocket trailing wall) to relieve pressure in the trailing flank. Optimization of the engine configuration should also address identifying nozzle spray configurations optimized for the rectangular pocket, and establishing reliable pilot fuel lightoff. The dual orifice pilot configuration is recommended as the best available means of providing this improvement.
4. The leading standard pocket rotor requires additional testing to identify avenues of continued development. Modifications to address the pilot lightoff difficulties

encountered with this configuration are required. The dual orifice pilot appears to be a likely method of improving the fuel lightoff performance.

LIST OF REFERENCES

1. "Power Density Performance Demonstration, Engine 0704-4 and 0704-5", C.R. Shoemaker, December 1991
2. "Performance Test of Dual Orifice Pilot Injection Nozzle, Engine 0705-1", C.R. Shoemaker, 5 March 1991
3. "Investigation into Changes in Engine Light-Off Performance using the 2 Orifice "Rabbit Ear" Pilot Configuration", A. Meyer, 30 Apr. 1991
4. "Demonstration of BSFC Capability for NASA 1007R Rig Engine, Engine 0704-10", C.R. Shoemaker, 20 November 1991
5. "Performance Test of Modified Dual Ignitor Engine, Engine Builds 0704-7, 0704-8 and 0705-3", C.R. Shoemaker, 4 October 1991
6. "Performance Test of Modified Dual Ignitor Engine, Engine Builds 0704-7, 0704-8, and 0705-3", C.R. Shoemaker, 4 October 1991
7. "Analysis of Experimental Pressure Traces from the Dual Ignitor Engine (Engine Build #0704-8)", J. Abraham and P. Epstein, 26 July 1991
8. Memo; J. Abraham to C. Irion, Subject: "Analysis of Experimental Pressure Traces from the Dual Ignitor Engine Build #070503 and Build #0704-8", 6 Aug. 91.
9. Memo; J. Abraham T. C. Irion, Subject: "Analysis of Experimental Pressure Traces from the Dual Igniter Engine #0705-3", 27 Aug. 91.
10. "Performance Test of Porting/Timing Engine 0704-9", A.E. Meyer, 4 December 1991
11. "Engine 0705-2, Performance Test of Catalytic Surface, Thermal Barrier Rotor", C.R. Shoemaker, 15 July 1991
12. "Performance Test of Leading Rectangular Pocket Rotor, Engine 0707-1", C.R. Shoemaker, 26 November 1991
13. Memo: J. Abraham to C. Shoemaker, Subject: "Correlation of Experimental and Analytical Results of Leading Rectangular Pocket", 6 Dec 1991
14. "Performance Test of Leading Standard Pocket Rotor, Engine 0707-2", C.R. Shoemaker and P. Dimpelfeld, 1 December 1991.

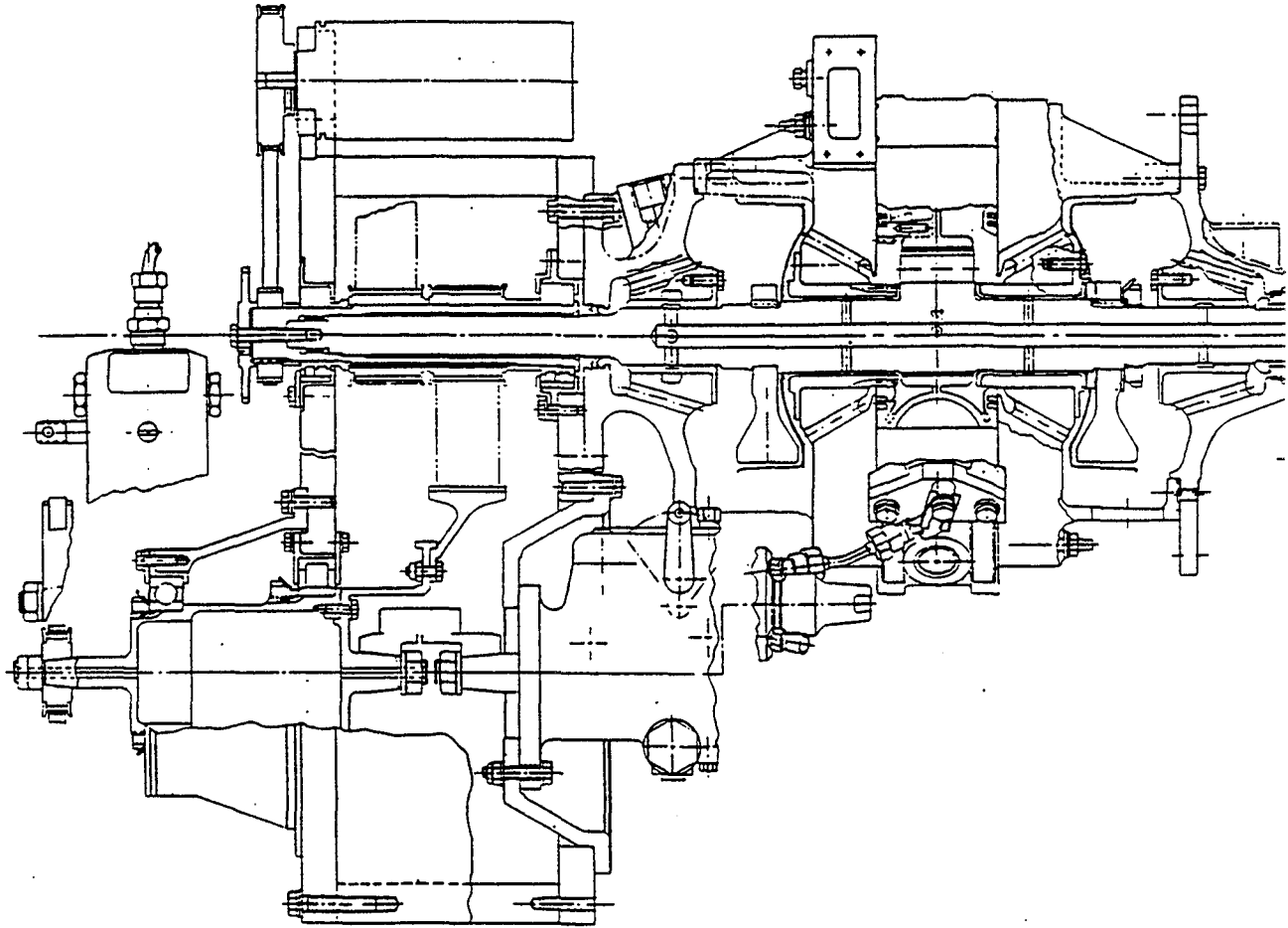


Figure 1. NASA SINGLE-ROTOR RIG ENGINE

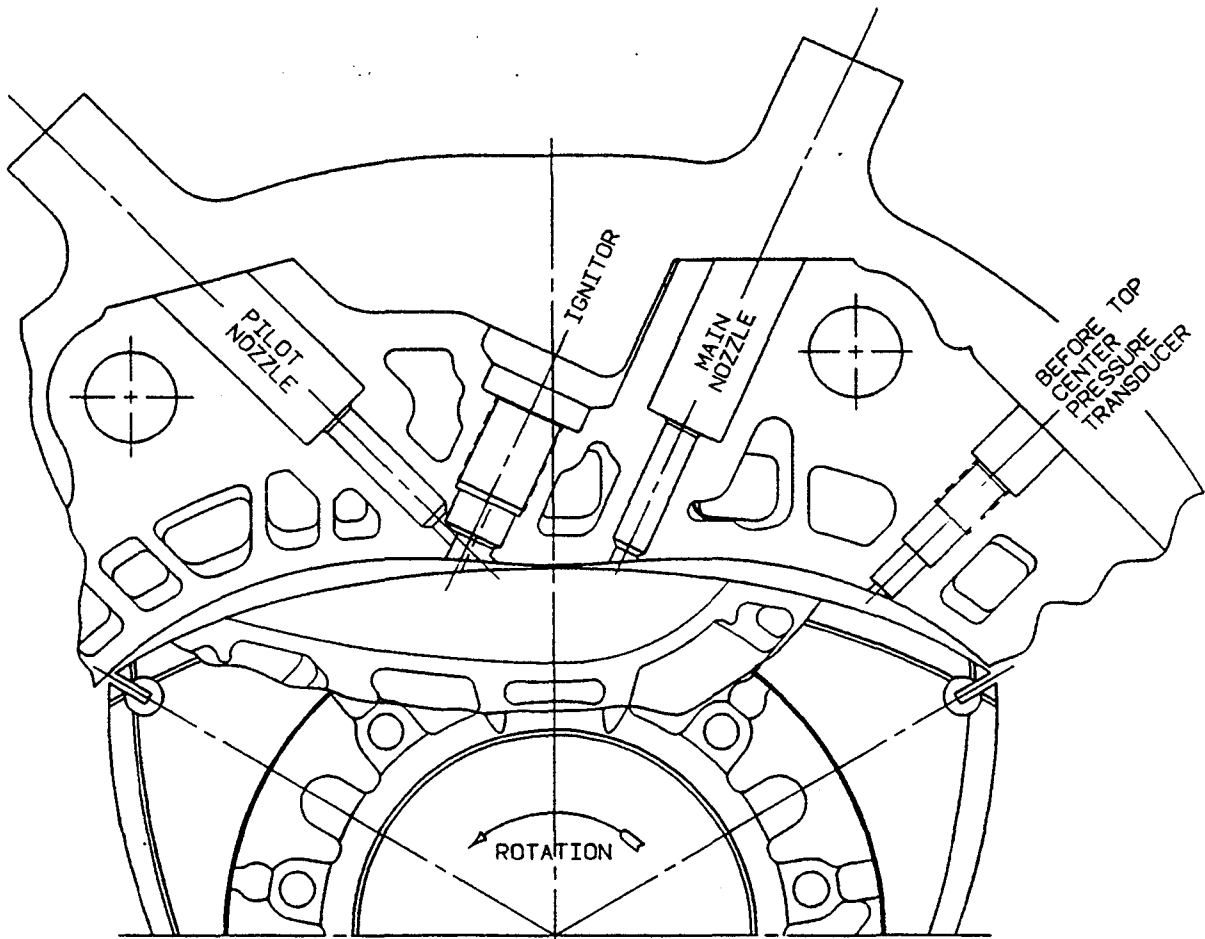


FIGURE 2

CROSS SECTION OF STANDARD
RIG ENGINE AT TOP CENTER
POSITION

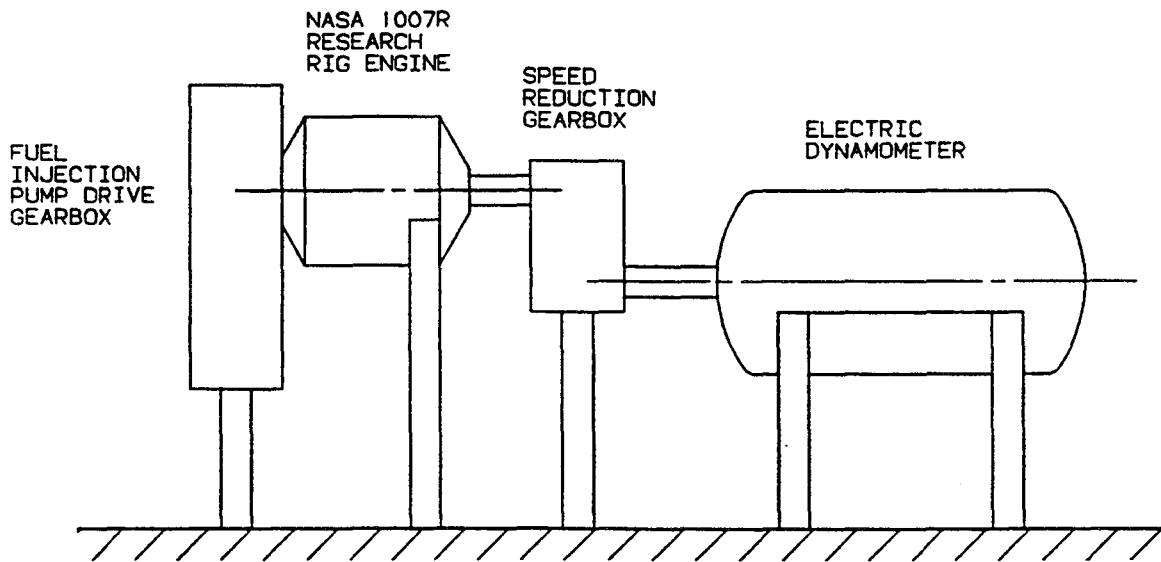


FIGURE 3

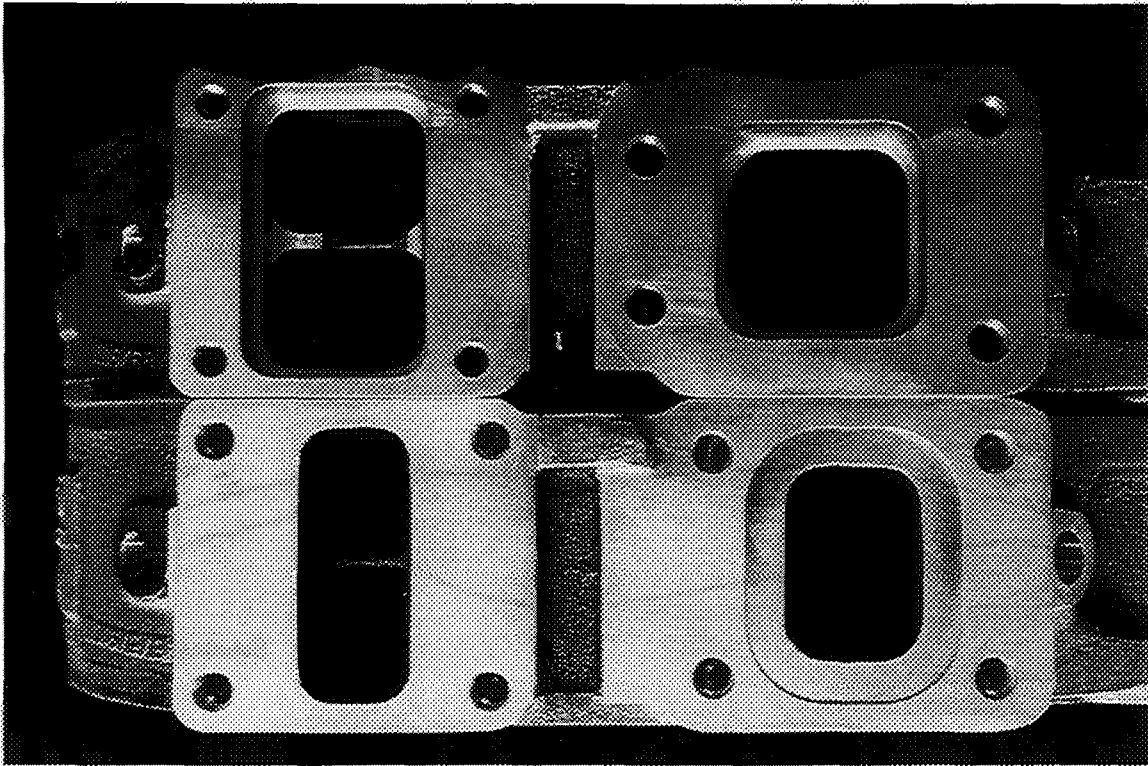
ENGINE AND DYNAMOMETER
DRIVELINE-WX20-6

TABLE I
NASA 1007R RIG ENGINE CONFIGURATIONS

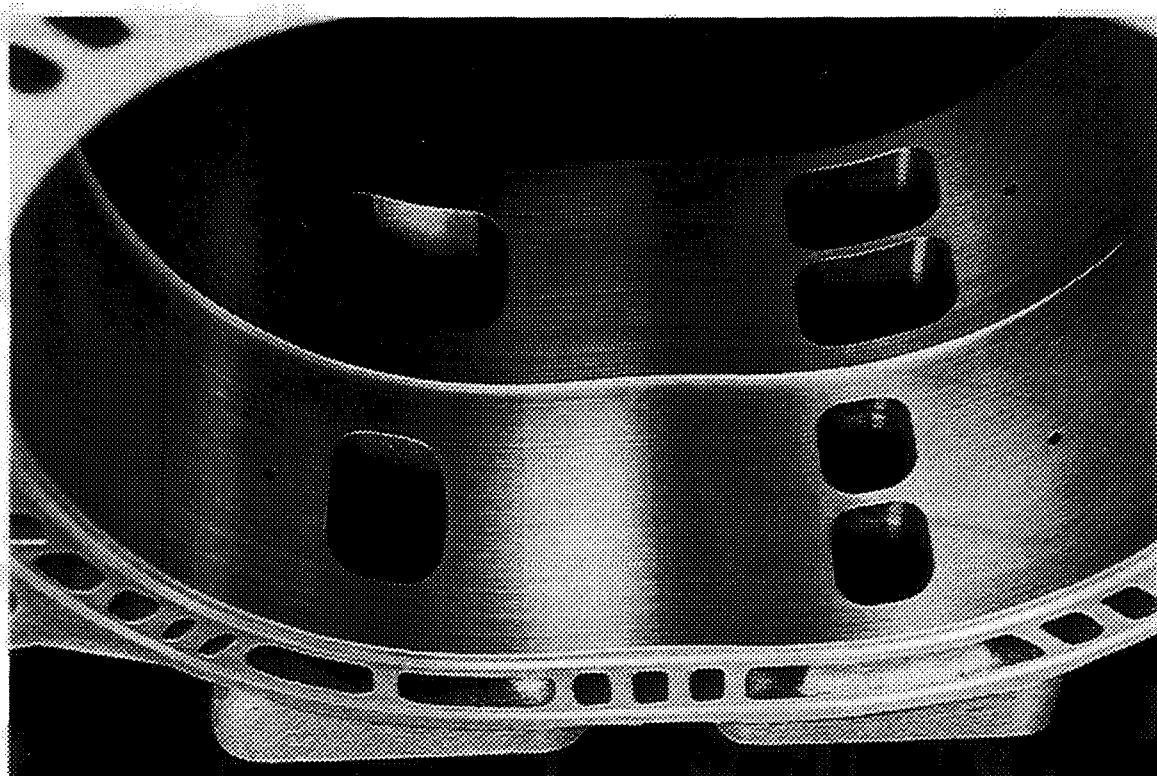
ENGINE TEST CONCEPT	POWER DENSITY DEMONSTRATION		DUAL ORIFICE PILOT NOZZLE		DUAL IGNITOR		
	200 HP						
ENGINE NUMBER	0704-4	0704-5	0705-1	0704-10	0704-6	0704-8	0705-3
Housing Rotor	210001	070X00118N1	070X00024A	070X00237A	NR10290	NR10290 (REWORK)	070X00267A
Rotor Assy.	NR10246N2	NR10246N2	NR10246N2	NR10246N2	NR10246N2	NR10246N2	NR10246N2
Rotor Compression Ratio	NJ12419N2 7.5:1	NJ12419N2 7.5:1	NJ12419N2 7.5:1	NJ12419N2 8.5:1	NJ12419N2 7.5:1	NJ12419N2 7.5:1	NJ12419N2 7.5:1
Rotor Bearing	210008N2	210008N2	210008N2	210008N2	NJ12462	NJ12462	NJ12462
Crankshaft	NJ11488	NJ11488	NJ11488	NJ11488	NJ11488	NJ11488	NJ11488
Apex Seals	ES10470	ES10470	NJ12463	NJ12463	NJ12463	NJ12463	NJ12463
Side Seals	NJ11154N2 Lap Butt	NJ11138N3 Lap Butt	210112N2 Lap Butt	NJ11138N3 Lap Butt	NJ11138N3 Lap Butt	NJ11138N3 Lap Butt	NJ11138N3 Lap Butt
Pilot FI Nozzle	210028N	210028N	070X0009, 10, 11A	NJ11961N156, N157, N158	210028N	210028N	210028N
Main FI Nozzle	210028N	210028N	210028N	210028N	NJ12394N	NJ12394N	NJ12394N
Turbocharger Turbine Housing	T04B/T04E 1.3 A/R	T04B 1.3 A/R	T04E 0.81 A/R	T04E 0.68 A/R	T04E 0.81 A/R	T04E 0.81 A/R	T04E 0.81 A/R
Spark Plug Plug Diameter	A5YC 12mm	A5YC 12mm	A5YC 12mm	C53YC 14mm	A5YC/NJ12564 12mm/10mm	A5YC/NJ12564 12mm/10mm	A5YC/A5YC 12mm/12mm
Manifold, Intake	210074	210074	210074	070X00159A	210074	210074	210074
Manifold, Exhaust	210075	210075	210075	NJ13005	210075	210075	210075

TABLE I (CONTINUED)

ENGINE TEST CONCEPT	CATALYTIC ROTOR	VARIABLE AREA PORT TIMING	LEADING RECTANGULAR POCKET ROTOR/ATC MAIN ROTOR HOUSING	LEADING STANDARD POCKET ROTOR/ ATC MAIN ROTOR HOUSING	DUAL POCKET ROTOR
ENGINE NUMBER	0705-2	0704-9	0707-1	0707-2	NOT TESTED
Housing Rotor	070X00118N1	070X00228A	NR10527	NR10527	NJ12997
Rotor Assy.	NR10246N2	NR10495	NR10514	NR10510	NR10512
Rotor Compression Ratio	NJ10071 8.4:1	NJ12522 7.5:1	NJ12975 8.5:1	NJ12960 8.5:1	NJ12964 8.5:1
Rotor Bearing	NJ12462	NJ12462	NJ12437	NJ12437	NJ12437
Crankshaft	NJ11488	NJ11488	070X00209A	070X00209A	T.B.D.
Apex Seals	NJ12463	NJ12463	070X00252AN1	070X00252AN1	NJ12463
Side Seals	NJ11138N3 Lap Butt	NJ11138N3 Lap Butt	070X00147AN3 Butt Butt	070X00147AN3 Butt Butt	NJ12958N3 Butt Butt
Pilot FI Nozzle	210028N	NR10139N4	210028N	210028N	n/a
Main FI Nozzle	210028N	210028N	210028N	210028N	070X00246AN, 070X00247AN
Turbocharger Turbine Housing	T04E 0.81 A/R	T04E 0.68 A/R	T04E 0.68 A/R	T04E 0.68 A/R	T.B.D. T.B.D.
Spark Plug Plug Diameter	A5YC 12mm	C63YC 4mm	RA6HC 12mm	RA6HC 14mm	T.B.D.
Manifold, Intake Intake Inserts	210074	070X00159A NJ12586,588,589	210074	210074	210074
Manifold, Exhaust	210075	NJ13005	210075	210075	210075



COMPARISON OF PORT OPENINGS OF STANDARD (BOTTOM)
AND VARIABLE PORT/TIMING (TOP) ROTOR HOUSINGS



FRONT: STANDARD REAR: VARIABLE PORT/TIMING
TROCHOID PENETRATIONS OF STANDARD AND PORT/TIMING ROTOR
HOUSINGS. NOTE THE AVAILABLE VARIATIONS IN PORT CLOSING AND
OPENING POSITIONS OF INTAKE AND EXHAUST PORTS. ROTATION IS
FROM LEFT TO RIGHT.

FIGURE 4

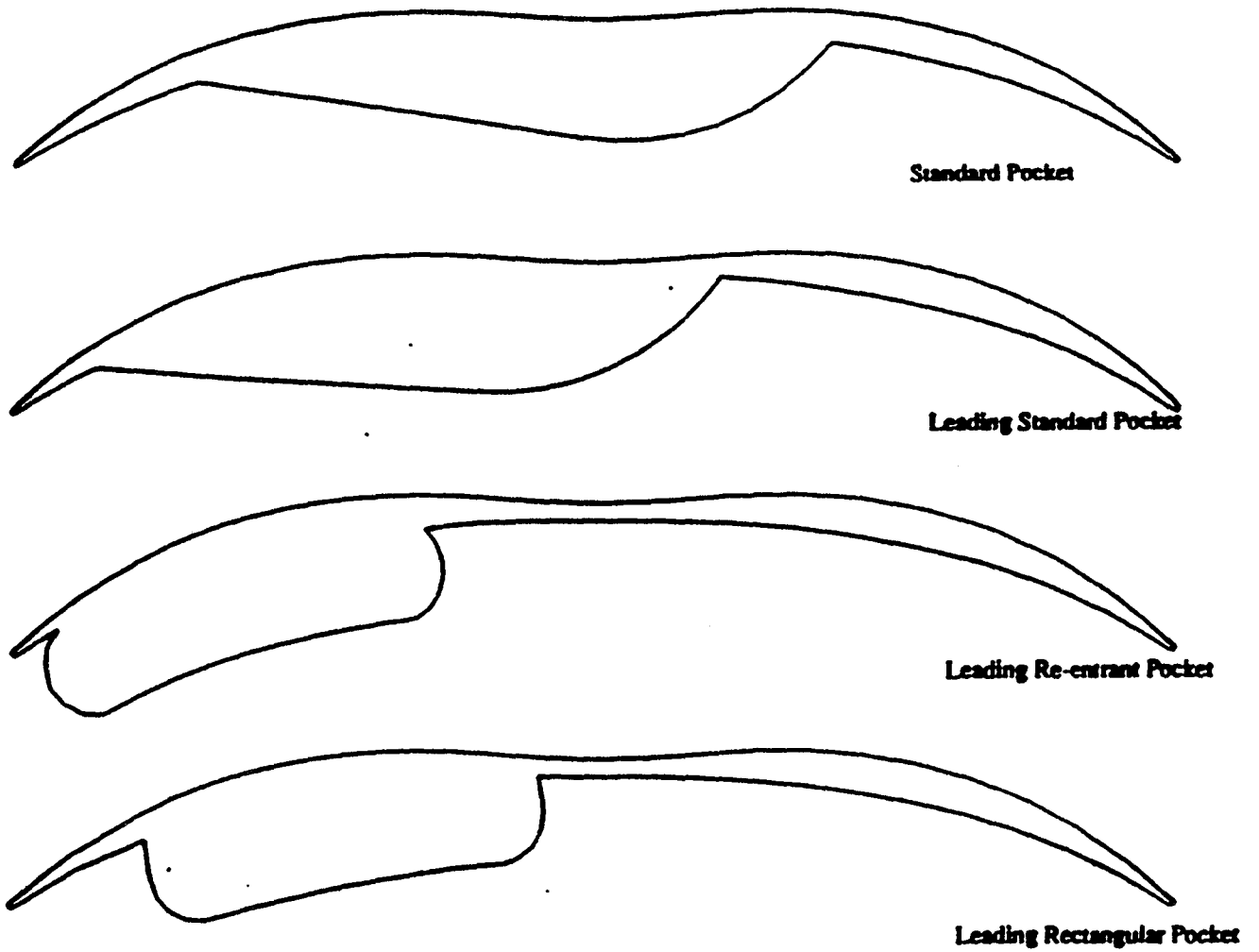
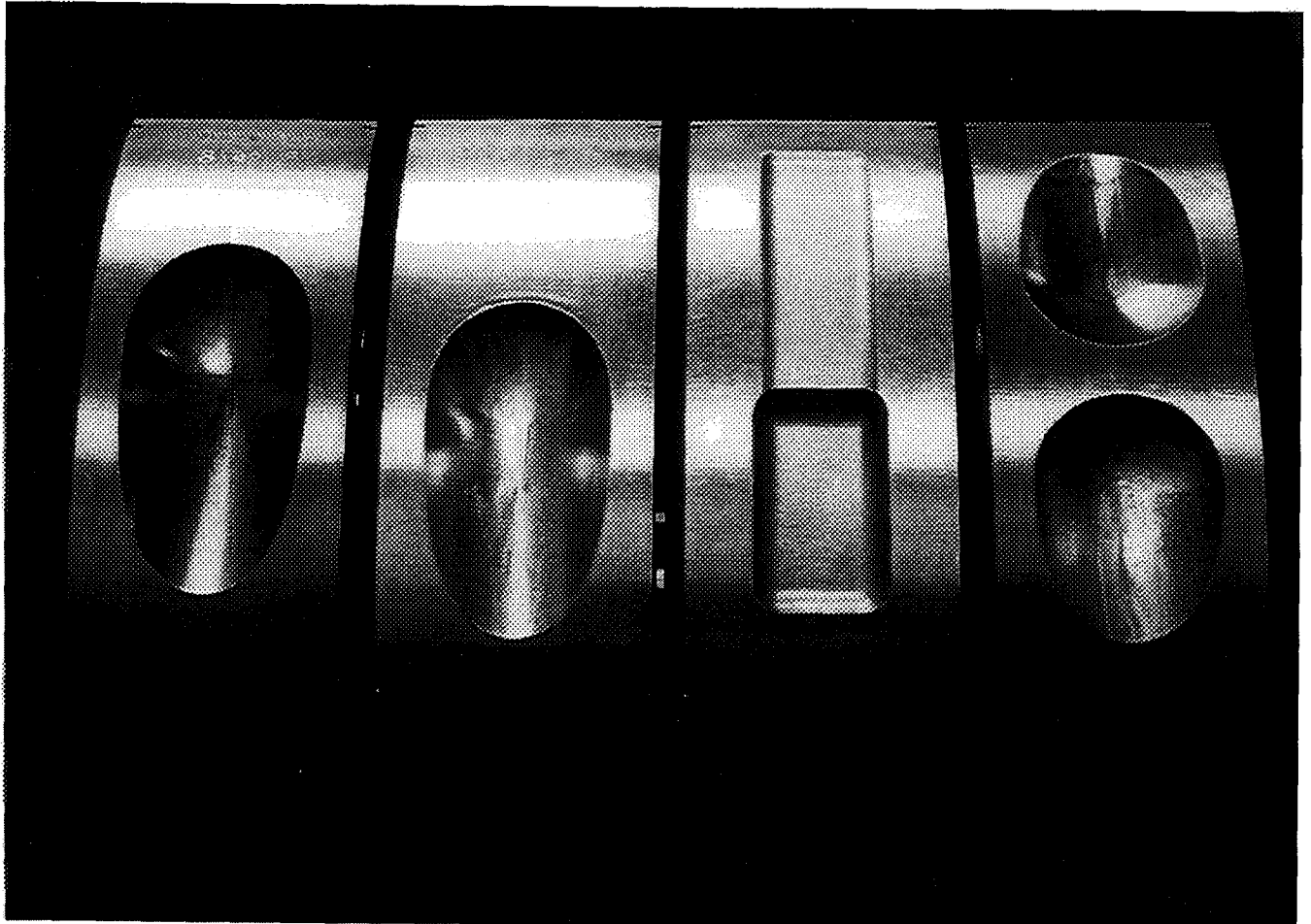


FIGURE 5:
SECTIONS THROUGH THE MIDPLANE FOR FOUR POCKET GEOMETRIES



COMBUSTION DEVELOPMENT ROTOR POCKETS

FROM LEFT TO RIGHT: STANDARD ROTOR POCKET; LEADING STANDARD ROTOR POCKET; LEADING RECTANGULAR ROTOR POCKET; DUAL POCKET. ALL ROTORS SHOWN ARE 8.4:1 COMPRESSION RATIO.

FIGURE 6

3.2 NEW/IMPROVED COMPUTATIONAL FLUID
DYNAMICS (CFD) CODES

INTRODUCTION

During the past decade Computational Fluid Dynamics (CFD) has evolved into a powerful tool to investigate physical problems. This evolution has been spurred by advances in computer hardware and software and by the development of more fundamentally based physical submodels.

During the past five years the techniques of CFD have been applied to stratified-charge rotary engine combustion. References 1-7 describe various aspects of the development and application of CFD to stratified-charge rotary engine combustion.

OBJECTIVES

The objectives of the work described in this section were:

1. To improve the CFD code so as to make them faster and more accurate;
2. To develop graphics visualization tools to enable the results to be examined and interpreted;
3. To use the tools developed in 1. and 2. above to optimize the stratified-charge rotary engine; and
4. To couple the three-dimensional CFD code and a structural analysis code to obtain better estimates of heat fluxes.

TECHNICAL APPROACH

The tasks which would fulfill the objectives 1. and 2. above were subcontracted to Princeton University while John Deere concentrated on the tasks which would fulfill the objectives listed as 3. and 4. above. The scope of the original subcontract to Princeton was changed in October 1990 because of changes in John Deere's rotary engine program. The change involved reductions in cost and duration by about 30%. As part of the agreement leading to this reduction, 'Improvements to Submodels' in section 3.1.2.3 of the statement of work was not done. Reference 7 describes the work done at John Deere to fulfill objective 4. Reference 8 is a report which describes the work done at Princeton to fulfill objective 1. Reference 9 is a report which describes the work done at Princeton to fulfill objective 2.

In order to fulfill objective 3 above, the following approach was taken. Through computations made during the period 1988-89 modifications to the main injector and pilot injector spray patterns and to the pilot cavity location had been suggested. These suggestions had been partially implemented in hardware and shown to improve performance. Initial computations

had also been made with a two igniter configuration. References 10-12 describe the analysis of the test data from the dual igniter configuration. During the period of the work reported here, additional computations were made for a two igniter configuration. An additional focus of the work was on changes to the geometry of the engine. Exploratory work was done to assess the feasibility of using air-assist injectors and to assess the effect of injection rates on engine performance with the objective of optimizing engine efficiency.

A STARDENT mini-supercomputer (Model 3000) purchased for the program and a slower STARDENT (Model 1500) were used to perform the computations. The STARDENT 3000 was used exclusively to make computations for this contract.

RESULTS

NOTE TO READER: Complete graphical illustrations in support of these analytical, iterative evaluations and discussion is provided in Volume II Appendix A. Some examples are included in this section for reference and are noted by an asterisk. However, for the complete association of illustrations and text (too voluminous to be included here) the reader is referred to Volume II Appendix A, "New/Improved Computational Fluid Dynamics (CFD) Codes/ Detailed Illustrations".

POCKET GEOMETRY

Depth of Pocket

The first set of computations were made with pockets of different depths. Figs. 1 (a)*-(c) show three such pockets. Fig.2* shows the computed pressure in the chamber for the three pockets respectively as a function of crank angle. It may be seen that the deeper and more compact pocket results in the fastest burning. However, from a practical point of view, a limit on increasing the depth of the pocket exists because of possible interference with the bearing. The alternate approach of increasing the K-factor (i.e. R/e ratio) was also considered. However, in order to obtain the same displacement with an increased K-factor the size of the engine has to be increased. If the size were to be kept the same, the increased efficiency on account of the increased depth of the pocket would not offset the reduced power on account of reduced displacement. Hence the next step was to consider relocating the pocket along the face of the rotor so that interference with the bearing could be avoided when the depth of the pocket was increased.

B. Relocated Pockets

Computations were made with the standard (baseline) pocket relocated circumferentially along the face of the rotor towards the leading edge and towards the trailing edge. In the case of the leading pocket the standard pocket was shifted toward the leading edge by 5 degrees whereas in the case of the trailing pocket the pocket was shifted toward the trailing edge by 10 degrees. (The angle of shift refers to the arc that defines the rotor surface).

Figs. 3(a)*-(e), 4(a)-(e), and 5(a)-(e) show the diffusivity contour lines in the plane of symmetry at different crank angles around top-center (TC = 1170 degrees) for the standard, the leading and the trailing pockets respectively. Figs. 3(a), 4(a) and 5(a) show that at 1140 degrees (30 BTC) most of the air in the leading and standard pockets has a diffusivity between 40 and 60 cm²/s and most of the air in the trailing pocket has a diffusivity between 20 and 40 cm²/s. Figs. 3(b), 4(b), and 5(b) show that at 1155 degrees (15 BTC) most of the air in the trailing and standard pockets has a diffusivity between 40 and 60 cm²/s, but most of the air in the leading pocket has a diffusivity above 40 cm²/s and significant amounts are above 60 and 80 cm²/s. Figs. 3(c), 4(c), and 5(c) show that at 1170 degrees (TC) the leading and trailing pockets are each similar to what they were at 1155 degrees, but the standard pocket has become similar to the leading pocket. Figs. 3(d), 4(d), and 5(d) show that at 1185 degrees (15 ATC) the standard and trailing pockets are each similar to what they were at 1170 degrees, but the leading pocket has a smooth distribution of diffusivity from 20 to 200 cm²/s. Figs. 3(e), 4(e), and 5(e) show that at 1200 degrees (30 ATC) the trailing pocket has not changed much, the leading and standard pockets have increased in average diffusivity. Throughout this interval the trailing pocket was significantly lower in diffusivity than the other two pockets, and the leading pocket was most often higher than the standard pocket. Also the diffusivity was generally highest in the region of the deepest part of the pocket where the fuel is injected.

Figs. 3(f)*-(j), 4(f)-(j) and 5(f)-(j) show the velocity fields in the plane of symmetry and in a plane above the rotor surface at different crank angles beginning at top center. Figs. 4(g) shows that beginning at 1185 degrees there is a recirculation set up in the leading pocket aligned with the symmetry plane of the rotor. It grows stronger through the rest of the calculation (Figs. 4(h)-(j)). In both the leading and standard pockets there is a weak recirculation above the pocket in the plane of the rotor surface (Figs. 3(h)-(j) and 4(h)-(j)). With the trailing pocket the flow reverses on the leading flank of the rotor (Figs. 5(f)-(j)).

Figs. 3(k)*, 4(k) and 5(k) are plots of the pressure along the rotor at different crank angles. With the leading pocket at 1185 and 1200 degrees the pressure on the trailing flank of the rotor is about 5 atm higher than the pressure on the leading flank (Fig. 4(h)). With the standard pocket the largest difference is only 2 atm (Fig. 3(h)). This difference is reflected in the higher velocities with the leading pocket. The trailing pocket shows a large dip in pressure at the leading edge of the pocket at 1155 degrees (Fig. 5(h)). This might be an effect of the narrow clearance between the rotor and housing at this time and might explain the reversed velocities seen on the leading flank.

Both the higher diffusivity and the recirculation are driven by the squish flow from the trailing flank of the rotor. The leading pocket increases the velocity of this flow both by having more mass above the trailing flank and by remaining close to the dip in the housing for a longer time than either of the other pockets. These computations with relocated pockets suggested that moving the pocket toward the leading edge would be helpful and moving it toward the trailing flank harmful.

Subsequent to these studies two parallel paths of study, both of which were logical steps from above, were undertaken. The first path focused on a leading pocket and on attempts to obtain recirculation in the pocket at earlier crank angles than with the leading standard pocket. Since the pocket was leading, the depth of the pocket could also be increased to utilize the advantages noted earlier with deep pockets. However these series of leading pockets had certain disadvantages. The long narrow trailing flank resulted in a higher compression pressure as the gas trapped by the minor axis and the rotor face on the trailing side would be compressed. Also as a result of this effect, the air trapped would not be utilized in the pocket for mixing with air- an effect which would be detrimental to performance at higher loads when the fuel air ratio would become very rich. The second path of study, pursued in parallel with the above, attempted to overcome some of these disadvantages. In addition it incorporated positive features from the use of dual injectors, another concept which had been explored.

Dual Injectors

This concept originated with efforts to obtain higher power with the standard pocket configuration. A single main injector would be limited in its capacity to provide sufficient fuel to the engine over a certain duration and distribute the fuel uniformly with the pocket. Hence two separate injectors were considered. Figs. 6*,7*-10 show liquid fuel distribution within the pocket at different crank angles. Notice that each one of the two injectors has a four hole pattern. The first injector (indicated at I1) begins injection at about 1035 CA. The second injector begins injection at about 1050 CA. Fig. 11* shows a typical vaporized fuel-air distribution in the pocket at 15 CA BTC. Pockets of richer-than-flammable mixtures are absent. Figs. 12-13* show the temperature contour lines 15 crank angle degrees before top-center and at top-center respectively. These figures indicate that burning is fairly rapid. However the shape of the pocket with the leading part shallower than the trailing part was not a good match for two main injectors. Hence such a change in injection strategy required a change to the pocket geometry as well, whereby the shallower part of the pocket (i.e. towards the leading edge) had to be increased in depth to reduce wall wetting. Such an increase in depth results in significant reduction in compression ratio. The compression ratio may be increased to its original value by including a hump in the center of the pocket- in principle creating two separate pockets, one for each injector. Fig. 14 (a)*-(b)* show the cross-sections of such a geometry. I1 and I2 and S1 and S2 indicate locations of the two injectors and spark plugs respectively. Figs. 15 (a)*-(f) show the computed velocity flowfield at the indicated crankangles. Figs. 15 (a)-(d) show the velocity with respect to the housing

and Figs. 15 (e)-(f) show the velocity with respect to the rotor. Fig. 15 (f) shows that at top-center there is a significant relative velocity with respect to the rotor generated by the squish which in turn results in a high level of turbulence as indicated by the diffusivity contour lines on Figs. 16(a)-(b). Notice that this geometry is still not very practical since the surfaces have sharp corners.

This restricted the cooling of the rotor. In addition there were physical limitations to placing two injectors and two spark plugs in the vicinity of the minor axis. With the considerations above and others discussed in the section on 'relocated pockets' earlier, a dual pocket concept was pursued.

The Dual Pocket Rotor

Fig. 17* shows a sketch of a 'dual pocket' rotor. Notice that there is a spark plug and injector on the leading side located downstream of the pilot cavity on the standard engine and a spark plug and injector located upstream of the pilot cavity location. Figs. 18 (a,b*-e*)-(h) show the computed flowfield at several crank angles for this pocket. 1080 CA is top-center. Rotation is counterclockwise on all figures. F/A denotes fuel/air mixture contours, T the temperature, D the diffusivity and v the velocity. Injection in the leading pocket starts at about 50 CA BTDC and ignition at about 25 CA BTDC. It may be observed from fig. 18 (b) that the squish flow into the leading pocket generates high diffusivity which results in fast vaporization and mixing of the vaporized fuel with the air. Combustion in the leading pocket is complete by 1125 CA. Injection in the trailing pocket starts at about 10 CA BTC and ignition at about 10 CA ATC. Combustion in both pockets is complete by about 1140 CA. The timings are different for the two pockets so as to obtain positive torque on account of combustion from both pockets. Fig. 19* shows typical computed pressures in the leading and trailing pockets with and without combustion. It may be seen that there are significant differences in the magnitude of the pressures in the two pockets at a given crank angle. The magnitude of the differences would depend on the position of the pockets and ignition timings, parameters which were explored in the study.

In order to provide guidance for optimization calculations of the two-pocket configuration with the 3-D model a zero-dimensional model which analyses the two-pocket configuration was also developed. The model was used to study the effect of spark timings, crank-angles at which combustion pressures in the two pockets peak, and to a lesser extent the location of the pockets and injection timings.

Fig. 20 (a)-(d) show the computed flowfield results for a case where the trailing pocket is moved closer to the trailing edge. In general, the cases where the pocket is moved away from the trailing edge appears to offer greater flexibility in injection and ignition timings.

Computations were also made with the dual pocket configuration at compression ratios of 8.5 and 7.5. At a compression ratio of 8.5 the indicated efficiencies were about 3% better

at 6000 rpm and at an imep of 190 psi (1.309 mPa) relative to the results at a compression ratio of 7.5. Optimization computations were also done for the dual-pocket rotor configuration at different loads and with different timings to identify the best strategy for varying loads and timings. It appeared from the computations that the best efficiencies are obtained when at relatively high load (about 200 PSI (1.378 mPa) IMEP), 25% of the fuel is injected into the trailing pocket and 75% into the leading pocket. As the load was reduced, the quantity of fuel injected into the trailing pocket is kept constant and the fuel quantity injected into the leading pocket reduced till the quantities of fuel injected into both pockets are about the same. At lighter loads the quantity of fuel injected into the trailing pocket should be reduced while keeping the quantity of fuel injected into the leading pocket a constant.

Fig.21 shows the computed flowfield at top-center for the dual-pocket configuration. Fig.22 (a)* shows the computed pressures in the leading and trailing pockets at high load (about 200 PSI IMEP (1.378 mPa)) when 25% of the total fuel is injected into the trailing pocket and 75% of the the fuel is injected into the leading pocket. Fig.22 (b) shows the computed pressures in the pockets when the load is reduced by keeping the fuel quantity injected into the trailing pocket the same as in (a) but reducing the quantity injected into the leading pocket so that it is 50% of what it would be in (a). Fig. 22(c) shows the computed pressures when the fuel quantity injected into the leading pocket is 25% of what it would be at high load i.e in (a). It may be seen that this strategy also keeps the peak pressures in the pockets within 1400 PSI (9.646 mPa). A set of computations have also been done to assess the effect on efficiency and peak pressures of injection and spark timings. Fig. 23(a) shows the computed pressures in the pockets when the injection and spark timings of the trailing pocket are adjusted to obtain 5% to 95% mass burned fraction in the trailing pocket from 0 CA ATC to 30 CA ATC. Figs. 23(b), 23(c) and 23(d) show the pressures when this burned mass fraction is obtained in the trailing pocket between 20 to 55 CA ATC, 50 to 75 CA ATC and 60 to 95 CA ATC respectively. The best efficiency is obtained for (c) though in this case the peak pressure in the trailing pocket is above 1500 PSI (10.335 mPa).

Computations were also made for the dual-pocket configuration where the volumes of the two pockets were varied. In these computations the volumes of the two pockets which were kept equal in the design version was varied in relation to each other. In general, the computations show that increasing the volume of the leading pocket and reducing the volume of the trailing pocket appear to result in better efficiency. There is a limit on the maximum possible depth of the leading pocket because of structural considerations. A configuration where the volume of the leading pocket is about twice the volume of the trailing pocket has shown the highest efficiency of the different cases computed. This is because in the leading pocket recirculation is generated which in turn results in better fuel-air mixing and faster burning. The limiting case of using only a leading pocket is also being studied in relation to the dual-pocket configuration. While this pocket results in somewhat similar efficiency to the dual-pocket configuration there may be a limit to the maximum load that could be obtained with the pocket.

at 6000 rpm and at an imep of 190 psi (1.309 mPa) relative to the results at a compression ratio of 7.5. Optimization computations were also done for the dual-pocket rotor configuration at different loads and with different timings to identify the best strategy for varying loads and timings. It appeared from the computations that the best efficiencies are obtained when at relatively high load (about 200 PSI (1.378 mPa) IMEP), 25% of the fuel is injected into the trailing pocket and 75% into the leading pocket. As the load was reduced, the quantity of fuel injected into the trailing pocket is kept constant and the fuel quantity injected into the leading pocket reduced till the quantities of fuel injected into both pockets are about the same. At lighter loads the quantity of fuel injected into the trailing pocket should be reduced while keeping the quantity of fuel injected into the leading pocket a constant.

Fig.21 shows the computed flowfield at top-center for the dual-pocket configuration. Fig.22 (a)* shows the computed pressures in the leading and trailing pockets at high load (about 200 PSI IMEP (1.378 mPa)) when 25% of the total fuel is injected into the trailing pocket and 75% of the the fuel is injected into the leading pocket. Fig.22 (b) shows the computed pressures in the pockets when the load is reduced by keeping the fuel quantity injected into the trailing pocket the same as in (a) but reducing the quantity injected into the leading pocket so that it is 50% of what it would be in (a). Fig. 22(c) shows the computed pressures when the fuel quantity injected into the leading pocket is 25% of what it would be at high load i.e in (a). It may be seen that this strategy also keeps the peak pressures in the pockets within 1400 PSI (9.646 mPa). A set of computations have also been done to assess the effect on efficiency and peak pressures of injection and spark timings. Fig. 23(a) shows the computed pressures in the pockets when the injection and spark timings of the trailing pocket are adjusted to obtain 5% to 95% mass burned fraction in the trailing pocket from 0 CA ATC to 30 CA ATC. Figs. 23(b), 23(c) and 23(d) show the pressures when this burned mass fraction is obtained in the trailing pocket between 20 to 55 CA ATC, 50 to 75 CA ATC and 60 to 95 CA ATC respectively. The best efficiency is obtained for (c) though in this case the peak pressure in the trailing pocket is above 1500 PSI (10.335 mPa).

Computations were also made for the dual-pocket configuration where the volumes of the two pockets were varied. In these computations the volumes of the two pockets which were kept equal in the design version was varied in relation to each other. In general, the computations show that increasing the volume of the leading pocket and reducing the volume of the trailing pocket appear to result in better efficiency. There is a limit on the maximum possible depth of the leading pocket because of structural considerations. A configuration where the volume of the leading pocket is about twice the volume of the trailing pocket has shown the highest efficiency of the different cases computed. This is because in the leading pocket recirculation is generated which in turn results in better fuel-air mixing and faster burning. The limiting case of using only a leading pocket is also being studied in relation to the dual-pocket configuration. While this pocket results in somewhat similar efficiency to the dual-pocket configuration there may be a limit to the maximum load that could be obtained with the pocket.

Figs. 24(a)*-(e) show the computed velocity flowfield in a case where the leading pocket has about twice the volume of the trailing pocket. It may be seen that recirculation appears in the leading pocket about 5 CA before top-center. This recirculation persists after top-center but disappears at about 60 CA after top-center. The trailing pocket does not show any recirculation. Figs. 25(a)-(e) show the computed velocity flowfield in a case where the trailing pocket has about twice the volume of the leading pocket. Though recirculation appears in the leading pocket past top-center, this is neither sustained nor significant. Figs. 26(a, c*, d) and 27(a)-(c) show the liquid particle and fuel-air distribution in the pockets for the cases corresponding to Fig.25 and Fig.24 above respectively. It may be seen that in the case where the leading pocket has less volume (Fig.26) there is significant impingement on the wall and the vaporized fuel-air mixture in the leading pocket is rapidly carried towards the leading edge.

Figs.28 (a)*-(c) and 29 (a)-(c) show computed velocity, liquid particle and fuel-air distribution for two cases with only leading pockets but with somewhat different geometries. Since the pocket volume is less than the dual-pocket volume the quantity of fuel injected is also less and the maximum load that can be obtained is less than with the dual pocket configuration. It may be seen from the figures that there is significant recirculation and mixing in these cases. The differences in pocket geometries do not appear to affect these conclusions.

Computations were also done with asymmetrically located injectors. These computations were done because of design limitations in installing all the injectors and spark plugs along the symmetry plane. The computations indicated that small asymmetries (say, about 2-3 mm) did not significantly affect performance. However computations indicated that larger displacements in the location of the injector tip from the symmetry plane would result in asymmetric distribution of liquid fuel and vaporized fuel, a condition that would be made worse by the nature of the flowfield.

Fig. 30* shows the computed velocity, liquid fuel and vaporized fuel distribution in the chamber when the injector tip is located on the symmetry plane. Fig. 30(a) shows the results in the symmetry plane and Fig. 30(b) is a top 3-D view. The distributions of liquid fuel and vaporized fuel are almost symmetric - the slight asymmetry arising from the effects of turbulence. The velocity flowfield on the downstream side of the leading pocket may be seen to be divergent out of the pocket. Fig. 31 shows the computed velocity, liquid fuel and vaporized fuel distribution in the chamber when the injector tip is located about 1 cm away from the symmetry plane. Because of the divergent nature of the flowfield, the vaporized fuel is carried even further away from the symmetry plane. Hence the flowfield is noticeably asymmetric. Fig.30 shows that for the symmetrically located injector there is better utilization of the air on the downstream side of the leading pocket than on the upstream side. This situation could be improved by changing spray patterns and spray angles, a possibility limited at present by the tilt of the injector. Fig.32 shows a cross-section of the dual pocket housing.

As pointed out earlier optimum combustion in the dual-pocket configuration would generate a significant pressure differential of 600 psi (4.134 mPa) peak differential at high loads

between the leading and trailing pockets. These pressure differentials arise because injection and ignition timings in the two pockets are independently controlled to obtain maximum work output from each individual pocket. Fig. 32* shows the dual pocket rotor housing. Fig.33* shows the pressure in the chamber at different crank angles around Top-Center for an operating condition of 6000 rpm and an imep of about 220 psi (1515 kPa). These pressure differentials would result in high gear loads. Rotor gear loads for this configuration operating under this condition have been made and found to be about 14220 N (about 3200 lbf). The gear will be unable to withstand such high loads for sustained periods of time. Hence initial testing of the rotor would have to be done at moderate loads (less than 750 KPa imep) where the pressure differentials could be restricted to be less than 2000 kPa. Additional optimization computations are being made for this pocket, in particular, under conditions where the pressure differential is less than about 2000 Kpa.

ADDITIONAL COMPUTATIONS

Effect of Injection Rates

It is believed that fuel injection rates are an important parameter affecting engine performance. Computations were done with different injection rates to assess this effect. Fig.34* shows two measured injection rates. They are for an Accumulator Unit Injector (AUI) and for a Stanadyne model DM pump. In previous engine tests the Stanadyne DM pump had given better performance. It may be seen from Fig.34 that the rate of fuel injection is greater at the start of injection for the AUI system than for the DM pump. This results in greater vaporization and the formation of richer mixtures at the start of injection with the AUI system. Figs. 35 (a)* and (b) show the prescribed injection velocities in the computations for the AUI and DM pumps respectively. These are approximations to the typical measured rates. Figs.36 (a)* and (b) show the injected (_____) and vaporized (-----) mass of fuel in the chamber as a function of crank angle for the AUI and DM pumps respectively. The relatively fast initial injection rate of the AUI system results in the formation of smaller drops and hence faster vaporization relative to the DM system. Fig.37 (a) and (b) show the liquid drop and fuel-air distribution in the chamber 15 CA degrees after the start of injection for the AUI system and the DM system respectively. Figs.38 (a)* and (b)* show the lean, flammable and rich fractions of fuel in the chamber as functions of crank angle for the AUI and DM pumps respectively. The AUI system, because of faster vaporization, has significantly greater quantities of rich fractions of fuel relative to the DM pump system. Figs. 39(a)-(b) show temperature and fuel/air distribution in the chamber at 1145 CA and 1165 CA for the AUI system. It may be seen that because of the greater quantities of rich fraction of fuel present in the chamber, the flame gets quenched. Figs. 40 (a)- (h) show the temperature , fuel/air and liquid fuel distribution in the chamber at different crank angles for the DM pump system. In this case the flame is not quenched.

Further computations with injection rates were obtained with the objective of obtaining a rate shape which would be optimum. Fig.41* shows 5 different rates for total delivery during each injection event of about 60 mm³ of jet-A fuel and engine rpm of 6000. The maximum

amount of flammable fraction of fuel-air mixture in the chamber has been obtained with the trapezoidal rate shape, indicated as 'A' on Fig.41. This is somewhat better (by about 10%) than the results with the AMBAC pump, indicated as 'B' on Fig.41. Fig.42* is a plot of the fractions of lean, flammable and rich vaporized fuel-air mixture as a function of crank angle degrees for shape 'A'. Fig.43* and Fig.44* show similar plots for rate shapes 'B' and 'C' respectively. Rate 'C' which approximates the Nippondenso pump rate results in somewhat lesser quantity of flammable fuel than the Ambac pump rate shape 'B'. The computations indicate that the linear rates 'D' and 'E' give the least amount of flammable fractions. These differences in the quantity of flammable fuel should result in differences in indicated efficiency. The computations were made with the N43 spray patte

Computations were also made to assess the possible effects of variations in L/D ratios of nozzles on fuel-air distribution and performance. Such variations would influence the spray angles, penetration and drop sizes. Fig. 45 shows the vaporized and liquid fuel distribution for a reference case at different crank angles. Fig. 46 shows the vaporized and liquid fuel distribution for a case where the spray angle is increased by a factor of two from the reference case and the penetration is consequently halved. Fig. 47* shows the vaporized fraction of injected fuel, and lean, rich, and flammable fractions for the reference case and Fig. 48 for the modified case. It may be seen that the reduced penetration appears to be detrimental to engine performance. These computations indicated that significant variations of L/D ratios of nozzles would have noticeable effects on engine performance.

CONCLUSIONS

The accuracy and speed of a three-dimensional code which had been developed through the Deere-Princeton collaborative work during the period 1985-89 were improved through the use of new computational techniques such as ADI methods and Stone's strongly implicit algorithms. Graphics visualization tools which could be used to examine and interpret the results from the 3-D computations were developed. With these computational tools and the use of dedicated mini-supercomputers changes to engine geometry, injector/ignitor locations and injector/ignitor strategies were explored. Three new promising engine configurations were identified. Time constraints, imposed, in particular by Deere's decision to exit from the Rotary Engine business, prevented these concepts from being optimized computationally or experimentally for best performance.

RECOMMENDATIONS

The following are recommendations for future work:

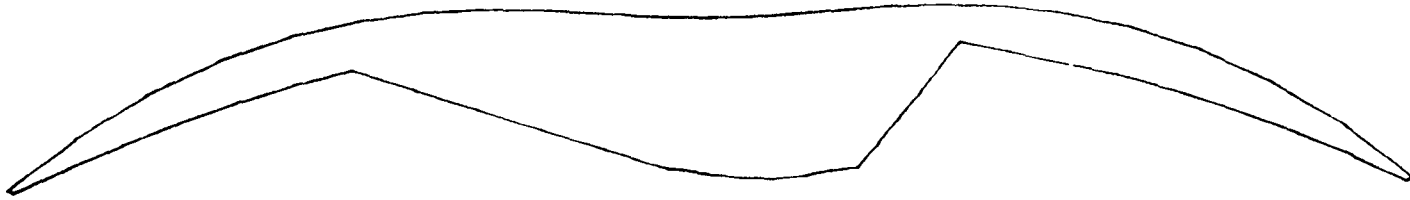
1. Injector/ignitor locations, spray patterns and geometry should be optimized for the leading standard, leading rectangular and dual pocket configurations.

2. An extensive series of hardware tests should be carried out for these configurations. The test results should be used to correlate with the computed results. Additional computations should then be made to further optimize these configurations taking into account the test results. This is an important and necessary stage in the development process because the codes are tools which should be used to provide guidance for experimental work and not to obtain absolute numbers. In addition the present version of the code does not include submodels for physical processes such as autoignition, the details of normal ignition, cycle to cycle variability, detonation nor has its accuracy been assessed for computing pressure waves. .R
3. Computations should be made to explore the sensitivity of computed results to variations in timings, ignition/injector locations, fuel/air ratios since it appears difficult to obtain correspondence between these parameters computationally and experimentally.
4. Additional concepts such as optimum injection rate profiles and air-assist injectors should be explored computationally and then experimentally as in step 2 above.
5. The code should be improved to handle autoignition, normal ignition and flows with and without combustion in cavities. Its accuracy in handling propagation of thin wave fronts should be assessed.

REFERENCES

1. Grasso, F., Wey, M.-J., Bracco, F.V. and Abraham, J., "Three-Dimensional Computations of Flows in a Stratified-Charge Rotary Engine," SAE Paper No. 870409, SAE Trans., Vol.96, 1987.
2. Abraham, J., Wey, M.-J. and Bracco, F.V., "Pressure Non-Uniformity and Mixing Characteristics in Stratified-Charge Rotary Engine Combustion," SAE Paper No. 880624, SAE Trans., Vol.97, 1988.
3. Abraham, J. and Bracco, F.V., "Comparisons of Computed and Measured Mean Velocity and Turbulence Intensity in a Motored Rotary Engine," SAE Paper No. 881602, SAE Trans., Vol.97, 1988.
4. Abraham, J. and Bracco, F.V., "Fuel-Air Mixing and Distribution in a Direct Injection Stratified-Charge Rotary Engine," SAE Paper No. 890329, SAE Trans., Vol.98, 1989.
5. Abraham, J. and Bracco, F.V., "3-D Computations to Improve Combustion in a Stratified-Charge Rotary Engine Part II: A Better Spray Pattern for the Pilot Injector," SAE Paper No. 892057, SAE Trans., Vol.98, 1989.

6. Abraham,J. and Bracco,F.V., "3-D Computations to Improve Combustion in a Stratified-Charge Rotary Engine Part III: Improved Ignition Strategies," to be presented at the SAE International Congress and Exposition, Detroit, February 1992.
7. Abraham,J., Ramoth,D. and Mannisto,J., "3-D Steady-State Wall Heat Fluxes and Thermal Analysis of a Stratified-Charge Rotary Engine," SAE Paper No.910706, 1991.
8. a) A Fortran 77 Library for Postscript Plotting, by M.J. Andrews, Princeton University, August 1990.
b) Notes on Animation, Princeton University, January 1991.
c) Rotary Engine Design Using Three-Dimensional Displays as a Diagnostic Tool for Computer Simulations, by Anna Thornton, Princeton University, 1990.
9. Some Elements of REC-91: A 3-D Code for Flows, Sprays and Combustion in Reciprocating and Rotary Engine, by V.Magi and F.V. Bracco, Princeton University, September 1991.
10. Abraham,J. and Epstein,P., "Analysis of Experimental Pressure Traces from the Dual Igniter Engine (Engine Build #0704-8), Report prepared on 26 July 1991.
11. Abraham,J. and Epstein,P., "Analysis of Experimental Pressure Traces from the Dual Igniter Engine Build #0705-3 and Build #0704-8," Report prepared on 06 August 1991.
12. Abraham,J. and Epstein,P., "Analysis of Experimental Pressure Traces from the Dual Igniter Engine Build #0705-4," Report prepared on 27 August, 1991.

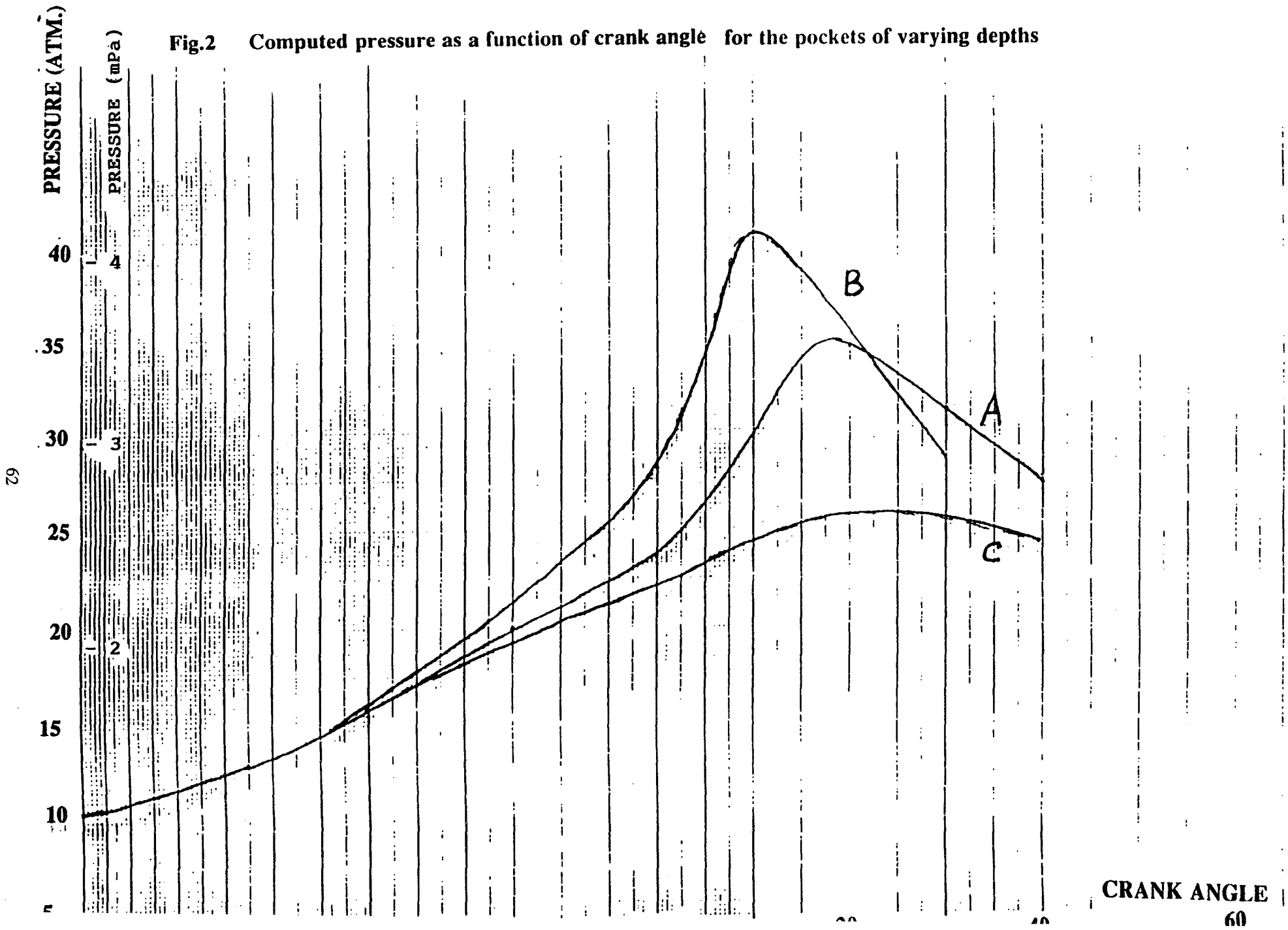


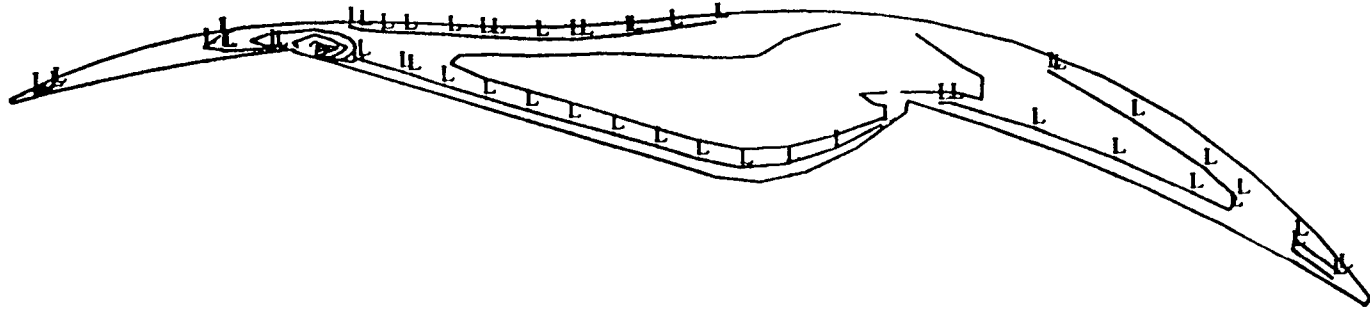
crank angle= 0.1
J= 7
T interval= 500.00K
H=4500.0000 ; L=4500.0000



I=13
T interval= 500.00K
H=4500.0000 ; L=4500.0000

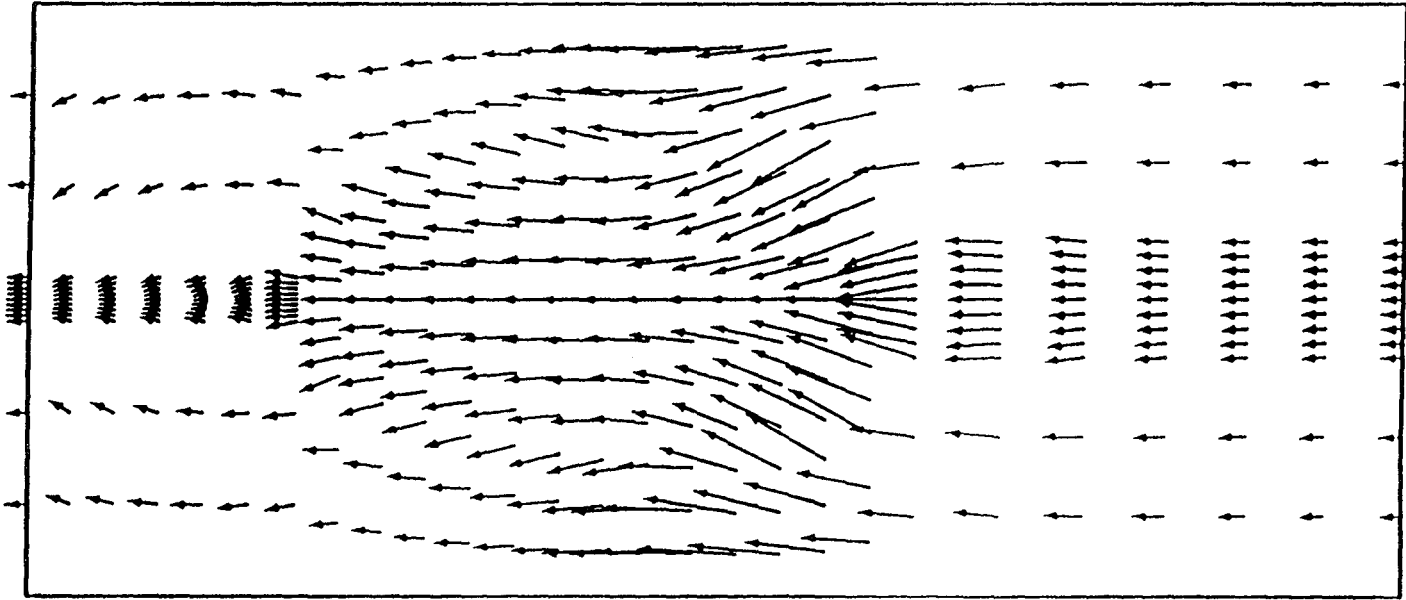
Fig.1 (a) Cross-sections of standard pocket geometry







DIFFUSIVITY, interval = 20.00 cm²/s
H = 200.0 ; L = 20.00
J = 7
crank angle = 1140.0

Fig. 3(a): Cross-section of combustion chamber along symmetry plane showing diffusivity contours at 1140 CA. for standard pocket rotor.



 100 m/s
 100 m/s
 K = 8
 crank angle = 1170.0

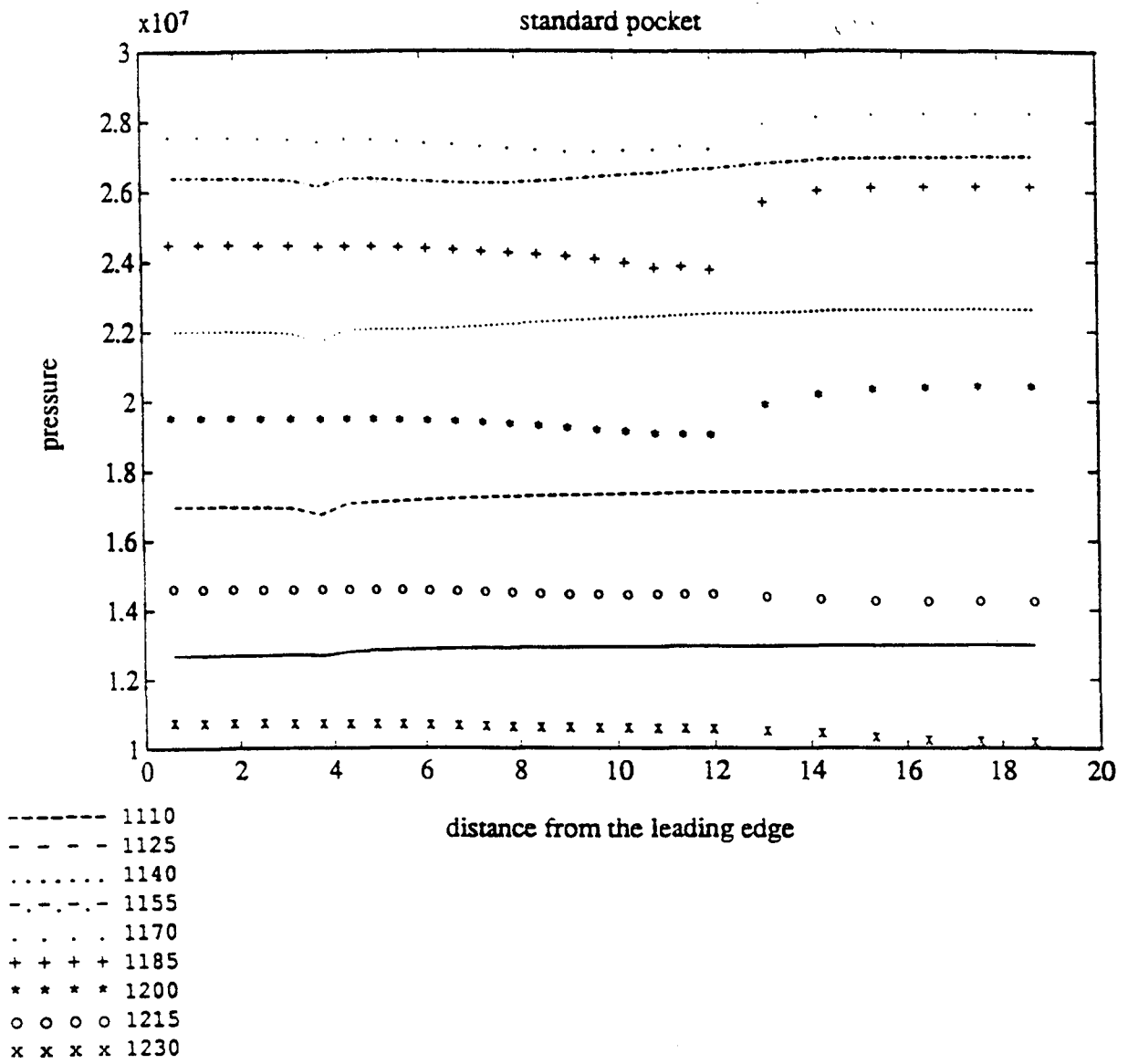


Fig. 3(k): Pressure along the rotor at different crank angles

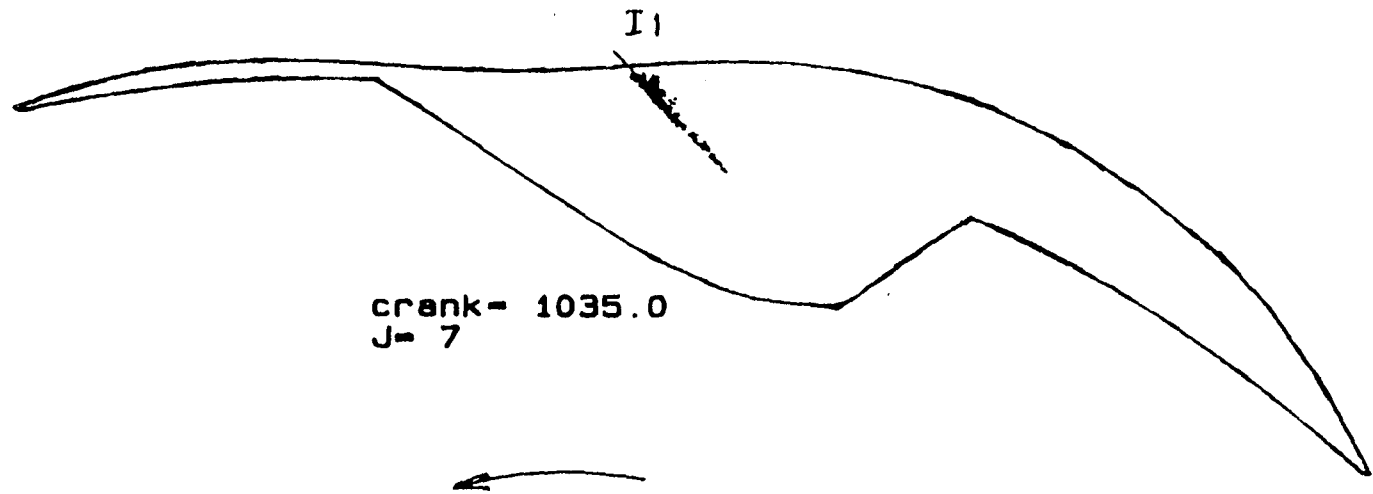


Fig. 6: Cross-section view of combustion chamber along symmetry plane showing liquid fuel distribution at 1035 CA (1080 is TC).

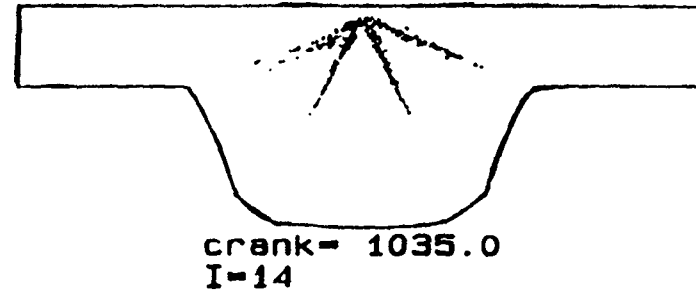
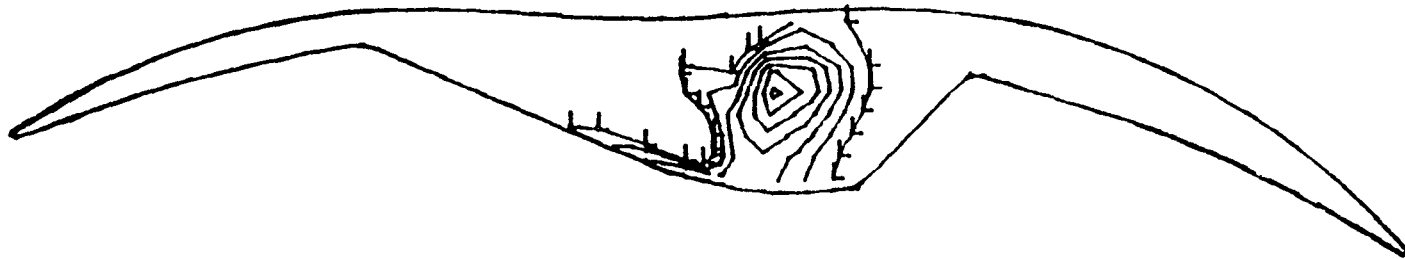
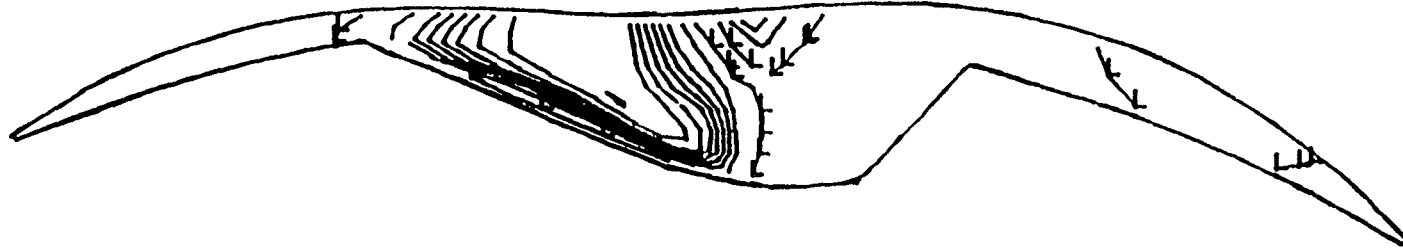


Fig. 7: Cross-section of combustion chamber showing liquid fuel distribution at 1035 CA. Injector has a 4-hole pattern.



crank angle= 1065.1
J= 7
fuel interval= 0.900%
H= 0.1200 ; L= 0.0300

Fig. 11: Cross-section view of combustion chamber along symmetry plane showing vaporized fuel distribution at 1065.1 CA.



crank angle= 1065.1
J= 7
T interval= 150.00K
H=2200.0000 ; L= 700.0000

Fig. 12: Cross-section view of combustion chamber along symmetry plane showing temperature contours at 1065 CA.

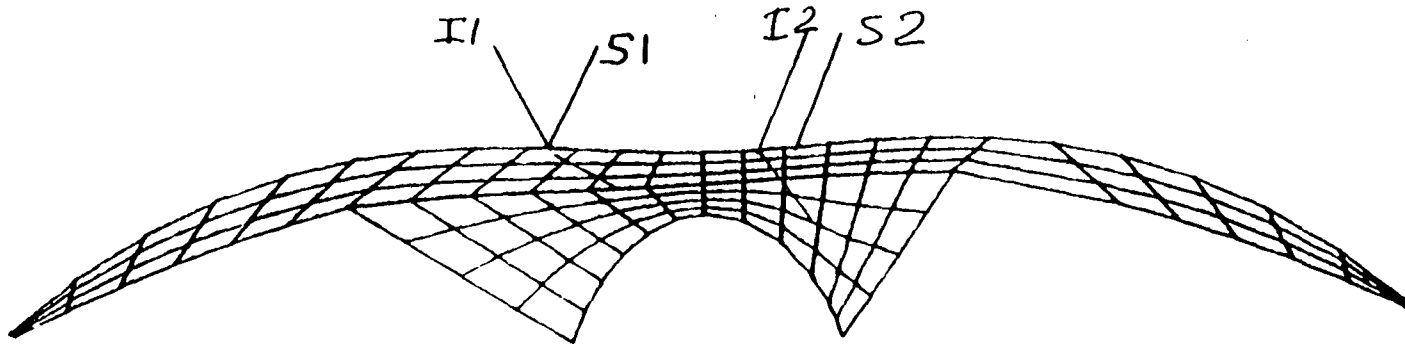


Fig. 14 (a): Cross-section view of combustion chamber along symmetry plane showing grid layout and locations of injectors and spark plugs.



CRANK= 27.000

I-13

Fig. 14 (b): Cross-section view of combustion chamber showing grid layout.

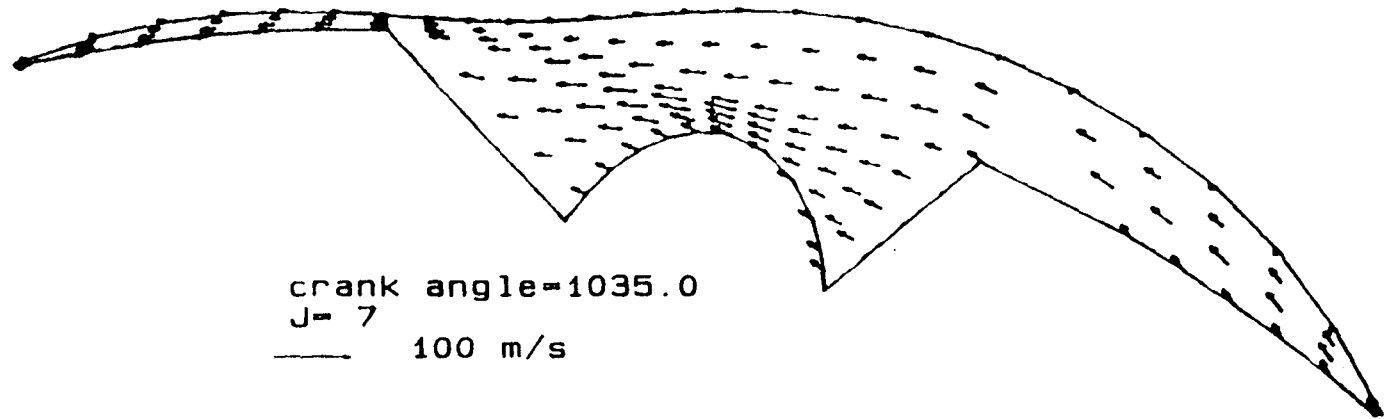


Fig. 15 (a): Cross-section view of combustion chamber along symmetry plane showing velocity vectors at 1035 CA.

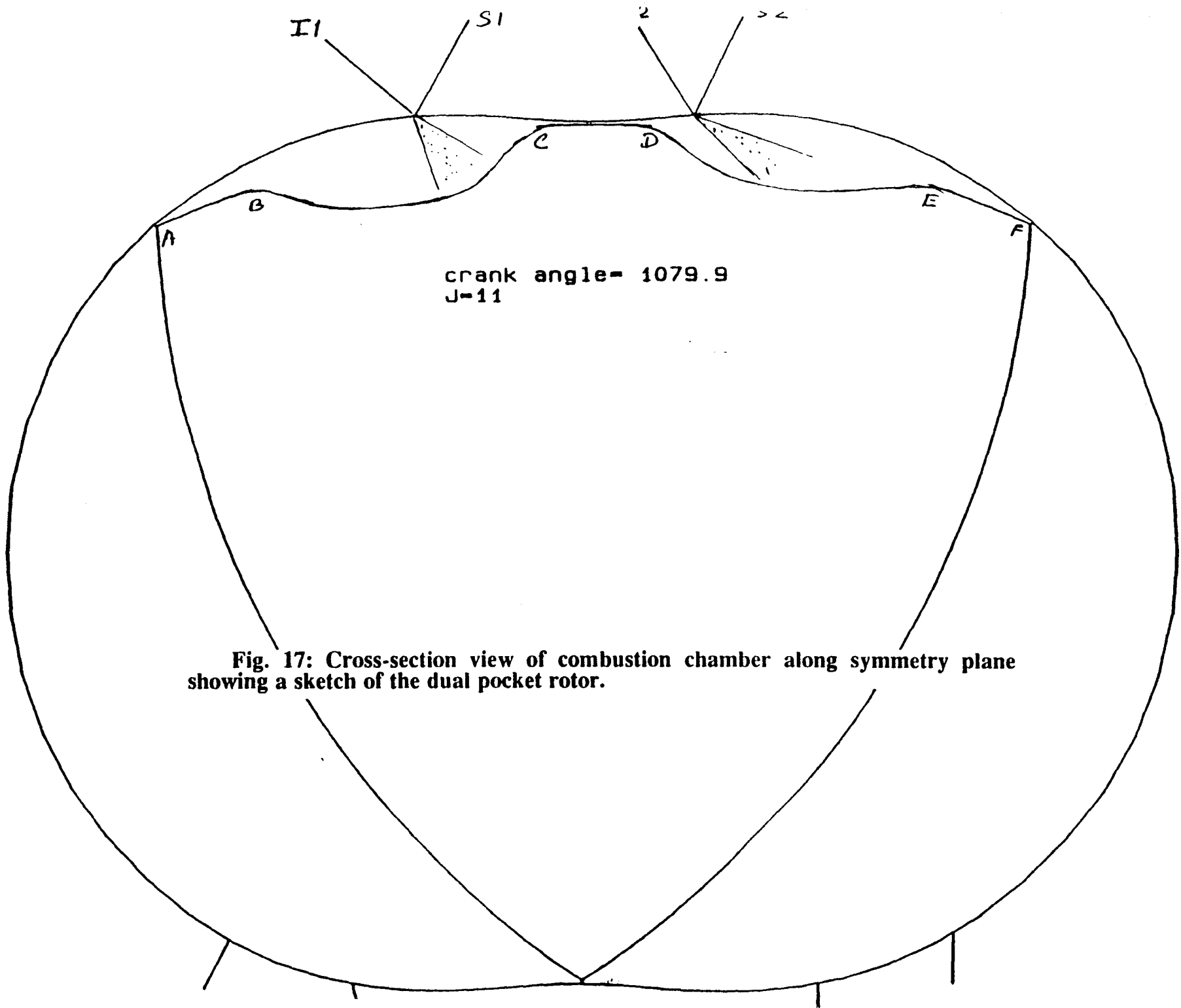


Fig. 17: Cross-section view of combustion chamber along symmetry plane showing a sketch of the dual pocket rotor.

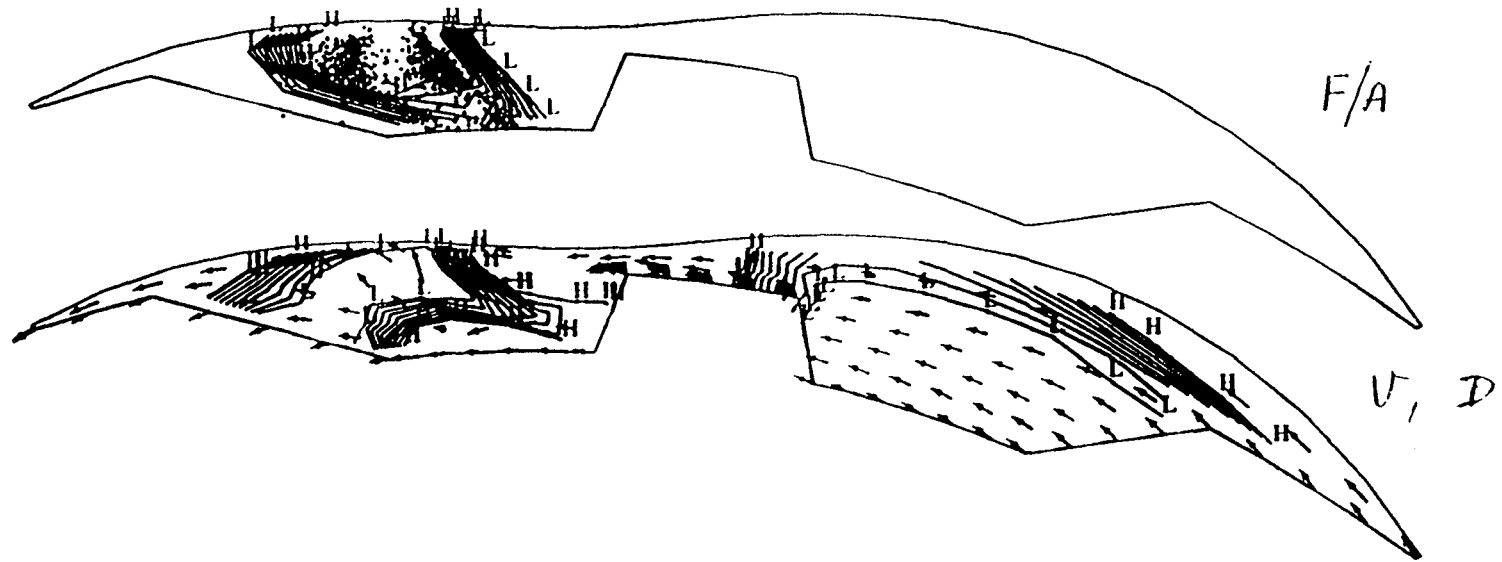
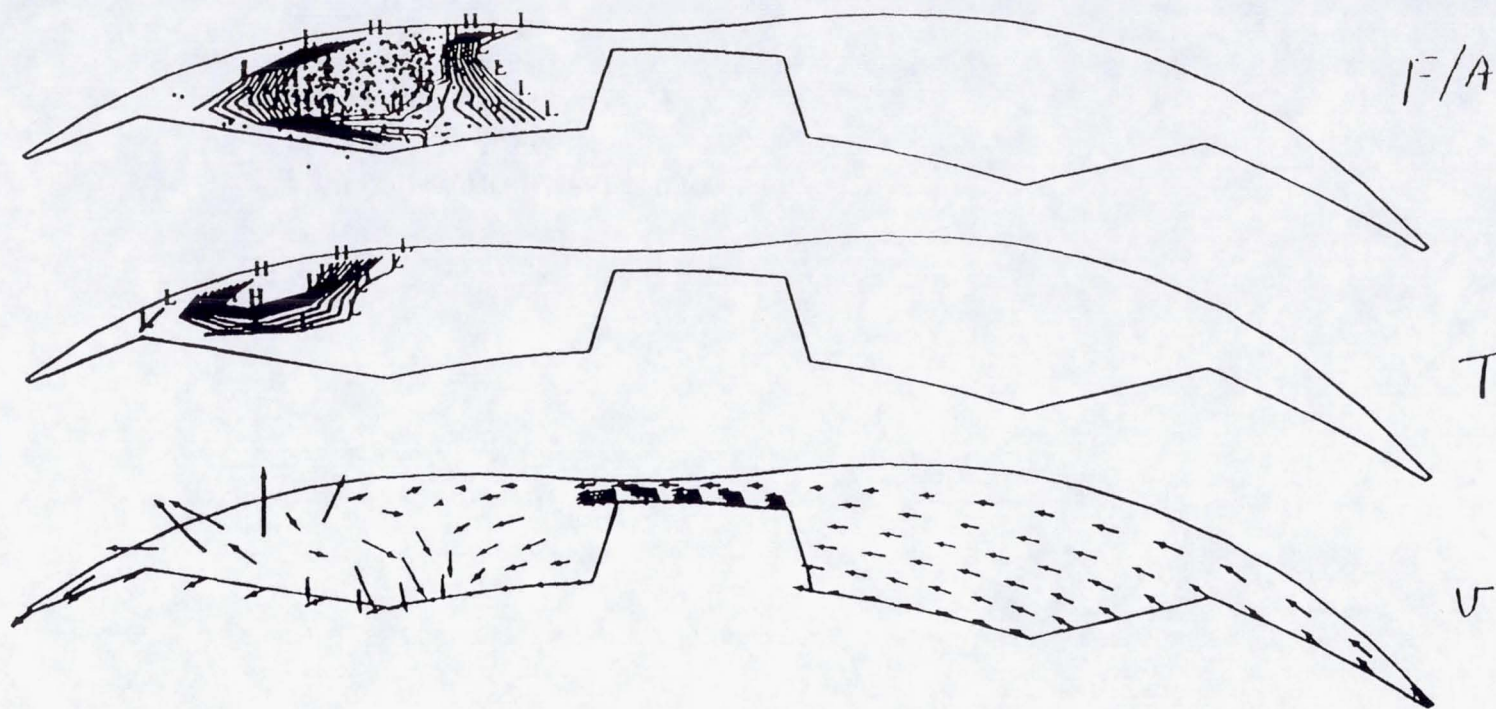


Fig. 18(b): Cross-section view of combustion chamber along symmetry plane showing liquid fuel and vaporized fuel distribution ,velocity vectors and diffusivity contours at 1050 CA.

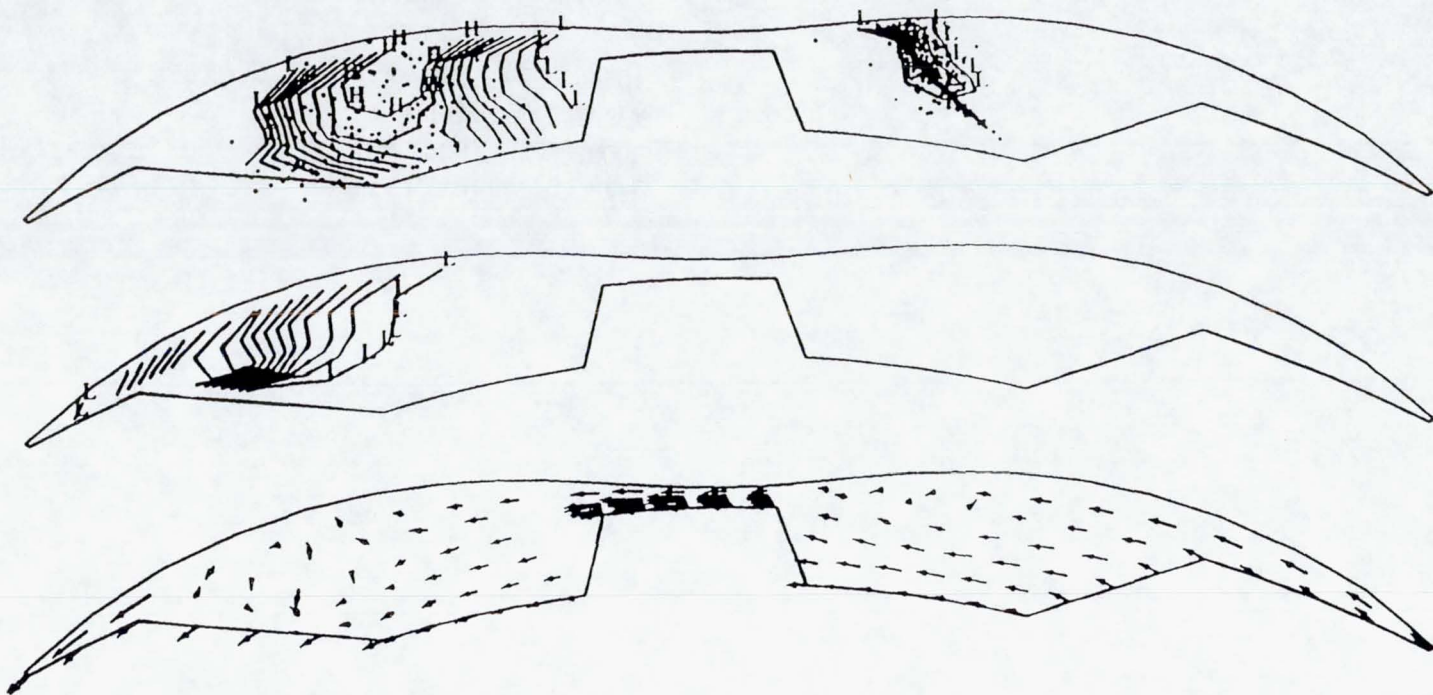
FUEL/AIR RATIO, interval = 0.1000E-01
 H = .1200 ; L = .3000E-01
 TEMPERATURE, interval = 155.6 K
 H = 2100. ; L = 700.0
 DIFFUSIVITY, interval = 55.56 cm²/s
 H = 600.0 ; L = 100.0



FUEL/AIR RATIO, interval = 0.1000E-01
 H = .1200 ; L = .3000E-01
 TEMPERATURE, interval = 155.6 K
 H = 2100. ; L = 700.0

→
 100 m/s
 J = 7

Fig. 18(c): Cross-section view of combustion chamber along symmetry plane showing distribution, temperature contours and velocity



F/A

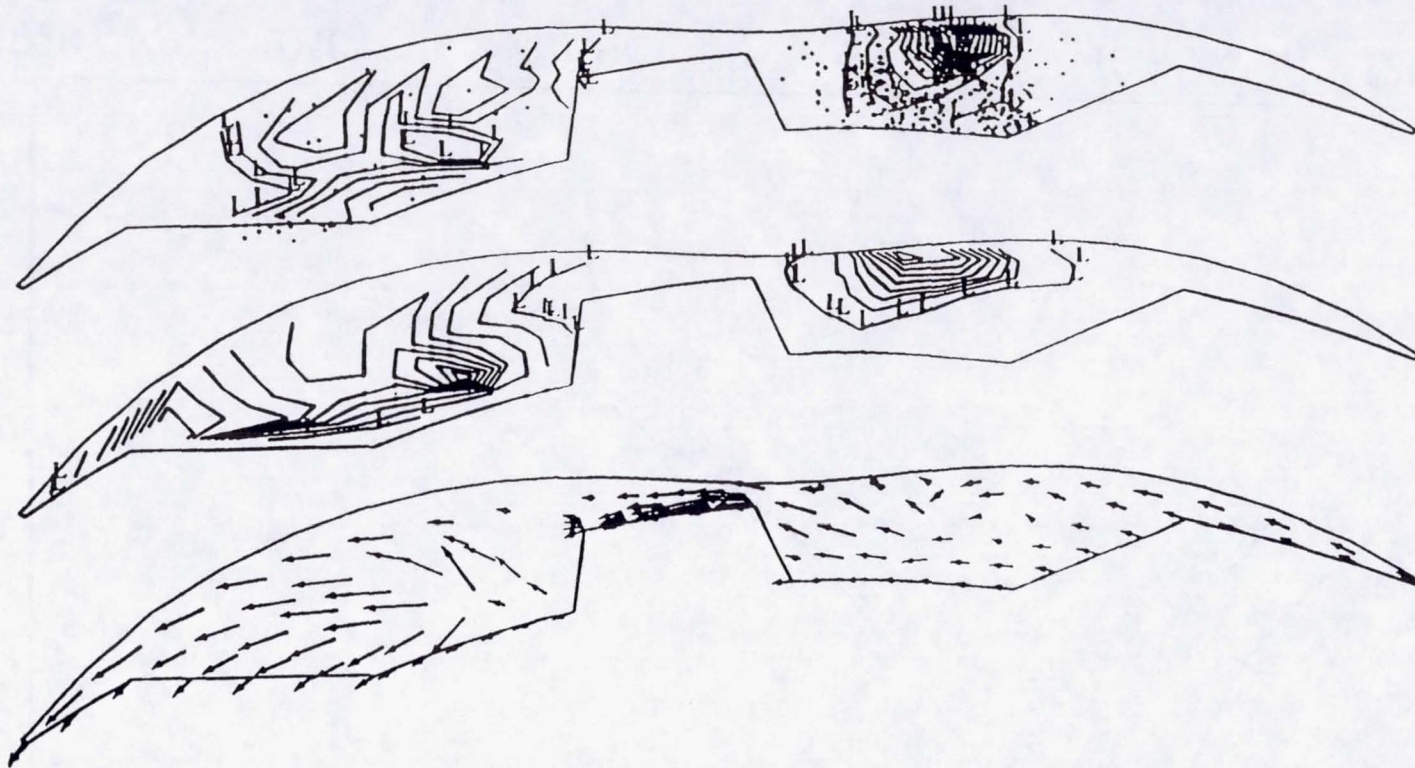
T

V

FUEL/AIR RATIO, interval = 0.1000E-01
H = .1200 ; L = .3000E-01
TEMPERATURE, interval = 155.6 K
H = 2100. ; L = 700.0

→
100 m/s
J = 7

ORIGINAL PAGE IS
OF POOR QUALITY



F/A

T

v

77

FUEL/AIR RATIO, interval = 0.1000E-01

H = .1200 ; L = .3000E-01

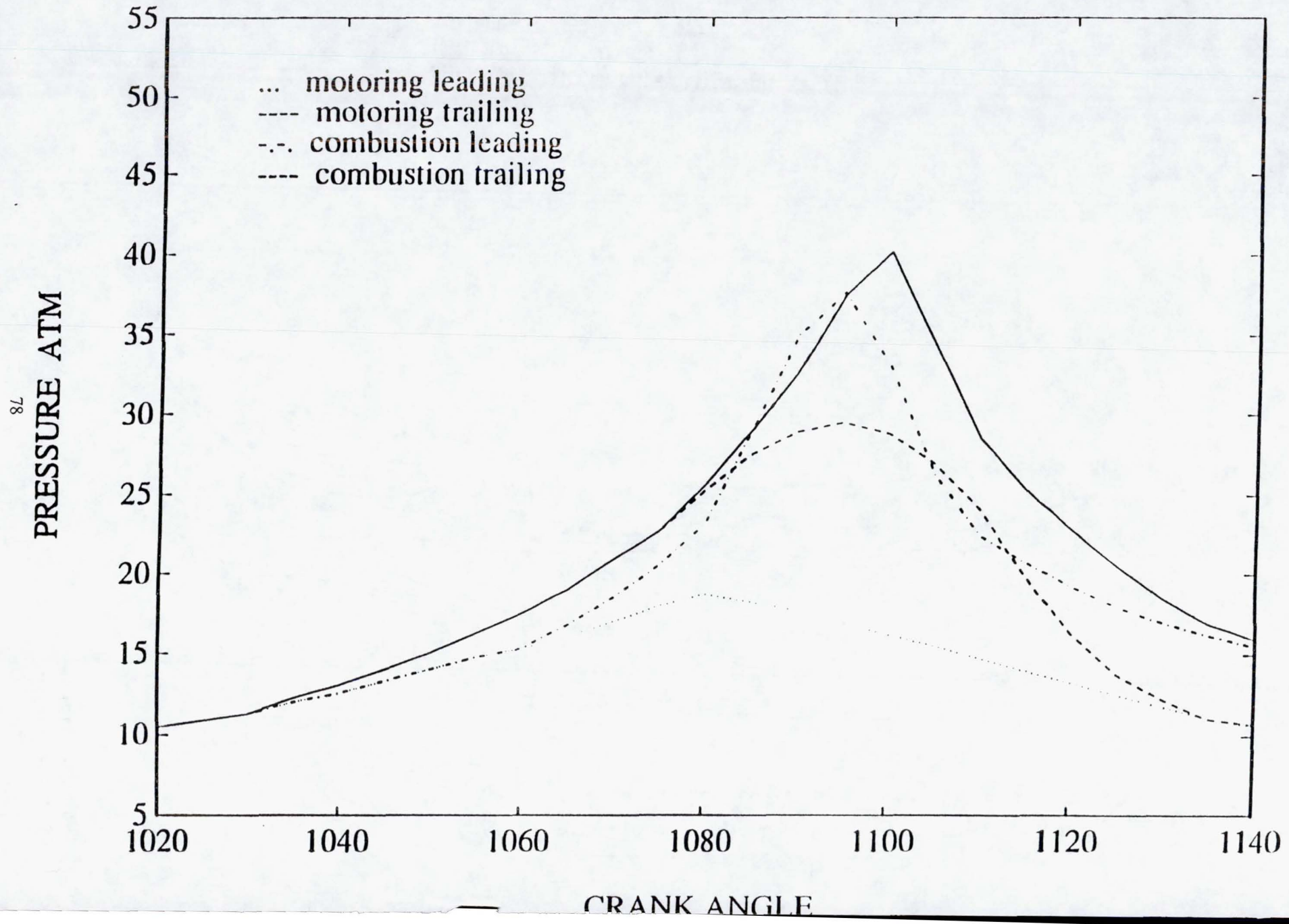
TEMPERATURE, interval = 155.6 K

H = 2100. ; L = 700.0

→
100 m/s
J = 7

Fig. 18(e): Cross-section view of combustion chamber along symmetry plane showing liquid fuel and vaporized fuel distribution, temperature contours and velocity

Fig. 19: DUAL CHAMBER PRESSURES WITH AND WITHOUT COMBUSTION



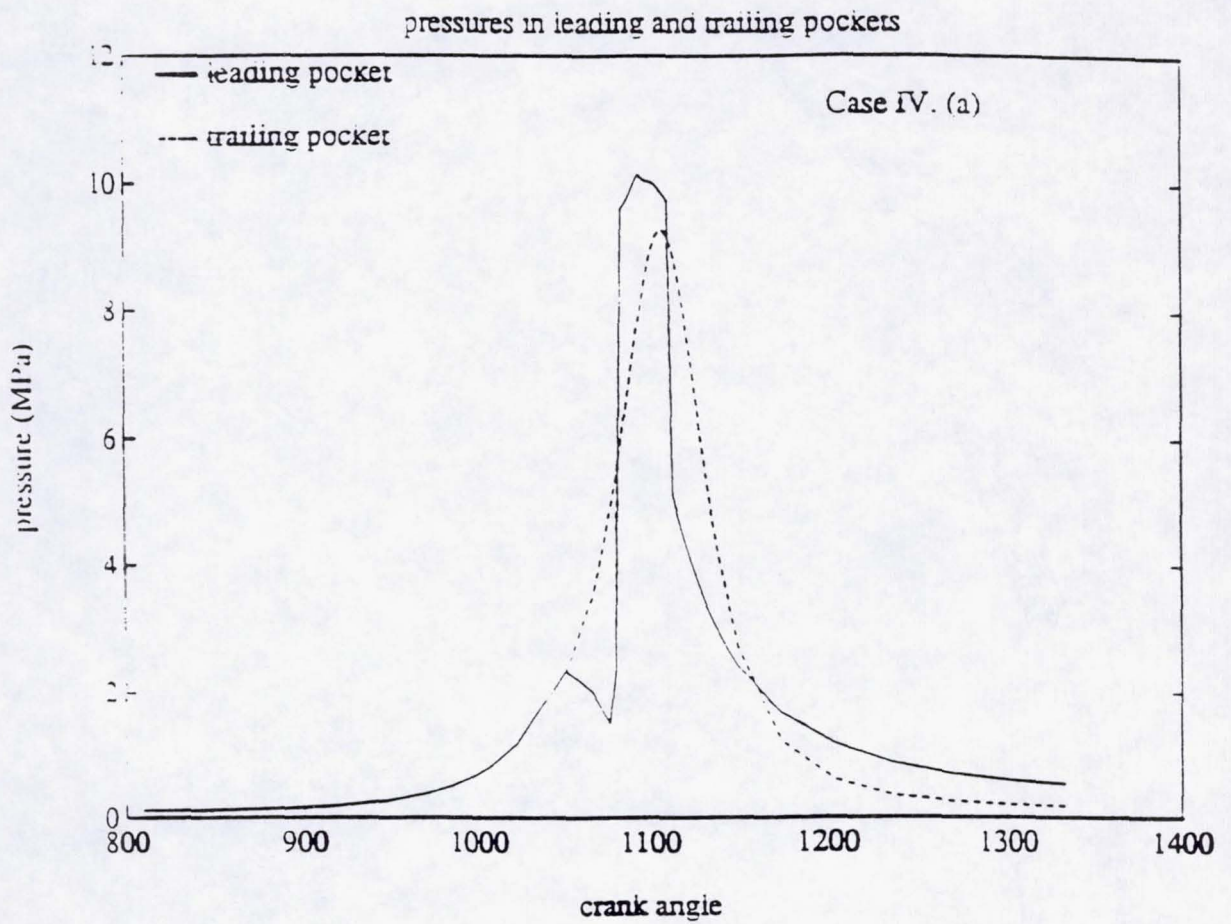
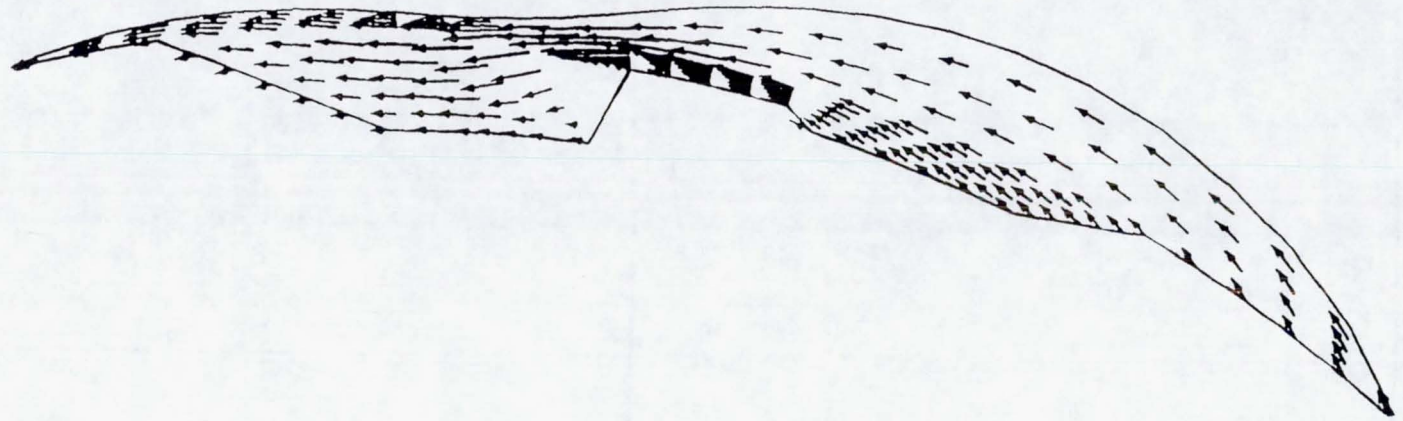
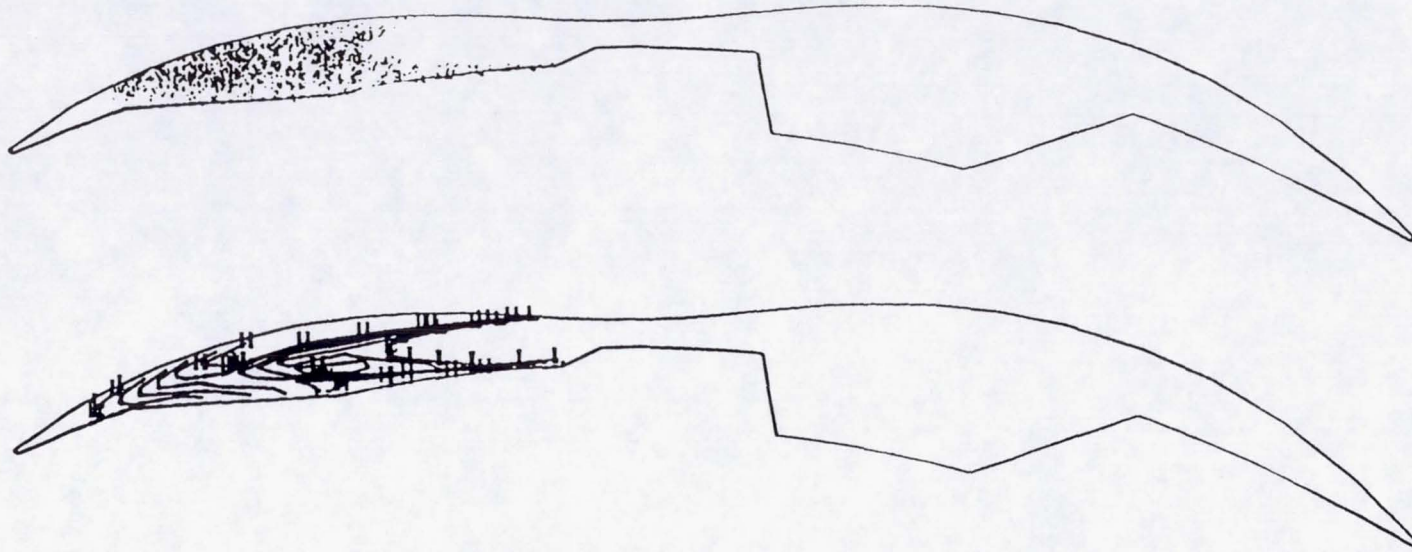


Fig. 22 (a): Computed pressures in the leading and the trailing pockets at high load (about 200 PSI IMEP) with 25% of fuel injected into trailing pocket and 75% of fuel injected into the leading pocket - Case (a)



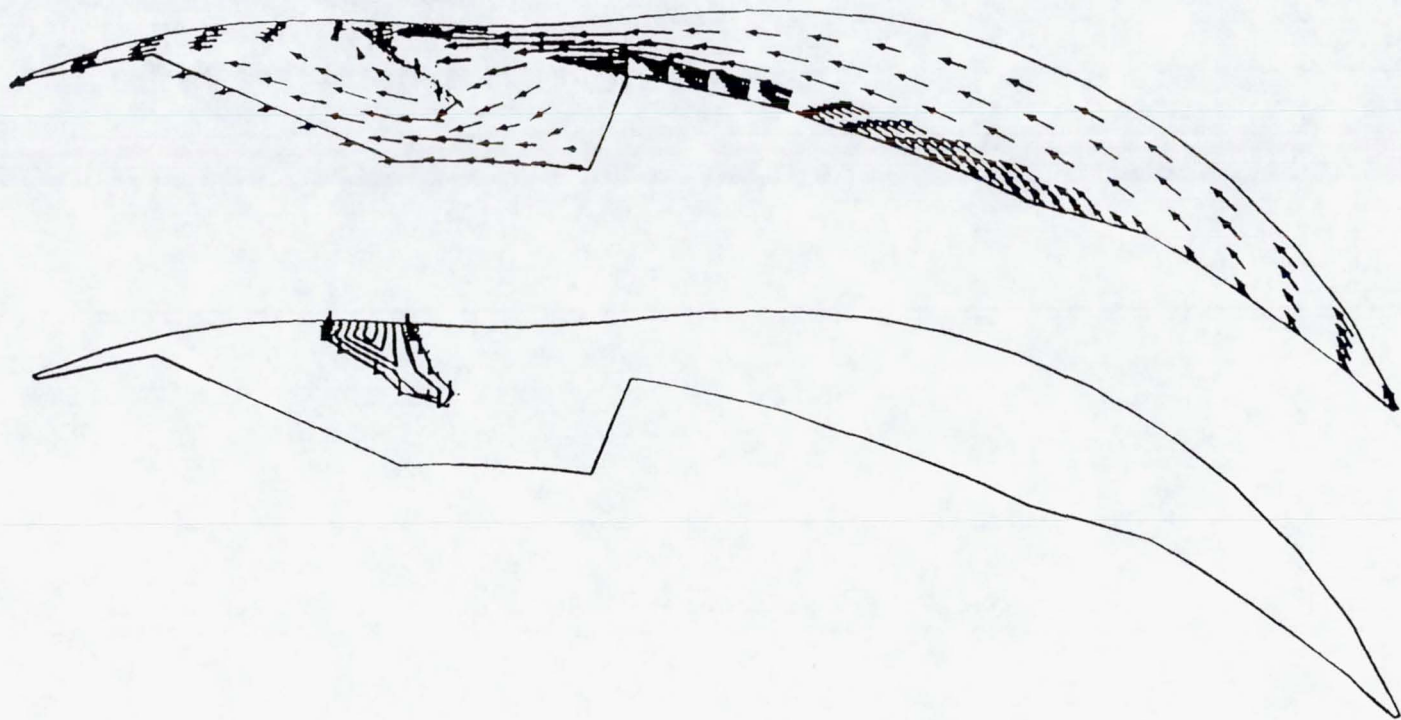
→
100 m/s
vertex limits of the region: (1, 7, 1) to (25, 7,11)

Fig. 24 (a): Velocity flowfield in the symmetry plane at 1135 CA



MASS FRACTION OF FUEL, interval = 0.18000E-01
H = 0.12000 ; L = 0.30000E-01
vertex limits of the region: (1, 7, 1) to (25, 7, 11)
crank angle = 25.0

Fig.26(b): Particle and fuel/air distribution in the chamber at 1165 CA



→
100 m/s
MASS FRACTION OF FUEL, interval = 0.18000E-01
H = 0.12000 ; L = 0.30000E-01
vertex limits of the region: (1, 7, 1) to (25, 7, 11)
@crank angle = 15.0

MASS FRACTION OF FUEL.

0.30000E-01

0.75000E-01

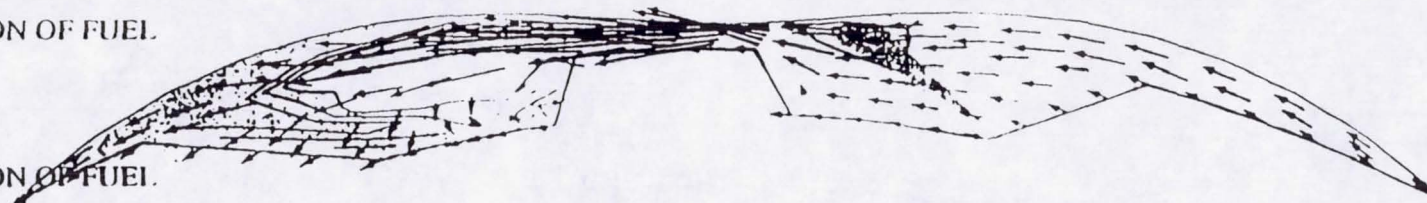
0.12000

MASS FRACTION OF FUEL.

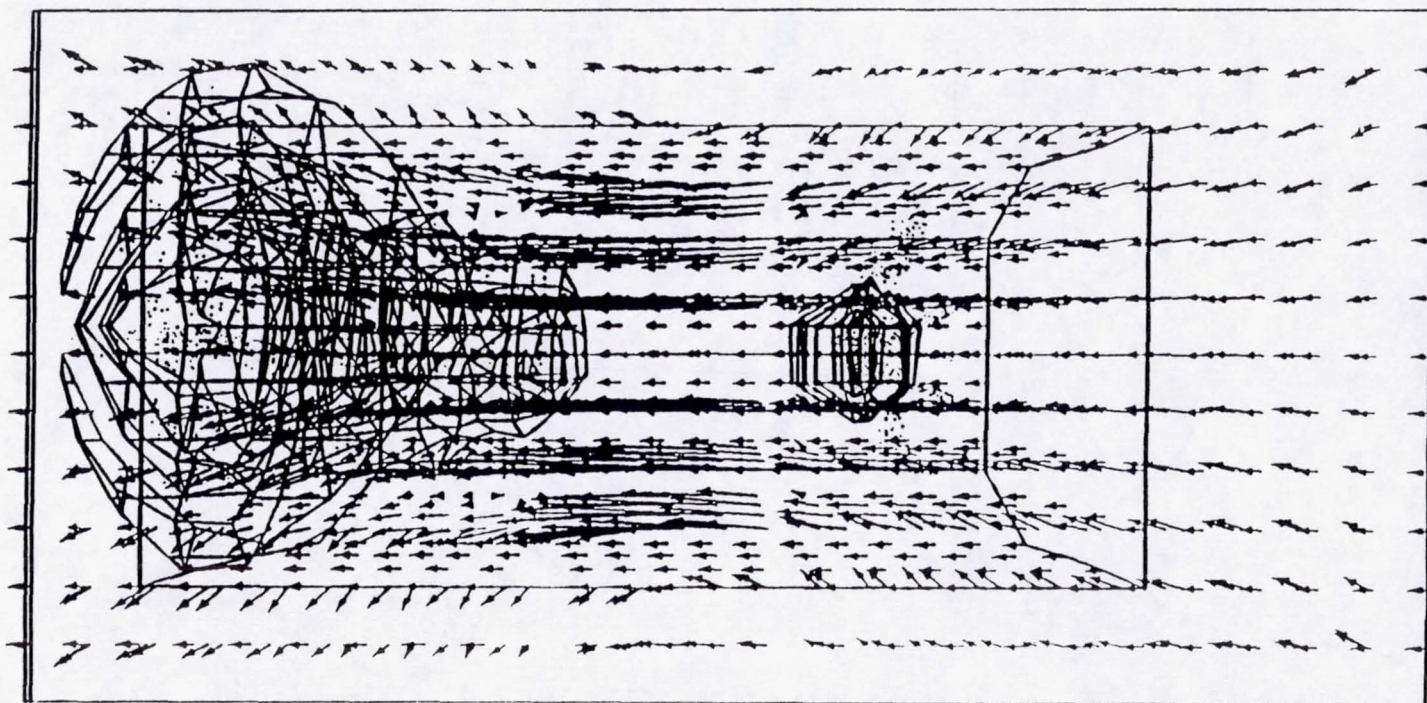
0.30000E-01

0.75000E-01

0.12000



(a)



(b)

→
100 m/s

→
100 m/s

vertex limits of the region: (1, 1, 1) to (25,13, 8)

Fig.30: Computed velocity, liquid fuel and vaporized fuel distribution in the

Fig.32 DUAL POCKET ROTOR HOUSING

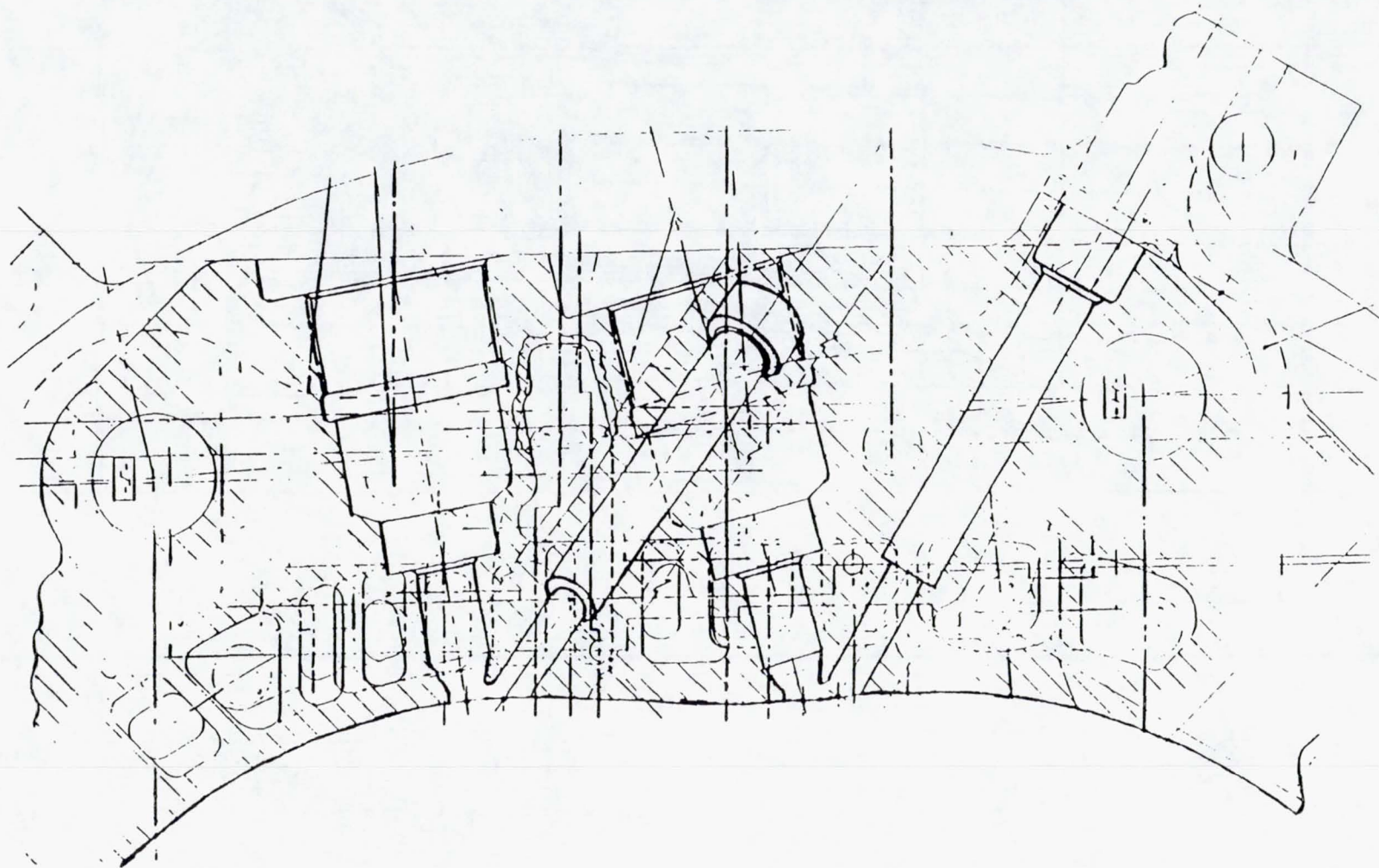


Fig.33: : Pressure in Dual Pocket Combustion Chamber

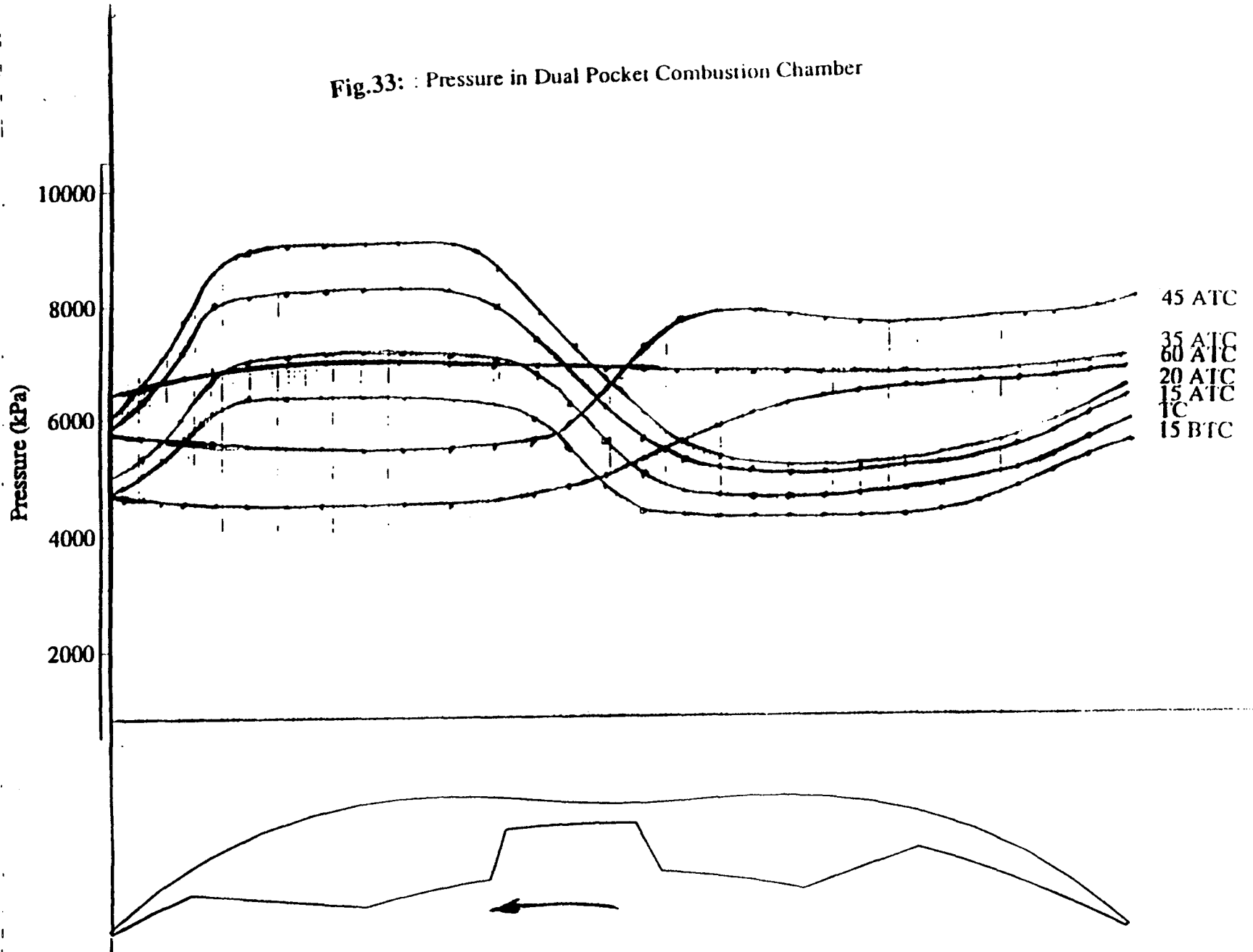
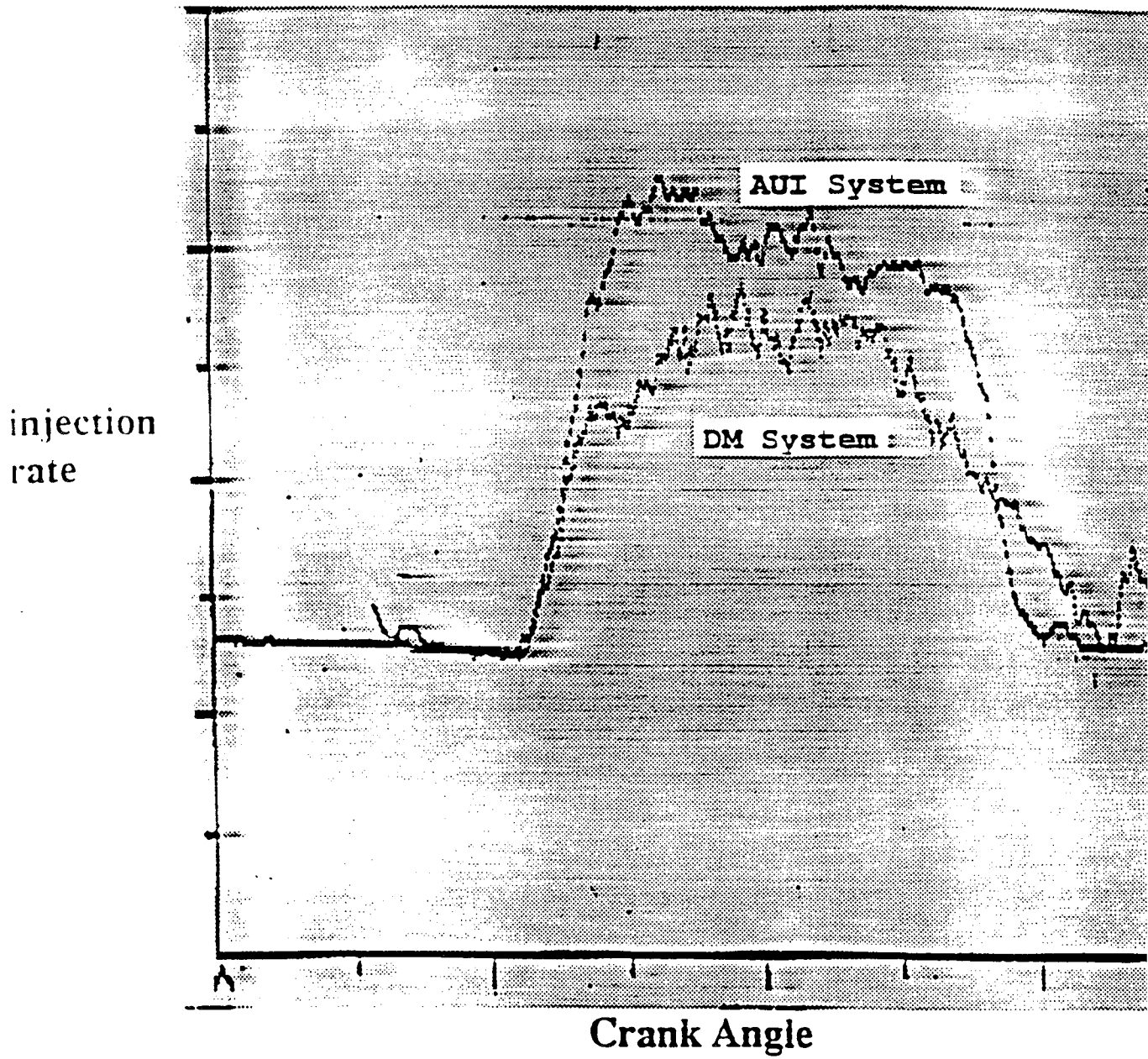


Fig.34

Injection rate comparison Stanadyne DM and AUI systems

8000 Rpm, 80 mm³



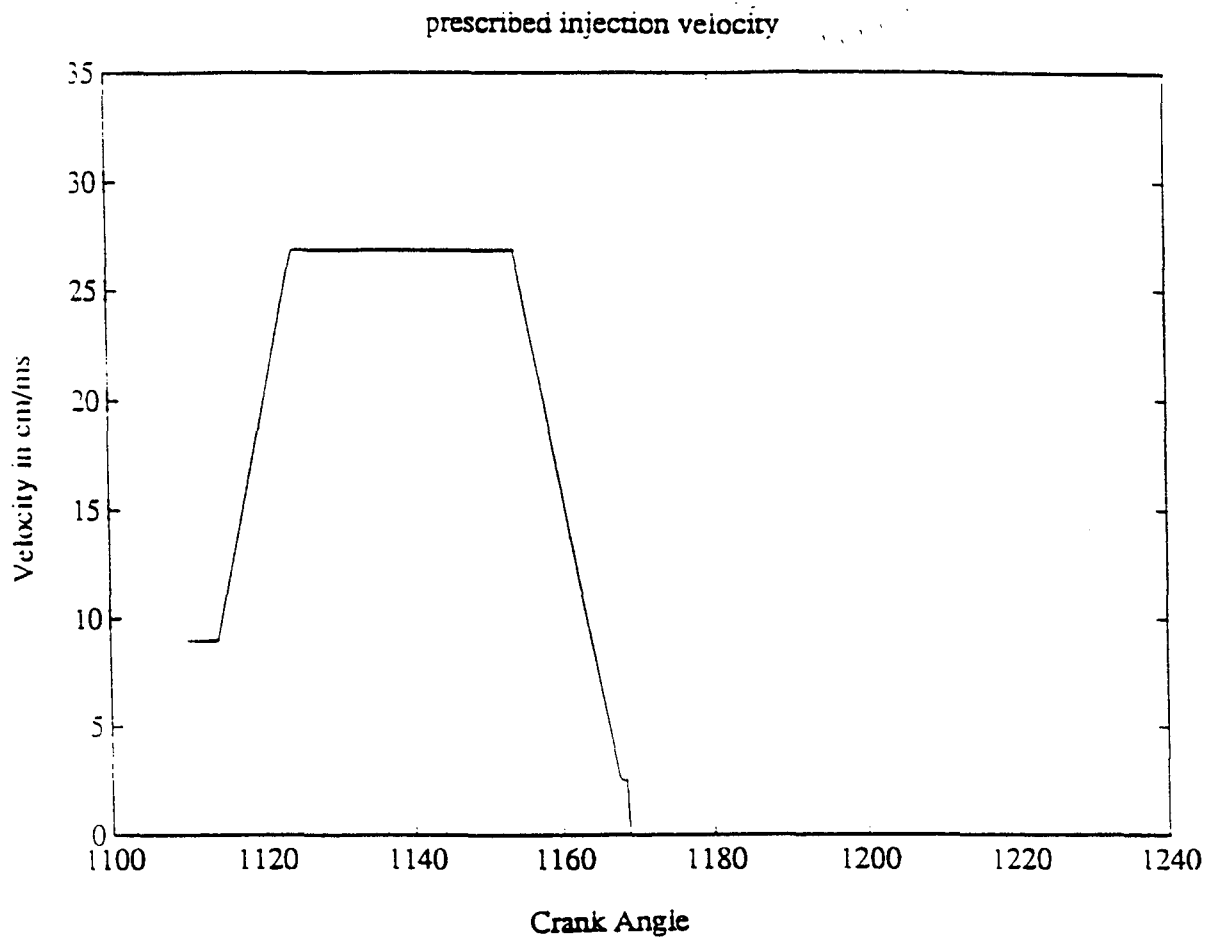


Fig. 35(a): Prescribed injection velocity for the AUI injection system

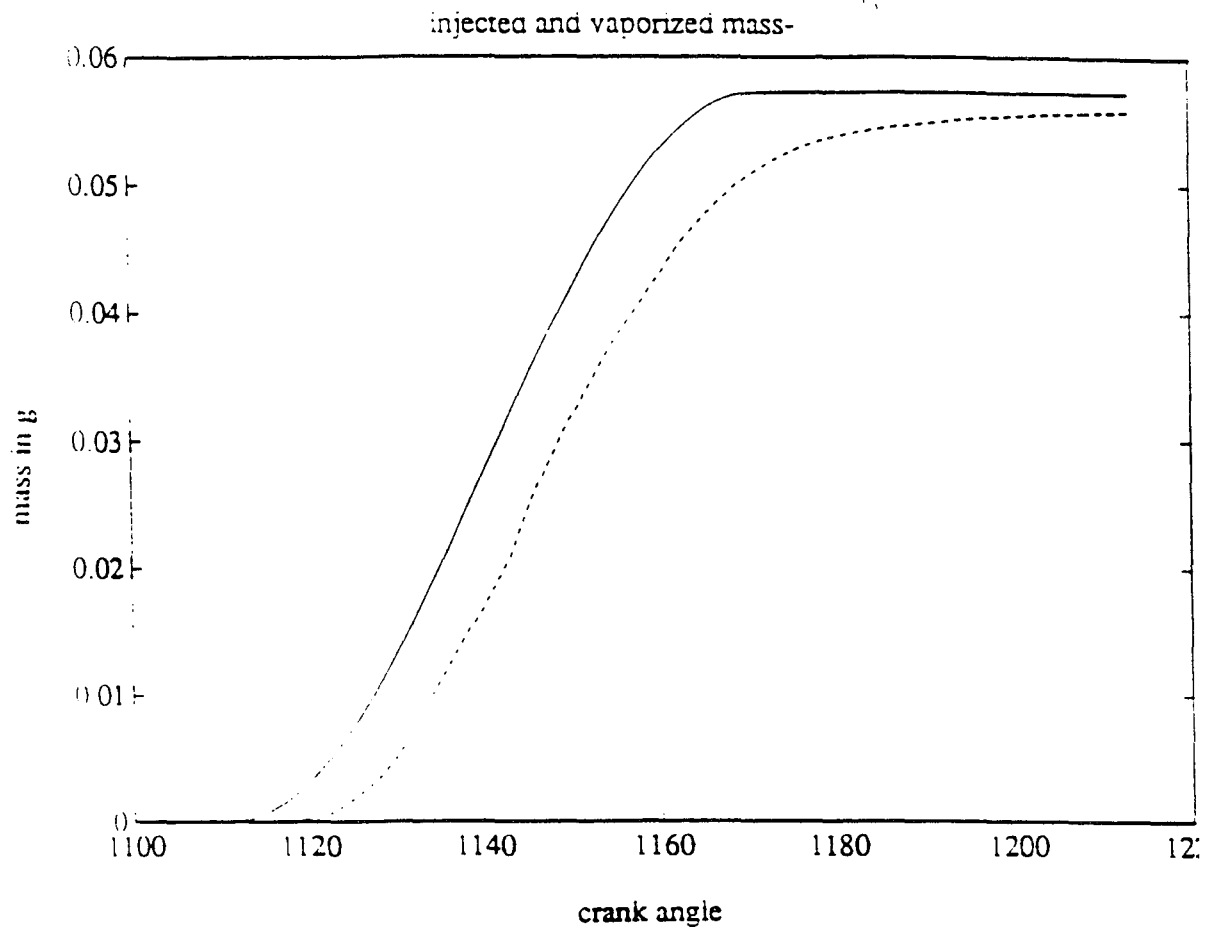


Fig. 36(a): Injected (-----) and vaporized(-----) mass of fuel for the AUI system

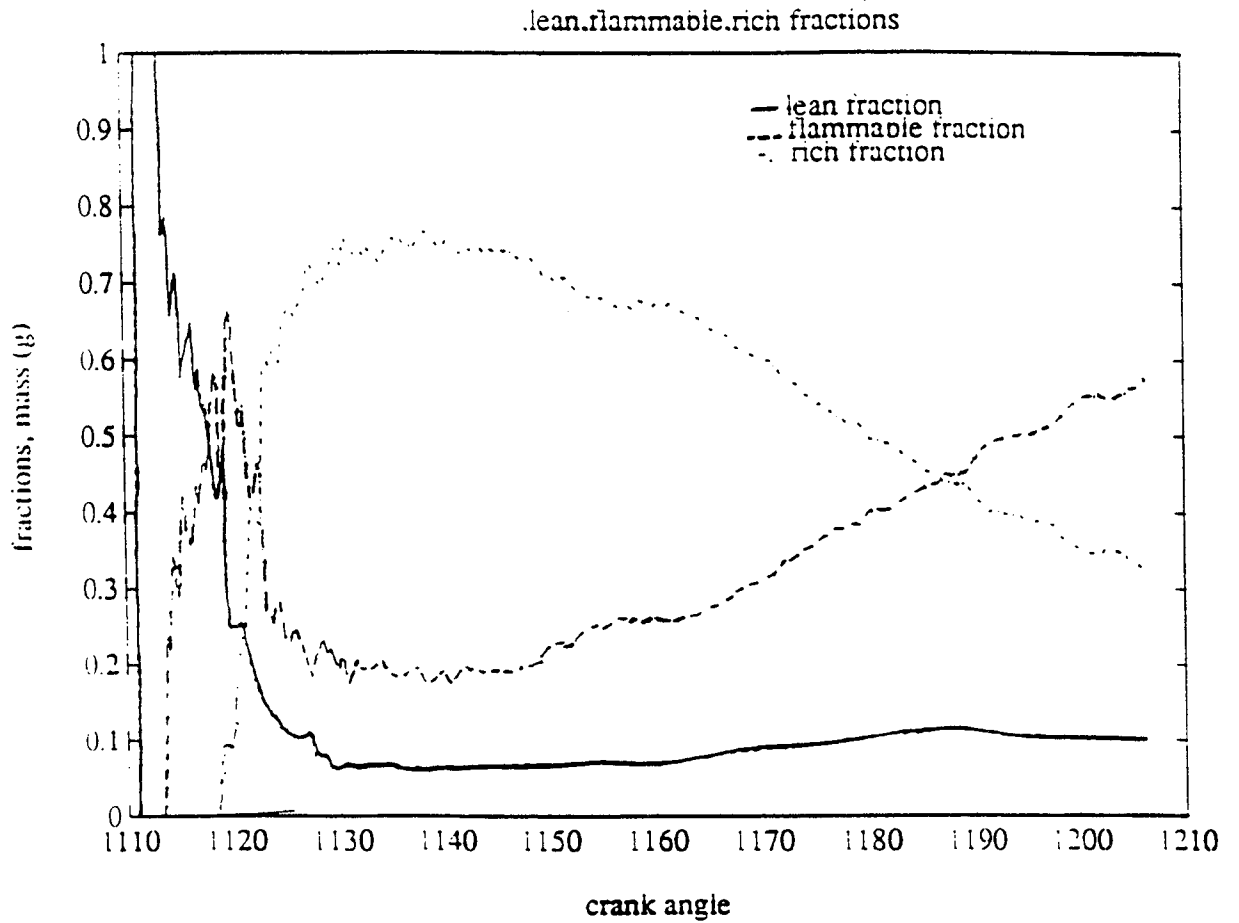


Fig. 38(a): Lean,Rich and Flammable fractions of vaporized fuel as a function of crank angle for the AUI system

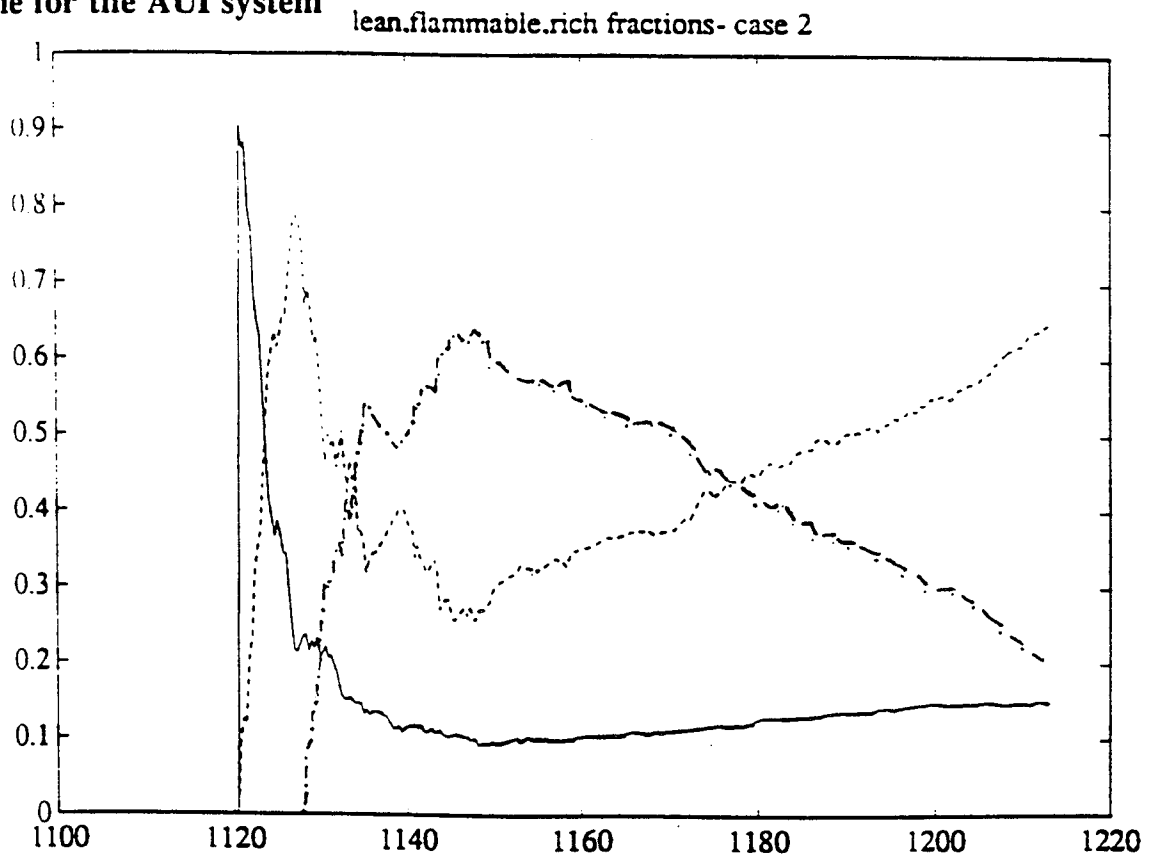
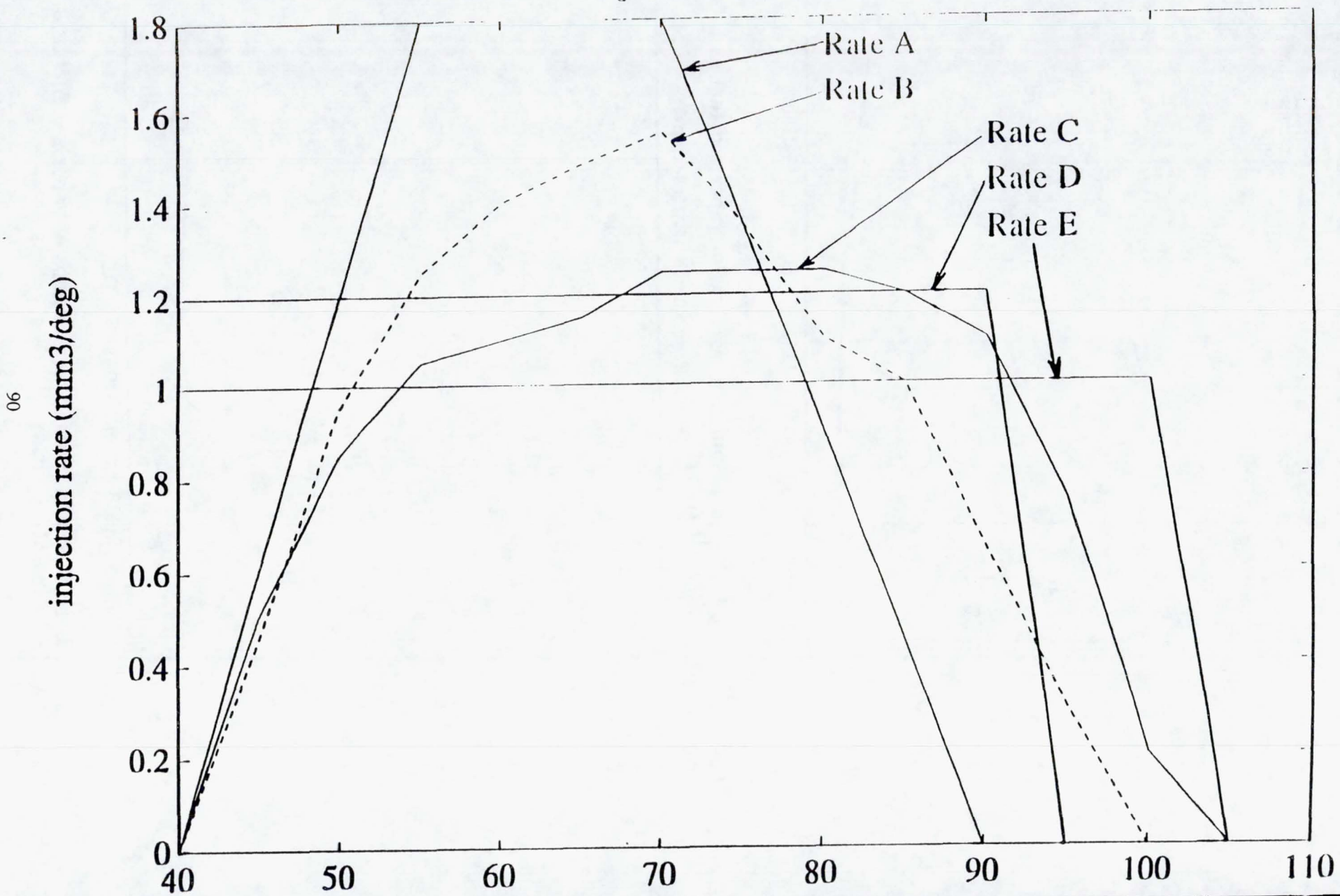


Fig. 38(b): Lean,Rich and Flammable fractions of vaporized fuel as a function of crank angle for the AUI system

Injection Rate Profiles



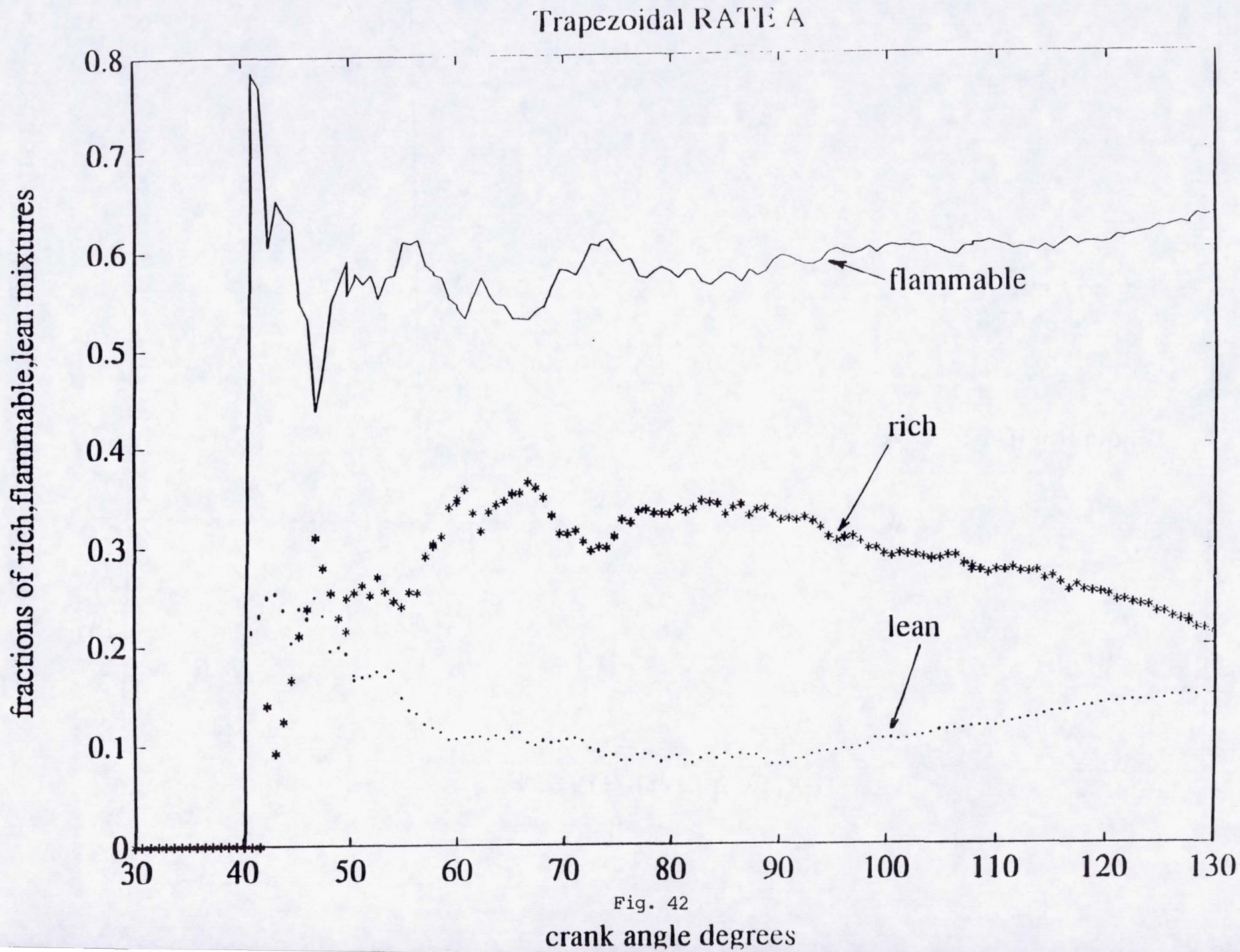
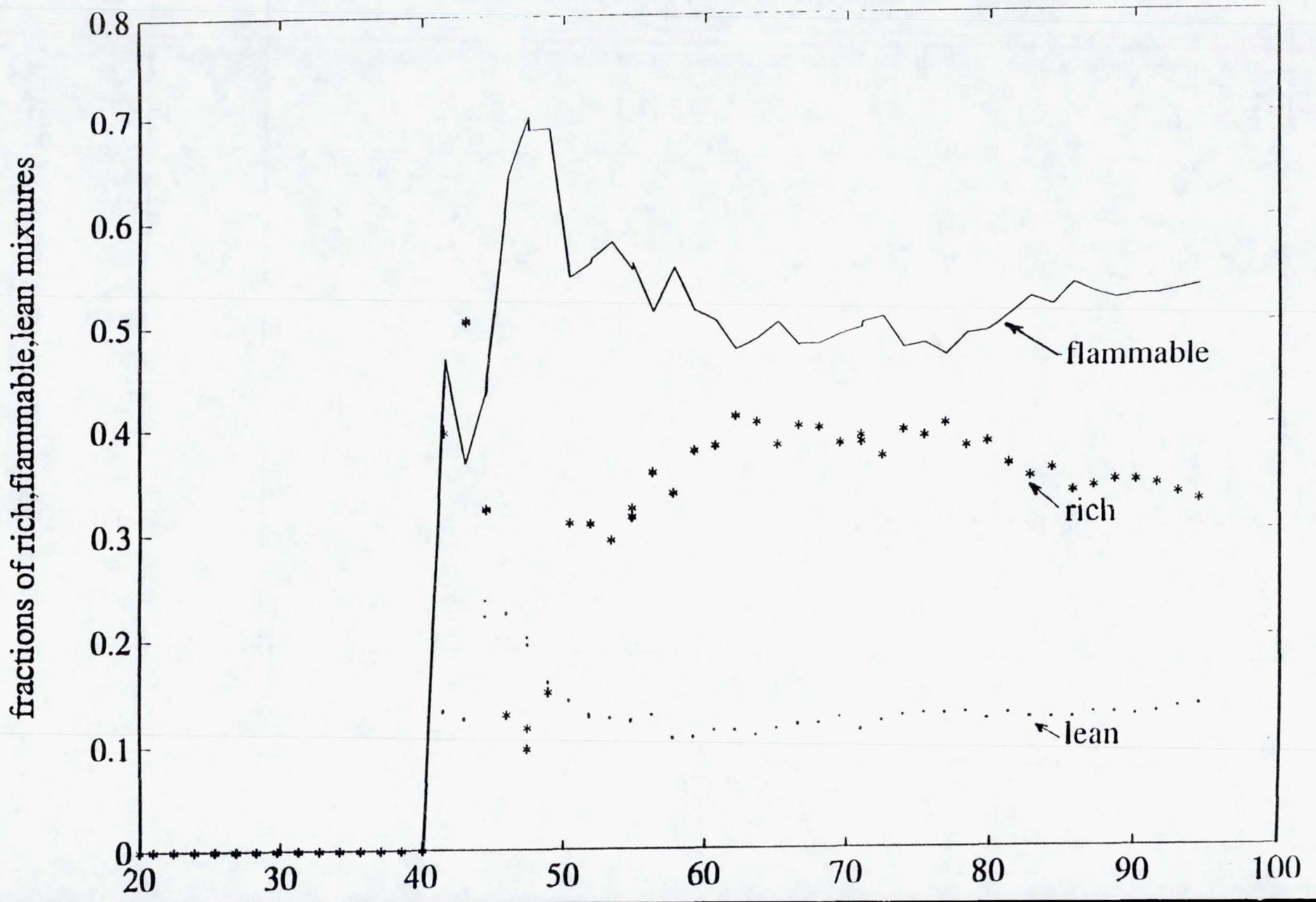


Fig. 42

crank angle degrees

AMBAC PUMP RATE B

92



Nippondenson pump RATE C

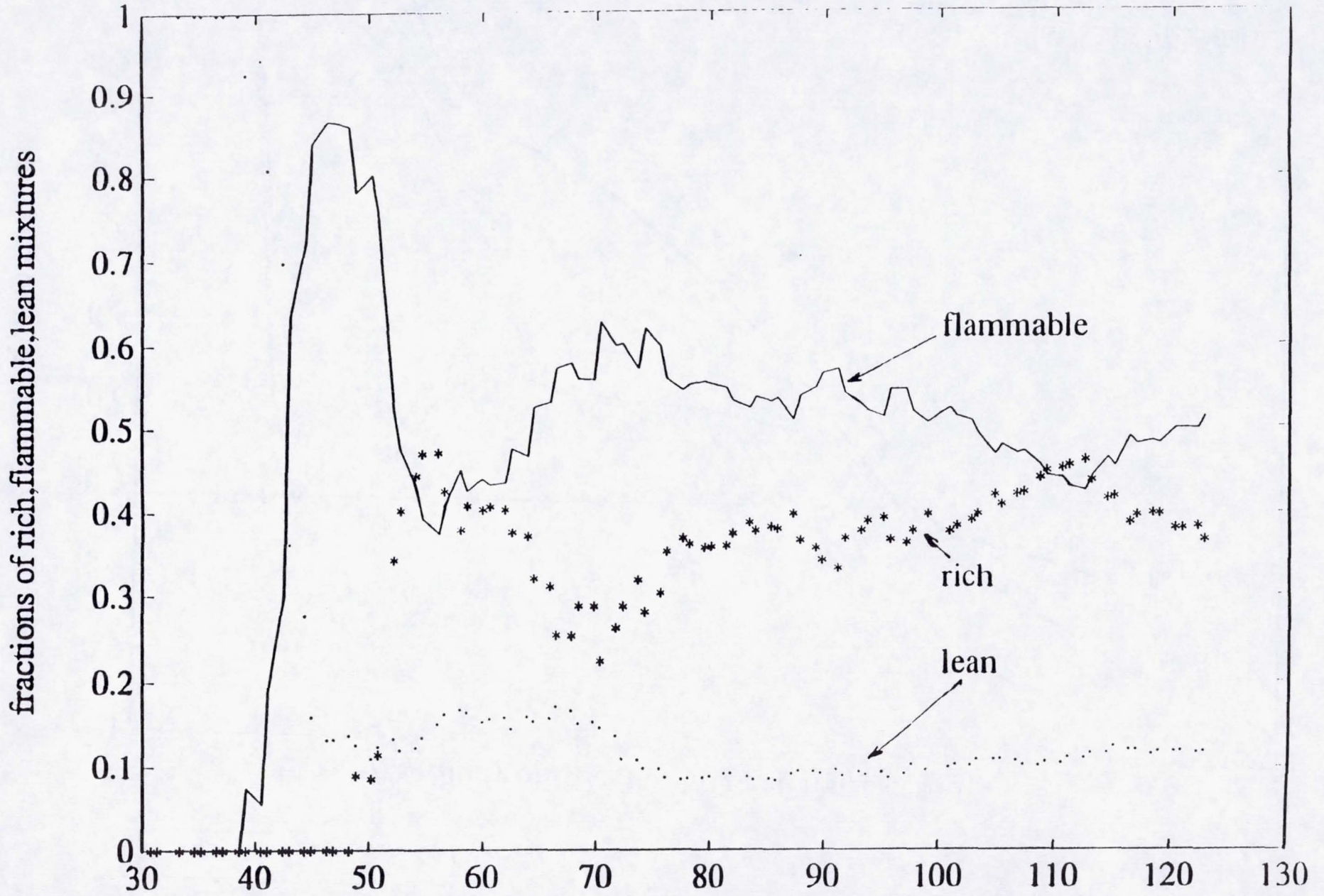
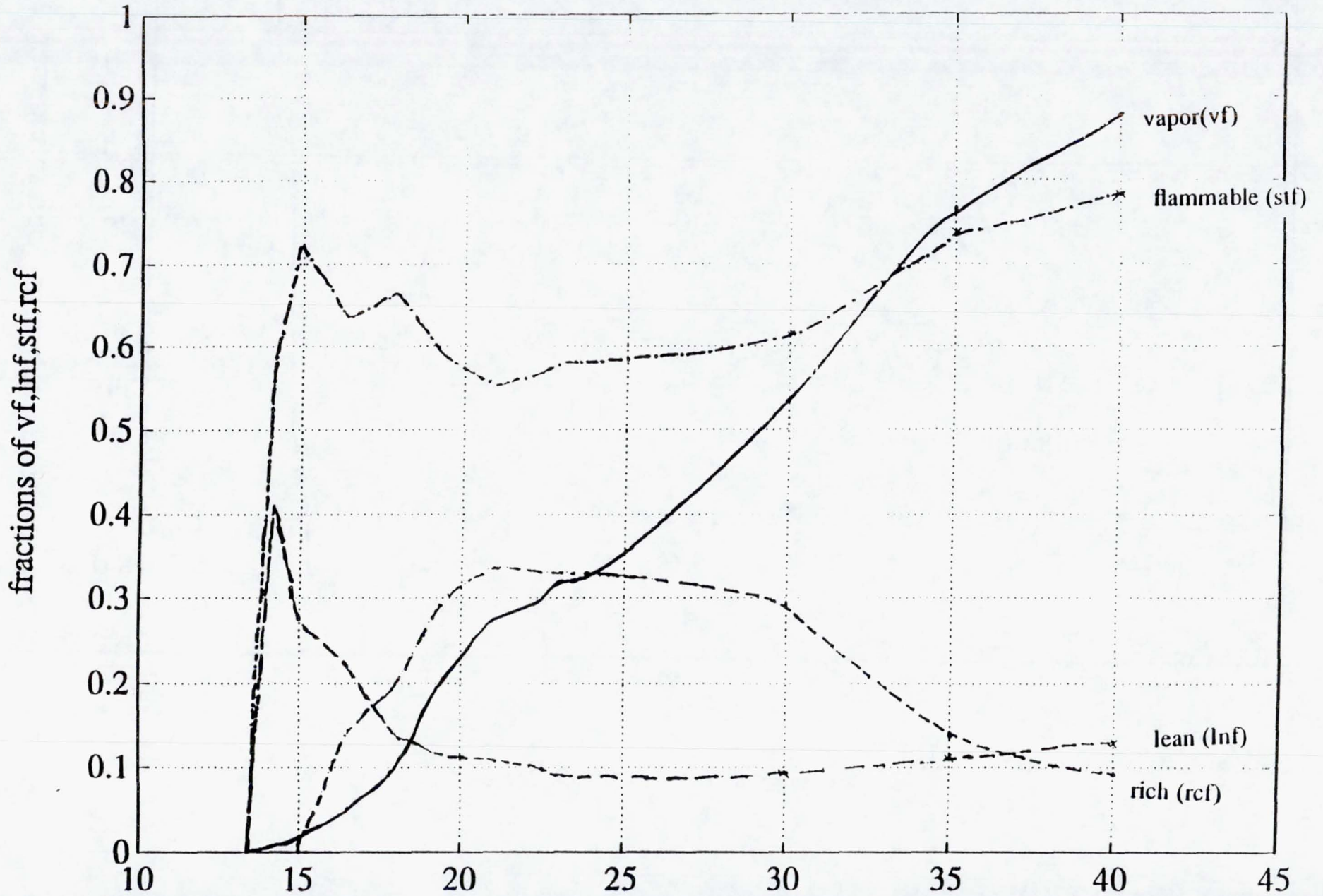


Fig. 44
crank angle degrees

Fig.47: Study of Effect of L/D ,reference case 1



4.0 CRITICAL TECHNOLOGIES

PRECEDING PAGE BLANK NOT FILMED

4.1 ADVANCED FUEL INJECTION SYSTEMS

PRECEDING PAGE BLANK NOT FILMED

PAGE 96 INTENTIONALLY BLANK

4.1 ADVANCED FUEL INJECTION SYSTEMS

INTRODUCTION

Fuel injection system research focused on identifying candidate systems for operation at high engine speeds and on supporting engine development tests.

Fuel injection system developers were surveyed in an attempt to identify a candidate fuel injection system suitable for operation with the Stratified Charge Rotary Engine (SCRE) at engine speeds exceeding 8000 RPM. A new concept based on a rotating valve which has the capability of very high injection frequencies and great flexibility in injection timing and injection rate shaping was selected. A feasibility analysis of the concept revealed no major impediments to further design development.

Engine testing and development of existing fuel injection systems was supported with NDenso A-Pumps and AMBAC M100 pumps. Injection rates were measured and engine tests were performed which indicated that the SCRE is relatively insensitive to fuel injection rate shape. Injection durations were shortened for use with the re-entrant and dual rotor combustion pocket concept tests. The pilot injection system was retuned and nozzle cooling improved to allow further development and refinement of the dual orifice pilot injection system.

The power output of the 70 Series Stratified Charge Rotary Engine (SCRE) has historically been limited by the fuel injection system. The rotary engine is inherently balanced and engines of this size can operate easily at speeds up to 10,000 rpm--racing engines have been run even faster.

The fuel specified for this engine (Jet A) has very little resistance to combustion so the residence time of the fuel in the combustion chamber must be kept to a minimum. If the residence time of fuel is small, a rotary engine can theoretically be run on conventional diesel and jet fuels and gasoline. JDTI has considerable experience running rotaries on Diesel and Jet-A and limited experience with gasoline, JP- 4, and JP-8.

The low residence time requirement dictates direct injection of the fuel into the combustion chamber. In addition to merely providing the fuel to the combustion chamber, the fuel injection system must distribute the fuel appropriately in the combustion chamber to facilitate fuel/air mixing. The system must also be capable of supplying the fuel over appropriate time intervals in order to control engine pressure rise rate and peak combustion pressure.

Techniques for directly injecting fuel into the combustion chamber are highly developed because of their use in diesel engines. Unfortunately, diesel engines are slow by comparison to the rotary with the highest speed diesel engines operating around 5000 RPM on a four stroke cycle. From the fuel injection standpoint, the rotary engine operates like a two stroke engine, so that instead of one injection being supplied for every second revolution of the

engine crankshaft one injection is required for each revolution of the engine crankshaft. Figure 1 shows the speed and fuel delivery requirements of the rotary engine compared to those of production diesel engines. The injection frequency for the small rotary is 5 times the maximum injection frequency of a diesel engine requiring a similar quantity of fuel per injection. Conventional fuel injection systems must be highly modified in order to operate with this rotary engine.

Considerable progress has been made toward providing a fuel system for the SCRE during two previous NASA contracts, NAS3-23056 and NAS3-24628. The fuel systems for the first engines consisted of two modified Stanadyne DM fuel injection pumps. These pumps are of the distributor variety, where one set of pumping elements is used to supply the fuel to up to 8 cylinders of a conventional engine. The output from the pumping elements is directed to each cylinder in turn by a rotating distributor valve, which may be integral with the pumping element. By eliminating the distributor function so that all output goes to one injector, high speeds are easily attainable. The DM pumps are limited to relatively small fuel delivery quantities, so engine torque and power output were limited. A higher output fuel system was necessary.

The next fuel system used on a SCRE was an Accumulator Unit Injector system designed and fabricated by Stanadyne. It utilized a solenoid valve and hydraulic servo circuit to modulate fuel being delivered from a high pressure rail. This system provided adequate fuel delivery and complete flexibility of injection timing and average injection rate. No improvement in engine performance was observed even with this added fuel system flexibility. The system was a unique prototype and suffered problems with reliability and durability which interfered with running the engine.

A more reliable fuel system was needed to support engine testing. Previous experience with AMBAC M200 pumps showed the feasibility of running multi-plunger "jerk" pumps up to 8000 injections/minute. A version of Nippondenso's A-Pump capable of operating at speeds up to 8500 RPM was developed. This pump proved reliable and provided adequate performance in terms of injection frequency and fuel quantity delivered. The A-Pump is limited to peak injection pressures of 9000 psi (62.01 mPa), which may not be sufficient to obtain best engine performance with some combustion chamber configurations. The 9000 psi (62.01 mPa) pressure limit is most likely to be detrimental to high power operation. The injection rate shape of the A-Pump based system is difficult to modify.

The following tasks were initially planned for the current contract.

- 1) Perform injection rate measurements on the existing injection systems in order to understand the effects of fuel injection rate on performance.
- 2) Develop a system for testing the benefits of higher injection pressure on the single rotor rig engine early in the program.

- 3) Support two rotor rig testing with a two rotor version of the existing single rotor Jerk pumps. A system for testing higher injection pressures or modified injection rate on the two rotor engine is expected to require considerable effort and not to be available until very late in the program. It is expected that any air system test work can be performed on the two rotor rig without the optimum fuel injection system if necessary.
- 4) Study the available fuel injection concepts in order to determine the best candidate fuel system for the two rotor rig engine. Procure and engine test the best system during the course of the program.

As a result of the program redirection as discussed in Section 2.0, the fuel injection effort was reduced. Hence, Task 3 was reduced in scope with no two rotor testing and Task 4 studies were terminated.

OBJECTIVES

The performance objectives of a fuel system for the SCRE are

- Injection frequency of 8000 injections/minute minimum with growth to 10,000 injections/minute.
- Maximum main fuel delivery of 100 mm³/injection minimum.
- Pilot fuel delivery of approximately 5 mm³/injection.
- Minimum main fuel delivery of 5 mm³/injection
- Useful life of 2000 hours.
- Not adversely affected by low temperatures and low pressures
- Multi-fuel capability
- Flexibility in injection timing, pressure, and rate shape. These parameters should be easily modified.
- Minimized drive power
- Lightweight
- Minimized peak drive torque
- Small intrusion into the rotor housing to simplify rotor housing cooling and improve rotor housing structural integrity.

- Failure modes which cause loss of engine control or loss of engine power must be minimized.

TECHNICAL APPROACH

Consideration and selection of the SCRE fuel injection system and the required characteristics of the system was divided into the four parts shown below:

1. Fuel System Survey

A survey of possible fuel injection systems for the SCRE was performed.

2. A-Pump Development

A-Pumps were used to support most of the engine development during the Phase III program. A two rotor A-Pump capable of 8000 injections/minute was developed for use with the 2 rotor engine. Fuel System configuration modifications were required in order to support improved engine configurations with enhanced combustion. Pilot fuel system development was required in order to obtain data with the dual orifice pilot nozzle system.

3. AMBAC M100 Injection System

An AMBAC M100 fuel system was procured in order to test the effect of higher injection pressure on engine performance and to provide shorter injection durations for some modified rotor configurations.

4. Injection Rate: Measurement and Shape

A long tube type injection rate measuring system was procured and utilized to measure the injection rates of the Stanadyne DM pumps, the AUI system, many configurations of the A-Pump, and the M100 pump.

Modifications were made to the A-pump to provide an injection rate shape matched to that of the Stanadyne DM pump in order to determine the effect of the rate shape on engine performance.

RESULTS

Fuel System Survey

Performance and packaging objectives for a fuel system for the SCRE were selected. Evaluation weights were applied to the objectives based on estimation of their importance in meeting the overall goals for an aircraft version of the SCRE (see Table 1). Six different fuel system candidates were considered for the future of this application.

The first system considered was the M100 pump with splitter valve described below. The major difficulty with this system for this study is the inability of the M100 to supply fuel to more than one rotor. There have been high speed M100 pumps tested in the past which could perhaps supply fuel to a 2 rotor engine at speeds up to 8000 injections/minute, but beyond that new designs with multiple hydraulic heads become necessary. These add considerable size and weight to the system. A secondary disadvantage of the M100 is the relative lack of timing and rate flexibility provided by this pump. For more details on the M100 system see below.

The second system considered was an improved jerk pump in which start and end of injection are controlled by a metering sleeve (See Figure 2). By moving the sleeve up and down the pumping position on the camshaft is altered and hence so are injection rate and timing (for details see section on injection rate below). A timing device added to the front of the injection pump allows independent control of injection timing. This system suffers from excessive size and weight, and some lack of timing flexibility depending upon the design of the timing device. The normal 10 degree advance timing device utilized on conventional diesel engines is not adequate for the rotary engine, which requires 40 degrees of advance in the current configuration. A fuel system used in combustion development benefits from additional timing flexibility until about 90 degrees of flexibility is achieved, since it is difficult to predict the proper timing for use with modified combustion chambers.

A third system considered was the use of conventional camshaft driven unit injectors (Figure 3). These are an improvement in capability over the previous systems, but still suffer from some limitation in timing capability. The packaging problem is considerable, since a camshaft would have to be designed into the hot side of the engine and sealed so as to contain oil. Fuel needs to be routed to the injector and leakage fuel returned to the tank. Any design would have to consider the necessity of frequent nozzle changes during engine development.

Fourth is a medium pressure common rail system (Figure 4). Fuel is supplied at an intermediate pressure in the range of 1000 to 5000 psi (6.89-34.45 mPa). The fuel charges an intensifier in the nozzle. When injection is required a solenoid is turned on which allows access to the low pressure side of the intensifier. The fuel charge is pressurized and fills an accumulator in the nozzle. The solenoid is de-energized, allowing the fuel in the low pressure side of the intensifier to bleed back to the tank. The pressure in the high pressure side of the intensifier is reduced, allowing the nozzle needle to lift and the fuel to be injected.

Weaknesses of this technique for use with the Rotary are the high fuel flow rates involved and the relatively inflexible injection rate shape.

The fifth system considered was a high pressure common rail system (See Figure 5). This system operates identically to the medium pressure common rail system except that the fuel is supplied at full injection pressure and the accumulator piston is not used. Direct solenoid control of the high pressure fuel allows both the start and end of injection to be controlled by the solenoid. A system like this was developed by Stanadyne and tested in an earlier program; details are provided in the section on injection rate.

The final system considered was a high pressure common rail system Appendix B, "Feasibility Analysis-Rotating Valve High Pressure Common Rail System" in which the fuel is turned on and off by a rotating metering valve, which is timed to the engine either mechanically or electronically. The metering valve eliminates the need for very high speed and precision solenoids. In addition, the depth of the slot in the metering valve can be controlled to facilitate injection rate shaping.

After rating each of the fuel systems for potential to meet the requirements of rotary engine fuel system (as defined in Table 1) a K-T analysis was performed. The results are as indicated in Figure 6. The rotating valve high pressure common rail fuel injection system appears to have the most potential for providing the best fuel injection for the SCRE.

A-Pump Development

Figure 7 shows a typical A-pump and its theory of operation. Pressurized fuel from the injection pump gallery fills the space above the plunger through the barrel port (1). The plunger moves upward until it closes off the barrel port for the start of injection (2). Further upward travel of the plunger causes fuel to be forced upward, lifting the delivery valve off of its seat and flowing outward through the injection line and nozzle (3). The plunger continues to move upward until a spill helix re-opens the barrel port. At this point the pressure above the plunger drops. The delivery valve returns to its seat, retracting a measured amount of fuel from the injection line and quickly dropping the pressure in the line (4). The quantity of fuel retracted by the delivery valve is determined experimentally to provide a residual pressure in the injection line when the delivery valve is seated, but not so much residual pressure as to force the injection nozzle to open a second time when the pressure wave from shutting the valve reaches it (a phenomenon known as a secondary injection).

In addition to the four single plunger pumps procured under the NASA Phase II program, three multi-plunger pumps have been procured which are capable of operating a two rotor engine at speeds up to 8000 RPM (slightly higher speeds can be obtained by simple governor modifications).

In order to make the multi plunger pump operate at the high speeds required for the rotary engine, we modified the camshaft to provide two lifts per cam lobe per revolution, installed a high force return spring, and increased the gallery pressure to 50 psi (0.344 mPa).

During the course of engine testing we experienced severe secondary injections at heavy loads with the four and five hole injection nozzles. The secondary injections are a consequence of increasing the injection line inner diameter (ID) from 1.2 mm to 1.5 mm, which was done in order to prevent exceeding the 9000 psi (62.01 mPa) pressure limit of the A-Pump. The solution used for this program was to increase the retraction of the delivery valve from 55 mm³ to 80 mm³. The increased retraction is not adequate at light loads and low speeds because the retraction is excessive and cavitation occurs. Flats cut on the delivery valve improved the situation, but did not solve it. Using large retraction volumes is inherently a poor solution because it lowers the efficiency of the pump--in order to inject 50 mm³ of fuel we must now pump 130 mm³.

Experience gained in the rate shaping test led to a means of eliminating the secondary injections. By changing the lift to port closing dimension on the pumping plunger (either by shimming the existing plunger or manufacturing new plungers) the rate of pumping can be decreased. A sufficient decrease in the rate of pumping allows using the original 1.2mm injection line diameter and using the original 55mm³ retraction delivery valves without causing secondary injections.

The reduction in pumping rate also causes an undesirable effect of changing the shape of the injection rate versus crank angle curve. Test data indicates that the change in injection rate versus crank angle will not degrade engine combustion and the increased pumping efficiency may improve engine operating efficiency very slightly.

A dual orifice pilot nozzle was tested and found to be quite beneficial for reducing fuel consumption. On the first engine the fuel system developed a severe nozzle seat cavitation erosion problem which caused degradation of engine performance after as little as 30 minutes of operation. A secondary problem of excessive pilot nozzle tip temperature caused frequent plugging of the pilot nozzle orifices with carbon. These problems are discussed in more detail in a detailed test report submitted to NASA LeRC as part of the contractual reporting entitled "Investigation Into Changes in Engine Light-Off Performance Using the 2 Orifice 'Rabbit Ear' Pilot Configuration", 30 April 1991. The second engine which had a dual orifice pilot incorporated a re-tuned pilot injection system and decreased pilot nozzle tip clearance. The re-tuned pilot system was trouble free throughout the 14 hours of the engine test.

The fuel systems for the two rotor engines were designed using the technology available at the beginning of the contract. The fuel systems therefore do not include the two improvements discussed above.

The two rotor rig engine designed for the phase III program is based on existing production engine designs, and therefore has a gear train for driving one injection pump. The fuel

injection pump must supply both pilot and main injection for each of two rotors. This is achieved by installing two main plungers and two pilot plungers in the pump, and appropriately phasing the camshaft lobes. The pilot plungers have a flat helix, so the amount of pilot delivery is fixed for any given pump. The phasing between the pilot and main injections can be modified by shutting down the engine and changing the thickness of shim between the plunger and the tappet. The shim has the effect of changing the starting and ending lift of the pumping stroke and therefore the injection timing.

The limitations of fixed pilot fuel delivery and pilot to main phase angle are judged to be acceptable for the two rotor rig engine. The major portion of development work on this engine involves the air delivery system, where fuel injection changes make only a minimal amount of difference. Fuel system and combustion development will continue to be performed on the single rotor rig engine.

During development of the system several real world problems were discovered. The wide range of speeds and large turndown ratios cause some difficulty in avoiding secondary injections and delivered quantity variations throughout the operating range. These difficulties are an inherent part of the pump line nozzle injection system due to the large volumes of fuel between the pumping element and the nozzle spray orifice.

Figure 8 shows the range of pilot fuel deliveries where acceptable fuel injection quality is obtained as a function of engine speed. If too much pilot fuel is delivered at high engine speed secondary injections occur. These injections can accelerate pilot nozzle coking, degrade fuel consumption, and cause excessively smoky exhaust emissions. More fuel can be delivered by increasing the nozzle orifice area, but this has deleterious effects on combustion performance. Fortunately, the NASA rig engine seems to operate well on pilot quantities which can be delivered without secondary injections.

If slightly too little fuel is injected through the pilot injector vapor bubbles can be formed in the injection lines between injections. These bubbles collapse under injection pressure, causing cavitation erosion of the walls of the tubing. In severe cases the tubing wall can rupture in as little as ten hours of operation. This situation caused us some difficulty with the dual orifice pilot system as discussed above.

As the delivered quantity is reduced further the system becomes unstable, so that the injected quantity and timing no longer repeat accurately from one injection to the next.

It is noteworthy that the range of fuel deliveries at which acceptable injection is obtained narrows as the speed is increased. Fortunately, it is possible to select an injection quantity such that the pilot fuel delivery is within the acceptable range throughout the engine speed range. Figure 9 shows the pilot quantity delivered as a function of engine speed.

As seen in Figures 10 and 11 the same injection variation phenomena occur with the main injection system to a smaller degree. Comparing Figures 10 and 11 we see that the region

of secondary injections grows smaller as the nozzle orifice area is increased. We operate on the single rotor rig engine with much larger main delivery quantities by increasing the nozzle orifice area. This is undesirable because it sacrifices combustion performance at the lower speeds and loads in order to allow high speed and load operation. A loss of high speed and load performance is also likely.

Figures 12 and 13 show the injection timings achieved with the two rotor rig pump. Experience with our commercial engine development venture indicates that these timings will operate the engine successfully. We will need to retard the timings at lower speeds in order to obtain the best BSFC and highest torque capability. Conventional fuel injection timing devices are normally of limited range and have only speed dependence. A design layout of an oil pressure operated timing device capable of electronic control was completed early in this program (Reference Drawing LS34507).

AMBAC M100 Injection System

In order to facilitate high speed and power operation and to obtain test data with higher injection pressures, a contract was provided to AMBAC for development of a M100 injection pump capable of running at 8000 RPM on our existing gearbox. The M100 can operate at pressures of up to 15000 psi (103.35 mPa) for short periods of time. The M100 pump is expected to perform reliably at pressures around 12000 psi (82.68 mPa) using our current injection nozzles.

To provide higher speed capability a splitter valve was developed. This technology will allow us to operate the system at speeds up to 10000 injections/minute if such proves to be desirable. The splitter valve can significantly reduce the size and weight of future injection systems by allowing both pilot and main injection from one injection pump outlet. The pilot injection was demonstrated to be repeatable for a wide range of main fuel delivery. The splitter valve is, however, sensitive to the residual pressure in the injection line and requires re-tuning of the system each time main injection nozzles are changed.

A schematic of the splitter valve system is shown in figure 14. The system currently requires a separate pilot supply circuit from the boost pump, but techniques for eliminating this circuit are under consideration.

Figure 15 shows a cross section of the pilot injector with attached splitter valve. Fuel is supplied to the nozzle at 80 psi (0.551 mPa) through a check valve in the fuel supply duct. This fuel charges the pilot pumping cavity to the left of the pilot piston. When the injection pulse is received through the pump inlet, the pilot piston is forced left, pressurizing the fuel in the pilot injector and causing pilot injection. After a sufficient quantity of fuel has been ejected from the pilot nozzle, the main piston is far enough left to open the ports to the main injector and main injection starts. Pilot injection ends when the pilot piston closes off the pilot fill port and comes to rest against the fuel remaining in the pilot pumping cavity. At

the end of main injection the spring returns the pilot piston to the left, and the whole process starts over again.

Figure 16 shows the experimentally determined main and pilot fuel flows as a function of engine speed. This fuel flow data is at full load; similar data taken at 25, 50, and 75 percent load indicate that the pilot delivery is not affected by the main injection quantity.

The pilot fuel injection quantity is affected by residual pressure in the injection lines. If the residual pressure in the injection line is too large the spring force is not able to overcome the pressure force on the main piston, and pilot injection ceases. This sensitivity to residual pressure may make the system difficult to use in an experimental situation.

Figure 17 shows the timing lead of the pilot injection before the main injection. These timings are almost ideal by our current estimate of fuel system requirements with conventional rotor pockets and pilot nozzles. While the lead of the pilot injection over the main injection is smaller than that provided by our current systems at low speeds, we believe this reduction in pilot to main lead will actually improve engine performance at in the lower speed range.

Additional data were taken using the main injection pump alone. This data shows the M100 injection pump to be capable of supplying $125 \text{ mm}^3/\text{injection}$ of fuel at around 12000 psi (82.68 mPa) with an acceptable 60 degree duration at 8000 RPM. This is adequate for us to obtain further information on the effect of injection pressure on engine combustion at high power.

A brief test of the M100 pump was performed on engine 0706-1 to evaluate the effect of the M100 injection rate, which is somewhat different from the injection rate of the A-Pumps. In general, performance with the M100 pump was found to be almost identical to performance with the A-Pumps. For details see the section on injection rate below.

The M100 pump was used as the main fuel injection pump for the last two rig engines run on this program. The primary reason for this was the higher rate of injection which allowed sufficient quantities of fuel to be injected in short durations for the experimental rotor pocket configurations. Performance data for Engine 0707-1, Leading Rectangular Pocket and Engine 0707-2, Leading Standard Pocket is provided in Section 12.0.

Injection Rate Measurement

Differences in performance have been observed between Rotary engines with various fuel injection systems.

The DM pumps showed better engine performance than data taken with the AUI injector system. This data is obscured somewhat by a difference in exhaust back-pressure between the two engines. See Figure 18.

The DM pumps showed better performance than was obtained with the A-Pumps. See Figure 19.

Fuel consumption was shown to decrease 6 percent on engine 0705-3 simply by changing the fuel injection line ID from 1.5 mm to 1.0 mm. See Figure 20.

Combustion modeling suggests the different fuel injection systems will provide different combustion efficiencies. Figure 21a shows five fuel injection rates for which performance was calculated. Rate A is a hypothetical injection system capable of producing a trapezoidal injection rate with a peak pressure around 14000 psi (96.46 mPa). Rate B is the AMBAC M100 fuel injection rate. Rate C is the Nippondenso A- Pump fuel injection rate. Rates D and E are hypothetical square wave injection rates. Figure 21b shows the rich, lean, and flammable fractions of the mixture in the combustion chamber as a function of engine crank angle degrees. For all these figures 90 degrees is engine minimum volume (TDC). The flammable mixture fraction calculates to be around 60% throughout the time of combustion with the trapezoidal rate injection system. Figure 21c shows similar results for the AMBAC M100 injection rate shape, except that the flammable portion is around 50% of the fuel in the combustion chamber. Figure 21d shows the same results for the Nippondenso A-pump injection rate shape. In this case the flammable portion of the fuel is between 45 and 55% depending upon the crank angle. From these modeling results one would expect the M100 and A-Pump systems to have similar engine performance, a result which was in fact obtained as discussed below.

Several schemes for measuring injection rate were evaluated. The long line technique described by Robert Bosch in SAE Paper 660749 was selected because of its simplicity and wide acceptance.

A contract was provided to Adiabatics Inc. of Columbus, Indiana to design and fabricate an injection rate measuring device and perform measurements at a variety of speeds and fuel deliveries on both the Stanadyne DM pumps and the Stanadyne AUI system. The full results are published in Adiabatics Technical Report "Injection Rate Measurement Stanadyne DM fuel Pump and AUI Injection System". Excerpts of relevant data are provided here.

After rate measurements were completed at Adiabatics, all of the hardware was returned to JDTI. The rate measuring equipment was set up in our fuel lab and utilized to measure the injection rate of various fuel injection systems which were used in engine testing during this program.

Measurement of the instantaneous rate of injection for the different fuel systems was performed. Figure 22 shows the difference in injection rate shape between the DM and AUI

systems. It is noteworthy that the injection rate trace from the AUI system is very clean. There is no indication of after-dribble, slow needle closing, or other deleterious injection effects which would explain the performance difference observed between the DM and the AUI injection systems.

Figure 23 shows similar data for the DM and A-Pump systems. One difference is that the A-Pump injection rate is somewhat higher than the injection rate of the DM pump. Some of the performance difference between the DM and the A-pumps may be attributed to differences in pump power requirements. The injection lines used with the A-pump are considerably longer than those used with the DM system. The injection rate at the end of injection is higher with the A-pump than with the DM system. These two factors make the A-pump hydraulically less efficient than the DM pumps were and may perhaps account for as much as two horsepower difference in pump drive power at these speeds and loads. The performance difference seen is on the order of 10 HP (7.5 kw), however, so this explanation is not sufficient. Motoring frictions of the two engines are within two horsepower of each other throughout the speed range where data were taken. Some difference in combustion efficiency between the two engines is necessary to explain the data. The engine with the DM pump on it has 5% lower airflow which experience indicates would be detrimental to performance.

Figure 24 shows the results from the A-Pump with 1.5 mm injection line versus the A-Pump with 1.0 mm injection line. The pump used had a 7.5 mm plunger, an 80 mm³ retraction delivery valve, and a snubber valve with a .7 mm diameter orifice. The nozzle was a Stanadyne slim tip pencil nozzle with four .009" diameter orifices. The major difference is a decreased peak injection rate and longer duration of injection for the better performing 1.0 mm ID system. In addition, the injection rate seems to be relatively constant compared to the injection rate of the 1.5 mm ID system.

Since the best performance obtained to date using a 6 hole shadowing spray pattern was obtained with the Stanadyne DM pumps, it was desirable to test the improved Non-Shadowing patterns using pumps with a similar injection rate shape. Unfortunately, the DM pumps can not deliver sufficient fuel for the power now being produced. It was therefore decided to reconfigure a Nippondenso A-Pump in order to match the Stanadyne injection rate shape.

Figure 25 shows the operating principle of the Stanadyne fuel injection pump. Pressurized fuel is metered through the metering valve and allowed to partially fill the cavity between the two plungers. As the distributor rotates, the inlet port connecting to the metering valve is closed and a discharge port leading to a fuel injector is opened. Further rotation causes the plungers to be driven inward by the cam lobes and deliver fuel into the engine. Start of injection occurs when the pumping elements first contact the cam. End of injection occurs when the pumping elements pass the cam nose.

Some consequences of this metering technique are:

- 1) The injection rate at the beginning of injection is higher than the injection rate at the end of injection because the injection is occurring over the cam nose.
- 2) The injection rate and timing of the start of injection vary with fuel delivery. Smaller quantities of fuel are injected at a lower rate.

In contrast, the pumping principle of a jerk pump (in this case the A-Pump) is shown in Figures 7-1 to 7-4. Fuel fills the space above the plunger when the plunger is below the fill port (7-1). The plunger is pushed up by the cam until the fill port is closed (7-2). The distance from the bottom of the plunger stroke to the position at which the port is closed is termed "lift to port closing" or LPC. The plunger continues to be pushed upward, pumping fuel (7-3). Finally, the plunger travels far enough so that the spill helix on the plunger lines up with the spill port, ending injection (7-4). In theory, this technique gives control over the timing and rate of both the beginning and the end of injection as a function of load. In practice, the beginning of injection is usually constant and the end of injection is varied.

Figure 26 shows the lift vs velocity curve for the A-pump camshaft. The pump was initially designed with LPC of 3 mm. This means that pumping occurred over range A. In order to match the pumping rate of the Stanadyne pump, it is desirable to set the LPC dimension to approximately 7 mm, so that pumping occurs over range B. It can be seen that the average pumping rate over range A is much higher than the rate over range B. This can be compensated for by increasing the plunger diameter as well as the LPC dimension.

A 10mm upper helix plunger was modified to obtain 7 mm LPC by grinding the fill port, grinding the top of the plunger, and placing a 1.5 mm shim under the barrel when installing the plunger in the pump. Grinding the plunger and fill port reduces the maximum fuel delivery available, but because the original 10mm plunger was capable of delivering 250 mm³/injection this was not a problem.

Figure 27 shows the injection rate curve achieved at 60 mm³/injection with the A pump compared with the injection rate achieved with the Stanadyne DM pump. As can be seen, the match is within the error band of measurement capability. Figure 28 shows the injection rate curves of the modified pump at a variety of fuel deliveries. It is seen that the A- Pump injection rate is somewhat higher at light loads than that of the DM pump. This is a consequence of the use of a lower helix plunger in the A-pump so that the beginning of injection stays at the same place on the camshaft. If further engine test data shows it to be desirable, a plunger could be manufactured with an upper helix so that the end of injection stayed constant; this would make the injection rates more similar at all fuel deliveries.

Engine testing of the modified Nippondenso A-Pump showed some performance improvement at light loads and a possible small loss in performance at heavy loads (See Figure 29). The differences are quite small and the performance may be the same within the accuracy of measurements.

Performance did not improve with the non-shadowing spray patterns (Figure 30). There is some question regarding the accuracy of this data because the performance of the engine degraded during this test; at the end of the test the performance with the N1 nozzle was .42 lb/hp-hr at best. The test cell gearbox broke before the cause of this performance loss was isolated.

Figure 31 shows a comparison of the injection rates for the baseline A-Pump configuration and the M100 fuel injection pump.

Figures 32 A and B show a comparison of the performance data obtained with the A-Pump and the data taken with the M100 pump. Figure 32a illustrates the significant shortening of injection duration with the M100 pump. The shortening of injection duration was directly applicable for use within the strict injection time constraints of the Leading Rectangular Pocket Rotor in Engine 0707-1. Only a limited amount of engine operation data with the pump was obtained. Figure 32b shows a comparison of the fuel consumption between the M100 and the A-Pump. Based on these 6 data points at 6000 RPM and the simulation predictions discussed above, it may be conjectured that there is no difference in engine performance between the A-Pump and the M100 injection systems.

CONCLUSIONS

A dual orifice pilot nozzle and fuel system configuration which will provide adequate life and reliability is feasible.

The rotating valve type high pressure common rail system has potential to provide the best fuel injection characteristics for the Stratified Charge Rotary Engine.

The SCRE with our conventional rotor pocket as described in drawing 617001N2 is relatively insensitive to changes in fuel system injection rate.

RECOMMENDATIONS

Pursue development of a rotary valve type high pressure common rail system for future aircraft type stratified charge rotary engines.

TABLE I

T E C H N O L O G Y R E V I E W

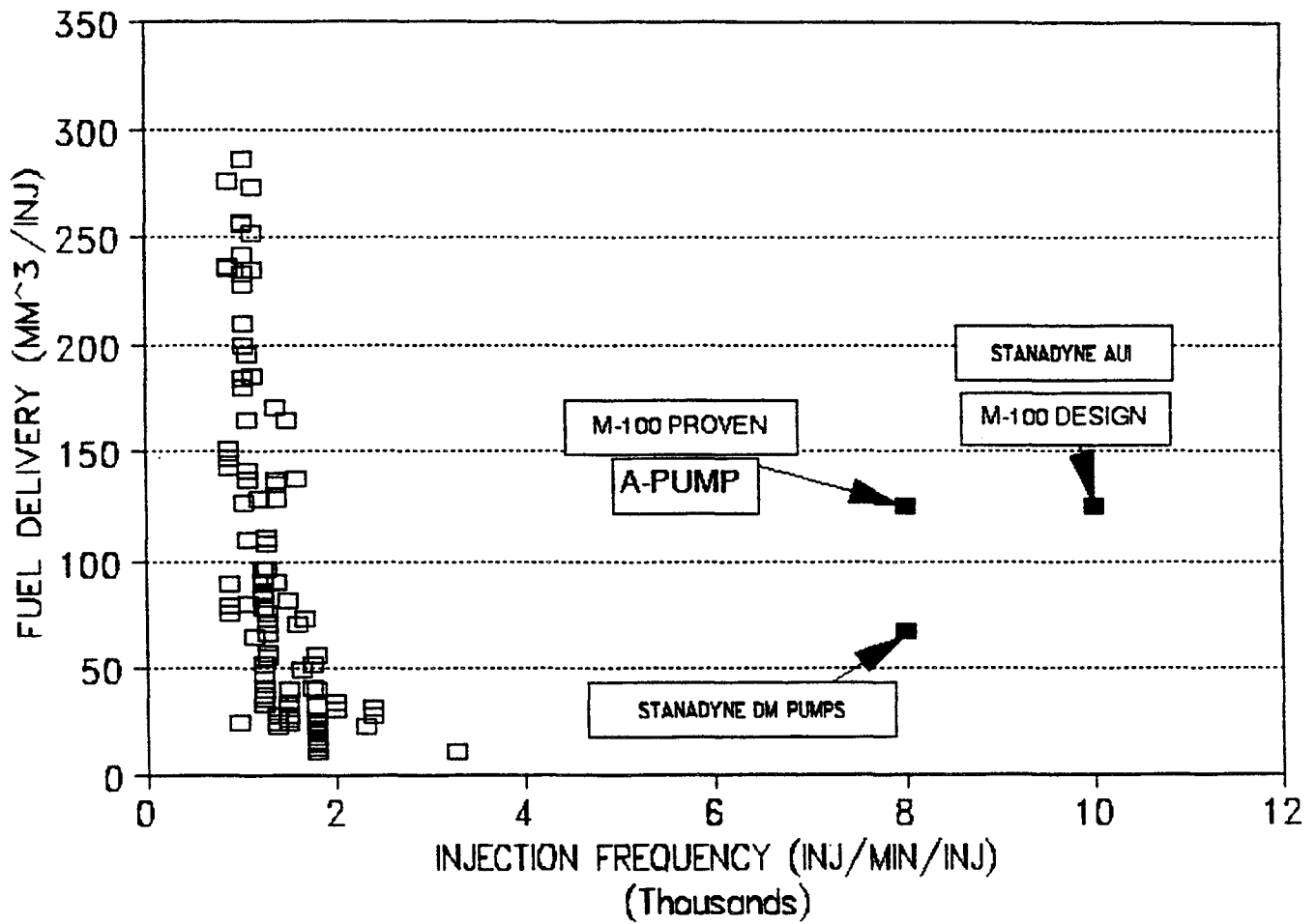
**K-T ANALYSIS OF EXISTING & ADVANCED
FUEL INJECTION SYSTEM TECHNOLOGY**

<u>CRITERIA</u>	<u>WEIGHT</u>
INJECTION FREQUENCY	10
ADEQUATE FLOW	10*
TIMING FLEXIBILITY (90 BTC TO TC)	10
MULTI-ROTOR CAPABILITY	9
INJECTION RATE CONTROL	8
MAXIMUM PRESSURE CAPABILITY	8
REPEATABILITY INJECTION TO INJECTION	7
ESTIMATED WEIGHT	7
PACKAGABILITY	7
PEAK DRIVE TORQUE	7
SAFE FAILURE MODES**	7
INDEPENDENT CONTROL OF EACH INJECTOR	5
ROTOR HOUSING INTRUSION	4
DRIVE POWER	3
DURABILITY	2
MULTI FUEL CAPABILITY	*

* SYSTEMS WERE ALL CONSIDERED TO BE EQUAL

** SYSTEMS WITHOUT SAFE FAILURE MODES CAN BE
MADE SAFE BY THE ADDITION OF EXTRA DEVICES

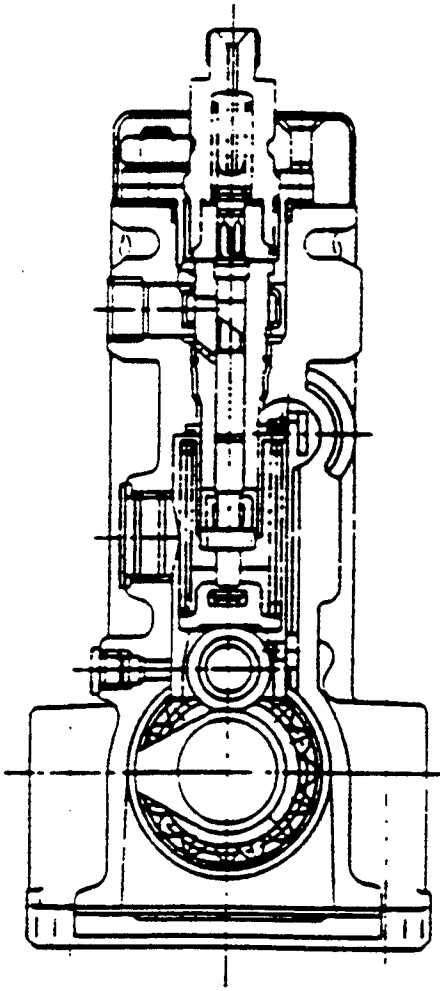
THE NASA CHALLENGE



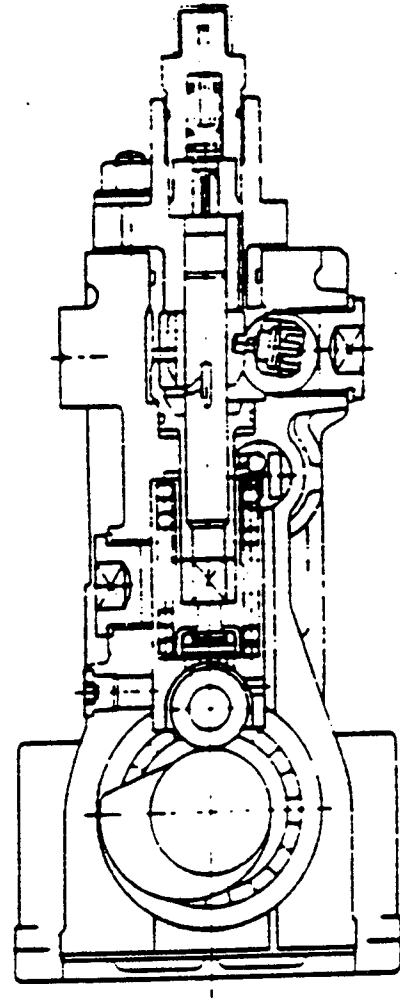
COMPARISON OF INJECTION FREQUENCY

Figure No. 1

RATE CONTROL JERK PUMP



CONVENTIONAL TYPE

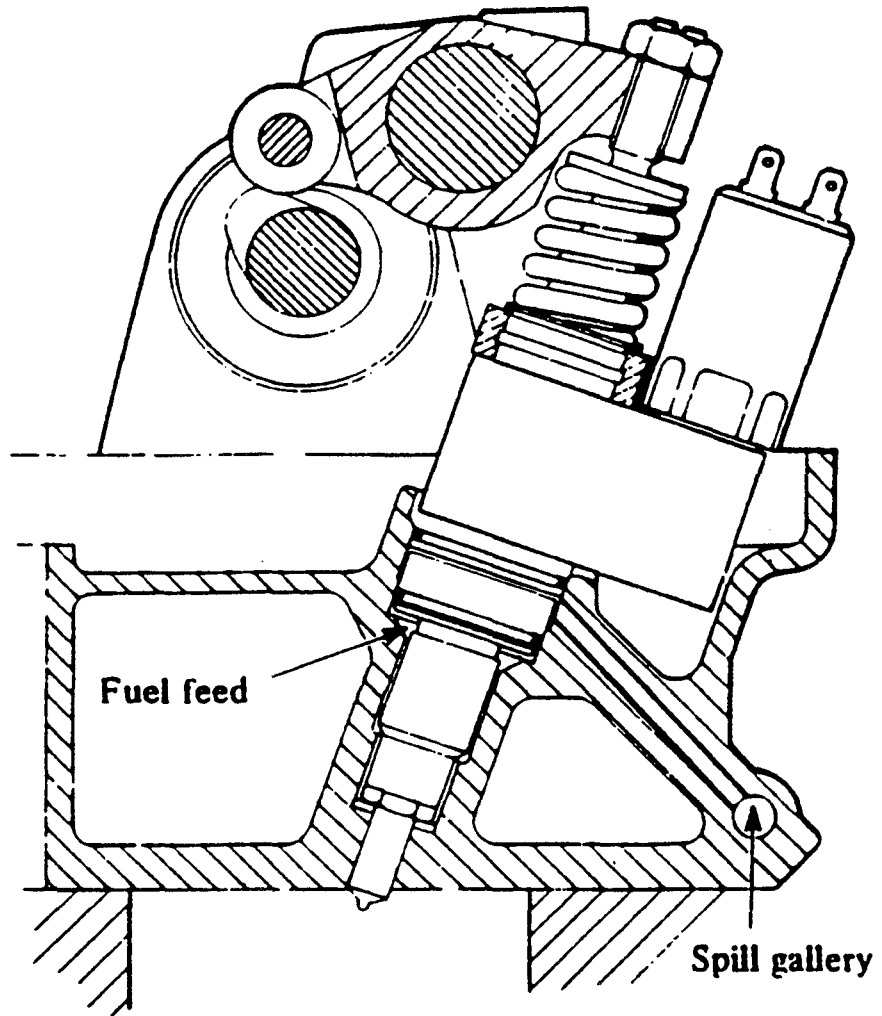


INJECTION-RATE-CONTROL TYPE

INJECTION RATE CONTROL

Figure No. 2

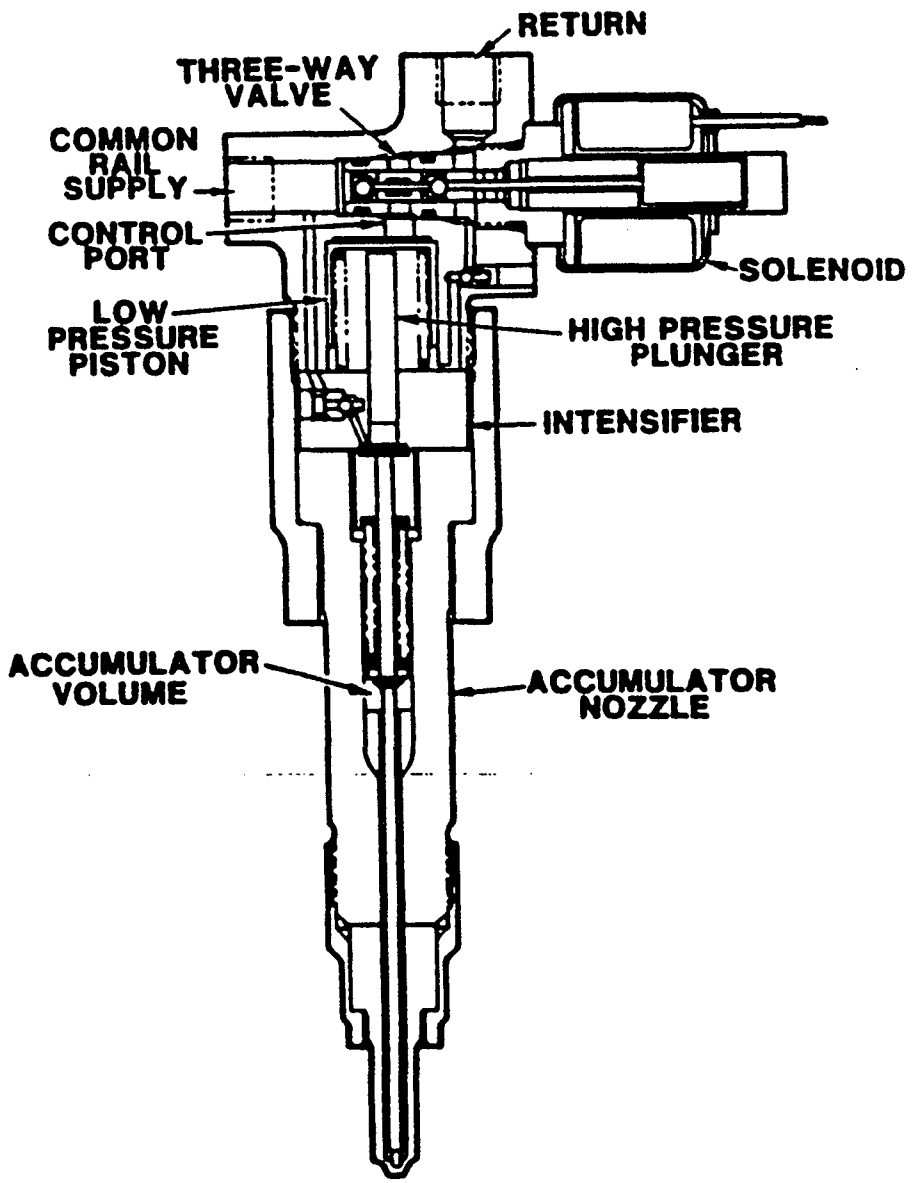
UNIT INJECTORS



CAMSHAFT DRIVEN INJECTORS

Figure No. 3

MEDIUM PRESSURE COMMON RAIL



HIGH PRESSURE COMMON RAIL
(REMOVE AMPLIFIER PISTON)

Figure No. 4

STANADYNE ACCUMULATOR INJECTOR OPERATION

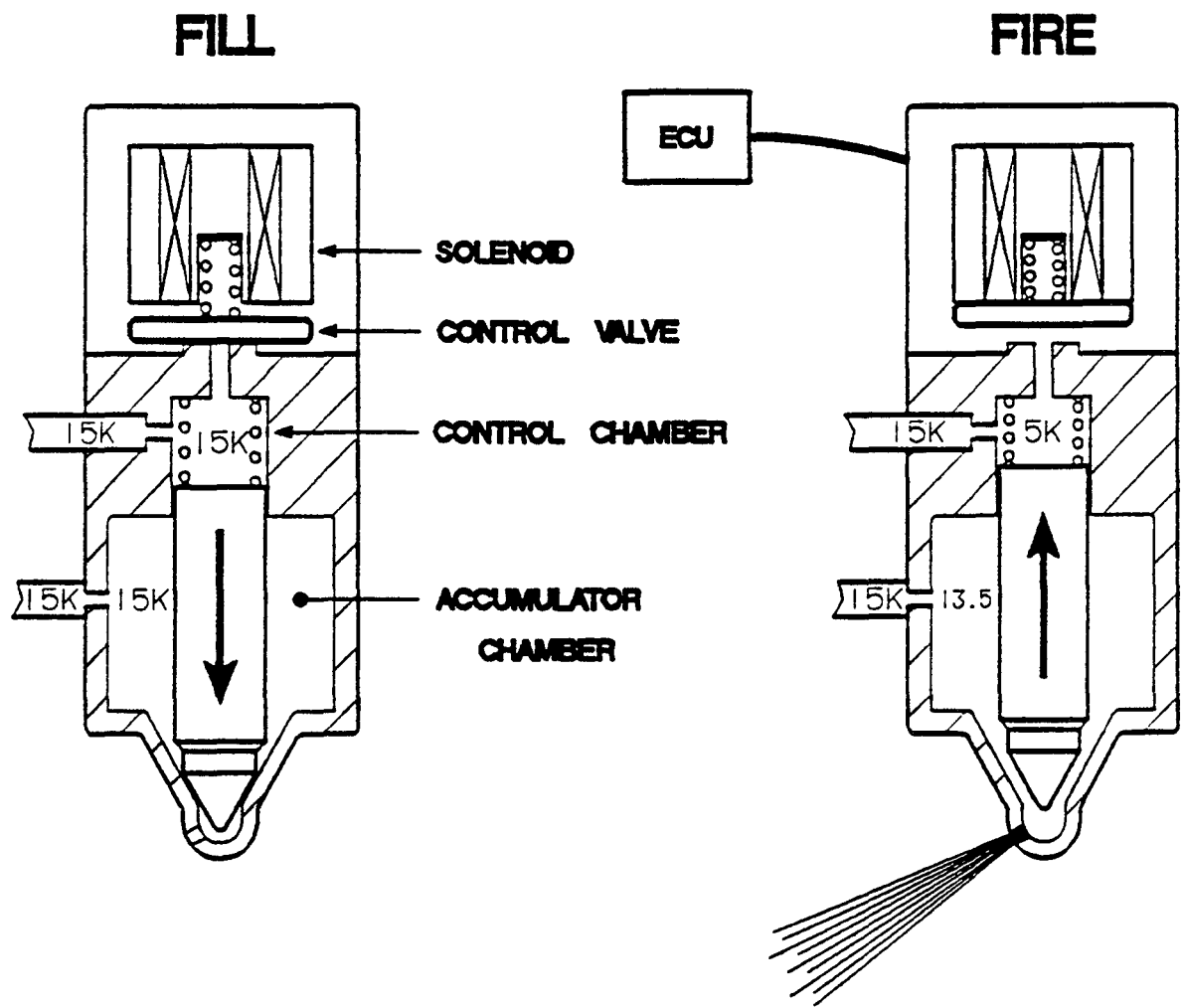


Figure No. 5

Results of K-T Analysis

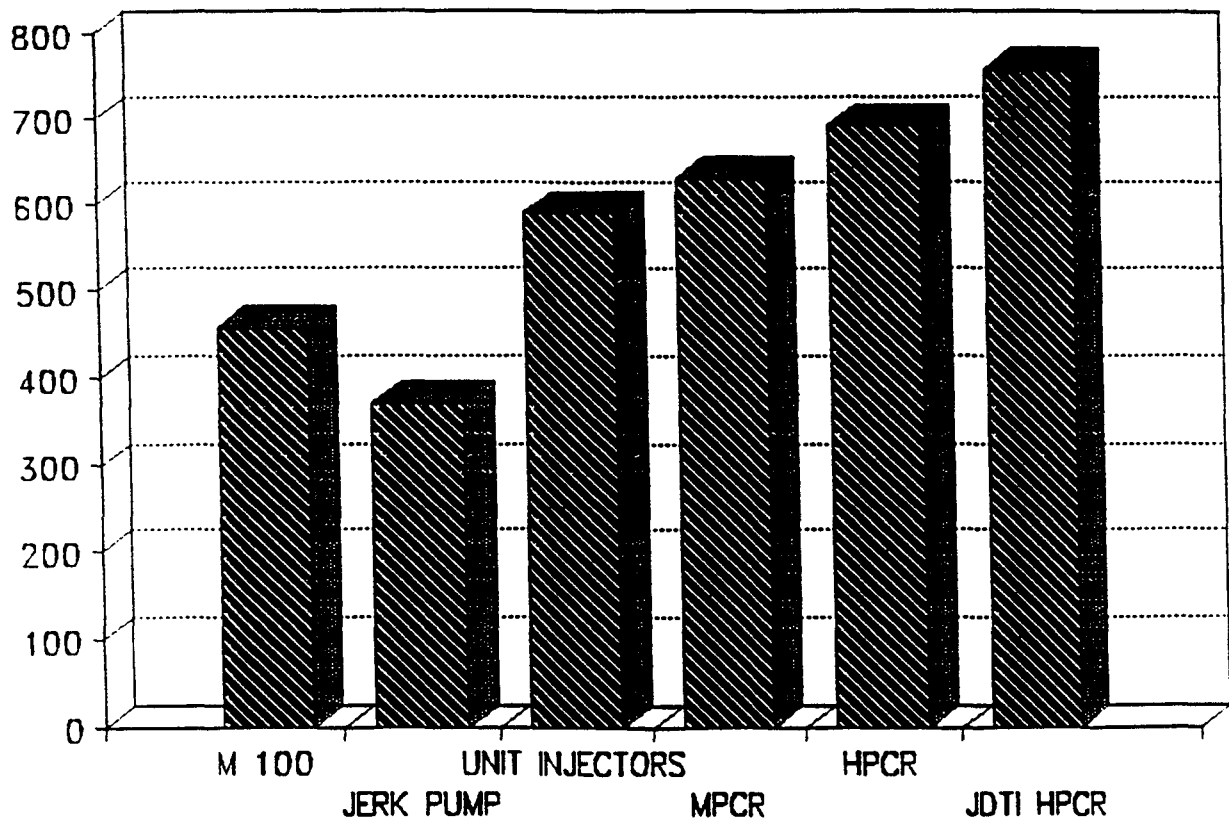


Figure No. 6

CURRENT SYSTEM (A PUMP)

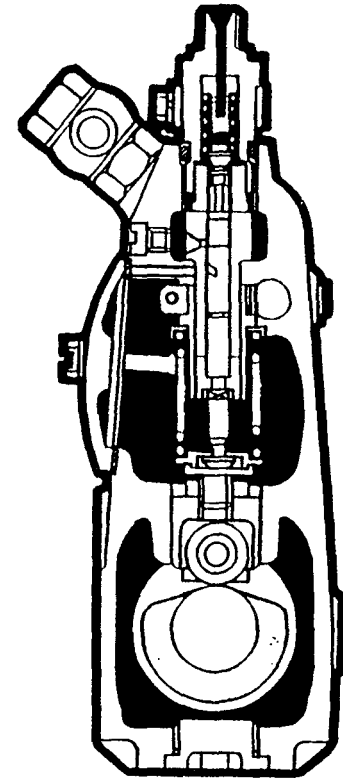
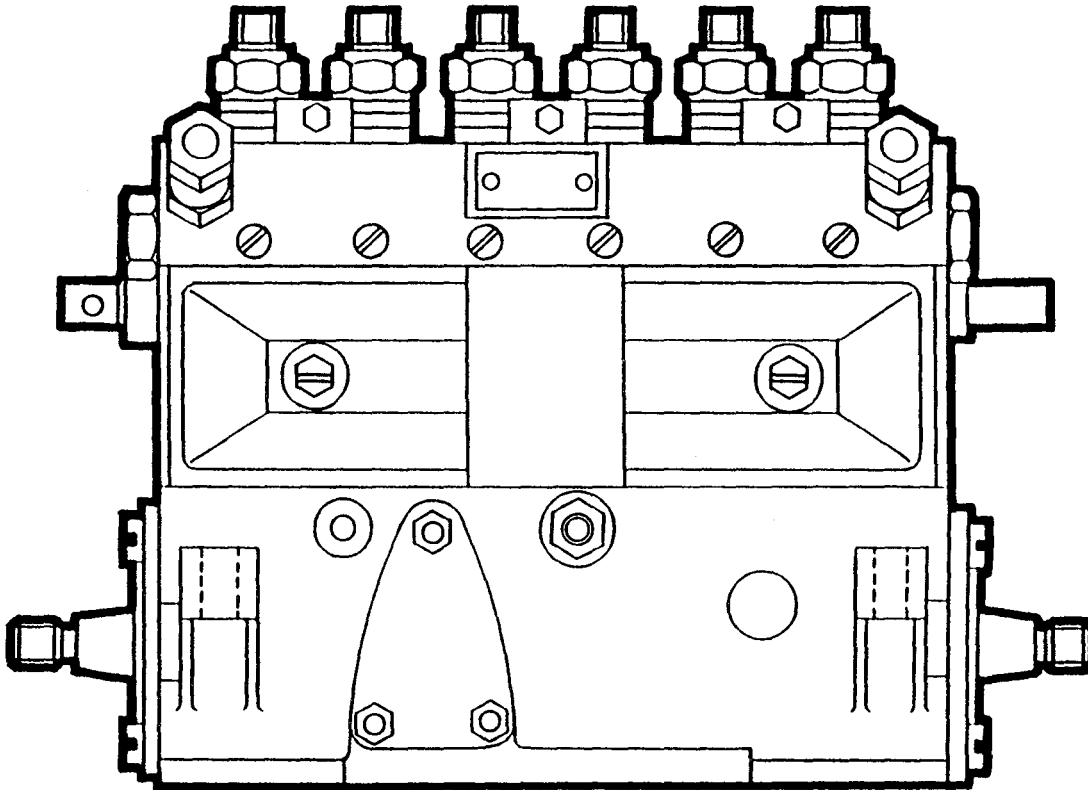
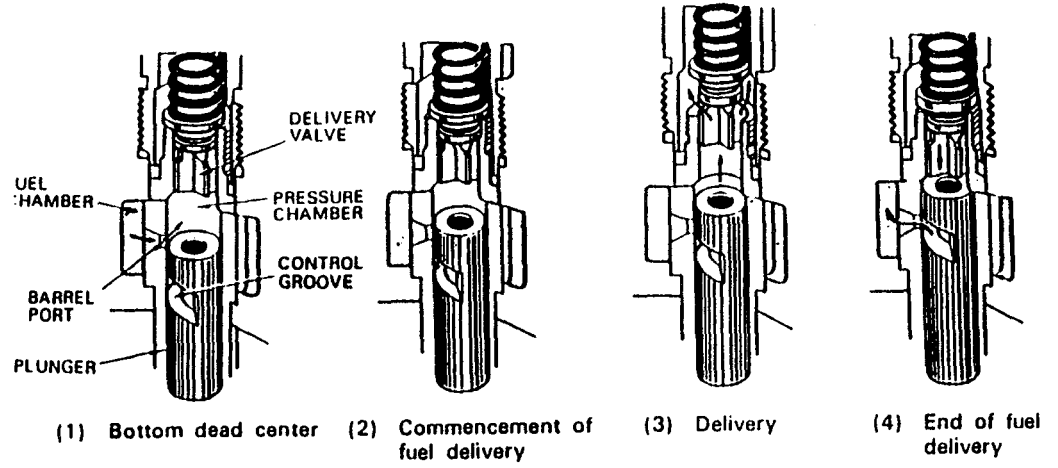


Figure No. 7

PILOT FUEL DELIVERY CHARACTERISTICS

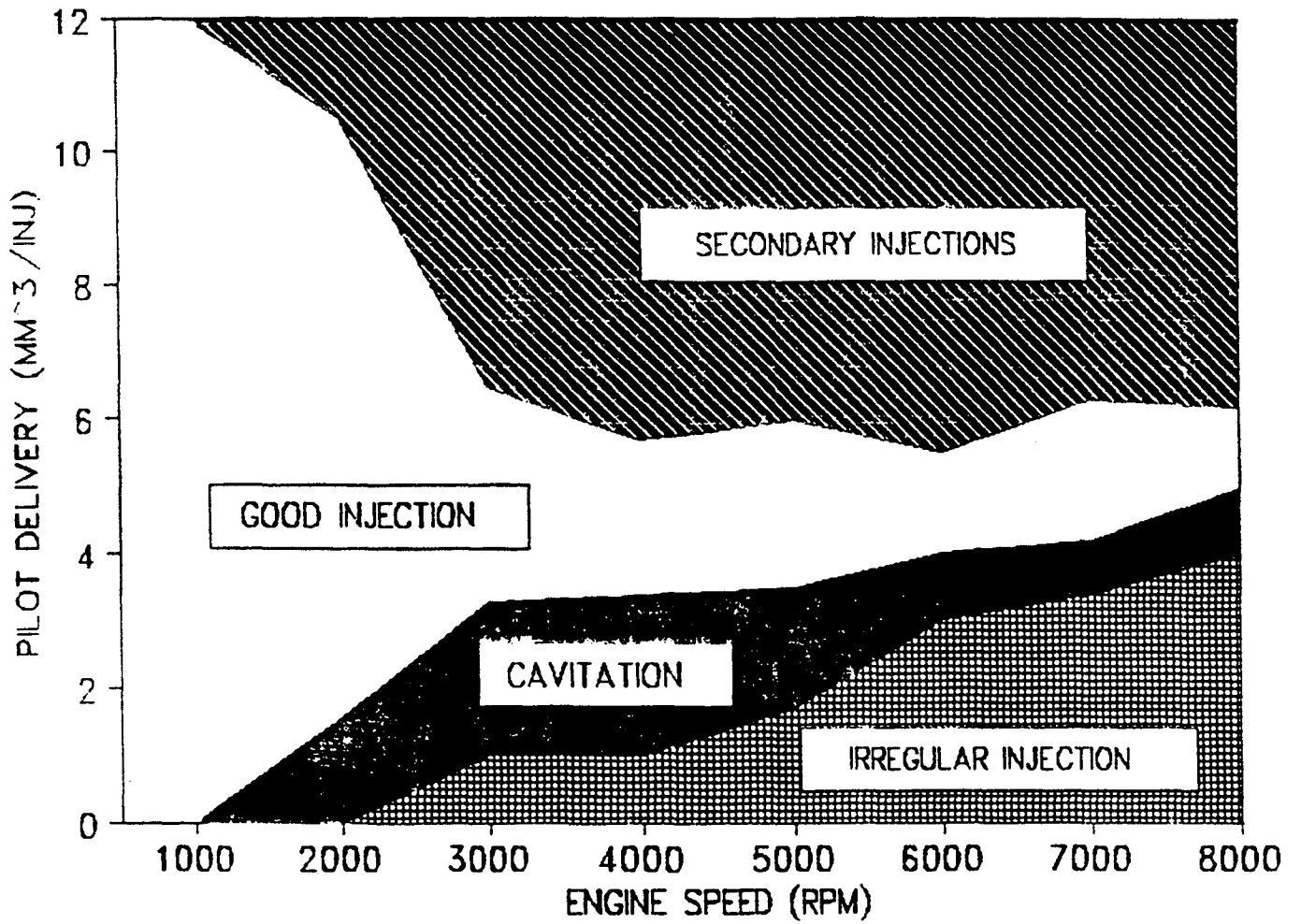


Figure No. 8

PILOT FUEL DELIVERY VS ENGINE SPEED

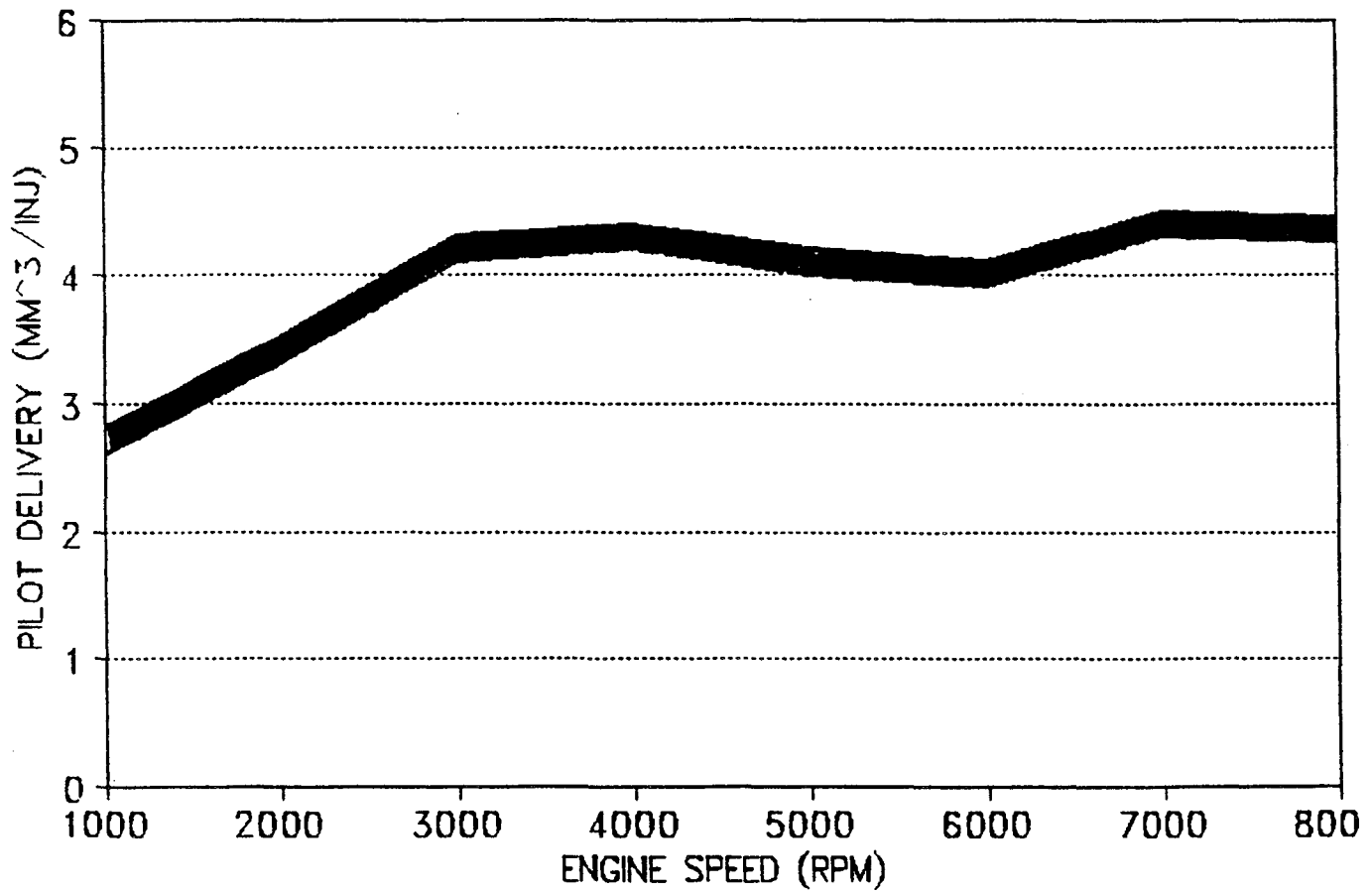


Figure No. 9

MAIN FUEL DELIVERY CHARACTERISTICS

.2 X 6 NOZZLE

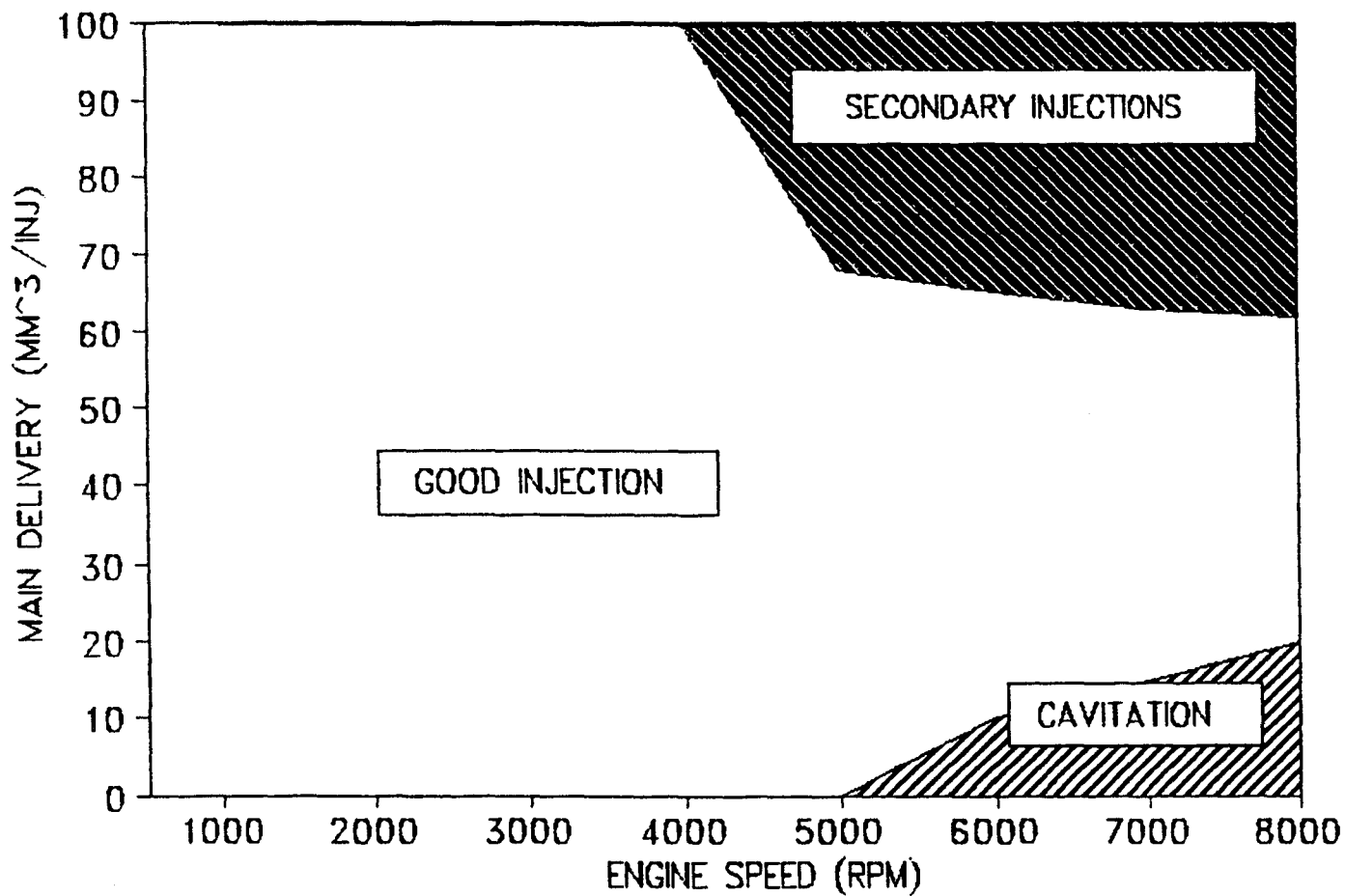


Figure No. 10

MAIN FUEL DELIVERY CHARACTERISTICS

.225 X 6 NOZZLE

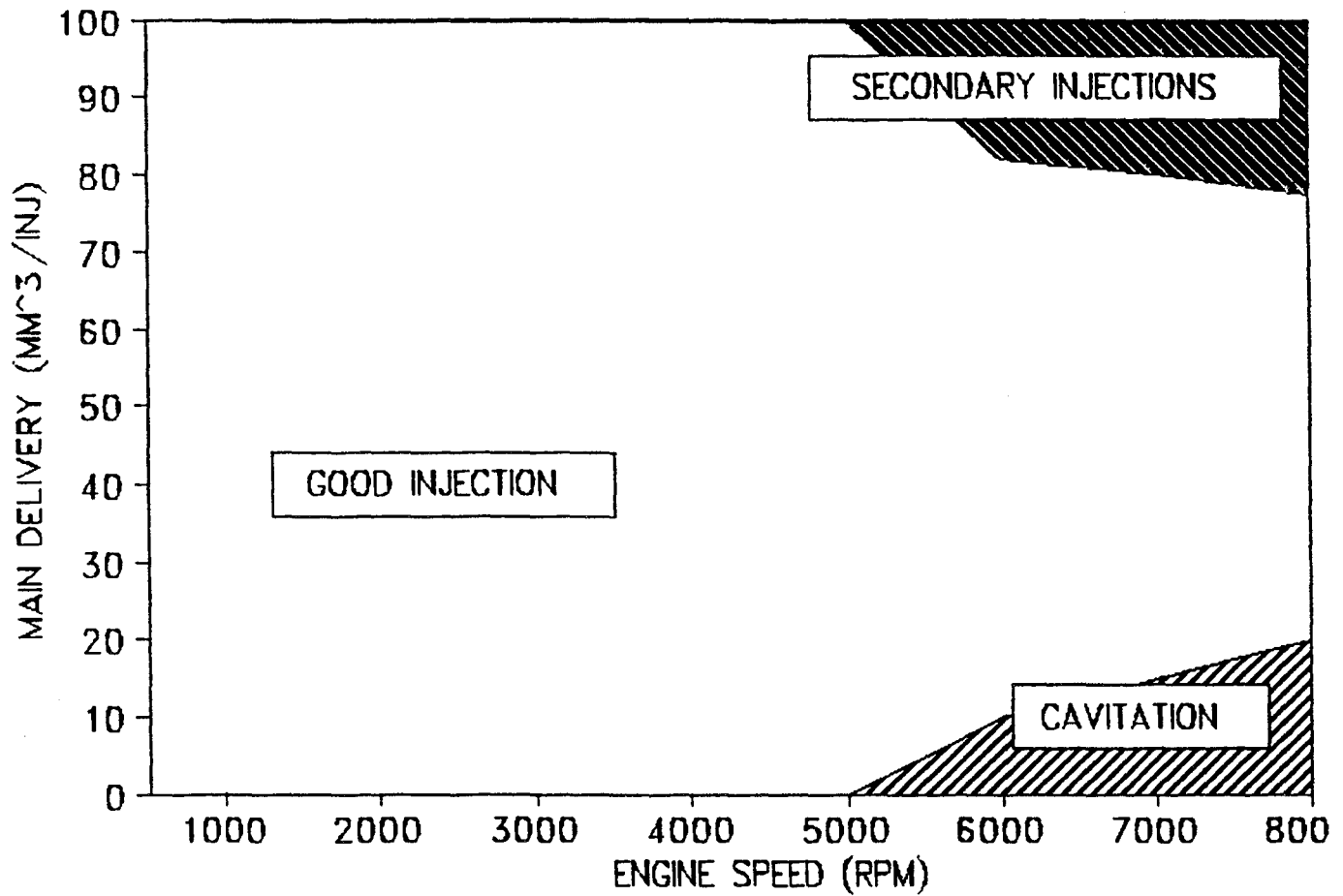


Figure No. 11

TIMINGS AT SELECTED OPERATING CONDITIONS

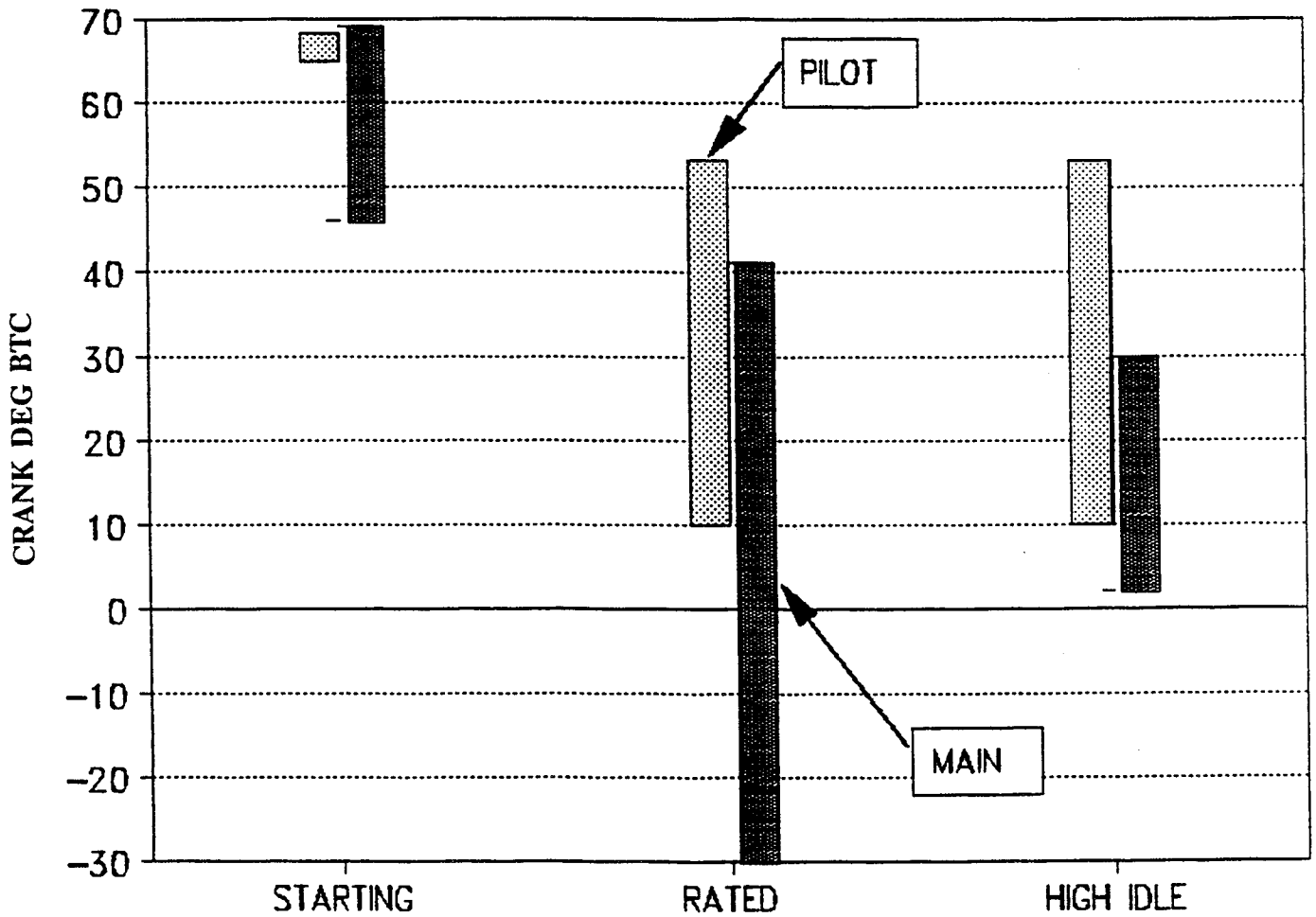


Figure No. 12

INJECTION TIMINGS AT FULL LOAD

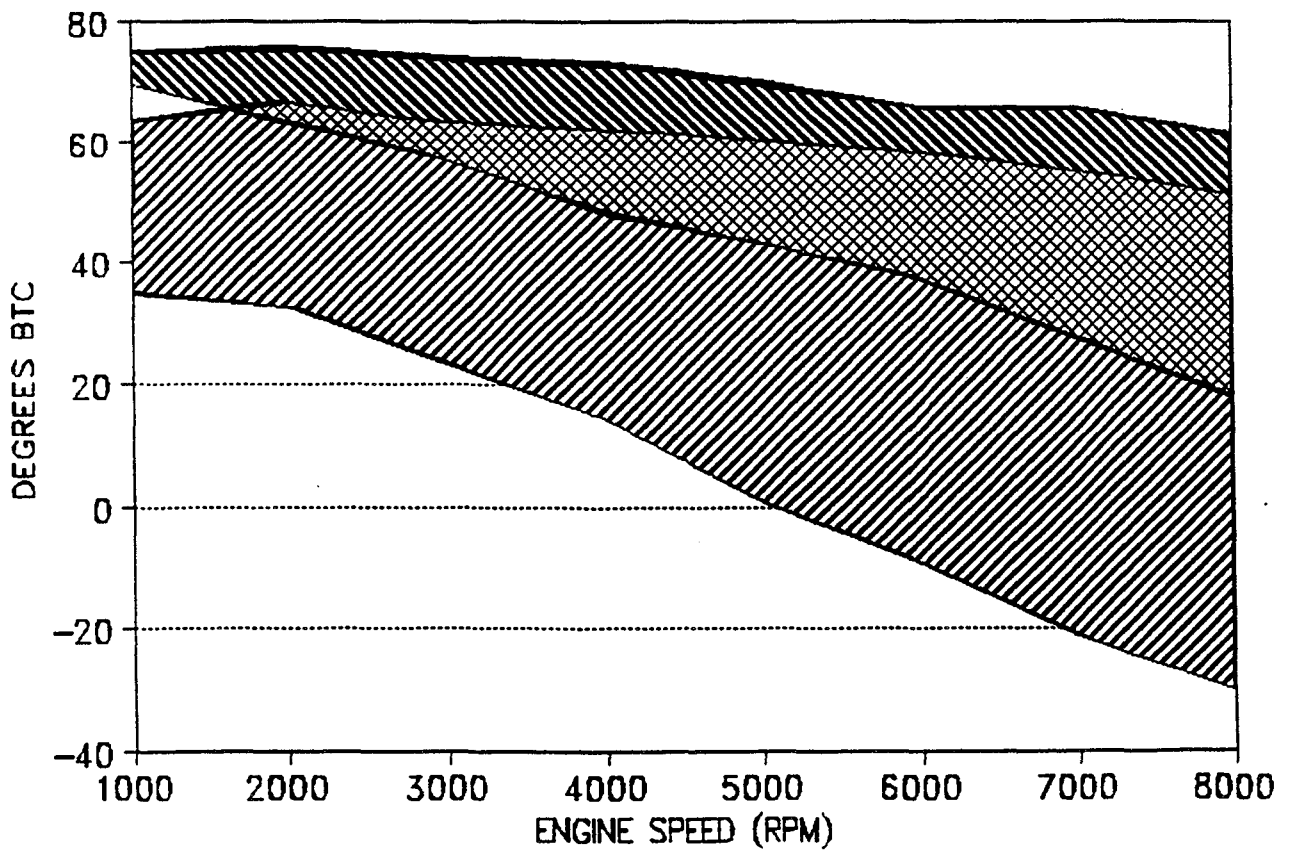
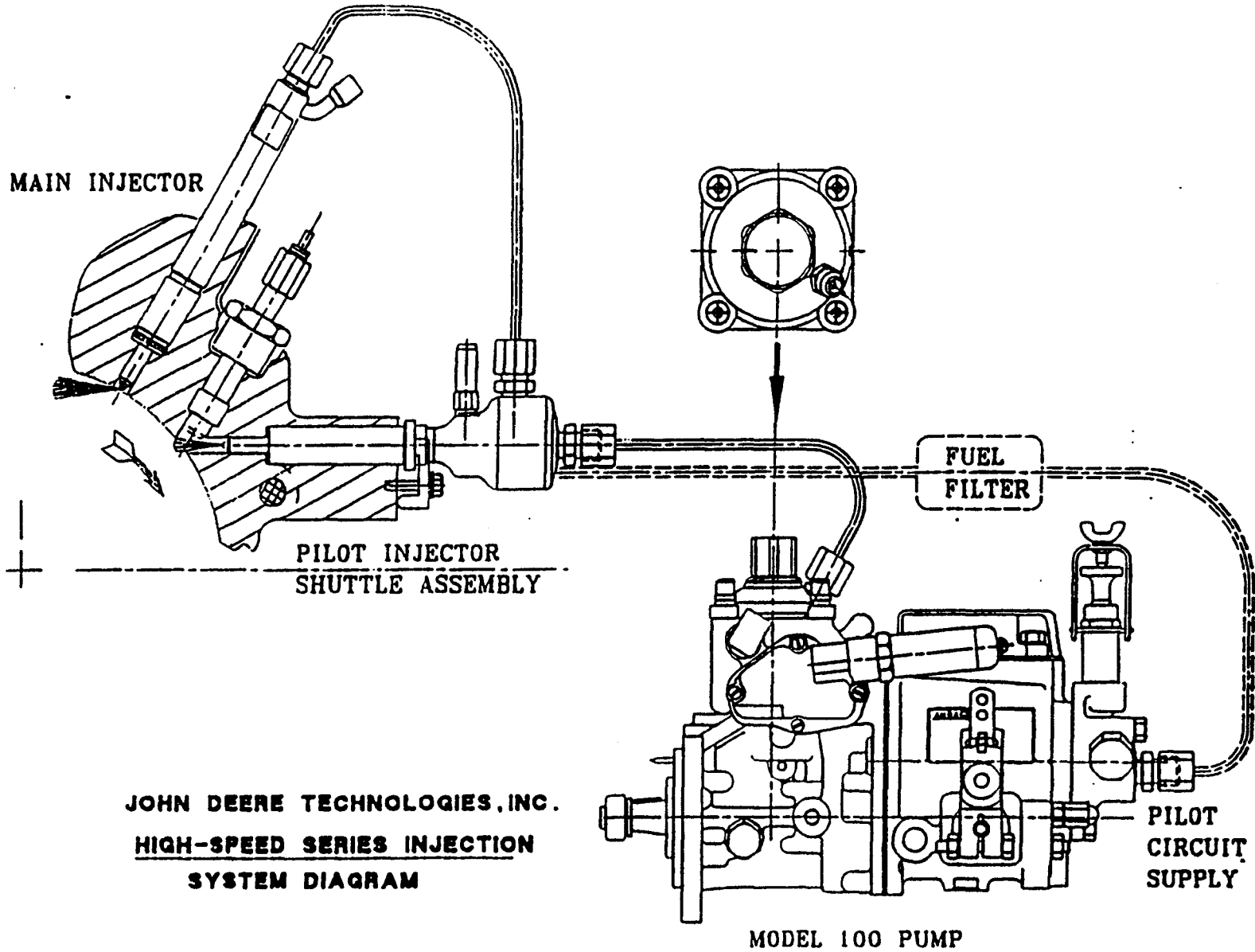


Figure No. 13

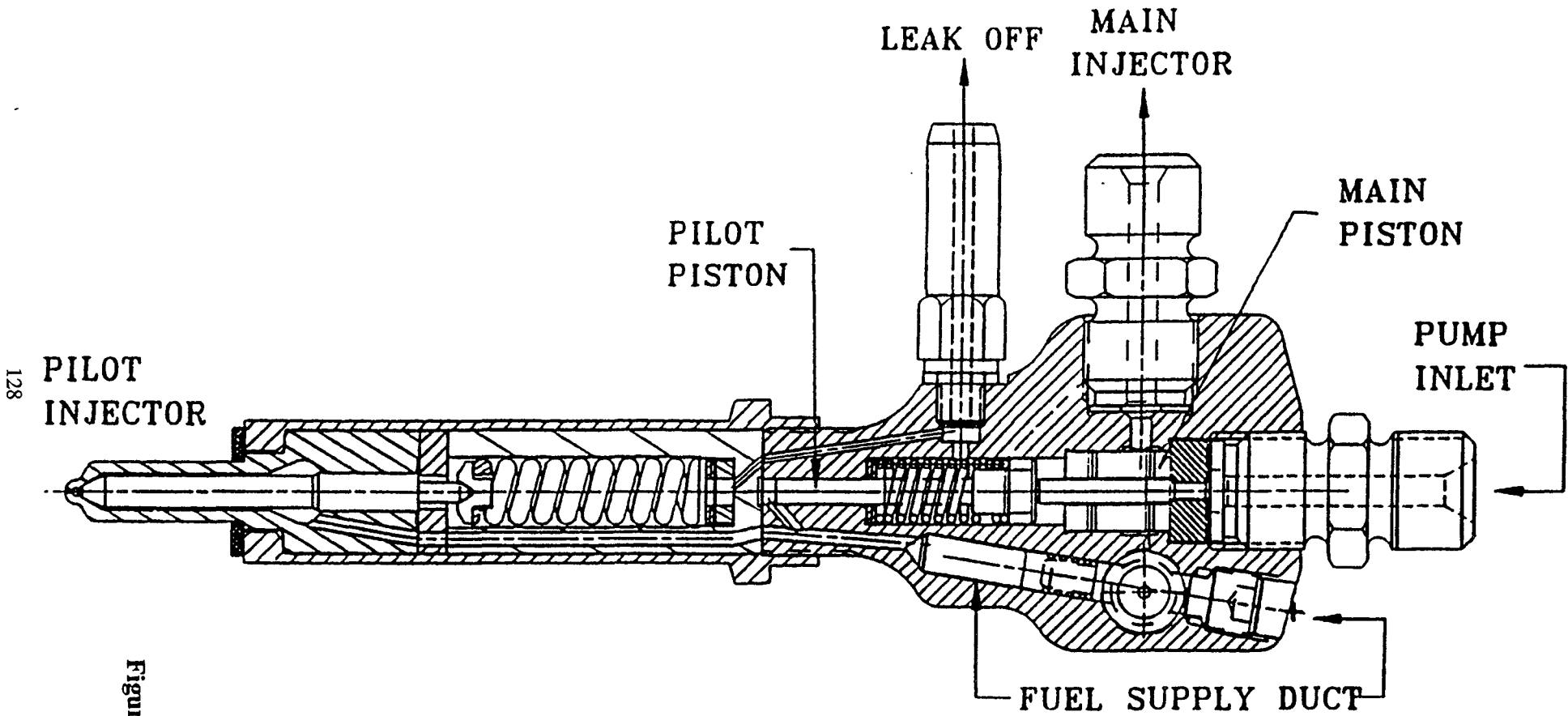


127

Figure No. 14

JOHN DEERE TECHNOLOGIES, INC.
HIGH-SPEED SERIES INJECTION
SYSTEM DIAGRAM

AMBAC INTERNATIONAL



128

Figure No. 15

Detail of Pilot Splitter Valve

100% FLOWS VS PUMP RPM

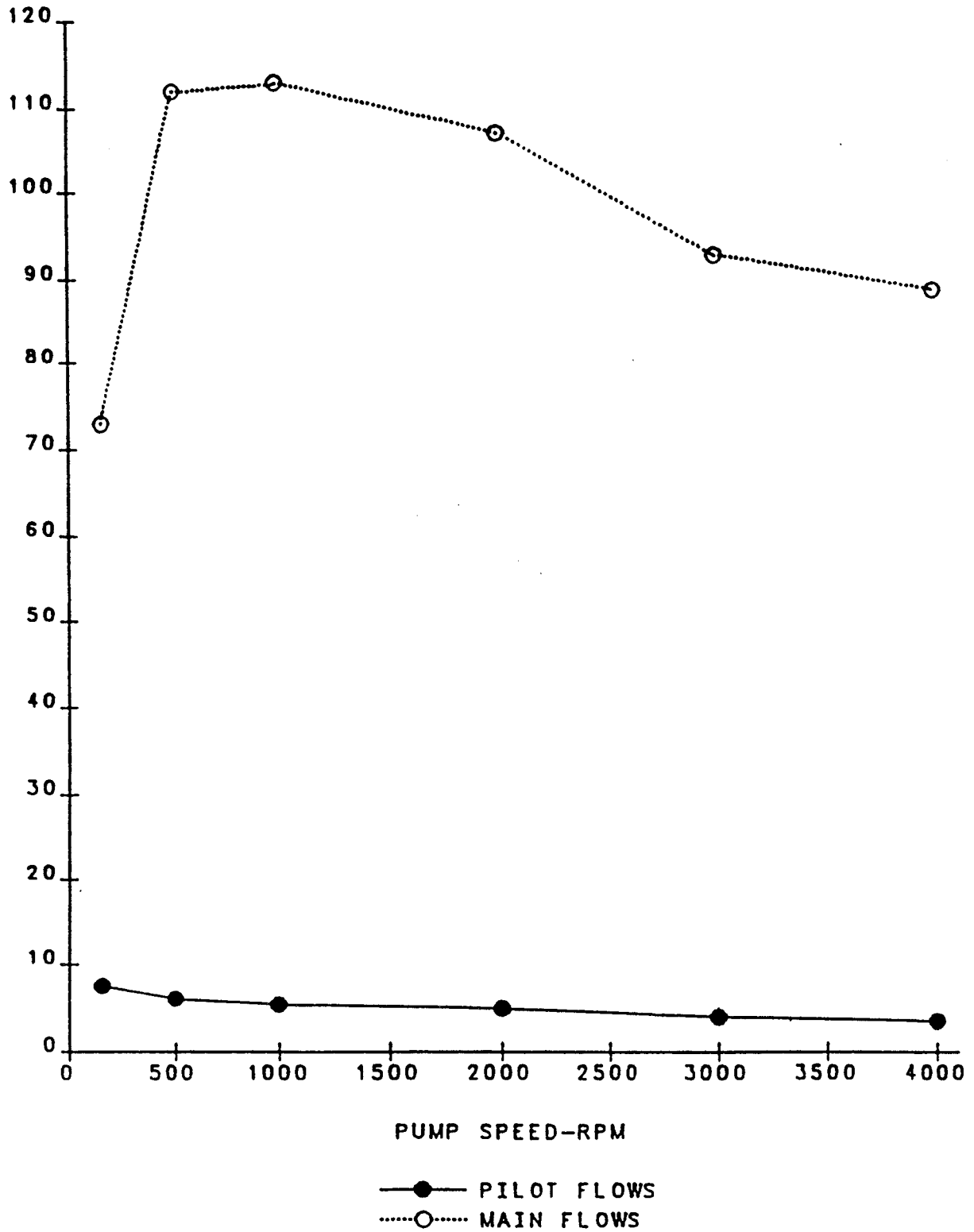


Figure No. 16

PILOT ENGINE DEGREES ADVANCE FROM MAIN

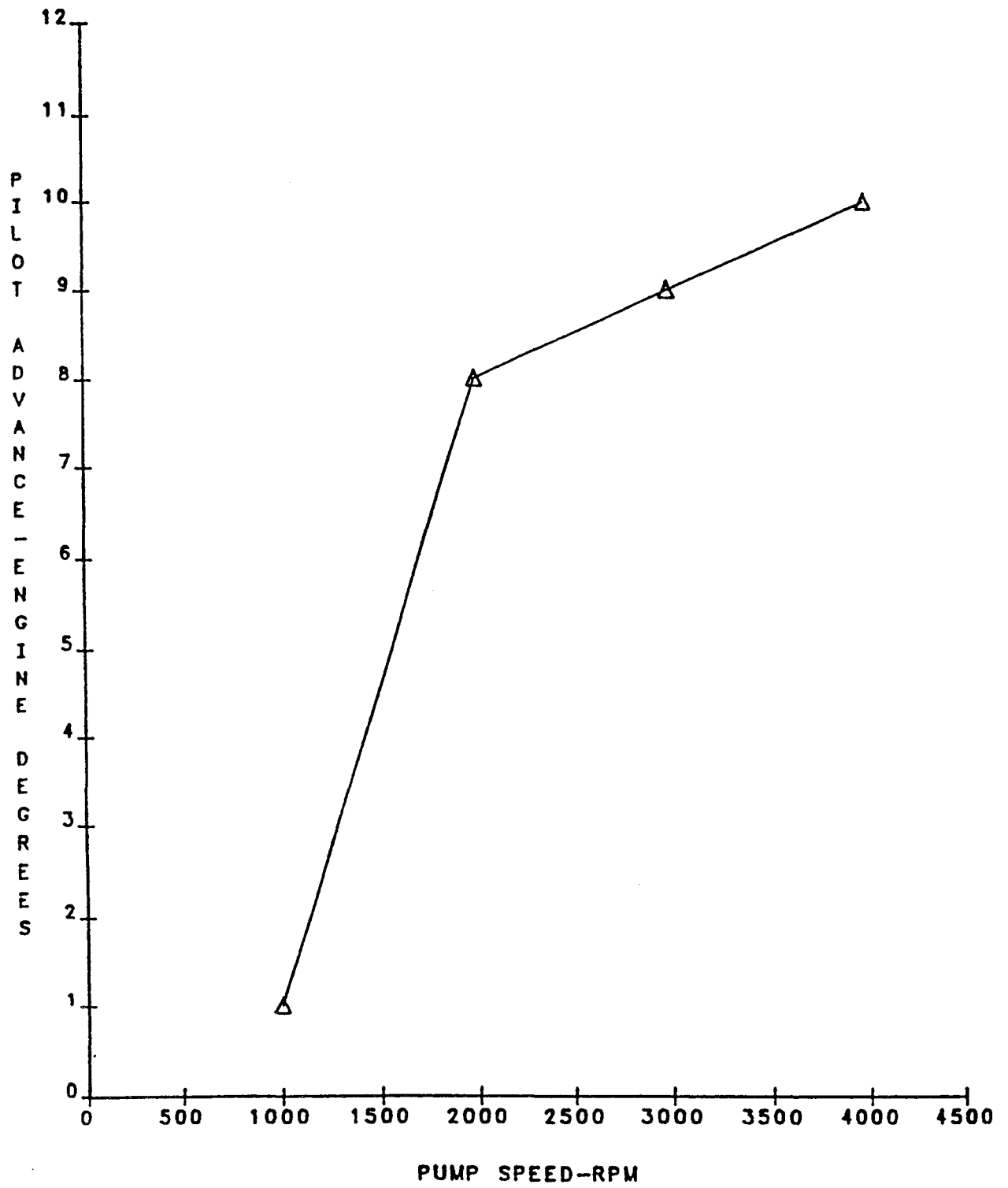


Figure No. 17

ESTIMATE OF INDICATED FUEL CONSUMPTION OF THE 70 SERIES ENGINE
CORRECTED FOR BACK-PRESSURE; NOT CORRECTED FOR F/A RATIO

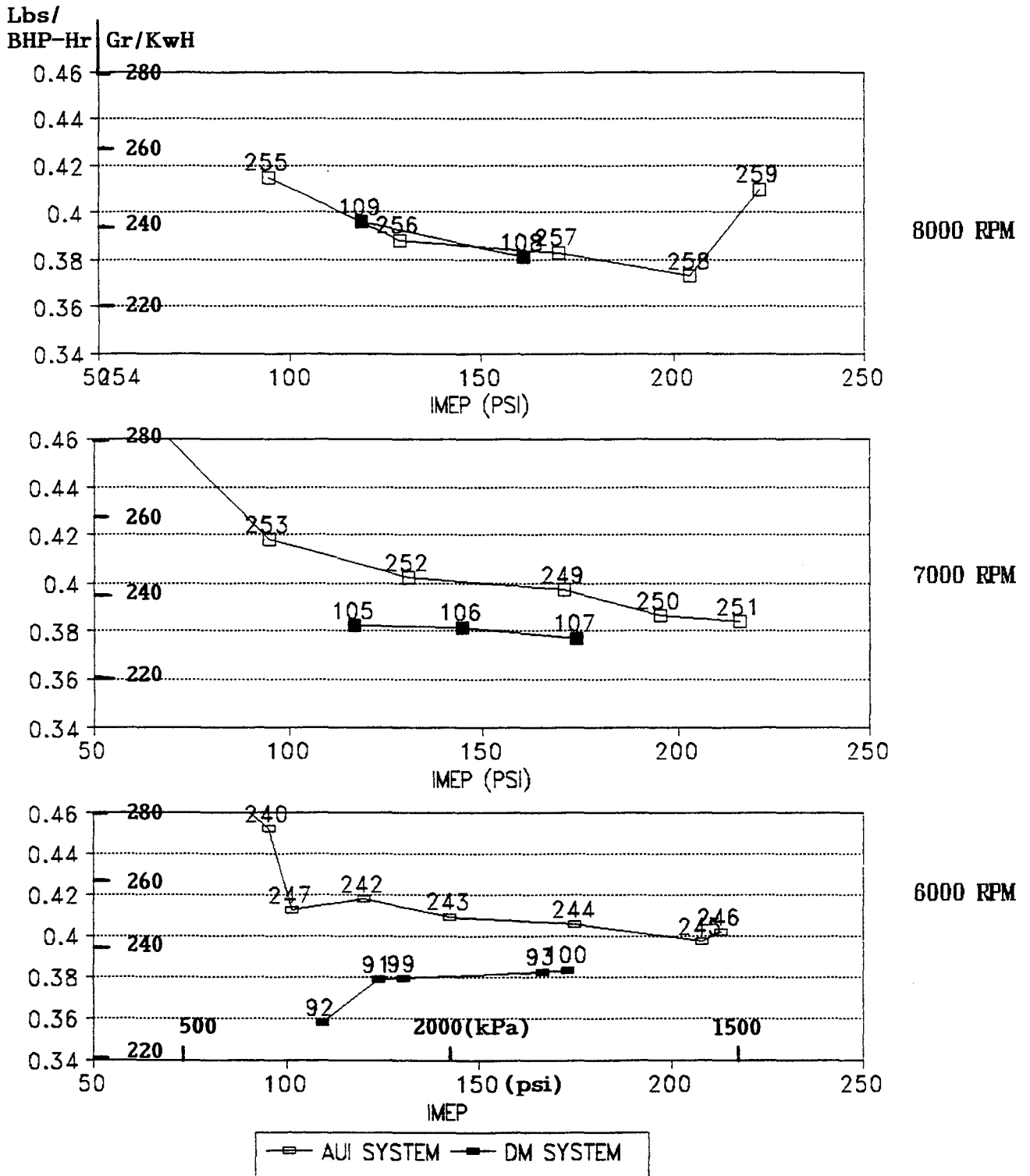
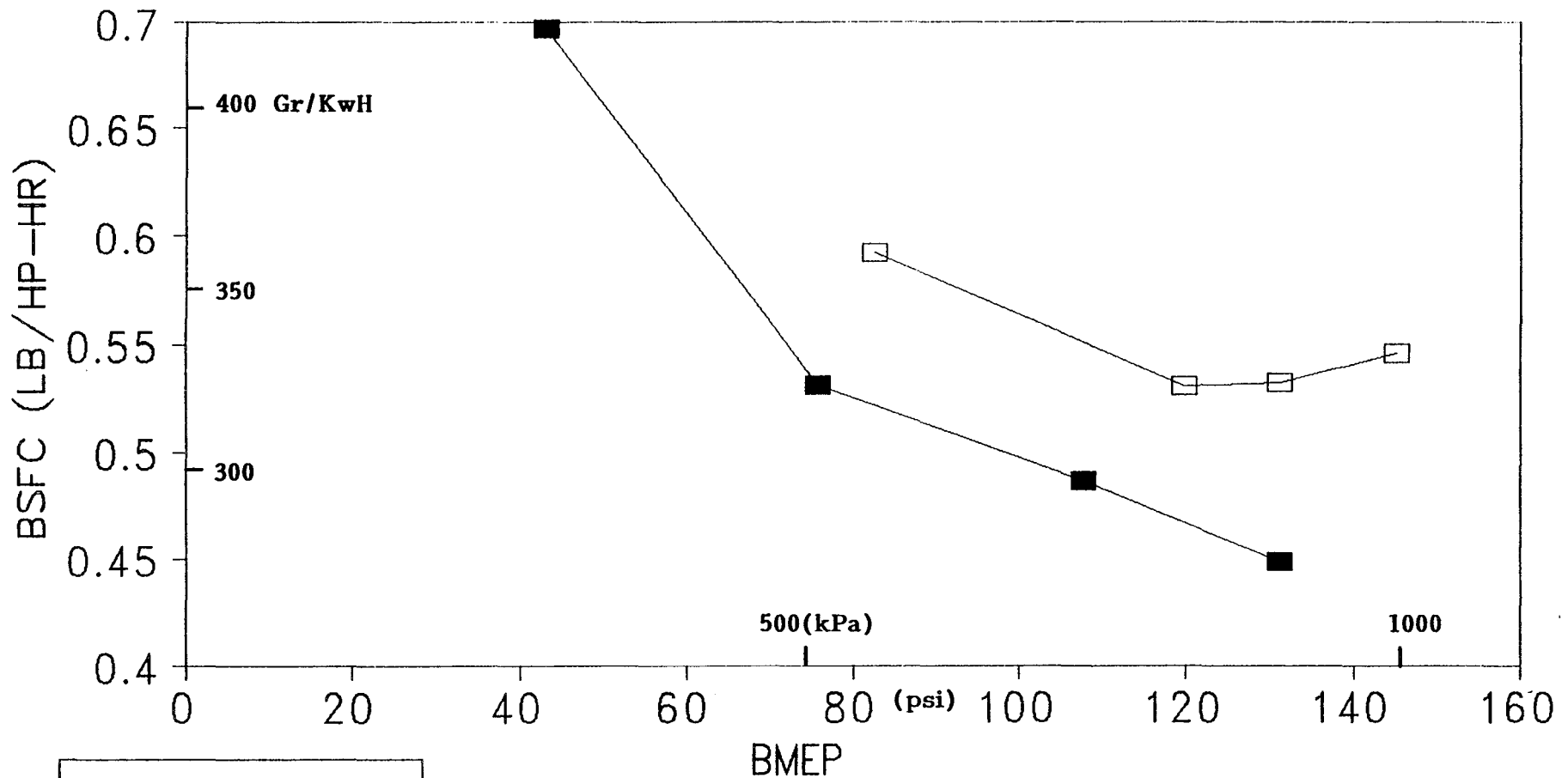


Figure No. 18

FUEL CONSUMPTION COMPARISON

DM PUMP (0702-1A) AND A-PUMP (0704-1)

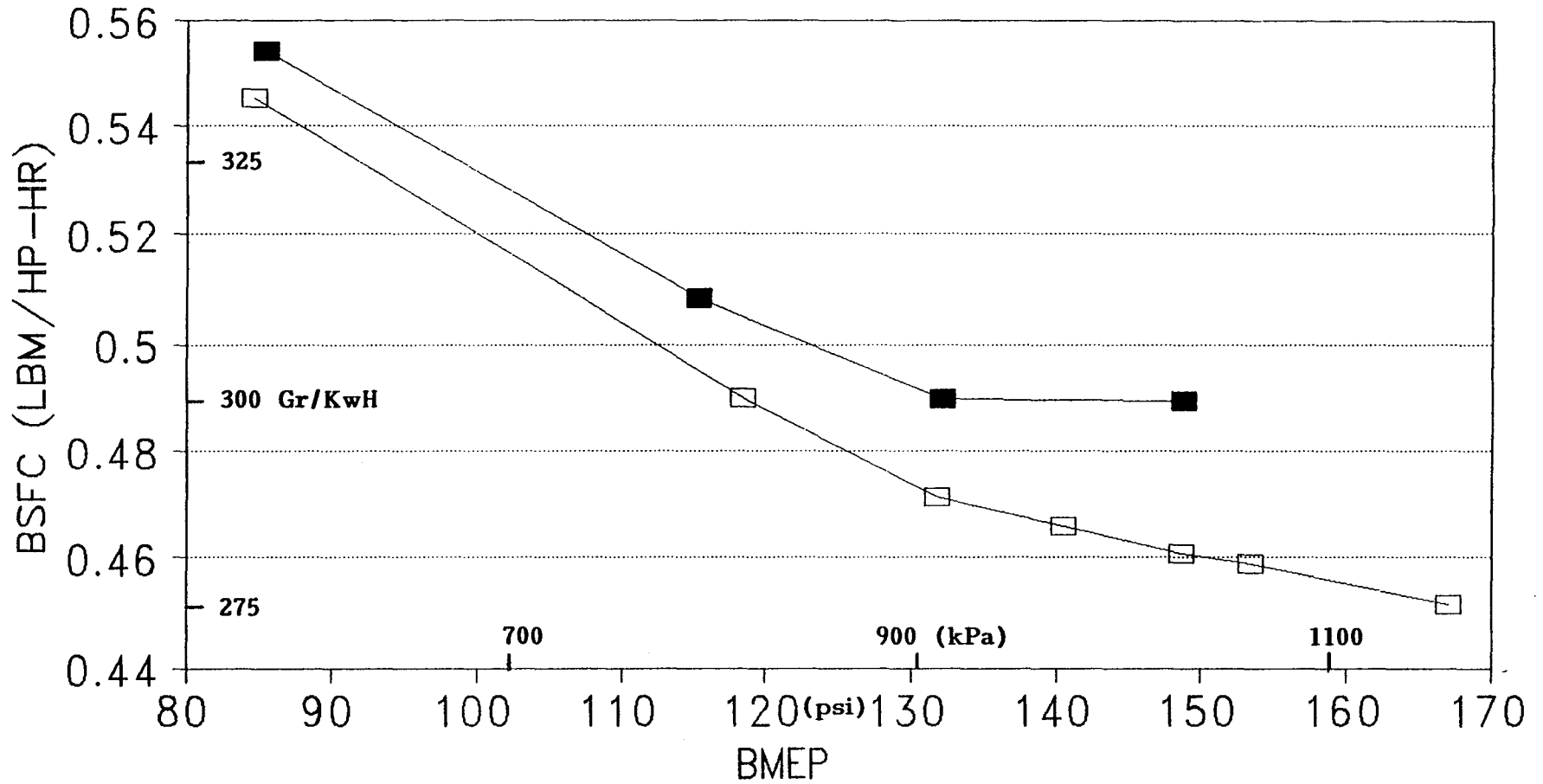


8.5:1 C. R.
 210028N1 MAIN NOZZLE
 210028N25 PILOT NOZZLE
 T04B TURBO, 1.14 A/R

—□— A-PUMP —■— DM PUMP

Figure No. 19

EFFECT OF INJECTION LINE ON PERFORMANCE ENGINE 0705-2, 5500 RPM



MAIN NOZZLE: NJ12394N1
PUMP: A-PUMP

—□— 1.0 mm ID Line —■— 1.5 mm ID Line

Figure No. 20

Injection Rate Profiles

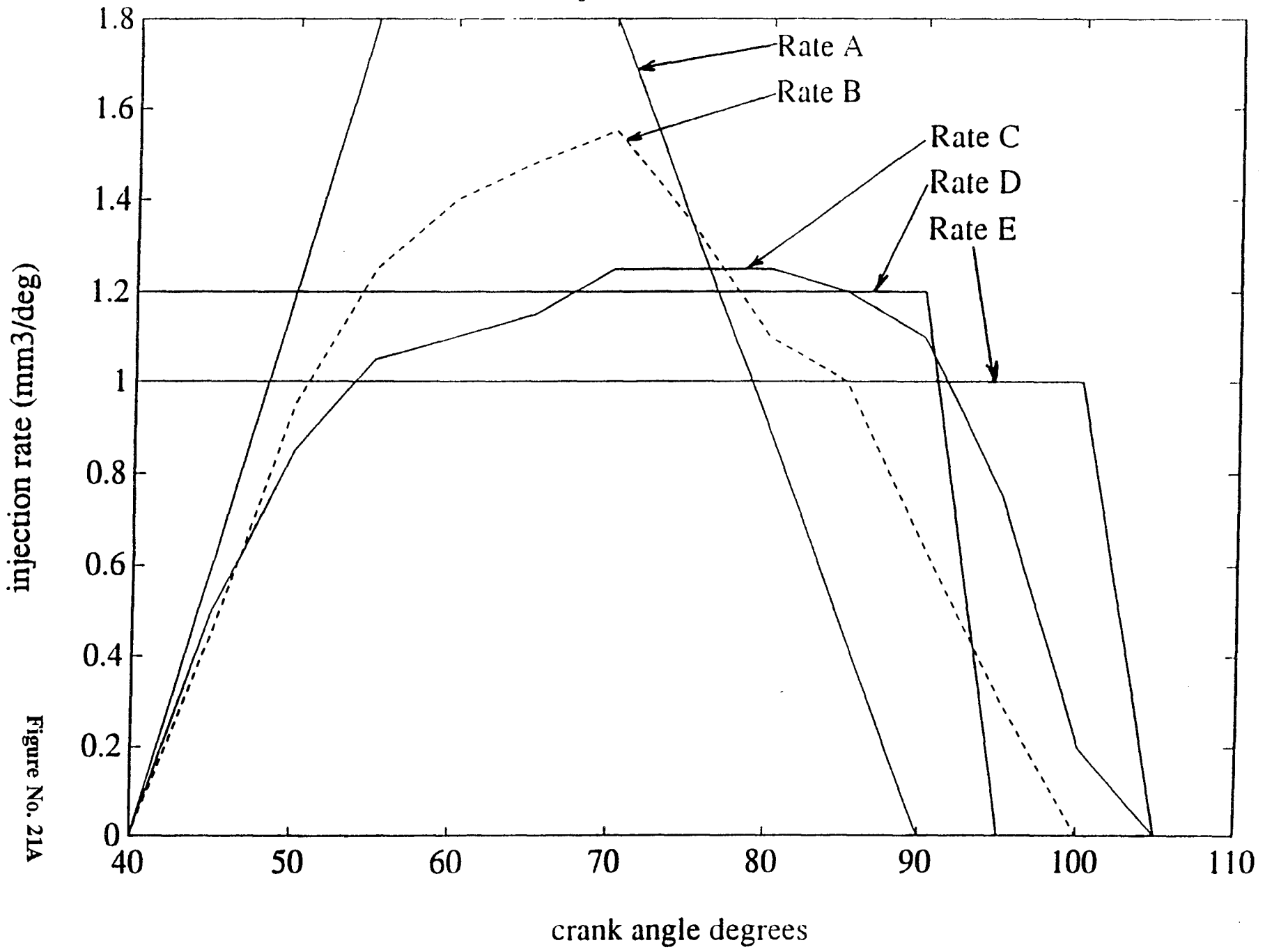


Figure No. 21A

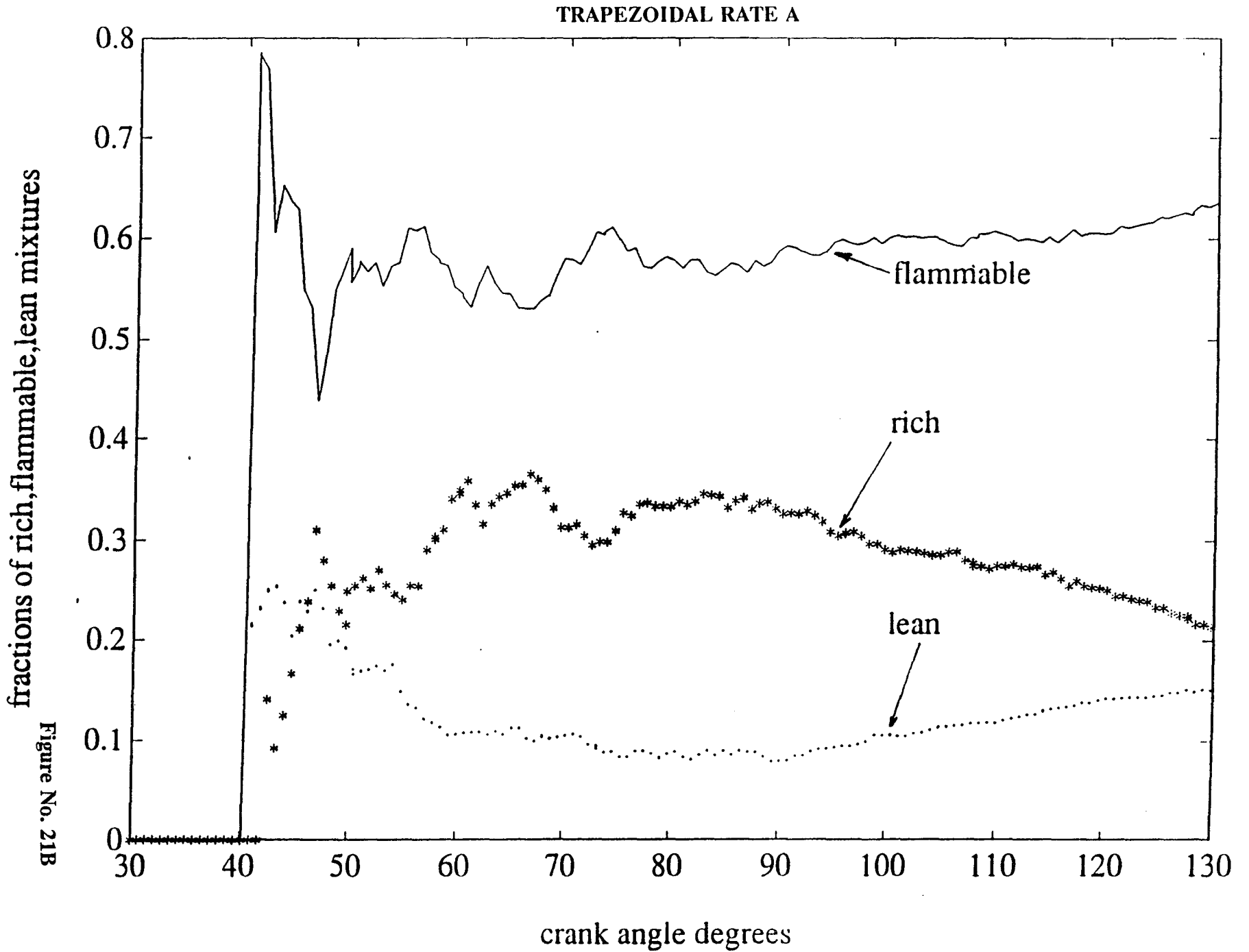


Figure No. 21B

Computed fractions of rich, flammable and lean mixtures in the combustion chamber as a function of crank angle degrees for rate 'A'

AMBAC PUMP RATE B

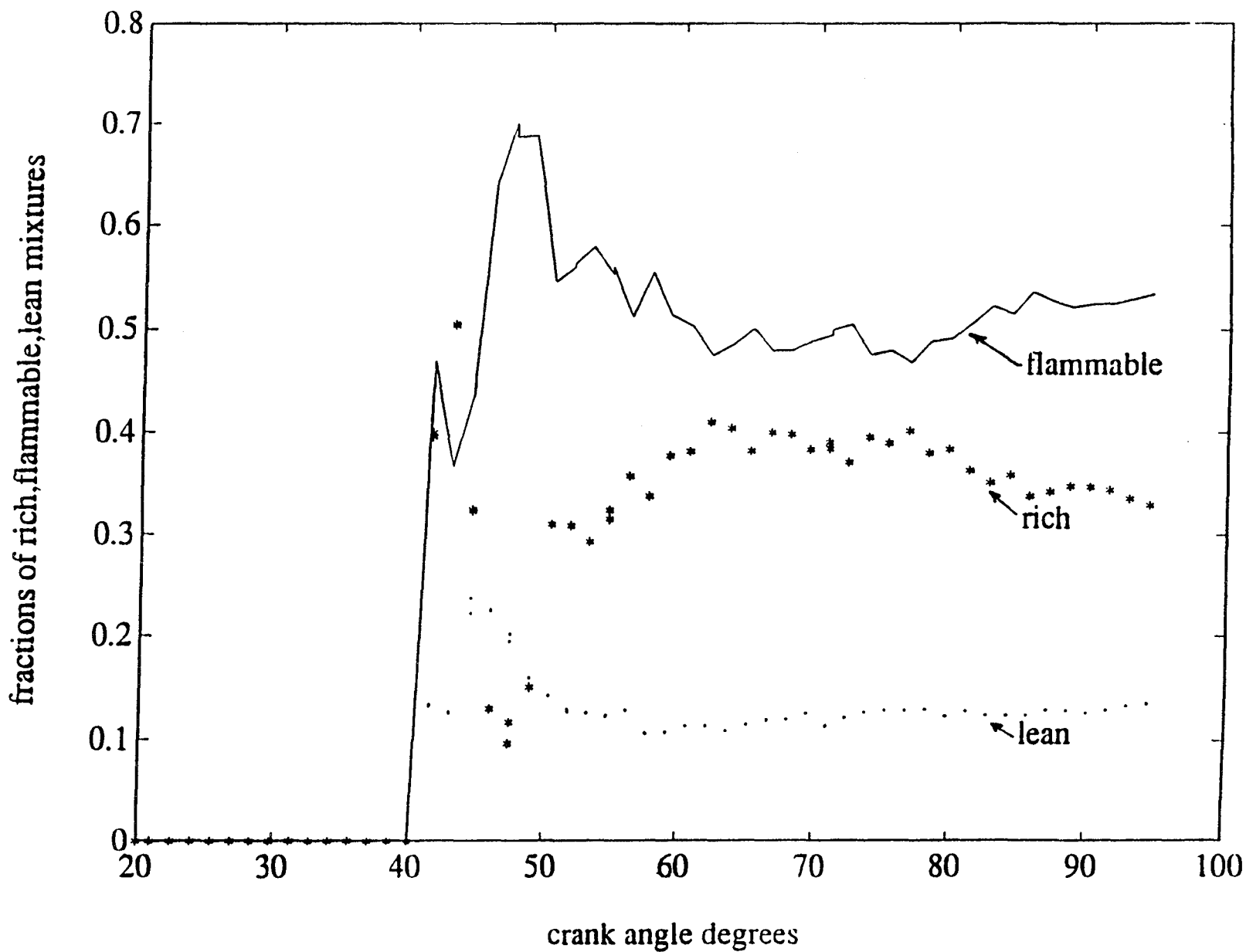


Figure No. 21C

NIPPONDENSO PUMP RATE C

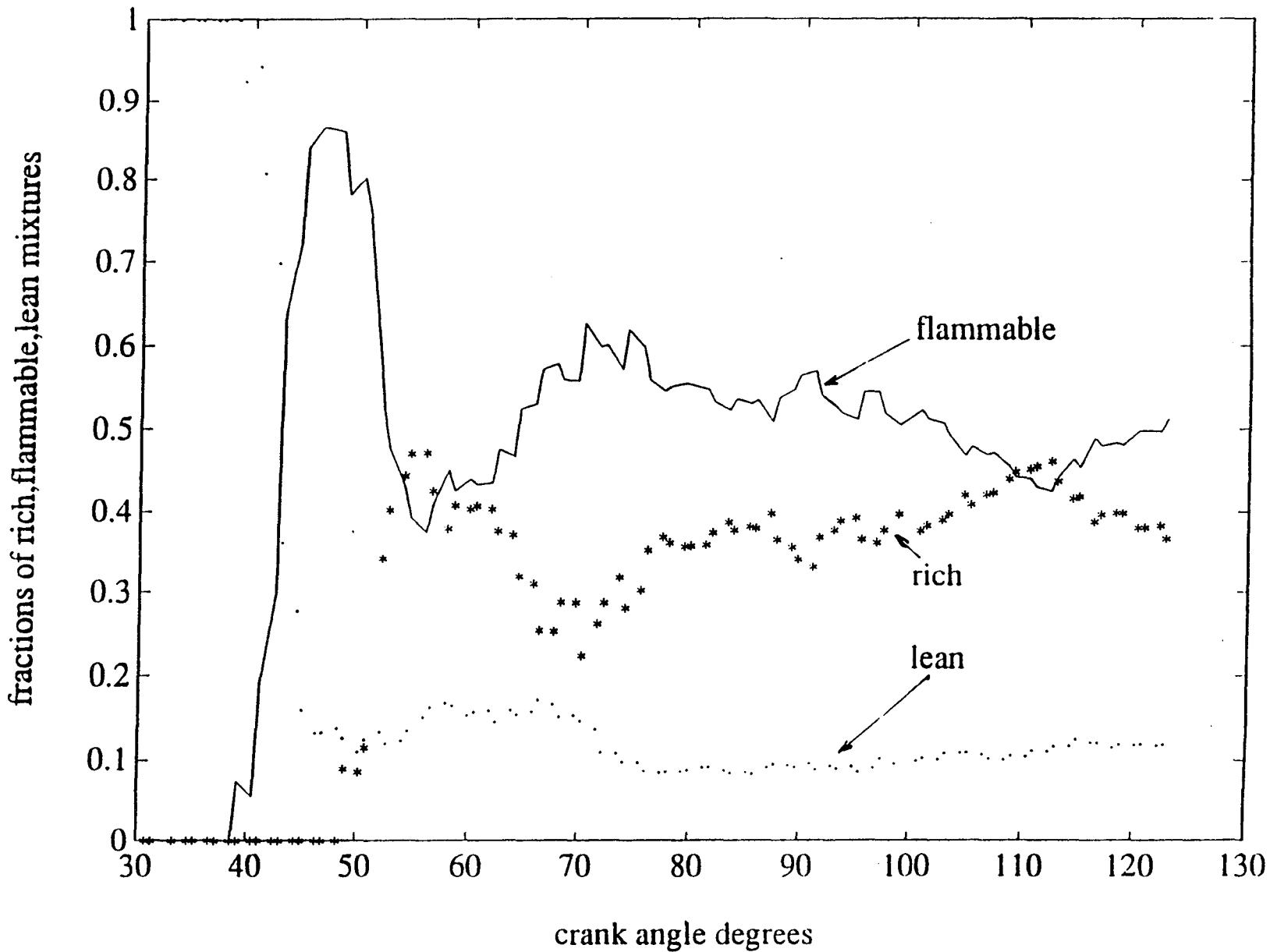


Figure No. 21D

Computed fractions of rich, flammable and lean mixtures in the combustion chamber as a function of crank angle degrees for rate 'C'

INJECTION RATE COMPARISON

6000RPM

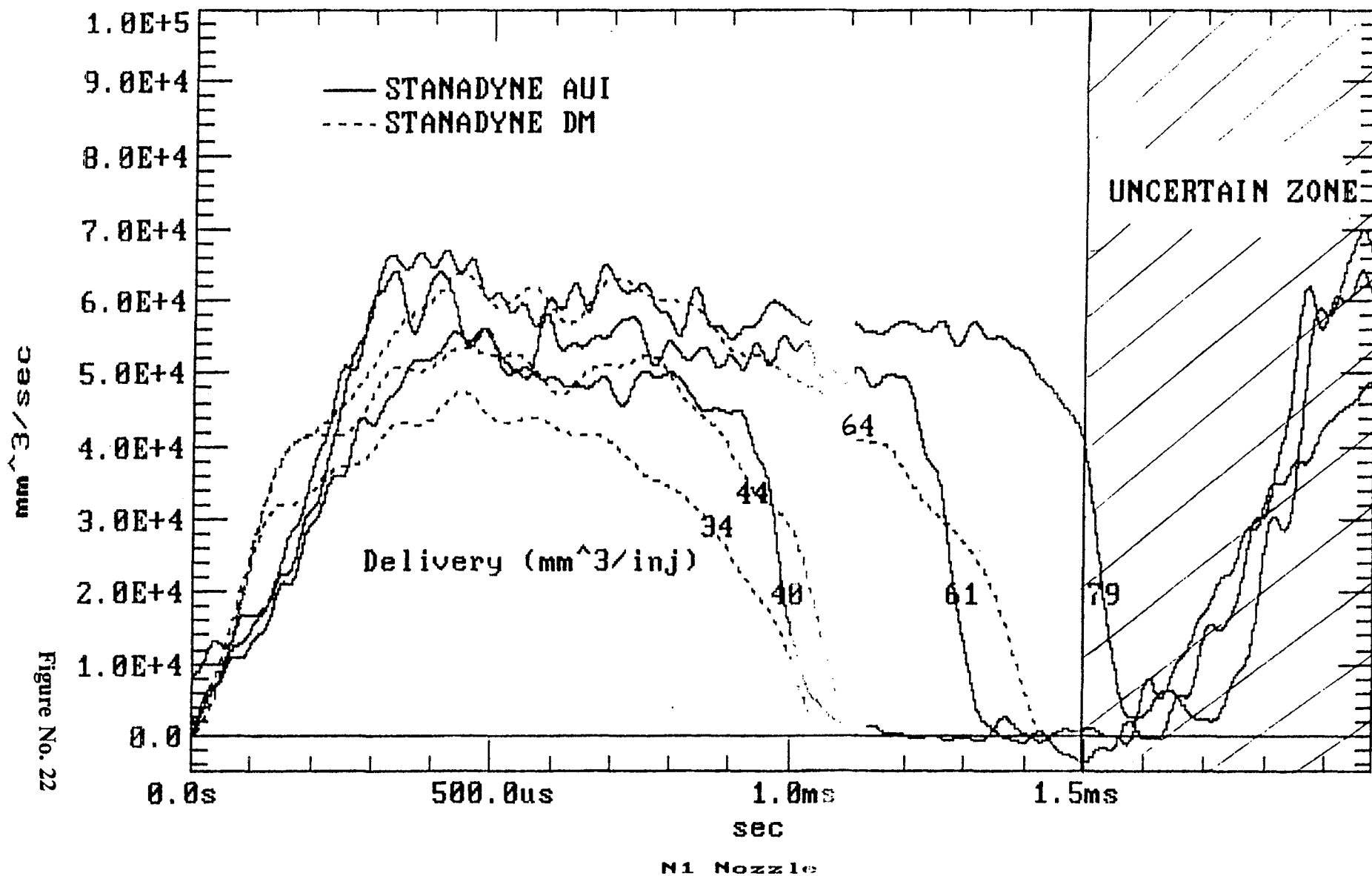
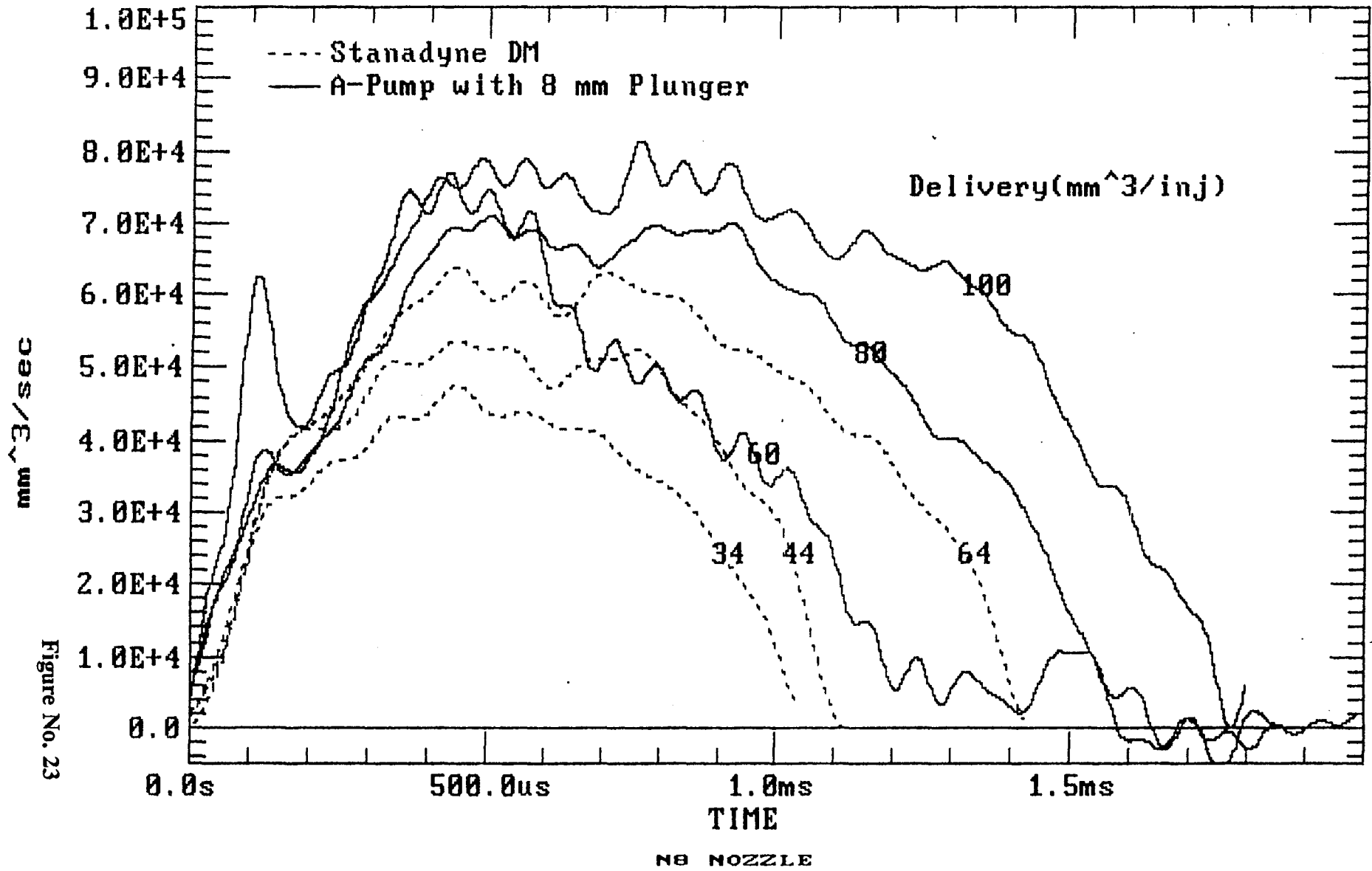


Figure No. 22

COMPARISON OF A-PUMP AND DM-PUMP INJECTION RATES

6000RPM

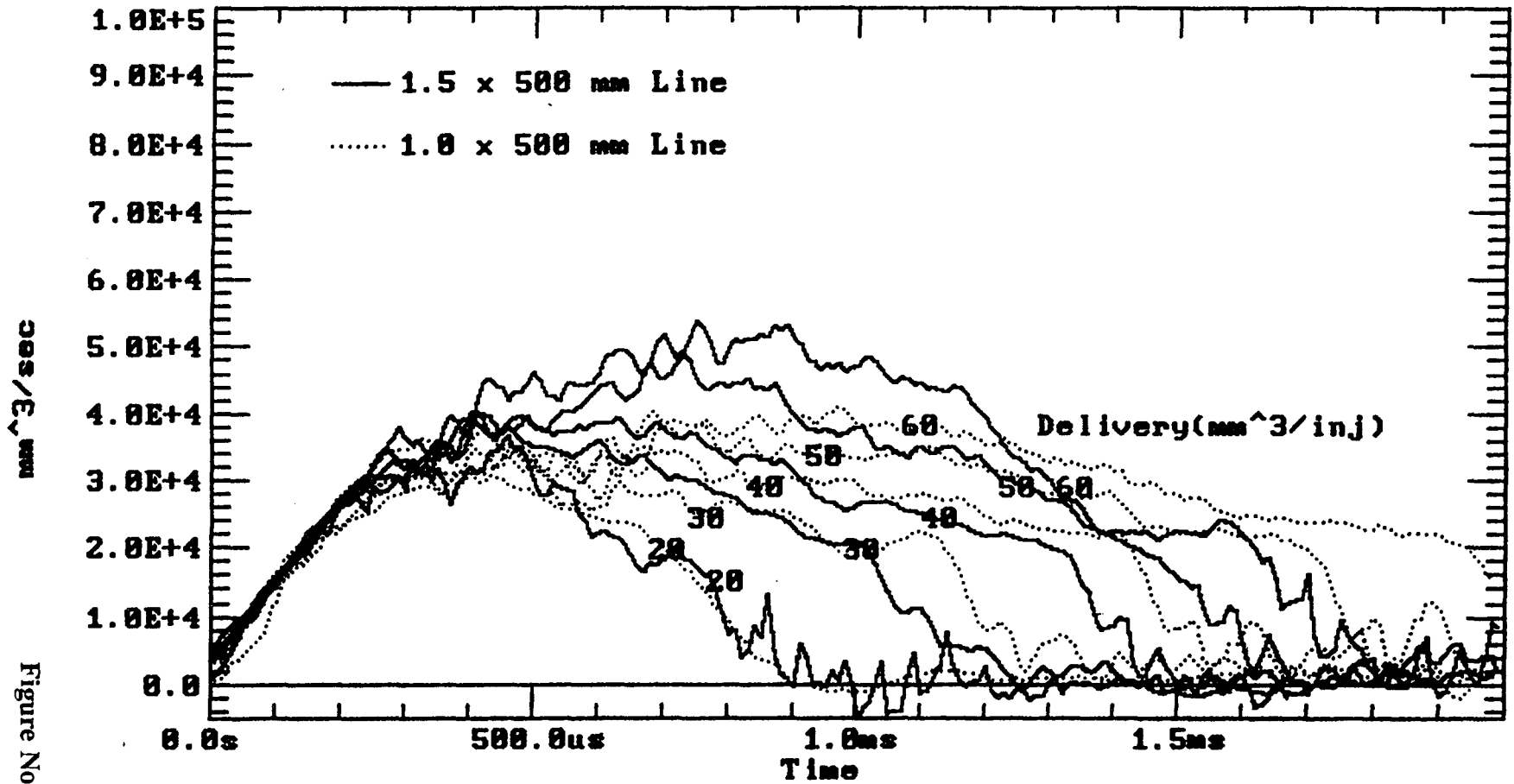


139

Figure No. 23

INJECTION RATE OF Nippondenso A-Pump

5500 RPM



140

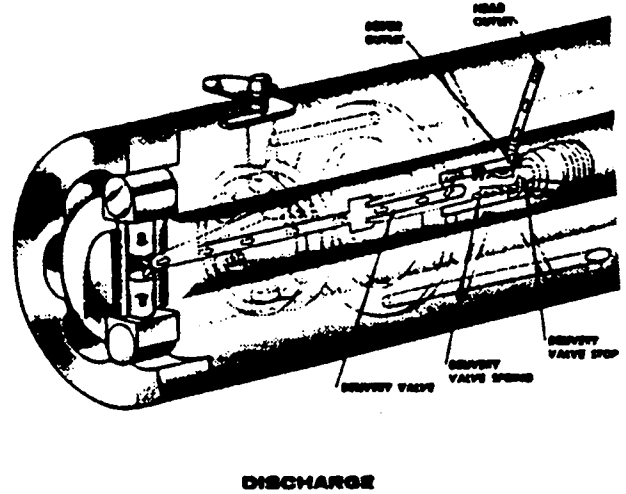
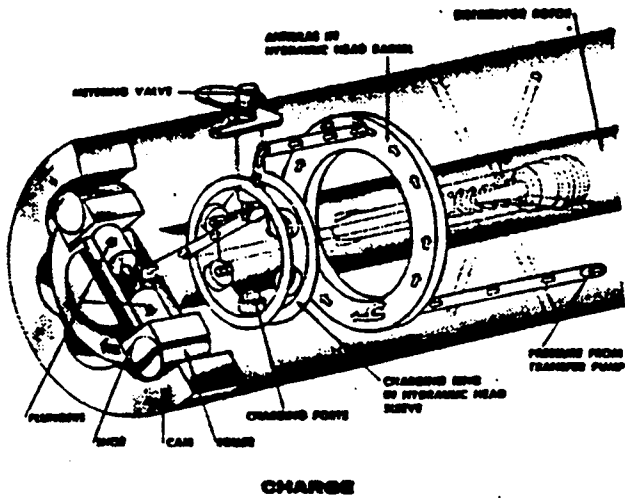
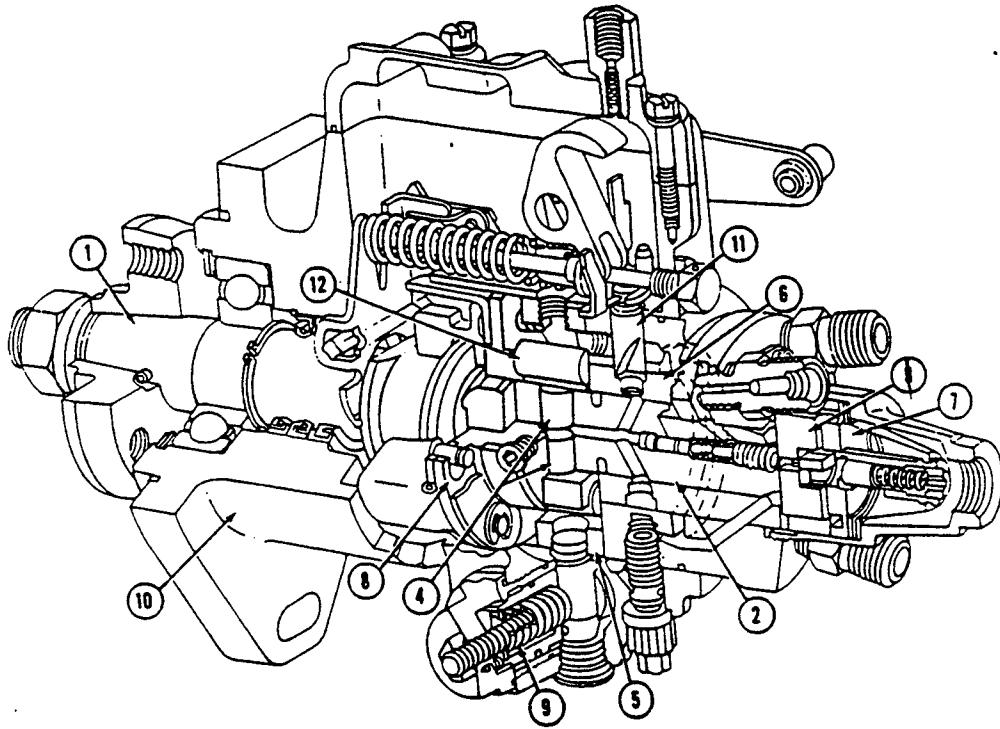
ccs/E_{mm}

Figure No. 24

4 x .009 NOZZLE

7.5 mm PLUNGER, 5-290 DELIVERY VALVE

10000 INJECTIONS/MINUTE



Stanadyne DM Fuel Injection Pump

Figure No. 25

A-PUMP CAMSHAFT FOLLOWER DISPLACEMENT CHARACTERISTICS

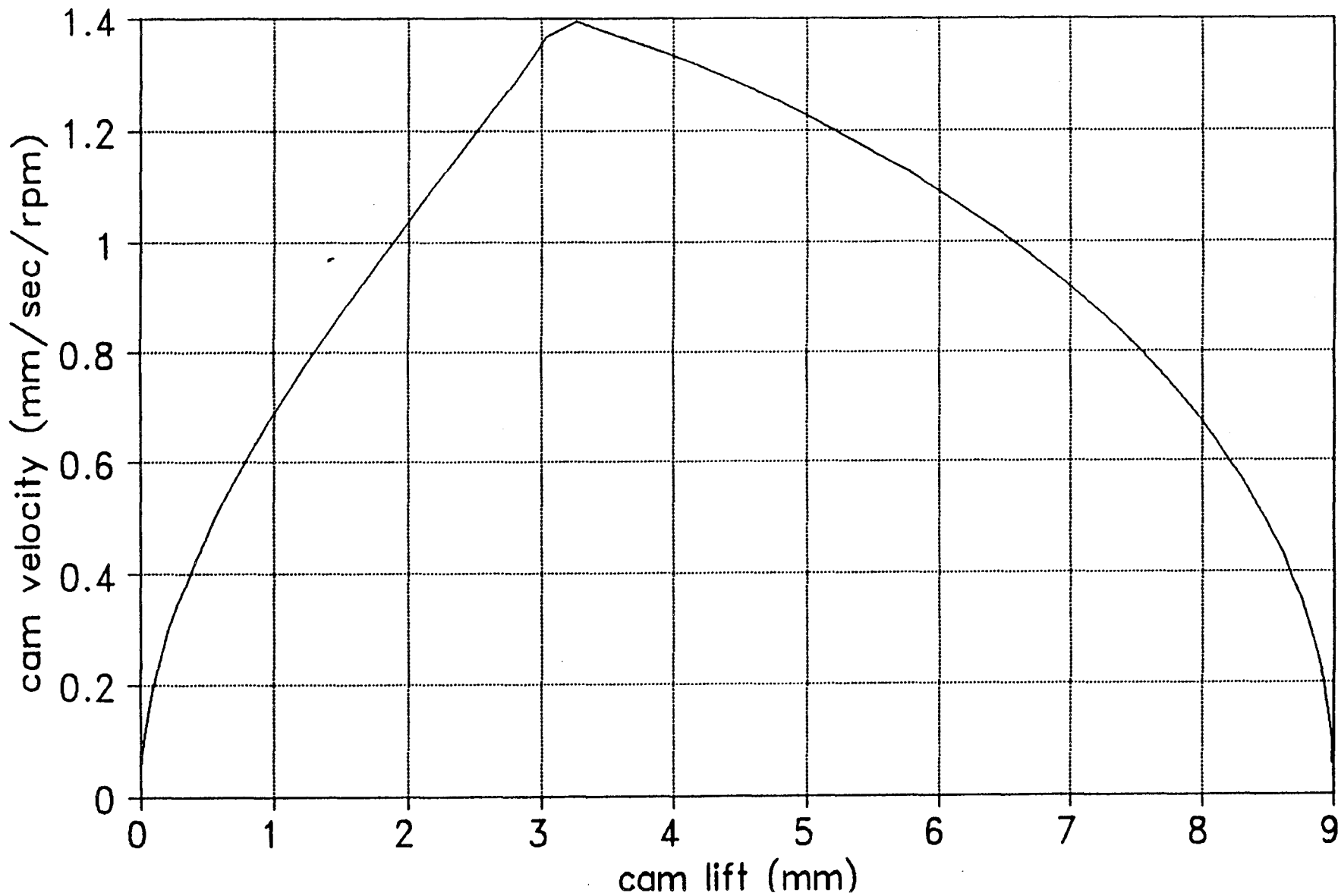
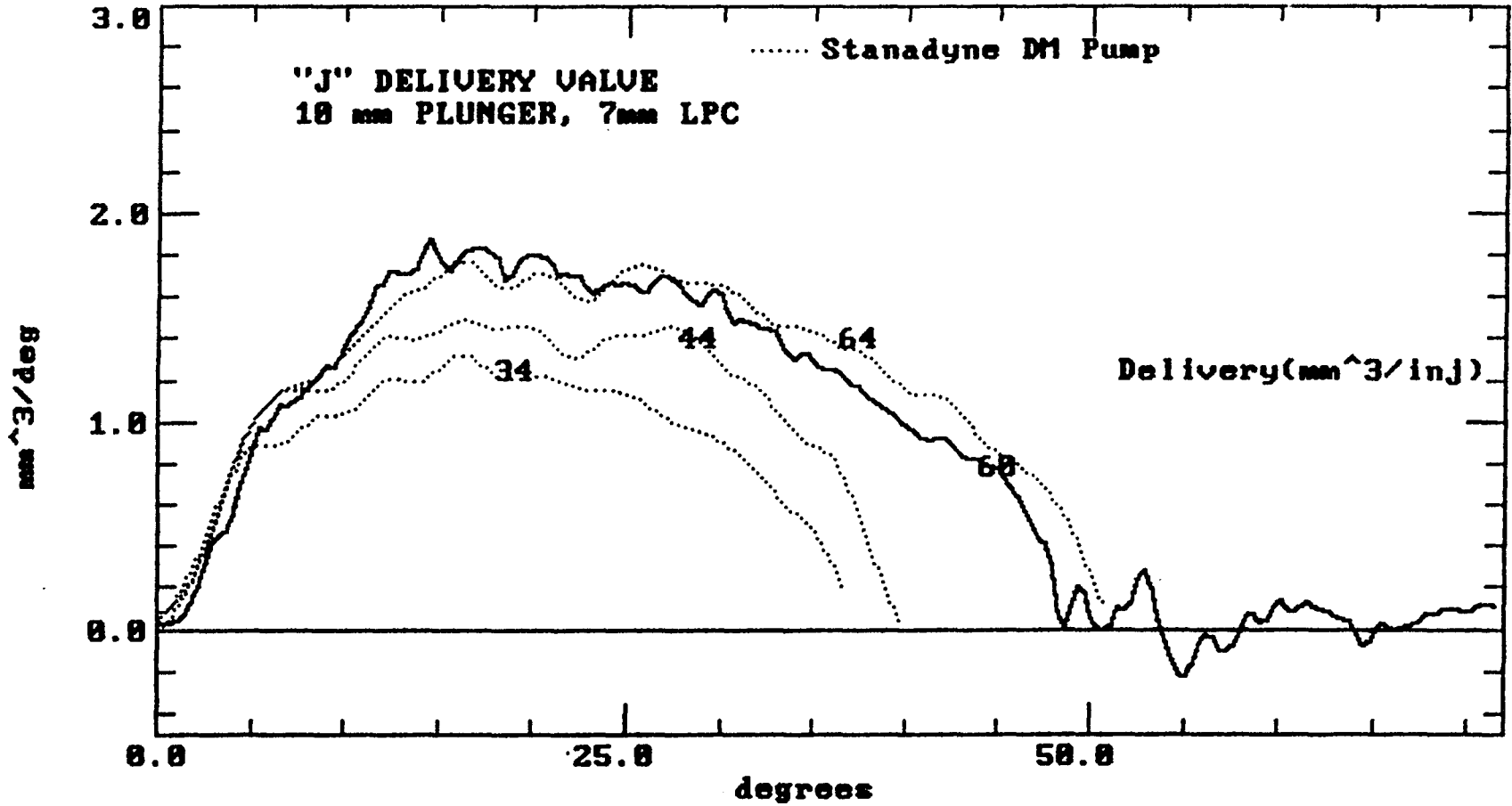


Figure No. 26

INJECTION RATE COMPARISON

6000 RPM

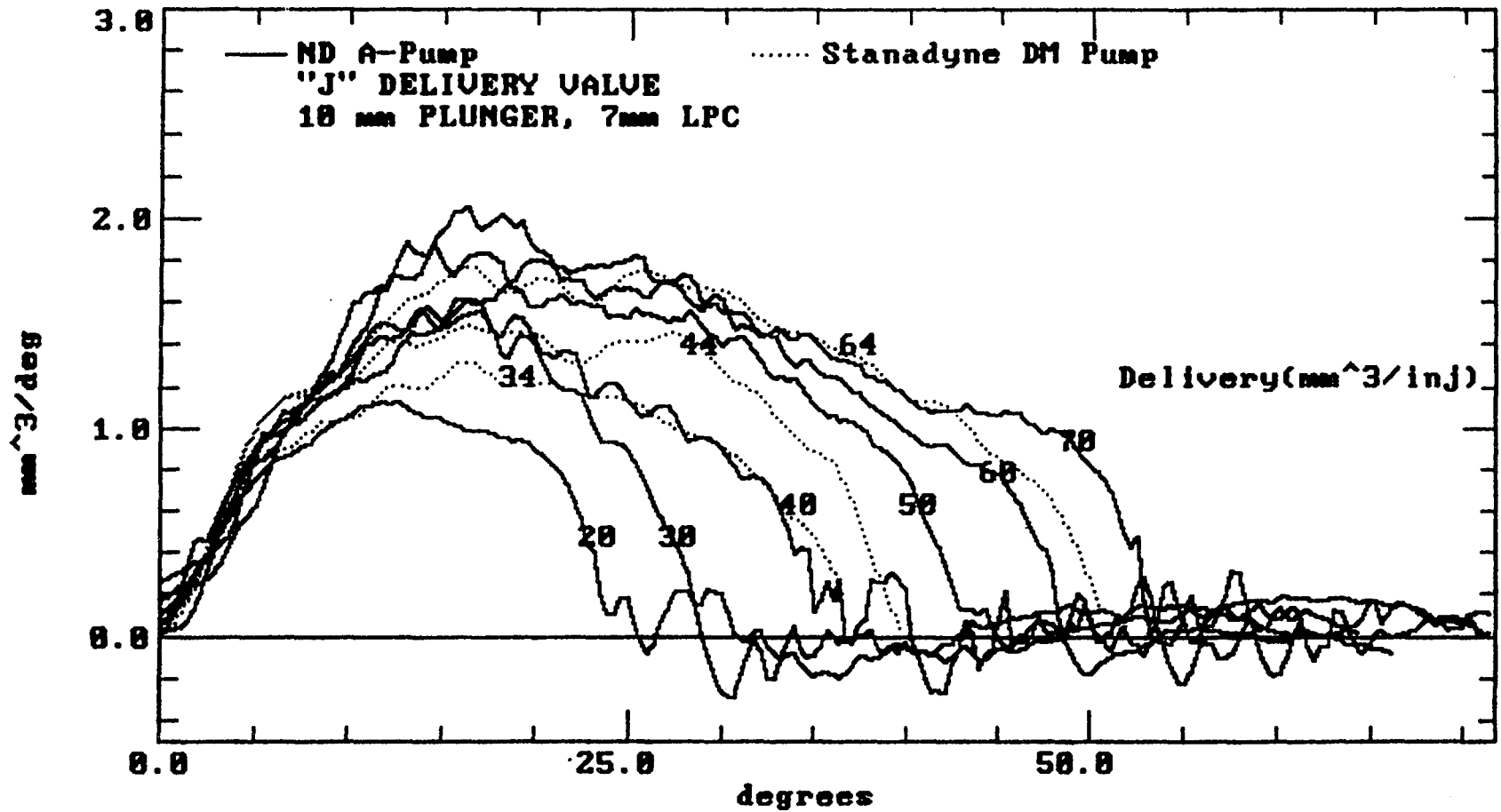


LINE: A-Pump; 2.0 x 500 mm Stanadyne; 1.5 x 50 mm

NOZZLE 210028N8

INJECTION RATE COMPARISON

6000 RPM



LINE: A-Pump; 2.0 x 500 mm Stanadyne; 1.5 x 50 mm

NOZZLE 210028N8

EFFECT OF RATE SHAPING ON BSFC

ENGINE 0704-10, 6000 RPM, N1 NOZZLE

145

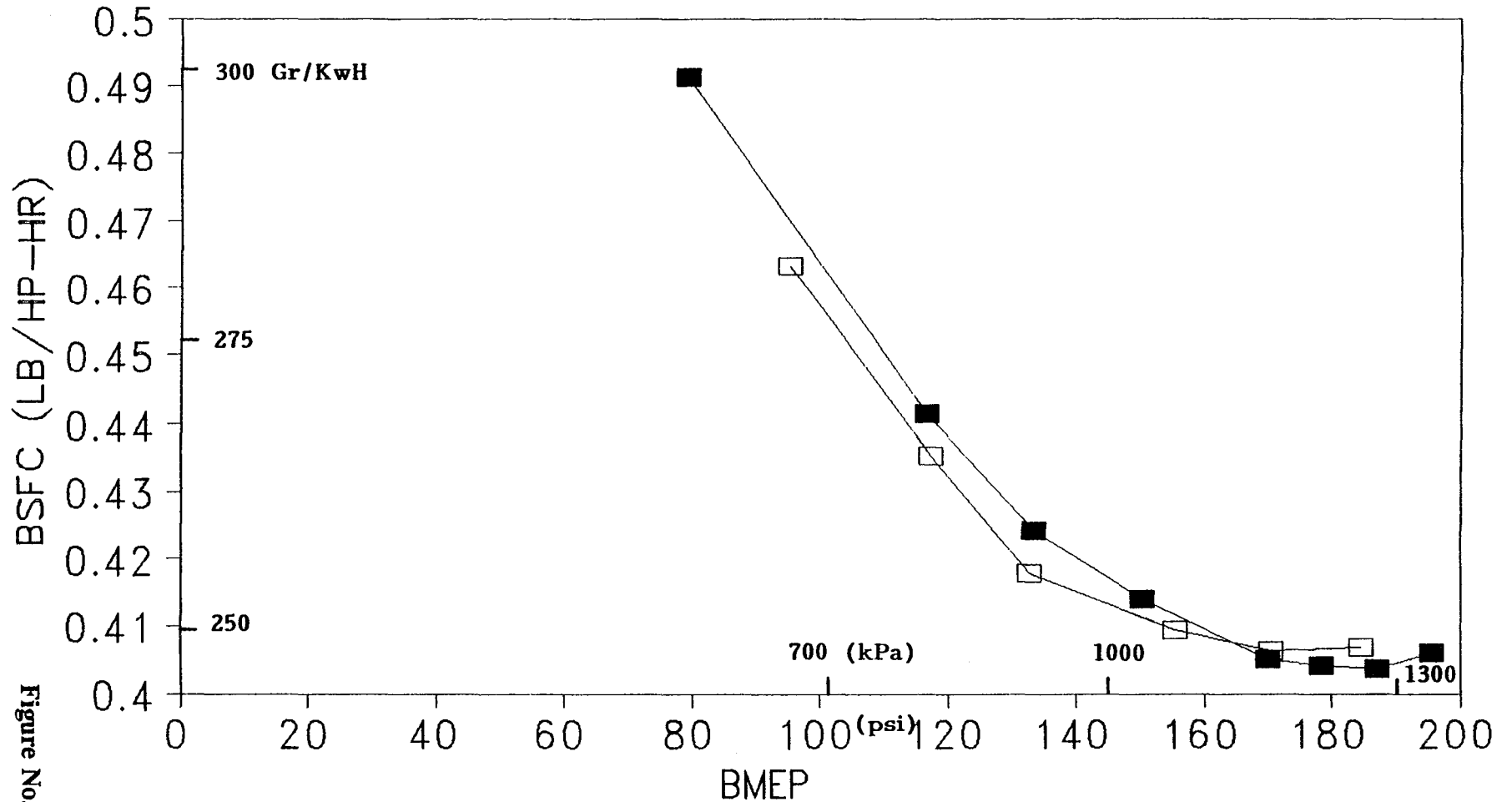
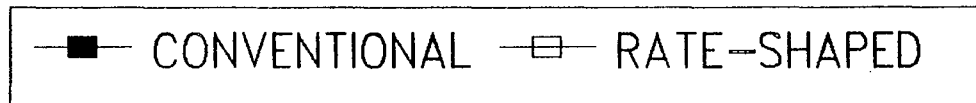
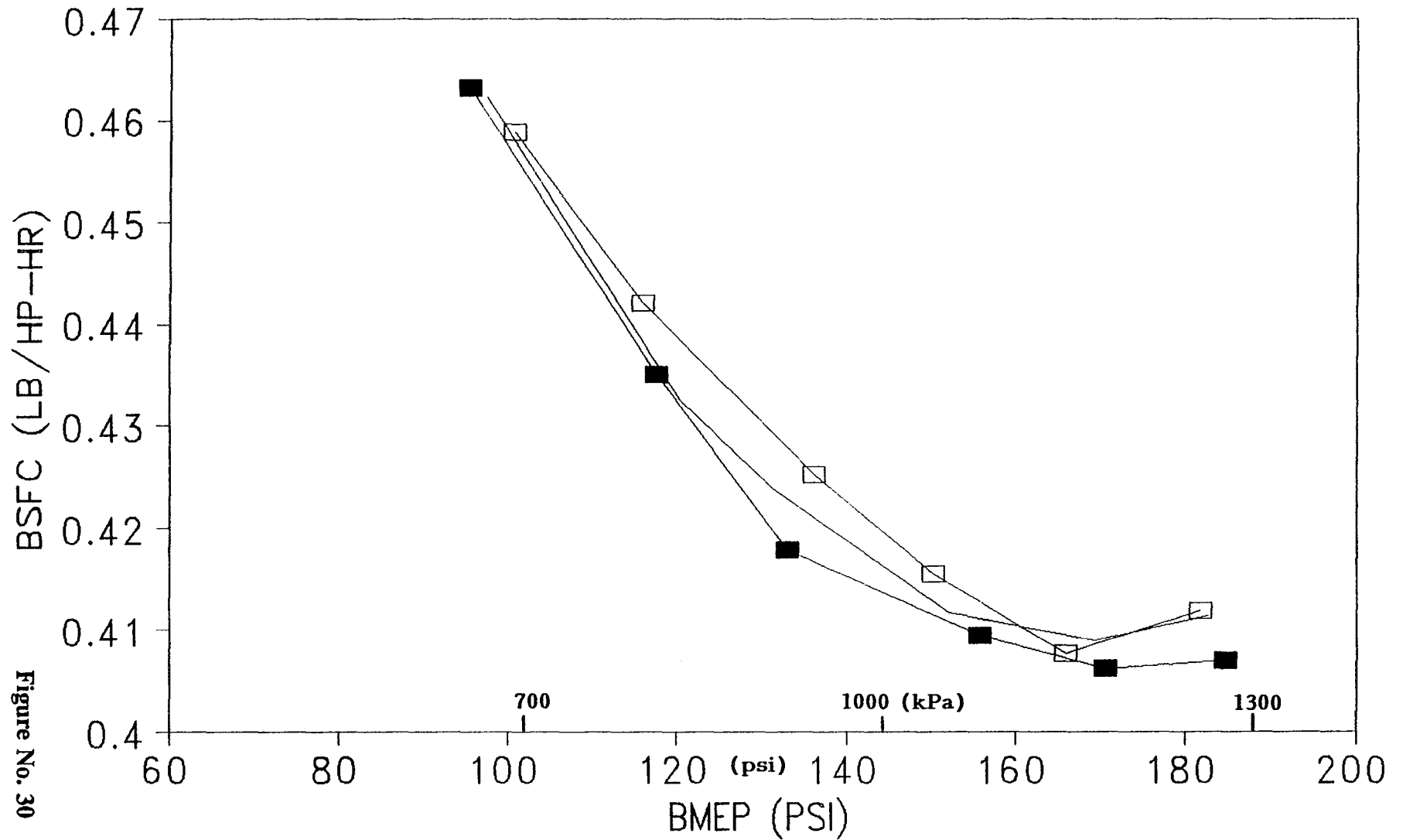


Figure No. 29



EFFECT OF NOZZLE ON RATE-SHAPED PUMP ENGINE 0704-10, 6000RPM



INJECTION RATE COMPARISON

6000RPM

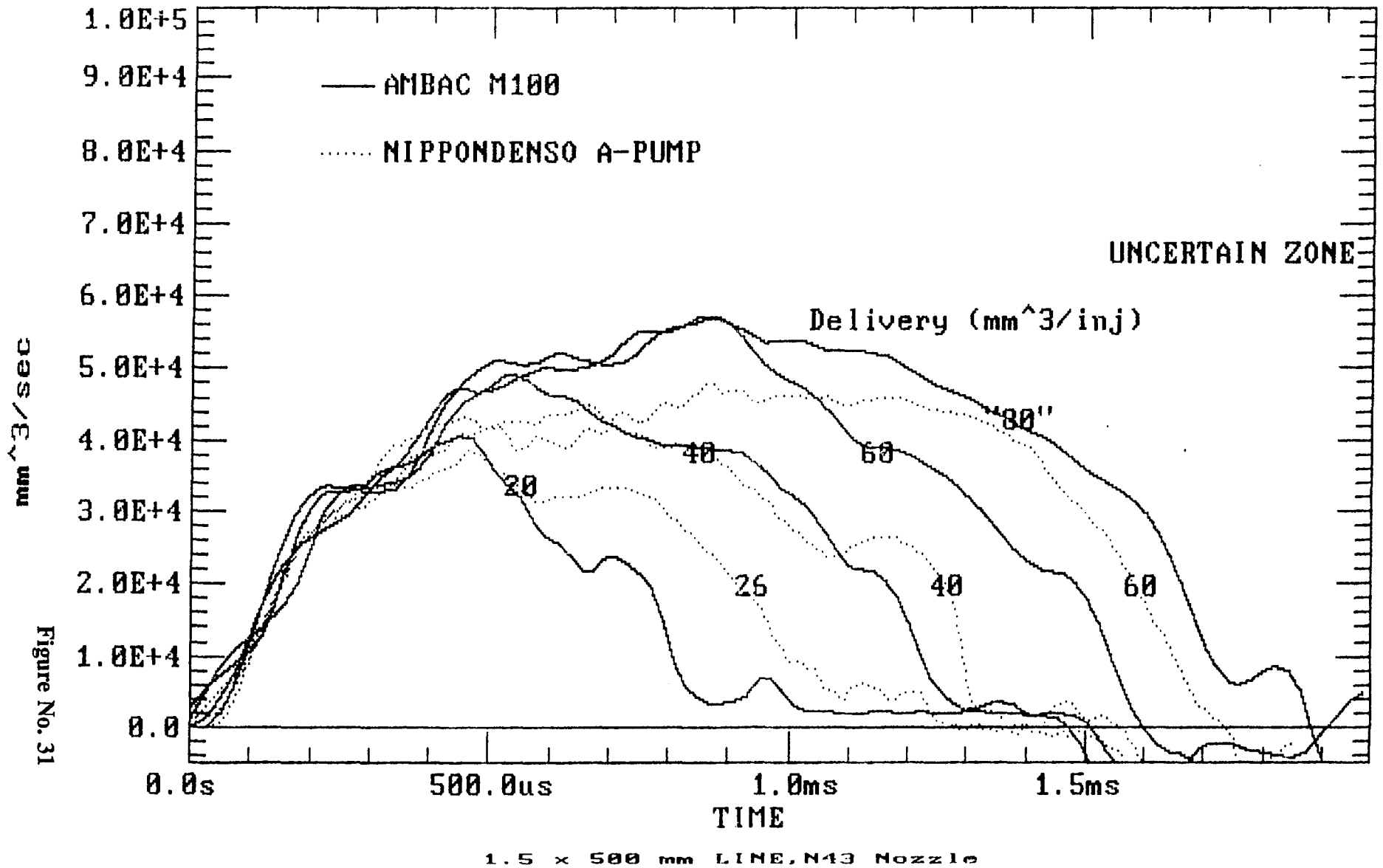


Figure No. 31

1.5 x 500 mm LINE, N43 Nozzle

Fuel System Performance

Engine 0706-1, 6000 RPM, N43 NOZZLE

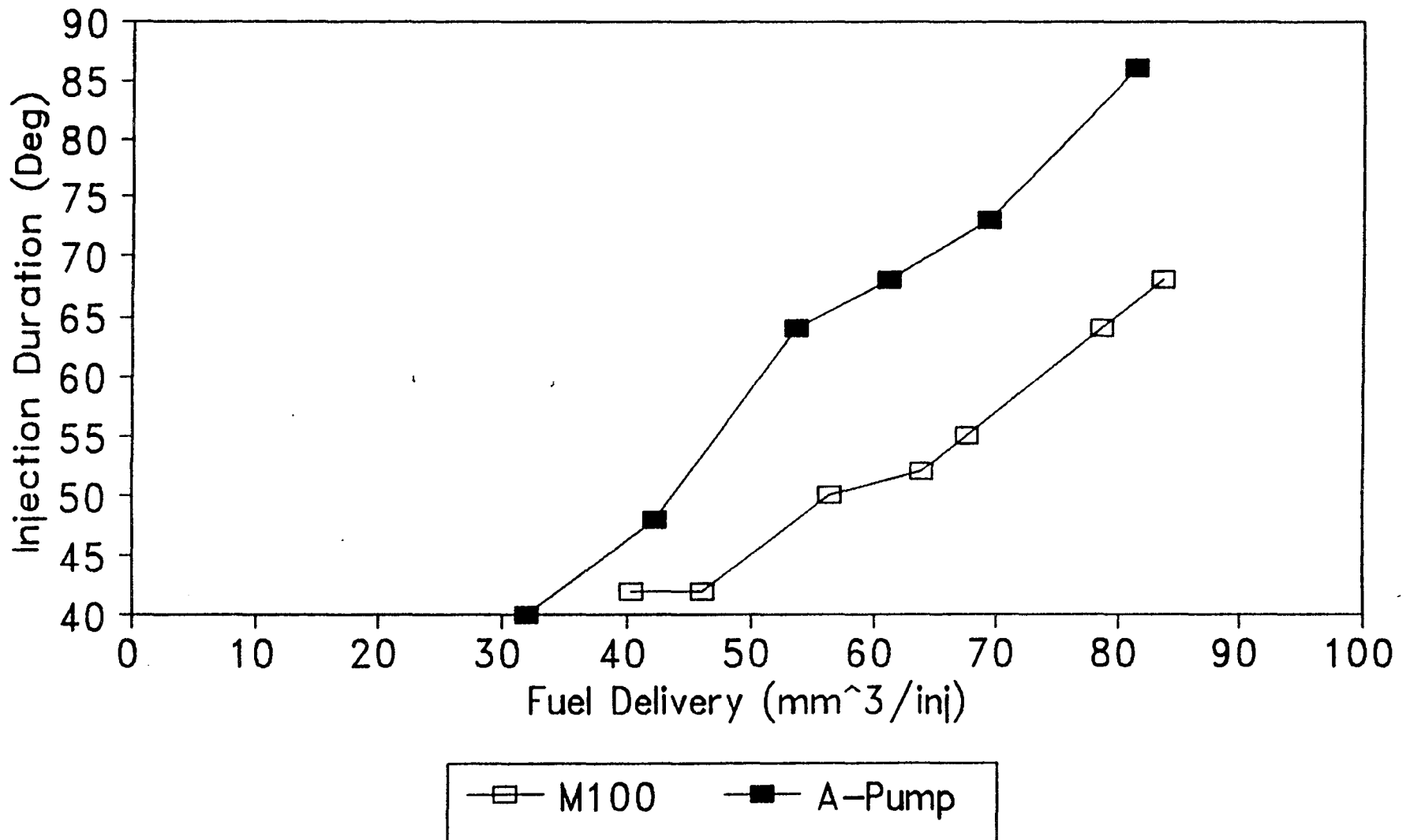
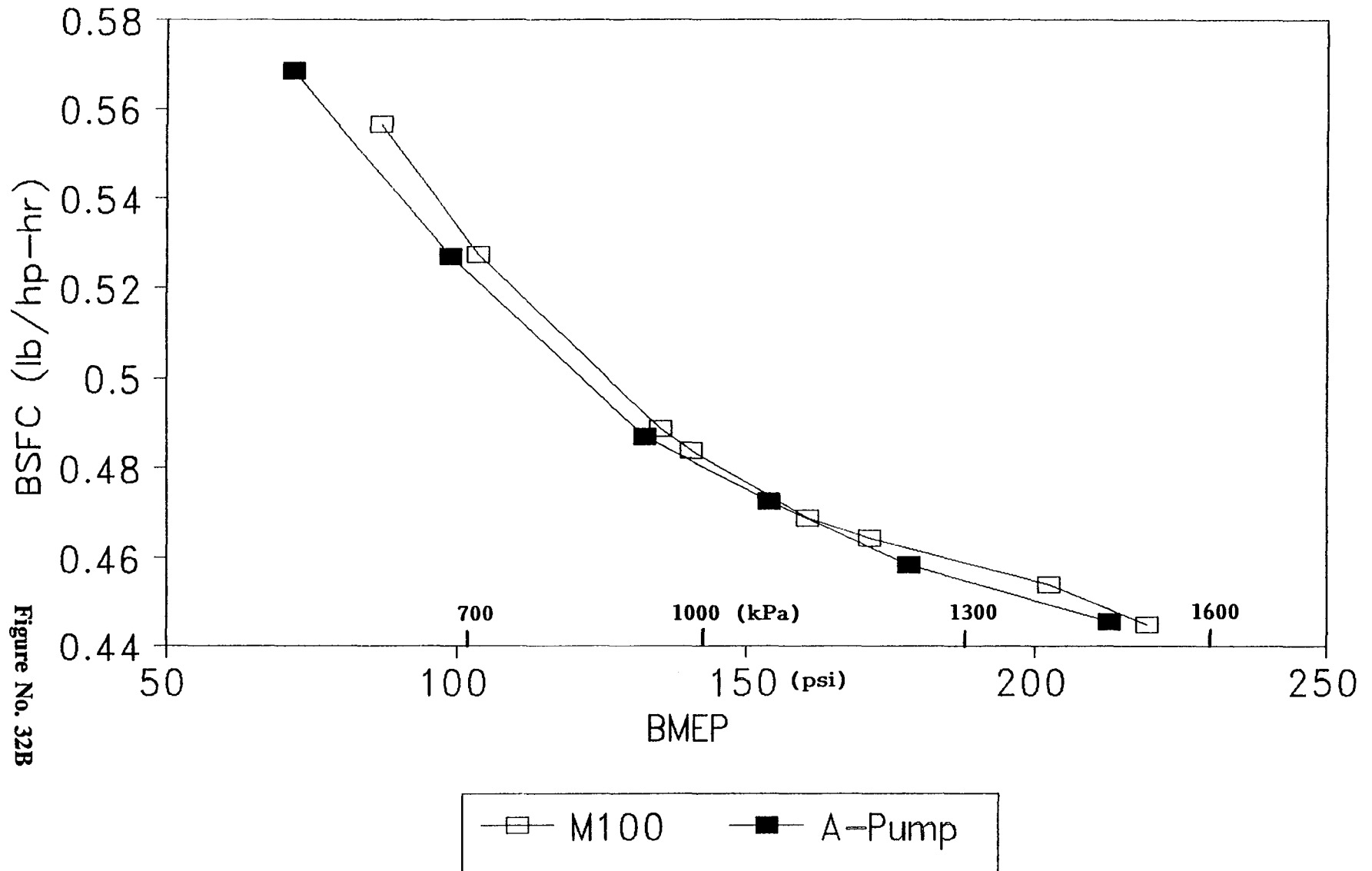


Figure No. 32A

COMPARISON OF A-PUMP AND M100 BSFC ENGINE 0706-1, 6000RPM, N43 NOZZLE

149



4.2 REDUCED FRICTION/IMPROVED TRIBOLOGY/SEALING

INTRODUCTION

Improvements in the tribological systems of the Stratified Charge Rotary Engine (SCRE) are required to improve efficiency and assure adequate durability at the desired aviation power ratings. Activities in this program focused on: a) measuring and reducing friction, b) measuring and reducing side seal leakage, c) improving sealing system durability, and d) improving the lubrication of the gas sealing system.

Engine tests were performed to measure friction, seal leakage and wear. Seal system materials were screened and engine tested, showing a fourfold improvement in apex seal durability. New seals were designed which analytically show promise for further reductions in wear and friction. An advanced synthetic lubricant was tested. Apex seal temperature was measured in a firing engine during an attempt to improve lubricant usage efficiency.

The specific objectives, technical approach, results and conclusions are discussed in the sections that follow.

OBJECTIVES

The objectives of the reduced friction and improved tribology/sealing methods task are listed below:

1. Reduce Engine Friction:

- a. Establish a method for measuring engine friction to facilitate comparison of test configurations.
- b. Measure engine friction for the baseline single rotor rig.
- c. Design sealing systems which lower friction by reducing loads and promoting the formation of elastohydrodynamic or hydrodynamic films.
- d. Validate new sealing system designs in engine tests, measuring friction and wear.

2. Improve Engine Sealing at the Design Point:

- a. Design sealing systems that control seal loading under high combustion pressure conditions to minimize wear.
- b. Design sealing systems with improved compliance to reduce combustion gas leakage.

- c. Select and test lubricants which can tolerate the expected high surface temperatures without forming detrimental deposits.
- d. Enhance delivery of lubricant to the wear surfaces to minimize consumption and deposit formation.
- e. Identify promising low wear material pairs using wear rigs and engine tests.

TECHNICAL APPROACH

The technical approach for reducing engine friction and improving engine sealing consisted of developing and utilizing an analytical seal dynamics model, bench screening and engine tests of new seal materials, and engine tests to evaluate present (and proposed) sealing grid friction and performance. The specific elements of this activity are described in the following paragraphs.

SEAL DYNAMICS MODEL

An existing apex seal dynamics model was available for use in this activity. This model calculates apex seal to trochoid loading based upon inputs of engine geometry, coefficients of friction, and measured or predicted combustion pressure indicator diagrams. This model was extensively modified to allow analysis of configurations other than the standard bar type apex seal. Corrections were made to the subroutine which calculates the contribution of slot friction to total apex seal load.

An example of the apex seal dynamics model output is shown in Figure 1. The two curves represent the two possible loading conditions which are dependent upon the direction of radial apex seal motion (or impending motion) relative to the rotor.

The inner curve represents the seal to trochoid load when the seal is moving out of the rotor slot, in which case slot friction is subtracted from the seal to trochoid load. The outer curve represents the loading when the seal is moving into its slot, and friction is added to the seal to trochoid load. Seal motion relative to the rotor occurs due to manufacturing and assembly tolerances, thermal and pressure distortions, bearing clearances, gear backlash and crankshaft deflections. Because of the complex nature and small magnitudes of these interacting causes, it is not possible at this time to predict with confidence the direction of seal motion at any point in the cycle. The objective when utilizing the dynamics model in the design process is to ensure that seal to trochoid load magnitudes are reasonable for both directions of seal motion throughout the cycle.

The apex seal dynamics model was used to determine the required dimensions of an apex seal which is predicted to offer improvements in friction and wear. The proposed new seal design is discussed in detail in the Results section of this report.

MATERIALS SCREENING TESTS

An Alpha LFW-1 wear rig was used to screen potential seal and counterface materials. The Alpha rig is a block-on-ring type tester that tests for basic material compatibility under dry sliding conditions. Previous investigations have shown the apex seals to operate under mixed lubrication conditions: a lubrication regime in which material compatibility is important in preventing catastrophic wear. The Alpha rig has shown, over decades of use, the ability to screen materials with sufficient accuracy to identify promising pairs for engine testing.

ENGINE TESTS

Engine tests were developed and run to obtain baseline data on rotor side seal gas leakage, engine power section friction, gas seal wear, and apex seal lubrication requirements. The individual test methods are described below.

Side Seal Leakage Test

A side seal leakage (blowby) test was developed to determine the volumetric flow of combustion gases past the rotor side sealing grid. The leakage test was run using a commercial configuration SCORE 70 (0.7 liter) single rotor engine. The power section of the engine did not differ significantly from the NASA 1007R rig engine except for the inclusion of special features intended to reduce blowby.

A blowby test cycle was devised to monitor the effect of speed, load, and test duration on side seal leakage. Blowby gas was directly measured by routing all crankcase blowby gases through a public utility type gas meter.

Friction Measurement Test

Engine friction was measured under firing conditions to determine the Friction Mean Effective Pressure (FMEP) of the present NASA rig engine configuration power section. The FMEP was obtained by calculating Indicated Mean Effective Pressure (IMEP) from the combustion pressure indicator diagrams and subtracting from this derived IMEP the Brake Mean Effective Pressure (BMEP) calculated from the engine dynamometer load cell. The resulting value is representative of the FMEP.

The IMEP calculations were found to be very sensitive to the assumed position of engine top center. Small changes in the location of engine top center produced large changes in calculated FMEP. The variability in FMEP with assumed top center location is shown in Figure 2. To improve confidence in the FMEP measurements, the actual rotor position at assumed top center was measured and compared to true top center (found by measuring the actual position of the rotor housing dowels). The top center position used to determine IMEP was then adjusted accordingly.

Seal Lubrication Test

Sacrificial lubricant consumption can be minimized by selecting a lubricant introduction location that promotes the deposition of the lubricant on the wear surfaces, while minimizing airstream entrainment or deposition on the rotor surface. The optimum lubricant introduction method can be determined by testing several lubricant introduction locations. The lubrication method which allows use of the lowest lubricant flow without causing breakdown of apex seal lubrication would be the preferred method. Monitoring the apex seal temperature for temperature increases while decreasing lubrication flow rates would provide the required indication of incipient lubricant film breakdown.

A pre-existing instrumentation system for measuring apex seal temperature in SCORE 580™ engines was used to attempt to select an improved lubricant introduction method. The SCORE 580 engine (5.8 litres per rotor) was used because the small size of the SCORE 70 engine's rotor precluded the installation of the required instrumentation. It is believed that lubricant delivery trends, if not absolute brake specific oil consumption requirements, will translate between the two engine sizes.

Instrumentation for the lubricant introduction test was configured with six apex seal thermocouples - two per apex seal - located as shown in Figure 3. The thermocouple voltages were processed by a signal conditioner module mounted in the rotor. Temperature signals were output from the module via a slip ring on the rotor side to a pair of carbon brushes mounted in one end housing, and ultimately to a decoder circuit in the control room. The decoder circuit provided synchronization pulses to the rotor module to control the sequence of the thermocouple channels that were monitored. Temperatures were displayed on a digital indicator, and were also recorded from the decoder's analog output onto a strip chart. The basic rotor instrumentation is shown in Figure 4.

The engine was configured to allow introducing seal lubricant in several locations;

- o Intake port drip bar (standard location).
- o Four axially spaced holes on the trochoid surface just after the intake port closing edge.

- o Three additional sets of axially spaced trochoid holes, two sets in the intake quadrant, one set just before the cold minor axis.
- o Single holes, one on each end housing, at locations similar to those shown in Figure 5, taken from General Motors Patent No. 3,814,555. (This patent claimed a 33% reduction in lubricant requirements compared with a fuel-oil mixture technique.)

Lubricant was supplied by a variable speed, variable displacement laboratory metering pump (Fluid Metering Inc., Model QV-0). The lubricant flow rate was monitored with a Pierburg Model PLU-103A High Precision Flowmeter.

RESULTS

The results of the engine tests for side seal leakage, friction measurement, and apex seal lubrication will be presented first. The results of the seal materials screening test and engine test of new seal materials will follow. The new sealing system design, which incorporates inputs from engine and materials tests, in addition to dynamic seal analysis, will be presented last.

ENGINE TESTS

Side Seal Leakage Test Results

The side seal leakage test was performed on a commercial configuration SCORE 70 (0.7 liter per rotor) single rotor engine, number 1007P001-4. The power section of this engine was essentially the same as the NASA rig engine, except for several features included specifically to reduce side seal leakage. The specific features and design rationale for inclusion of each feature are identified in Table 1.

The side seal leakage test consisted of the test cycle shown in Table 2. The test cycle was devised to determine the effects of speed, load, and cumulative engine operating time on side seal leakage. The total test time was 126 hours.

The crankcase blowby gas flow and the static leak-down test pressure were measured at the end of each test cycle. The results of the test are shown in Figure 6. The upper plot shows the increase in blowby over the duration of testing, while the lower plot shows the static leak-down test results. Static leak tests are routinely performed to give an indication of sealing system condition.

Crankcase gas blowby was not significantly reduced by the seal grid features designed to reduce blowby when compared with a standard configuration engine. The leak test results for engine 1007P001-4 are considered to be very good, indicating that the side seals and apex seals remained in good condition. The increase in blowby gas flow indicates that side seal gas leakage was likely worsening primarily due to factors affecting sealing during operation, and not due to degradation of the seal's physical condition.

TABLE 1

FEATURES TO REDUCE SIDE SEAL GAS LEAKAGE

Design Feature	Reason for Incorporation
Butt-Butt Side Seals	Reduce interaction of motion between side and button seals. Allow each element to respond to housing surface irregularities independently.
High aspect ratio side seals (Deep side seal grooves with matching tall side seals)	Reduce tilting tendency of side seals. Tilted side seals may not seat uniformly on side housing surface, and may have inhibited freedom of motion in rotor grooves.
Increased preload button springs.	Increase button seal actuation force against side housing.
Reduced axial rotor clearance. (Wet hub clearance)	Reduce relative motion between side seals and rotor by reducing rotor axial motion within engine.
Enlarged blow-by recovery annulus.	Improve the capability to internally recirculate blow-by gases.

Disassembly of engine 1007P001-4 revealed heavy carbonaceous deposits located inboard of the side seal grid, most heavily concentrated near the apex buttons. The deposits are clearly an indication of excessive side seal grid leakage. Faint patterns in the deposits suggest that the predominant leak paths may have been across the button seal faces. The rotor side deposits are shown in Figure 7. Despite the presence of the deposits all the seals were free in their slots. The deposits may, however, serve to inhibit seal performance during operation, perhaps by impeding the flow of gas to the underseal volumes, or by preventing the seals from achieving good contact against the seal slot walls. It is speculated that seal leakage is a self generating phenomenon; seal leakage promotes deposit formation which in turn further impairs seal performance.

Another possible contributor to rotor side deposits and side seal leakage is the narrow width of the SCORE 70 engine combustion chamber. The proximity of the end housings to the fuel spray may encourage partially combusted fuel to condense on the end housing surfaces and to collect in the side seal crevice volumes, promoting deposit formation and attendant seal leakage. JDIT's SCORE 580 engine with a similar side sealing grid has not exhibited any blowby or rotor side deposit problems in thousands of test hours. The SCORE 580 end housings are over twice the distance from the fuel sprays as in the SCORE 70 engine.

TABLE 2
SIDE SEAL LEAKAGE TEST CYCLE

SPEED (RPM)	ENGINE LOAD - BMEP		CYCLE DURATION (HOURS)
	PSI	kPa	
4000	65	447	1
4000	120	827	1
5000	65	447	1
5000	120	827	1
6000	65	447	1
6000	130	896	1

Friction Measurement Test Results

Total engine friction was measured on the NASA rig engine 0706-1 under motoring and firing conditions. Engine 0706-1 was of the standard NASA rig engine configuration (0.7 liter per rotor) except for the inclusion of Ferrotic SK dual corner (clevite corners) apex seals mated against a Jetkote thermal spray applied Chromium Carbide-Nichrome ($\text{Cr}_3\text{C}_2\text{NiCr}$) trochoid coating, and the use of an experimental synthetic lubricant. These features were included because they represented the most likely near-term improvements in the sealing system which were anticipated to be incorporated into future engine builds.

Results of the Friction Test are shown in Figures 8, 9 and 10. These figures show the total measured FMEP for the engine's power section, accessory drive gearbox, and fuel injection pumps.

Friction (FMEP) was found to increase with engine speed, and to decrease with engine load. Possible reasons for the inverse relationship of friction and load involve the effect of combustion pressure on engine bearings and seal elements. Combustion pressure forces act on the rotor to counter centrifugal force. To a limited degree bearing friction will be reduced with increasing engine load. Combustion pressure also affects the sealing elements' friction. Combustion pressure acts to increase apex seal to slot friction. If the apex seal to rotor relative motion is outward during high pressure intervals of the combustion cycle, the effect of increased apex slot friction on the apex seal will be to reduce the apex seal load on the trochoid surface. Reducing the apex seal load on the trochoid directly reduces engine friction.

Seal Lubrication Test Results

Apex seal temperature during engine operation was monitored to determine the optimum method and flow rate of seal lubricant introduction. Apex seal temperatures were measured using instrumentation developed for and installed in a single rotor SCORE 580 engine.

The seal temperature data plotted against lubricant flow rate at an engine speed of 2400 rpm is shown in Figure 11. During engine operation at 2400 rpm and load of 120 psi 827 kPa) bmep, the seal lubrication rate was incrementally reduced to determine the minimum lubricant usage requirement. The minimum lubricant flow rate was to be indicated by a rise in apex seal temperature.

No temperature rise was indicated over the range of lubrication rates explored from 1% of fuel flow (the traditionally specified rate) down to 0.08% of fuel flow. The absence of a temperature rise at the low lubrication rate may be due to several factors:

1. Insufficient time may have been allotted for the depletion of lubricant introduced at relatively high rates. (0.08% rate was run for only five minutes to prevent undetected catastrophic wear.)
2. Thermocouple response time may not have allowed resolution of temperature transients.
3. Rotor oil seal leakage may have allowed sufficient lubricant to reach the seals, obviating the need for any additional seal lubricant. (At the condition run, fuel flow was 100 lbs/hr (45.36 kg/hr). At a seal leakage rate of 1% of fuel flow, sufficient lubricant would likely reach the apex seals without additional sacrificial supply. This leakage rate, one pound per hour, would not ordinarily be detectable with standard test cell instrumentation unless steady test points of approximately four hours or more were run.)

To improve test procedure sensitivity, it is recommended that any future apex seal temperature testing be run at higher engine loads, where oil seal leakage would be a smaller fraction of total apex seal lubrication requirements.

All six apex seal thermocouples failed before any additional testing was performed. The failure mode of the thermocouples has not been identified because the engine was not disassembled. Past failures in similar testing were due to fatigue or abrasion where the thermocouple wires exited the seals, looped inside machined cavities in the button seals, and attached to solder pads on the rotor. Larger diameter rotor buttons (which have been run in unrelated tests) are recommended to be fitted to the instrumented rotor to allow more room for wiring on any future builds.

MATERIAL SCREENING TESTS

Seal and trochoid coating material screening tests identified seven promising new material combinations, successfully engine tested one new material wear pair, and evaluated an experimental lubricant.

MATERIAL SCREENING

Twenty five apex seal and trochoid material pairs were screened in the materials bench testing process. The methodology and selection of the proposed materials are discussed in detail in Appendix 1.

The following material combinations were found to merit further evaluation in engine testing:

<u>Seal Material</u>	<u>Trochoid Coating</u>
PM-212	LW 1N-30 (Tungsten Carbide-Cobalt)
PM-212	Triballoy T-800
PM-212	Stellite 6
Si ₃ N ₄	Triballoy T-800
Si ₃ N ₄	44\430
Triballoy T-800	Triballoy T-800
NJS 234 (Gopalite)	Triballoy T-800

MATERIAL ENGINE TEST

One new material wear pair was tested in the NASA 1007R rig engine. The combination tested was Ferrotic SK apex seals running against Chrome Carbide-Nichrome, Jetkote applied, trochoid coating. The material pair performed extremely well with a seal wear rate of only 0.0017 inches (0.043 mm) per 100 hours of operation. The testing included engine operation at engine loads up to 277 psi (1.908 mPa) Brake Mean Effective Pressure (BMEP). No visible trochoid coating deterioration was detected. The standard material combination, Clevite apex seals and Tungsten-Carbide, Detonation Gun (D-Gun) applied trochoid coating has an historical average apex seal wear rate of 0.007-0.009 inches (0.178-0.229mm) per 100 hours.

LUBRICANT TEST

An experimental high temperature capability lubricant was tested in three engine tests. The lubricant is a proprietary formula manufactured by AKZO Corporation, designated E90046. Deposits formed on the rotor flanks and rotor faces were judged to be excessive relative to

the conventional lubricants generally used. Evidence of the deposits interfering with side sealing function was not conclusive.

SEALING SYSTEM DESIGN

New rotor side and apex seals were designed to reduce seal related friction, wear, and gas leakage. Design inputs included engine test results of present grid configurations, seal dynamic analysis, and the objectives of reducing friction while improving gas sealing performance, and reducing seal loads to reduce seal wear.

Rotor Side Seal Design

The rotor side seal design includes features to increase side seal compliance with mating surfaces and to reduce effects of external seal tilting forces. Two side seal designs were prepared and one configuration was procured.

The standard configuration side seals are made to fit curved rotor grooves with a radius approximately parallel to and inboard of the rotor face contour. The seals' primary mating surface is the flat side housing. The side seals' curved shape will allow uniform contact with the side housing to be disturbed if the seals tilt in their groove. Conditions that may cause a tilting moment on the seal include: 1) uneven pressure distribution on the seal, 2) friction forces on the seal, 3) axial rotor motion, and 4) side housing distortion. Loss of uniform contact between the side seals and side housing will possibly allow gas leakage.

To eliminate the loss of uniform side housing contact when the seal tilts, several straight element side seal concepts were explored. A segmented side seal was proposed, with each curved seal replaced by two straight elements joined with a secondary button seal at the center. This configuration is shown in Figure 12. Design layout of this proposal revealed an interference with the side housing dummy port feature. The concept was modified as shown in Figure 13 to incorporate three straight segments per seal joined with two secondary buttons.

The three straight element segmented seal has two drawbacks: 1) there are four additional junctions per seal which may be leak paths for gas, and 2) the rotor grooves are difficult to machine.

The three straight element side seal configuration was procured for a proof of concept test. The test objective was to determine if improved side seal compliance would reduce leakage. This test was not performed because of the reduced scope of the NASA Phase III program.

Rotor Apex Seal Design

An apex seal system was designed to minimize wear and friction by controlling gas pressure loading and enhancing lubricant film formation. This seal configuration is shown in Figure 14 and is characterized by a mushroom shaped bar with a larger than standard (6x) tip radius and two secondary seal elements at the seal to slot interface.

The mushroom shape provides pressure balancing to control pressure induced seal to trochoid forces. The secondary seals prevent high gas pressure from creating high side loads and the attendant high seal to slot friction force which can disrupt seal behavior. The large tip radius enhances the formation of a lubricant film which can reduce friction and wear.

Figures 15 through 18 are plots of seal to trochoid forces for the standard and new mushroom apex seals at 160 HP (120kw) and 200 HP (150kw), as predicted by the apex seal dynamics model. Figures 15 and 16 compare the predicted seal forces for the standard and new design apex seals at 7000 RPM and 160 BHP (120kw). Figures 17 and 18 provide the same comparison at 8000 RPM and 200 BHP (150kw). Loads for the mushroom seal are predicted to be lower than for the standard seal for most of the cycle. Predicted peak seal loads are dramatically reduced by up to 50% for the 200 HP (150kw) operating condition.

Additional discussion of the benefits of the mushroom seal design is provided in Appendix 2. Seal analysis results for the mushroom seal configuration and two other candidate seal design systems are provided in Appendix 3.

CONCLUSIONS

- 1) The Score 70 NASA engine side and button seal performance deteriorates with increasing engine operating time. The deterioration is not due to wear or mechanical changes of the sealing elements. Deposit formation associated with seal leakage is the likely cause of the sealing performance degradation. The deposits appear to cause the deterioration by interfering with seal motion and/or impeding the flow of actuating gas pressure to the underseal volume.
- 2) The geometry of the SCORE 70 engine may contribute to the formation of deposits due to the proximity of the fuel sprays and partially combusted fuel to the crevice volumes.
- 3) Engine friction increases with engine speed, but decreases slightly with engine load. The inverse relationship of friction with load may be due to the following:
 - A) Combustion pressure forces reducing peak engine bearing loads and thereby reducing bearing friction losses.
 - B) Combustion pressure loading on the apex seals which is believed to reduce the seal to trochoid force. The combustion pressure reduces the load by increasing the seal to slot friction force while the seal moves outward relative to the rotor.
- 4) New apex seal designs are feasible which may reduce engine friction and wear. The new seal designs would reduce friction and wear by controlling pressure loading, increasing lubricant film thickness, decreasing contact stress, and providing a more favorable height to volume wear rate ratio.
- 5) New seal and trochoid coating materials offer the potential for greatly enhanced seal life. One apex seal and trochoid coating material pair (Ferrotic SK/Chrome Carbide-Nichrome) demonstrated a four-fold reduction in wear rate compared to the standard (Clevite/Tungsten Carbide) material combination. Other material combinations showed potential for excellent wear resistance in wear rig tests. These material combinations included such materials as the self lubricating, NASA developed, PM-212, Triballoy T-800, and Silicon Nitride.

RECOMMENDATIONS

- 1) Fabricate new gas sealing systems in accordance with the concepts discussed herein. Test the seal systems by measuring friction, wear and gas leakage.
- 2) Engine test the apex seal and trochoid coating material combinations judged most promising in the materials screening tests. Bench tests should also be performed to determine if any of the materials react with common lubricant additives to form anti-wear films.
- 3) Repeat the seal lubrication test after making the following instrumentation and engine improvements:
 - A) Utilize new or reconditioned rotor oil seals.
 - B) Incorporate larger diameter apex button seals to provide more space for the apex seal thermocouple wiring.
 - C) Use stranded thermocouple wiring to increase durability.
 - D) Devise a means for measuring crankcase oil consumption with greater sensitivity.

APPENDICES

- 1) Memo, Dan Newman to C.E. Irion, "LFW-1 Testing of Apex Seal Trochoid Coating Material Couples for Potential Reduced Friction," 3 December 1991.
- 2) Memo, Jon Lauter to Engineering, "Mushroom Apex Seal Rationale," 17 July 1991.
- 3) Memo, A. Leto to J. Lauter, "Mushroom Apex Seal Design," 29 October 1991.

RECOMMENDATIONS

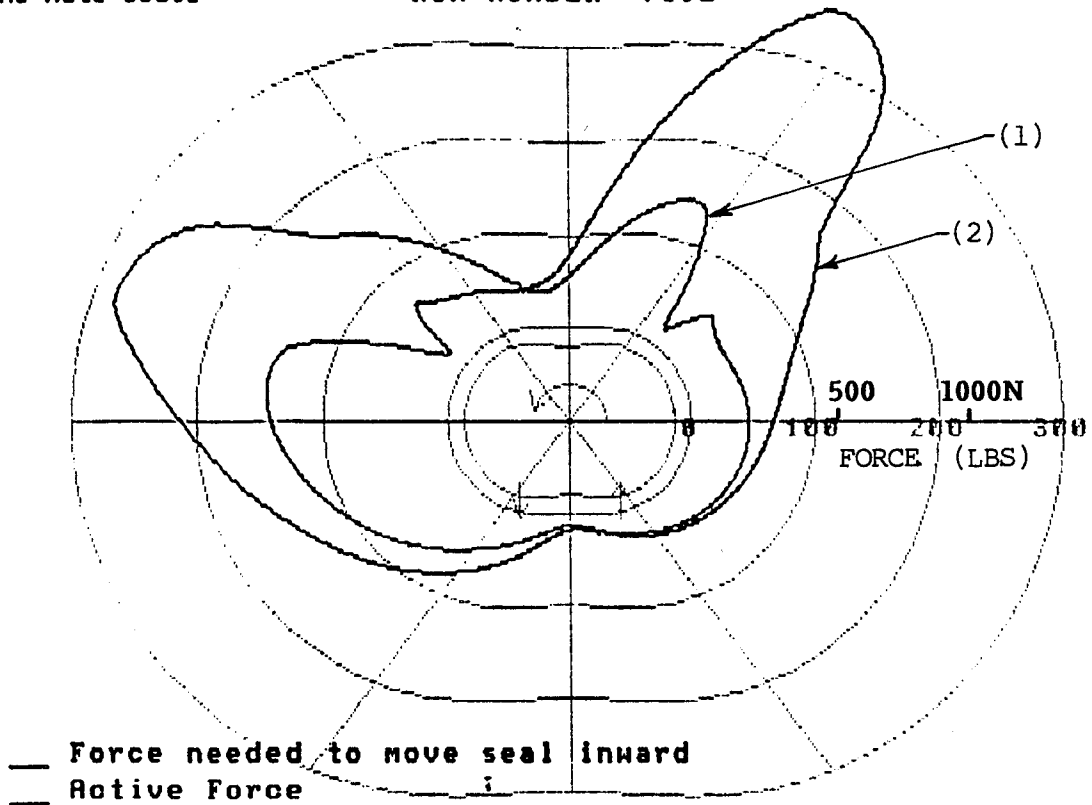
- 1) Fabricate new gas sealing systems in accordance with the concepts discussed herein. Test the seal systems by measuring friction, wear and gas leakage.
- 2) Engine test the apex seal and trochoid coating material combinations judged most promising in the materials screening tests. Bench tests should also be performed to determine if any of the materials react with common lubricant additives to form anti-wear films.
- 3) Repeat the seal lubrication test after making the following instrumentation and engine improvements:
 - A) Utilize new or reconditioned rotor oil seals.
 - B) Incorporate larger diameter apex button seals to provide more space for the apex seal thermocouple wiring.
 - C) Use stranded thermocouple wiring to increase durability.
 - D) Devise a means for measuring crankcase oil consumption with greater sensitivity.

APPENDICES

- 1) Memo, Dan Newman to C.E. Irion, "LFW-1 Testing of Apex Seal Trochoid Coating Material Couples for Potential Reduced Friction," 3 December 1991.
- 2) Memo, Jon Lauter to Engineering, "Mushroom Apex Seal Rationale," 17 July 1991.
- 3) Memo, A. Leto to J. Lauter, "Mushroom Apex Seal Design," 29 October 1991.

No Auto Scale

RUN NUMBER =70JL



- 1) Seal Moving Outward Relative to the Rotor Slot
- 2) Seal Moving Inward Relative to the Rotor Slot

FIGURE 1

SAMPLE OUTPUT OF APEX SEAL DYNAMICS MODEL

FRICION CALCULATIONS

ENGINE 0706-1, 6000 RPM

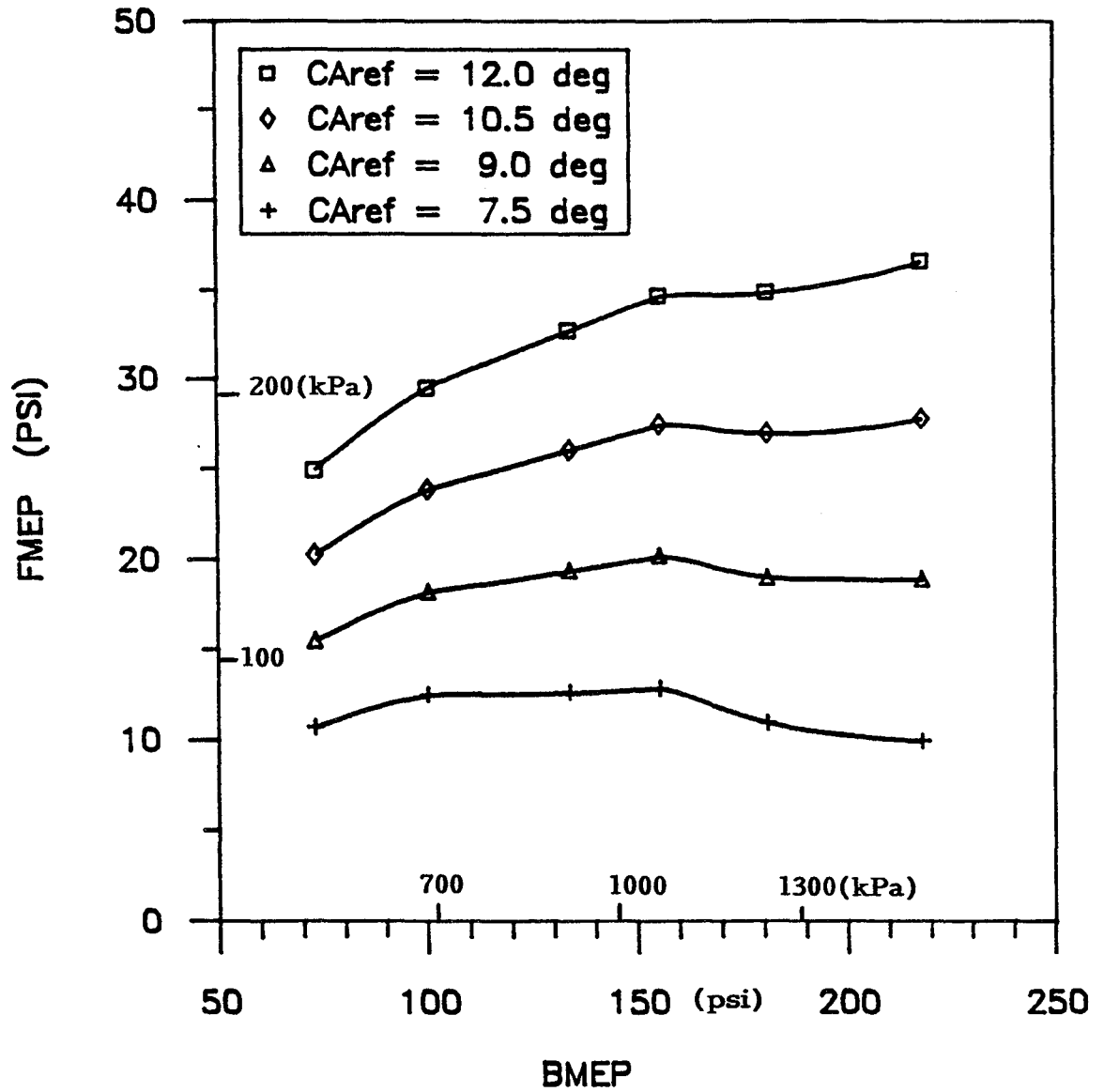


FIGURE 2

VARIABILITY OF FMEP WITH TDC POSITION

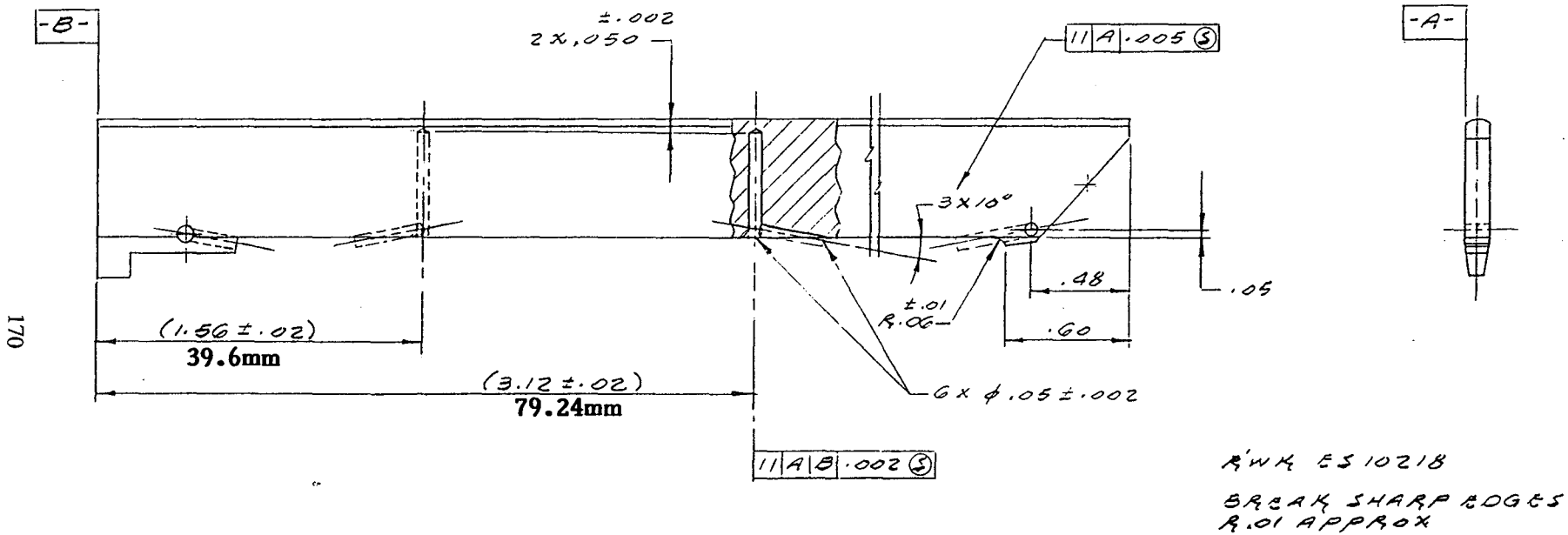


FIGURE 3

APEX SEAL THERMOCOUPLE LOCATION

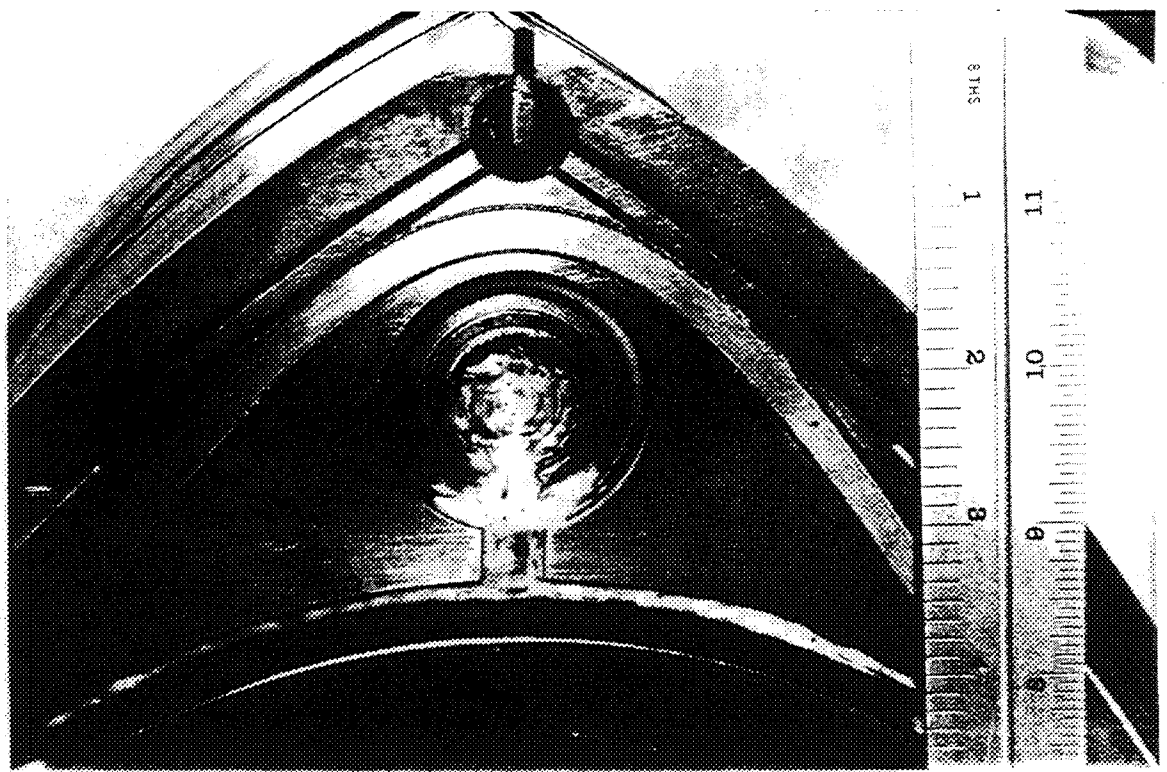


FIGURE 4
SIGNAL CONDITIONING
MODULE, INSTALLED

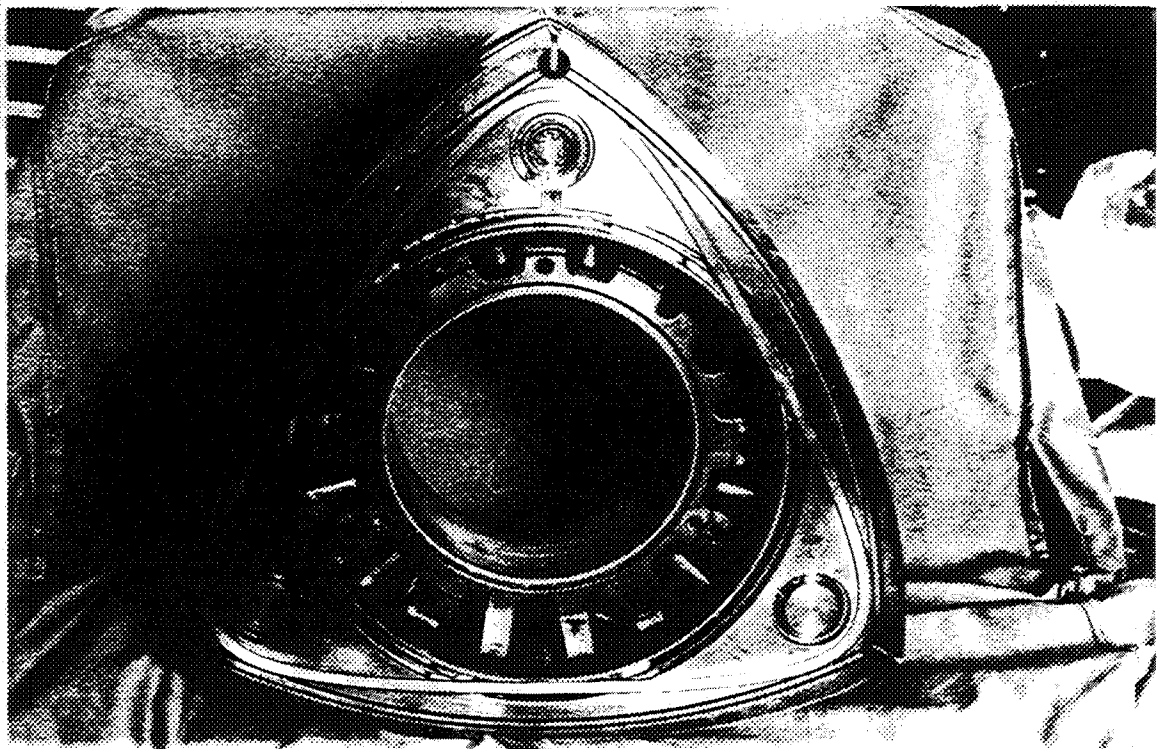


FIGURE 4
ROTOR INSTRUMENTATION

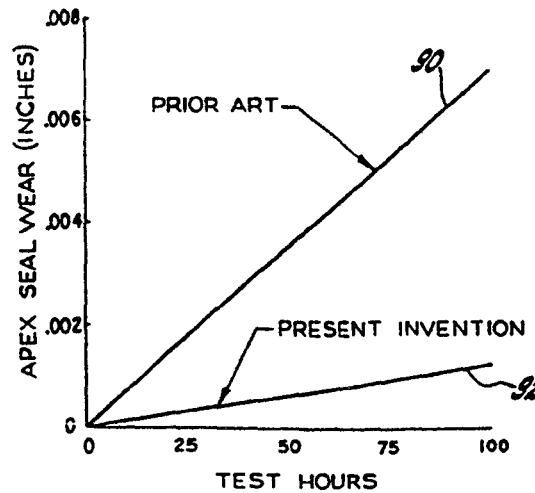
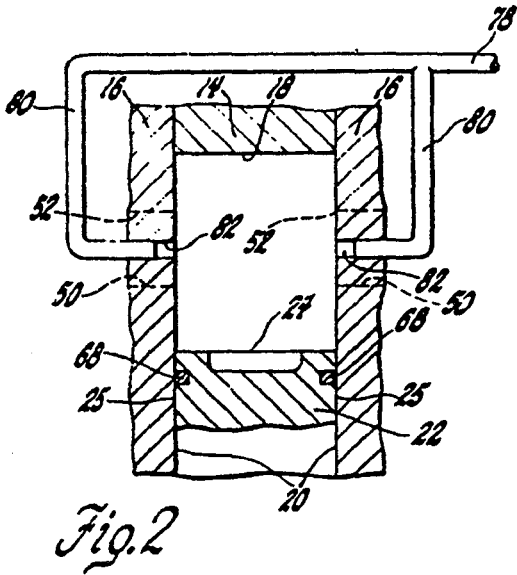
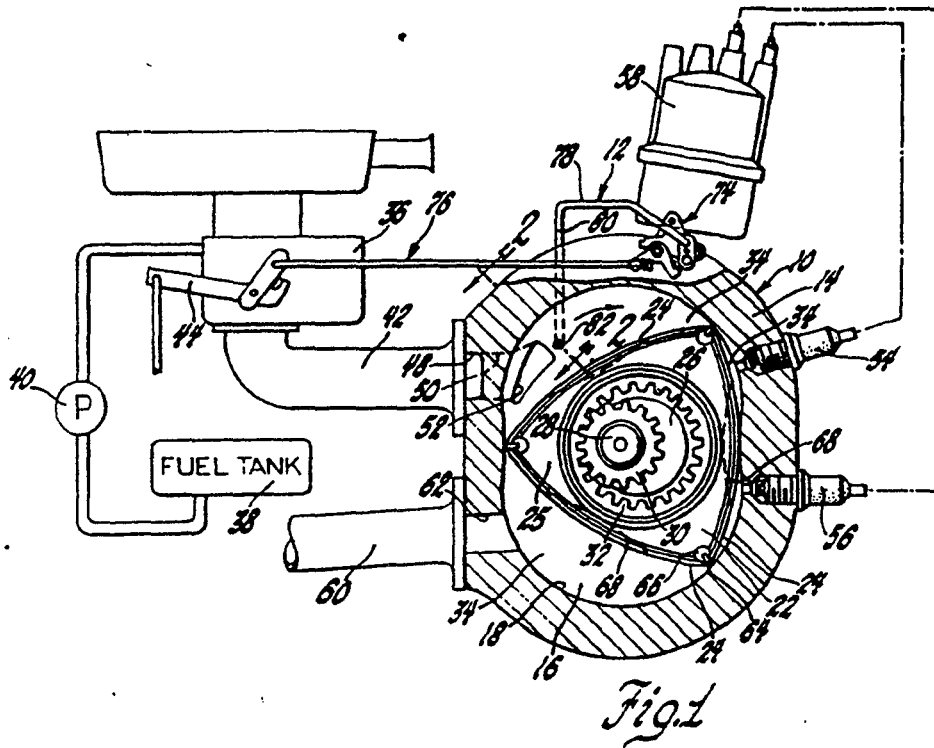


Fig. 3

FIGURE 5

END HOUSING OIL INTRODUCTION LOCATION:
Reference General Motors Patent # 3,814,555

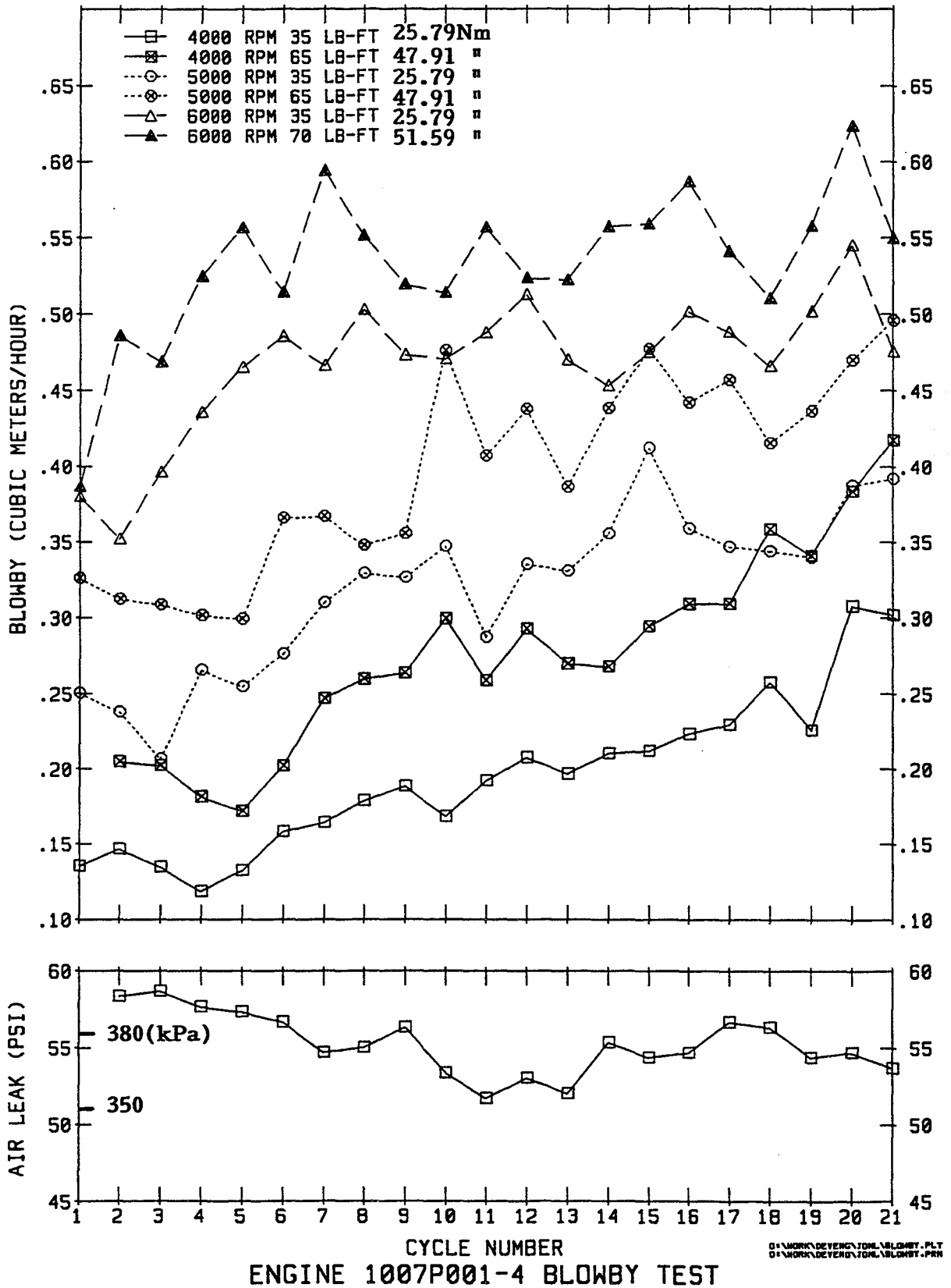




FIGURE 7

ROTOR DEPOSITS - BLOWBY TESTS

FRICTION MEP VERSUS BRAKE MEP

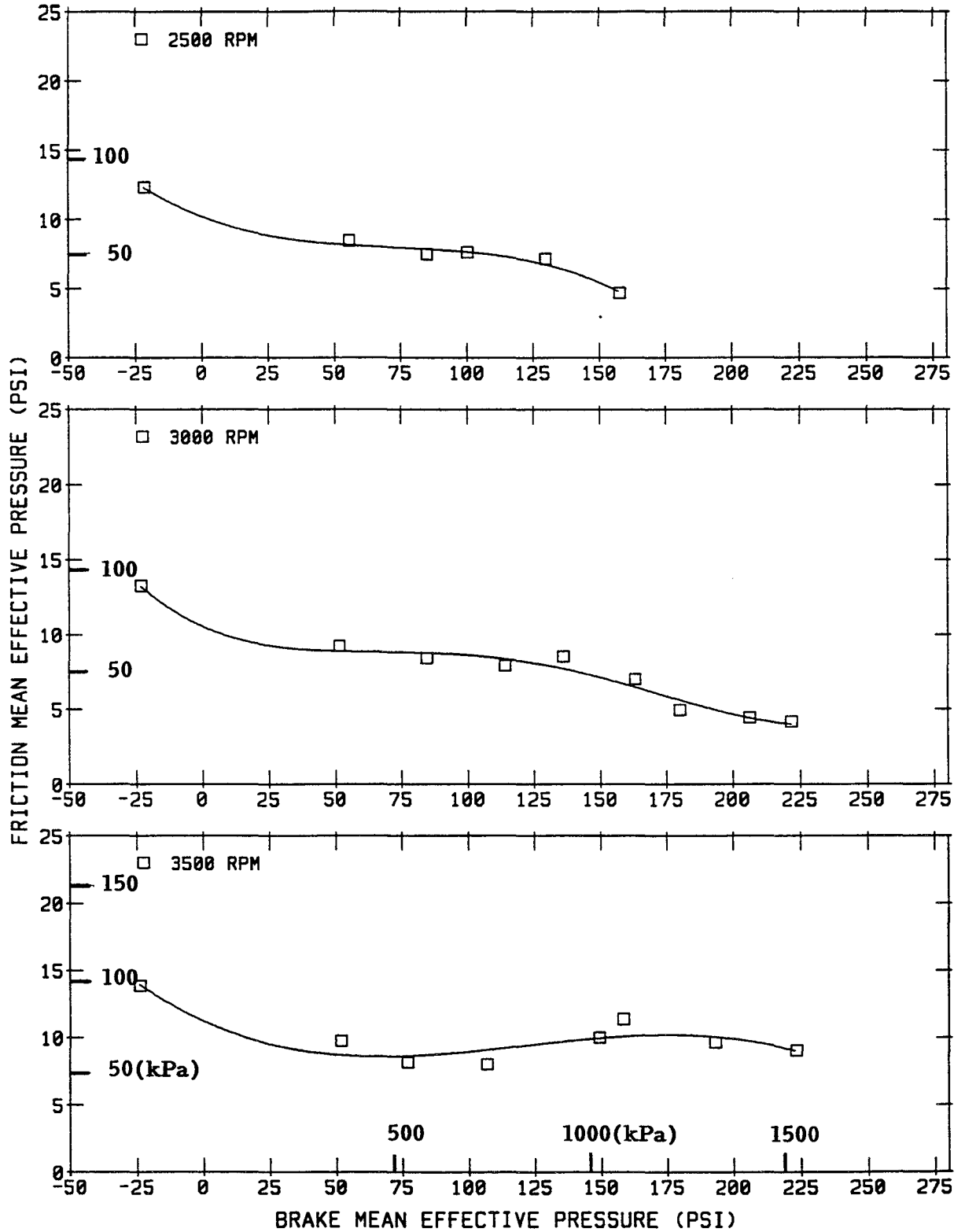


FIGURE 8

FRICTION MEP VERSUS BRAKE MEP

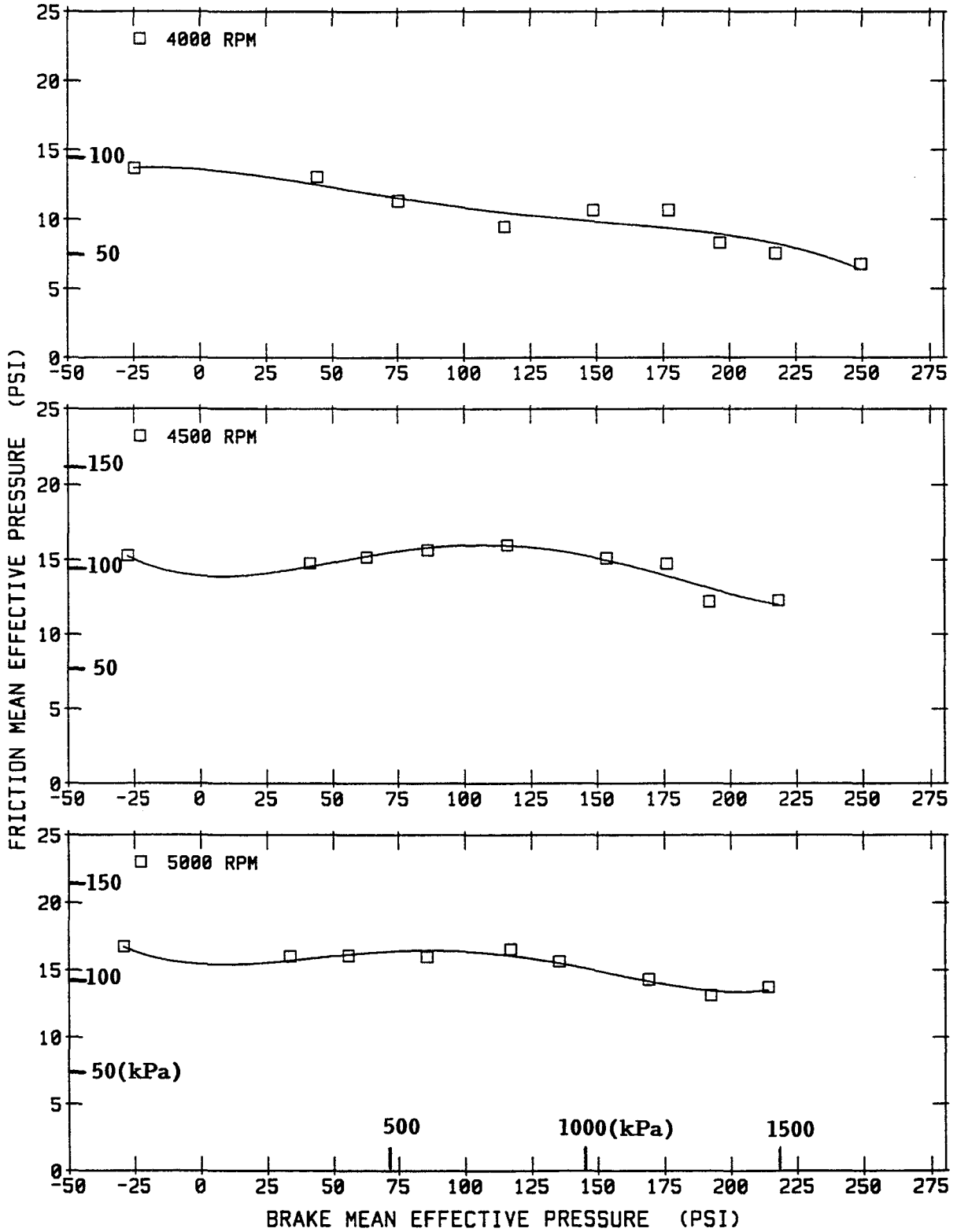


FIGURE 9

FRICTION MEP VERSUS BRAKE MEP

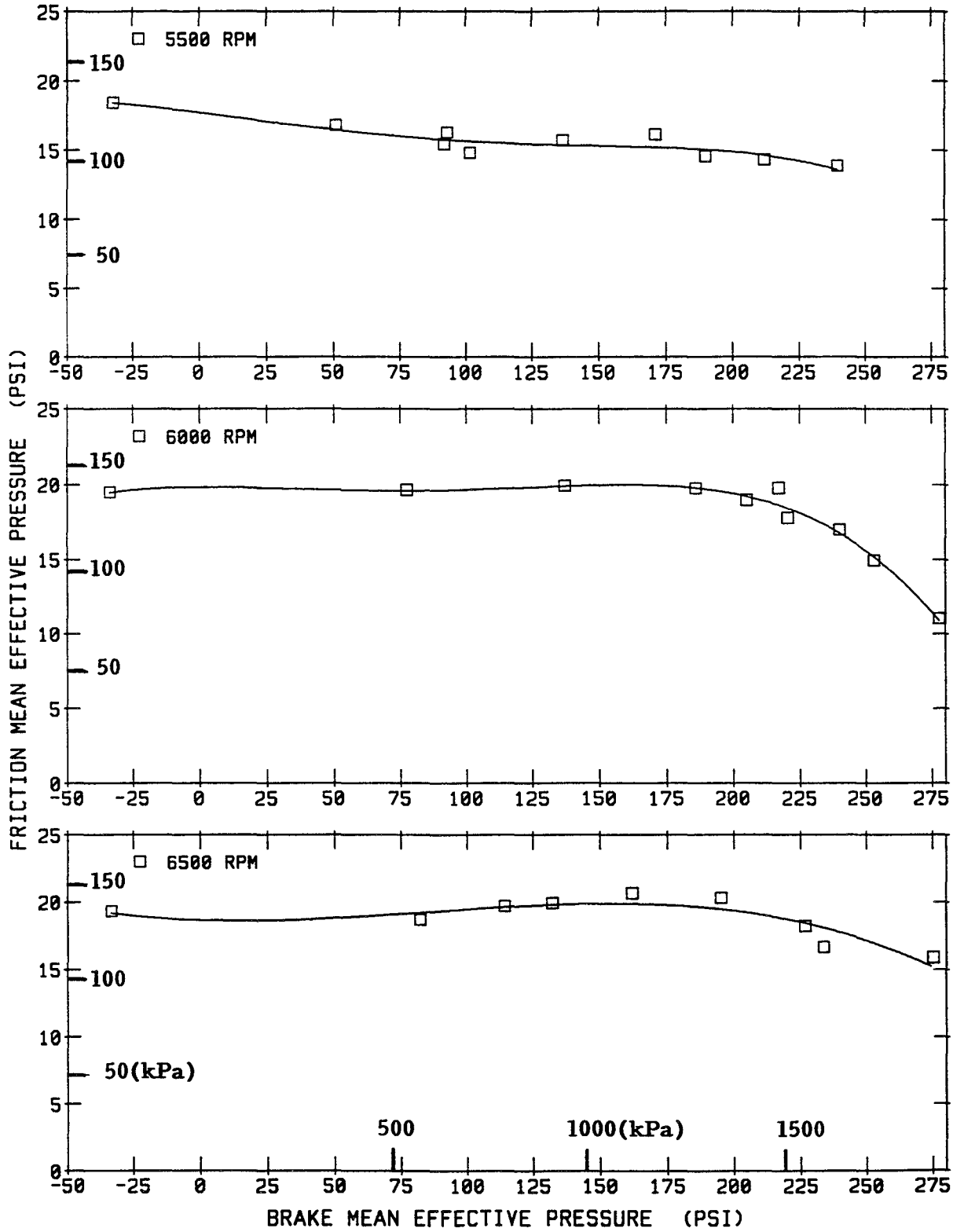


FIGURE 10

APEX SEAL TEMPERATURE AT 2400 RPM

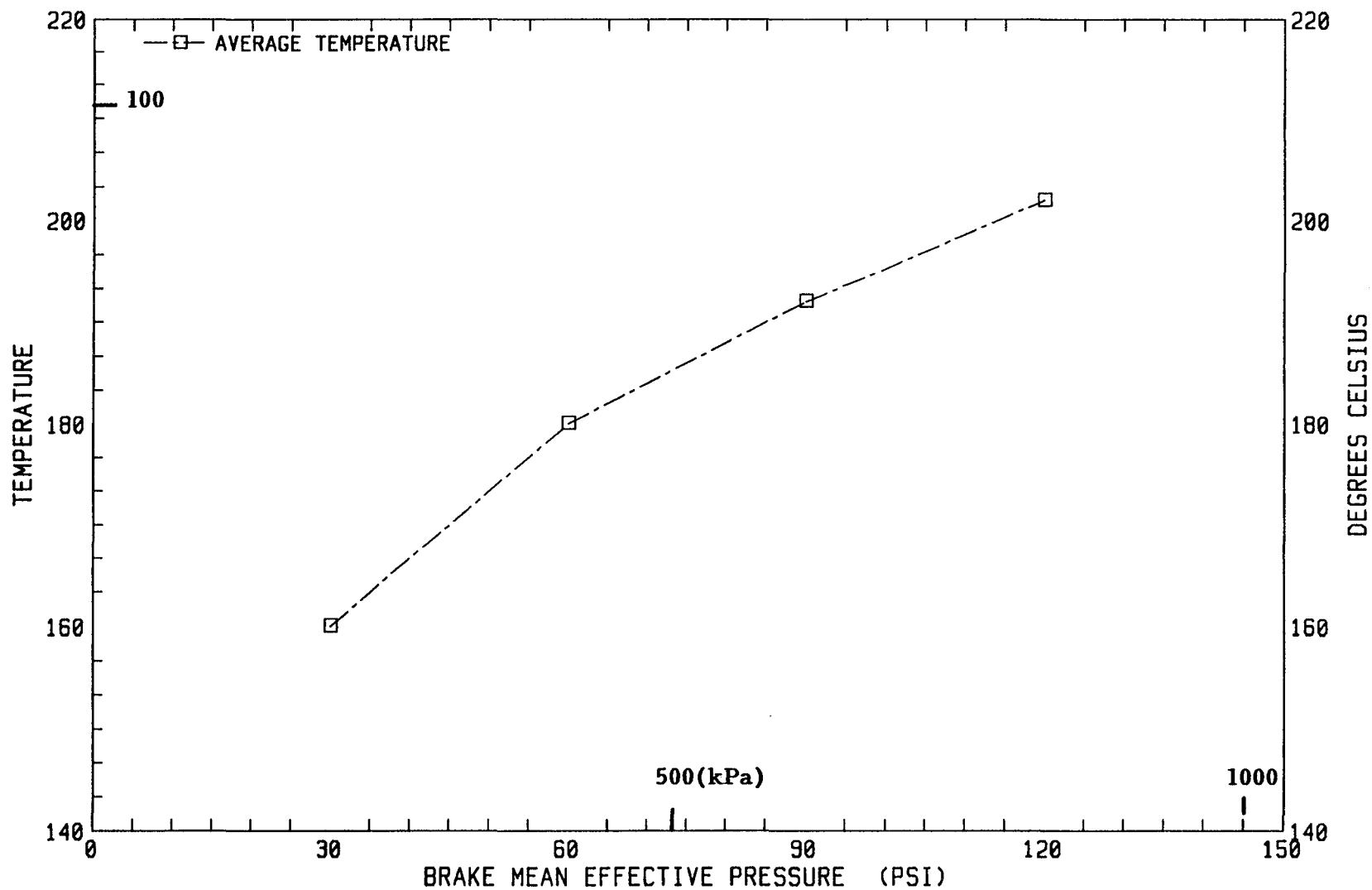


FIGURE 11

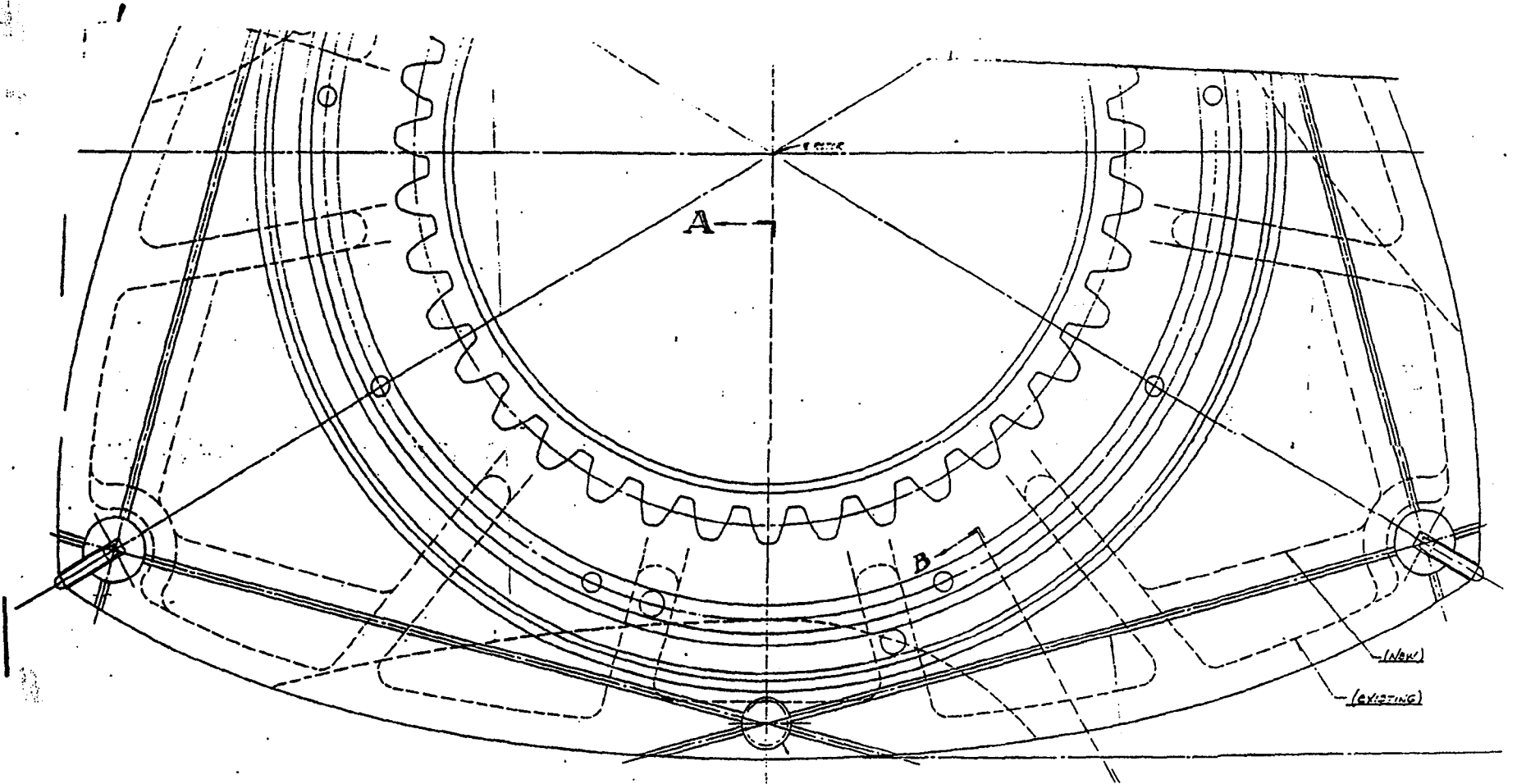


FIGURE 12

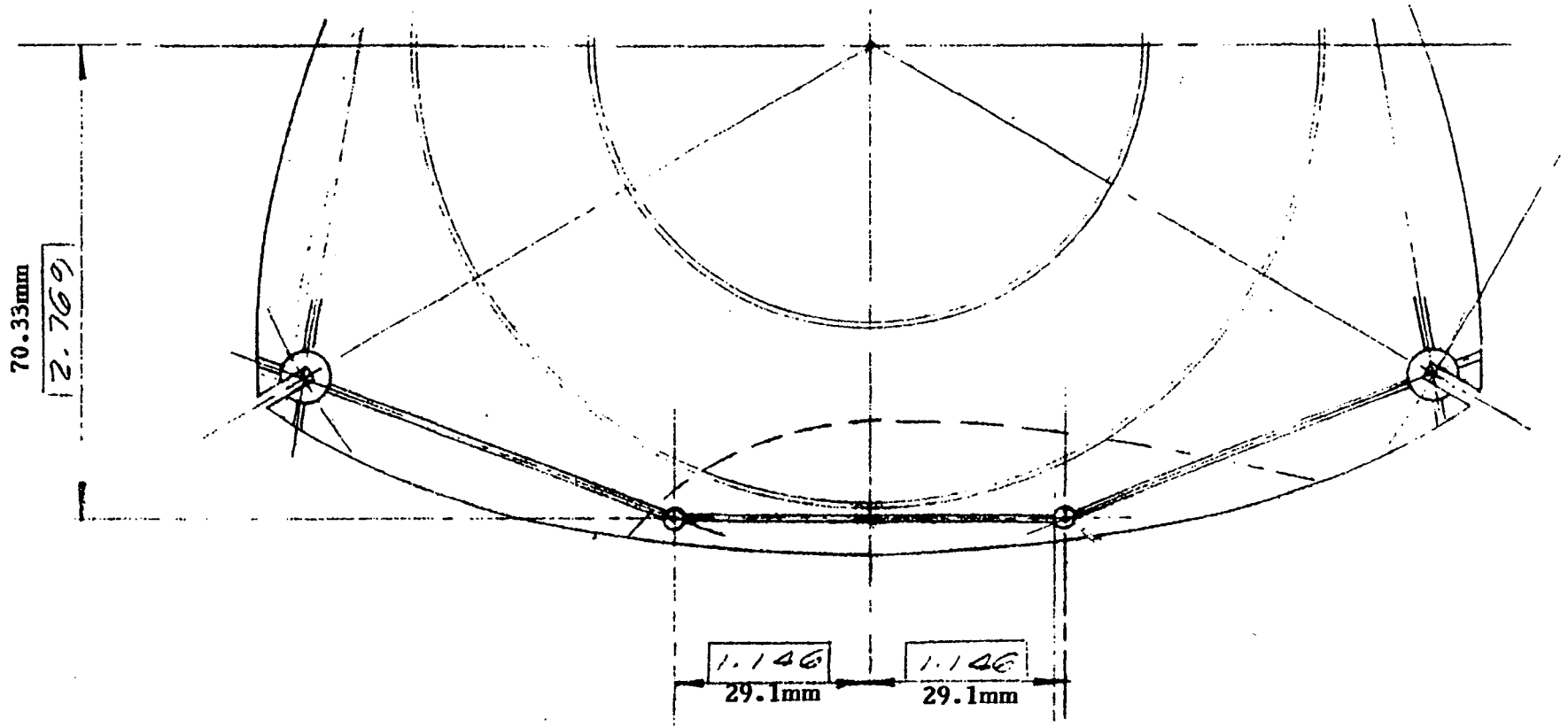


FIGURE 13

THREE-PIECE STRAIGHT SIDE SEALS

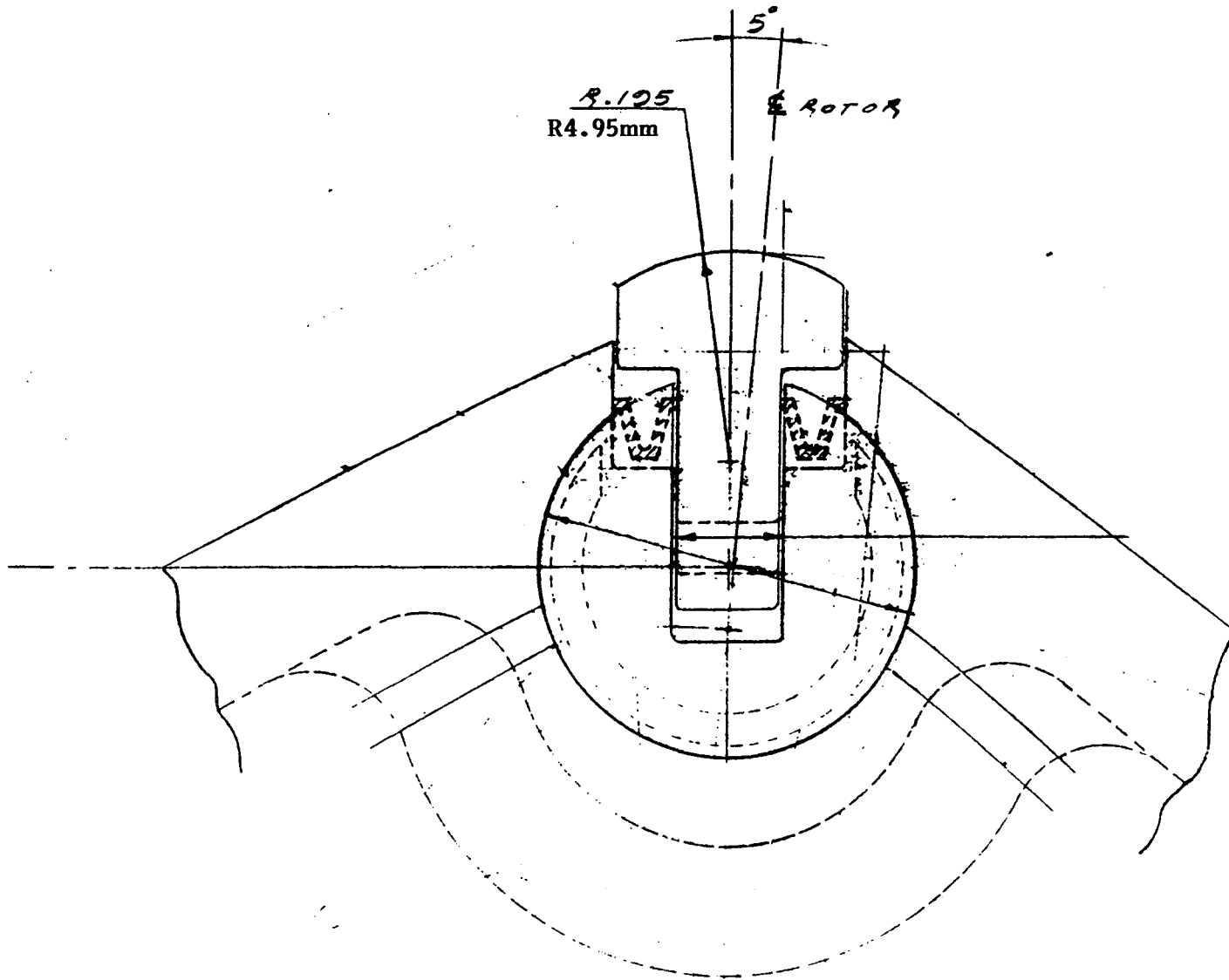
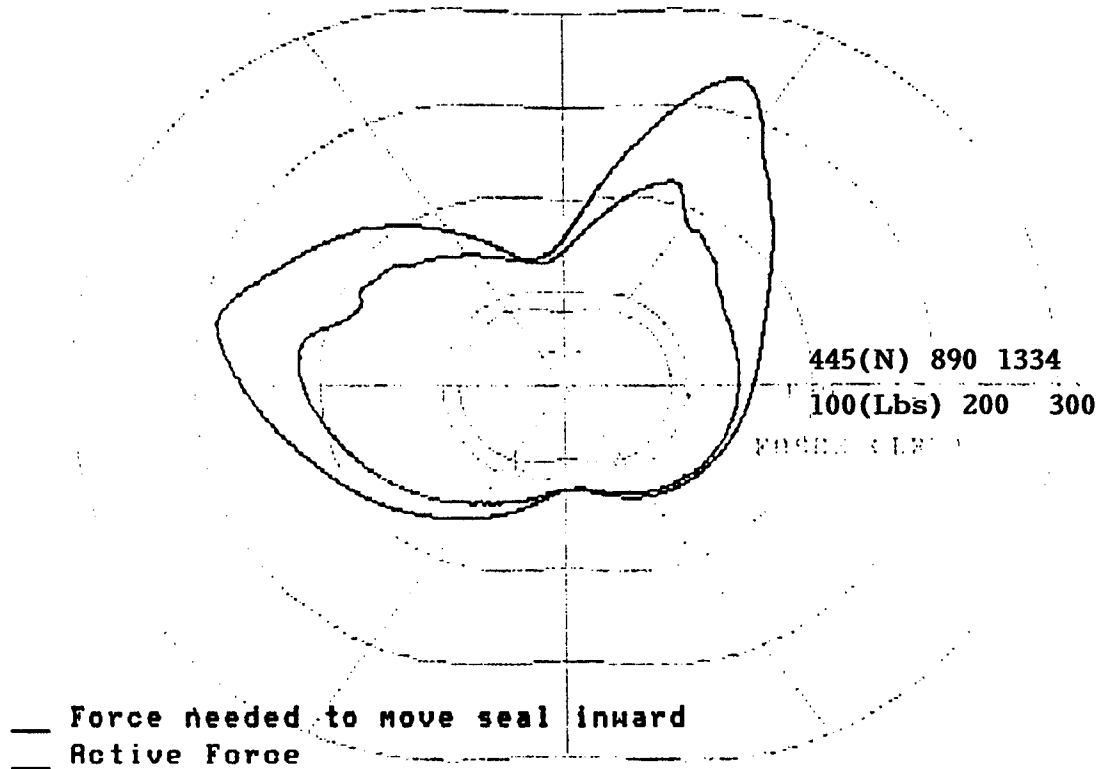


FIGURE 14

MUSHROOM SEAL WITH SECONDARY ELEMENTS

No Auto Scale

HOUSING FORCE NEEDED TO MOVE SEAL
RUN NUMBER =7JL16



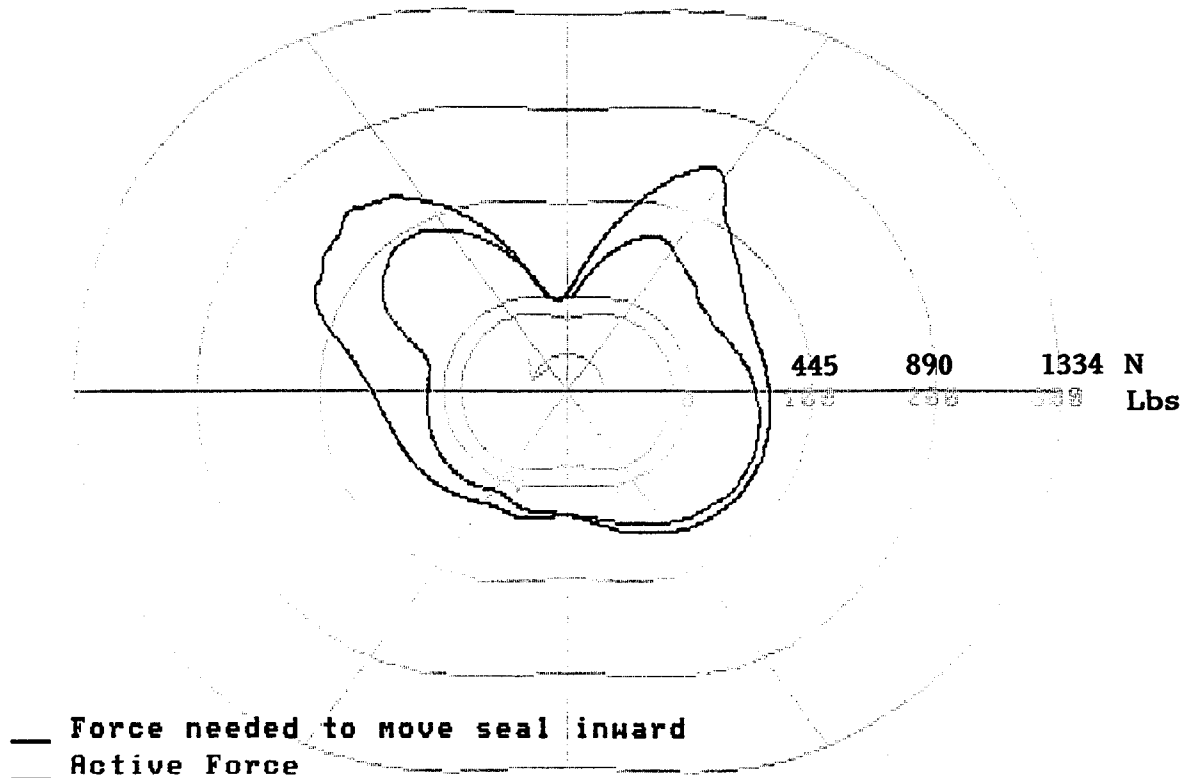
STD CONFIG, 160HP IND CRD, 7800RPM
(120kW)

FIGURE 15

STANDARD SEAL CONFIGURATION:
SEAL TO TROCHOID LOADS AT 7000 RPM AND 160 BHP
(120kW)

No Auto Scale

RUN NUMBER =25Jul12



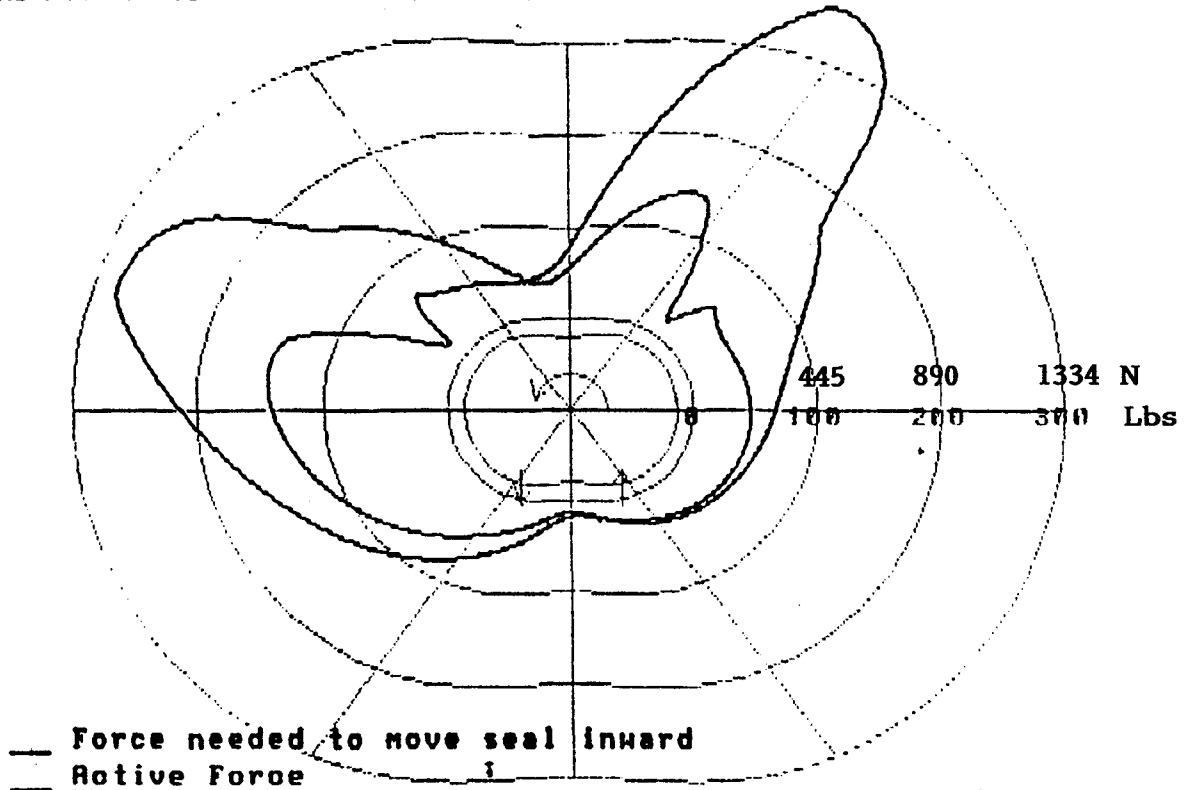
7000rpm 160hp 5deg tilt ferrotic .096 stem, .195 radius
(120kW)

FIGURE 16

**NEW MUSHROOM SEAL DESIGN:
SEAL TO TROCHOID LOADS AT 7000 RPM AND 160 BHP
(120kW)**

No Auto Scale

RUN NUMBER =70JL



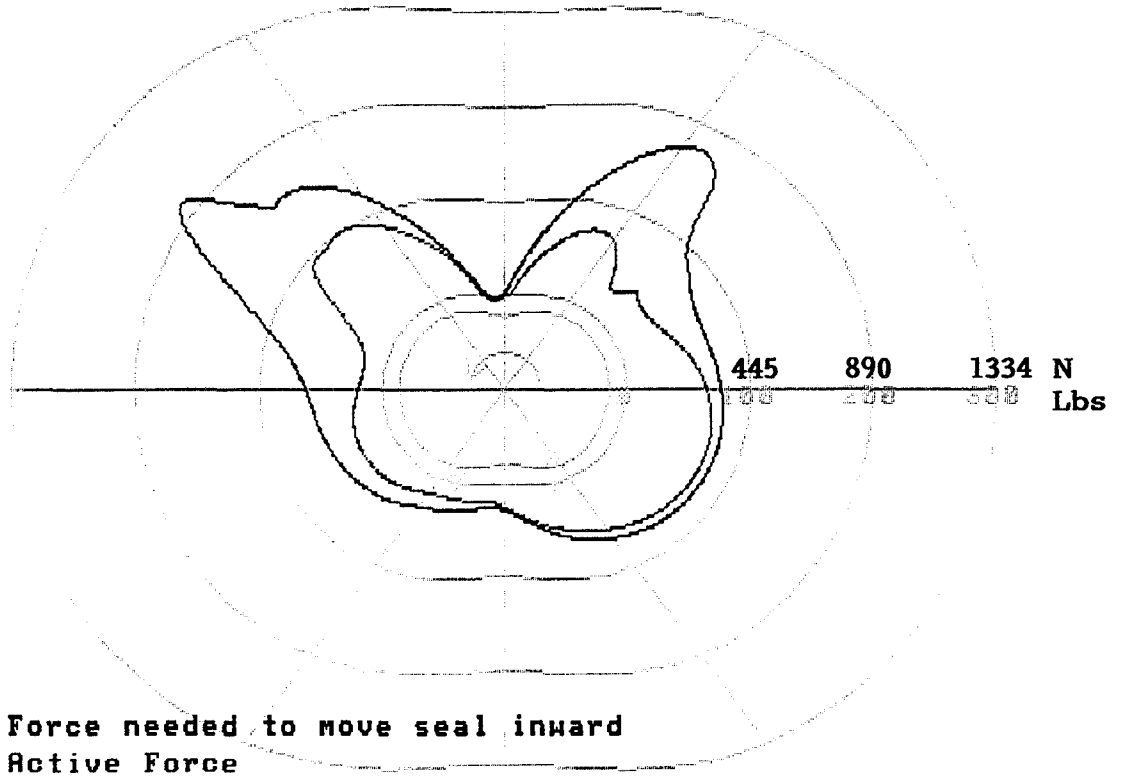
STD. CONFIG., 200HP @ 8000RPM
(150kW)

FIGURE 17

STANDARD SEAL CONFIGURATION:
SEAL TO TROCHOID LOADS AT 8000 RPM AND 200 BHP
(150kW)

No Auto Scale

RUN NUMBER =25jul1



8000rpm 200hp 5deg tilt ferrotic .096 stem, .195 radius
150kW 2.44mm 4.95mm

FIGURE 18

**NEW MUSHROOM SEAL DESIGN:
SEAL TO TROCHOID LOADS AT 8000 RPM AND 200 BHP
(150kW)**

4.3 LIGHTWEIGHT/LOW CONDUCTIVITY PARTS

PRECEDING PAGE BLANK NOT FILMED

4.3 LIGHTWEIGHT/LOW CONDUCTIVITY PARTS

INTRODUCTION

Several Lightweight/Low conductivity components for the Stratified Charge Rotary Engine were identified during the NASA Phase III sixth month program review. The Lightweight/Low Conductivity engine components, proposed for the rotary engine critical technology enablement program, were anticipated to provide improved engine performance. The components identified were:

- a. Lightweight Rotor - Titanium
- b. Composite Structural Material End Housing

Subsequently, due to the restructuring of the Phase III contract only the Lightweight Rotor was continued into final design, hardware procurement and parts readied for testing. The Composite Structural Material End Housing effort was terminated after completion of a conceptual design layout. A brief discussion of the Composite End Housing design and benefits is provided.

LIGHTWEIGHT ROTOR

OBJECTIVE

Conduct a candidate material screening study and select the best applicable material to provide the lightest rotor assembly configuration while operating at the NASA Enablement Rig Engine design conditions.

TECHNICAL APPROACH

A wide variety of rotor designs and rotor constructions were considered in selecting the best Lightweight Rotor design candidate. The search included a review of three decades of rotor design and a review of recently developed material technologies.

Primary considerations in selecting the Lightweight Rotor design were the capability to withstand the NASA rig engine design operating conditions, the potential for maximum weight reduction, and the probability of successful fabrication.

The design operating conditions anticipated for the stratified charge rotary engine are shown in Figure 1. Figure 1 is an estimated indicator card for engine operations at 160 bhp (120kw)

and 8000 rpm. The indicator card depicts a peak combustion pressure of 1110 psi (7.65 mPa) and a peak combustion chamber temperature of 3500° R (1671° C).

Candidate rotor materials and design configurations which were considered are listed in Figure 2.

Selection of the most promising Lightweight Rotor candidate material and design is described in detail in JDTI Rotary Engine Division Report "Lightweight Rotor Candidate Material Screening Study" 25 March 88, NAS3-24628.

The selection report recommended a titanium material rotor as the lightest rotor configuration having a relatively high probability for successful fabrication of a prototype rotor. The report's recommendation was approved by the NASA Project Manager for design and fabrication.

Rotor design layout effort was initiated and was supported by design analysis which drew on the successful experience of JDTI Series 70 engine rotor design, analysis, fabrication and test experience. Finite element stress analysis utilizing ANSYS method code was employed to examine temperature distributions, resulting thermal stresses, inertial loading, and pressure loading. The maximum stress range throughout the rotor structure was determined for all rotor positions and predicted engine operating conditions. Design considerations included rotor fabrication, assembly, bearing retention, and thermal conductivity amongst others.

RESULTS

The Lightweight Rotor design effort resulted in the release of detail design drawings for a Titanium Rotor. The following drawings describe the complete rotor design:

<u>TITLE</u>	<u>DRAWING NO.</u>
Rotor & Bearing Assembly, ADE	NR10252
Rotor, Titanium, Gear & Adapter Assembly, ADE	NR10251
Rotor, Titanium, ADE	NJ12479
Rotor & Bearing Assembly, DE	NR10447
Rotor, Titanium, Gear & Adapter Assembly, DE	NR10446
Rotor, Titanium, DE	NJ12870

As discussed in Section V of the referenced report, the Howmet Ti-Cast Division was selected to provide investment rotor castings. The casting material selection was titanium 6-2-4-2 (Ti-6Al-2Sn-4Zr-2Mo). This decision was based on additional material studies (after the screening report) that revealed the 6-2-4-2 has a higher strength/density ratio for elevated temperature applications than the titanium 6-4 material. Howmet proceeded to develop investment patterns for both ADE and DE rotor castings.

Trial machining of the cast titanium 6-2-4-2 alloy material was initiated concurrent with the rotor pattern development so that the methods of machining the rotor casting material were developed when castings became available.

Both ADE and DE rotor assemblies have been completed and are available for testing in either the NASA 1007R Enablement Rig Engine or the NASA 2013R Rig Engine.

Figure 3 illustrates the rotor assembly cross-section and major components. Also provided are actual weight savings when compared to the original 17-4PH material workhorse rotor assembly designed for the NASA 1007R Enablement Rig Engine. Figure 4 lists the advantages of lightweight rotor assemblies when incorporated into the rotary engine power section.

Figure 5 shows the rotor casting and completed rotor assembly. The surface of the casting is the final chemical-milled surface. The completed rotor assembly includes the bolted-in rotor gear and oil seal adapter (not visible).

An additional benefit of the titanium Rotor design is the low thermal conductivity of the titanium. The thermal conductivity of the titanium 6-2-4-2 material is only 30% of the thermal conductivity of the 17-4PH material. The selection of titanium as the rotor material provides a means to examine reduction of heat transfer to the rotor cooling oil.

The titanium 6-2-4-2 material has several drawbacks which must be taken into account. The investment castings of titanium are expensive, and the as-cast parts require chemical milling. The chemical milling is required to remove an approximate 0.030 inch (0.762mm) thick case of alpha-phase titanium to ensure the desired metallurgical properties are obtained. Titanium is difficult to machine. The titanium rotors also require NiBron plating of the apex seal slots and rotor gear mating surfaces to prevent galling.

COMPOSITE DRIVE END HOUSING

Restructuring of the NASA Phase III contract eliminated the final design, hardware procurement and testing of the composite drive end housing. Figure 6 illustrates the end housing conceptual design configuration and Figure 7 presents comparative material data. An approximate 27% weight saving was estimated for this lightweight end housing design.

CONCLUSIONS

1. A lightweight, Titanium 6-2-4-2, Rotor has been successfully designed, investment cast and machined to provide finished rotor assemblies ready for engine testing. The Titanium 6-2-4-2 rotor provided a 35% rotor assembly weight reduction relative to the 17-4PH stainless steel rotor previously used.
2. Composite construction methods for the rotary engine End Housing application may provide substantial weight savings.

RECOMMENDATIONS

Engine test the titanium rotor assemblies to determine their performance and mechanical capabilities.

SCRC1-40T
ESTIMATED INDICATOR CARD
160BHP (120Kw)/8000RPM

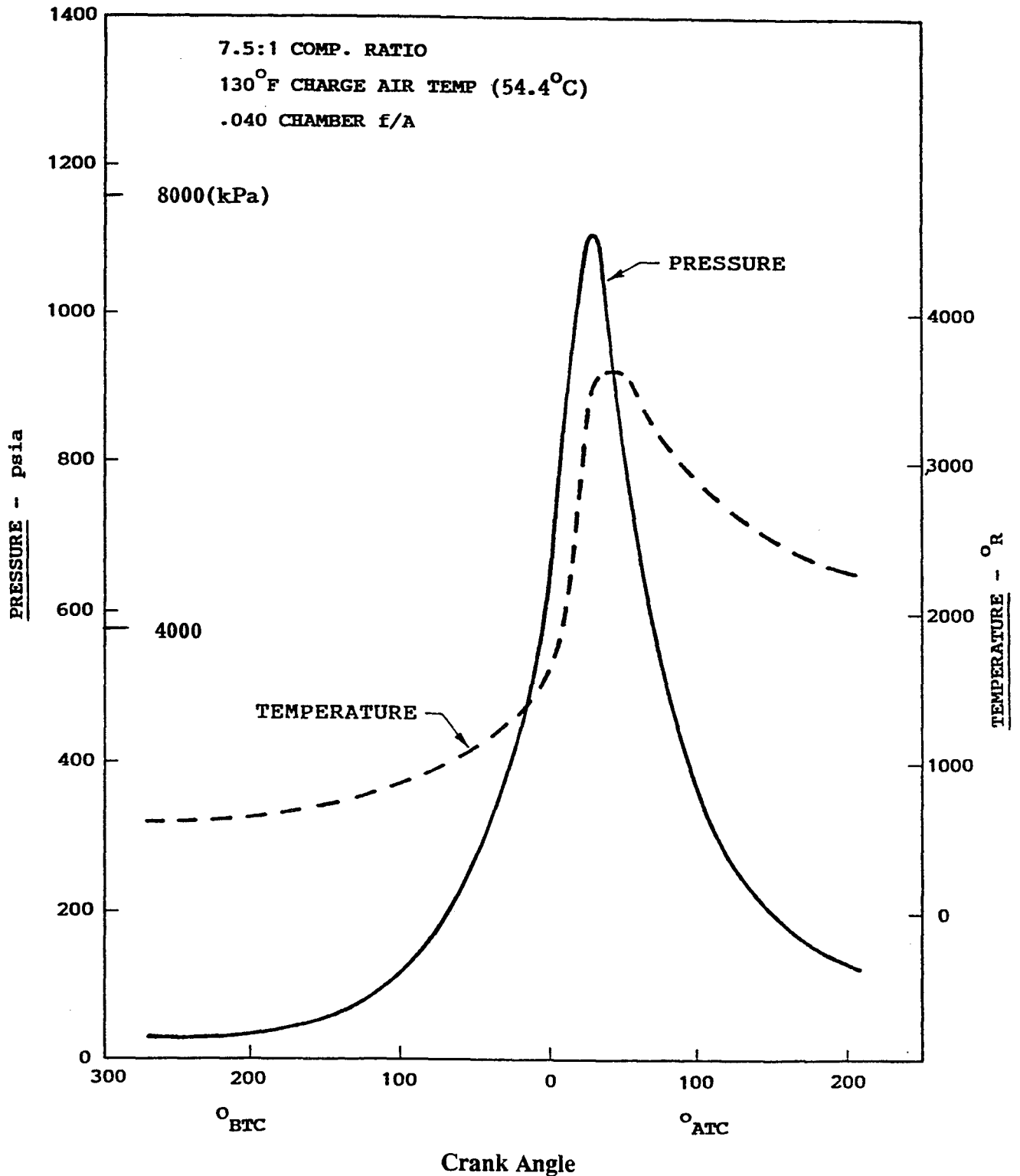


Figure No. 1

CANDIDATE MATERIALS AND CONFIGURATIONS

17-4 OPTIMIZED, (BASELINE) DETAIL, 7.7 LB (3.49kg)

INVESTMENT CAST TITANIUM 6-4

SAND CAST ALUMINUM

SQUEEZE CAST ALUMINUM

FORGED ALUMINUM (3 PIECE)

METAL MATRIX COMPOSITE

REINFORCED PLASTIC (TORLON) & METAL HOT SECTION

CERAMIC (MONOLITHIC)

THREE PIECE ROTOR

SELF BROACHING BEARING SUPPORT

SEMI-FLOATING BEARING

THERMAL BARRIER

INTEGRAL GEAR

Figure No. 2

ROTOR ASSEMBLY WEIGHT COMPARISON

**17-4PH Workhorse Rotor Weight 10.7 Lbs. (4.536kg)
Titanium Rotor Weight 7.0 Lbs. (3.175kg)**

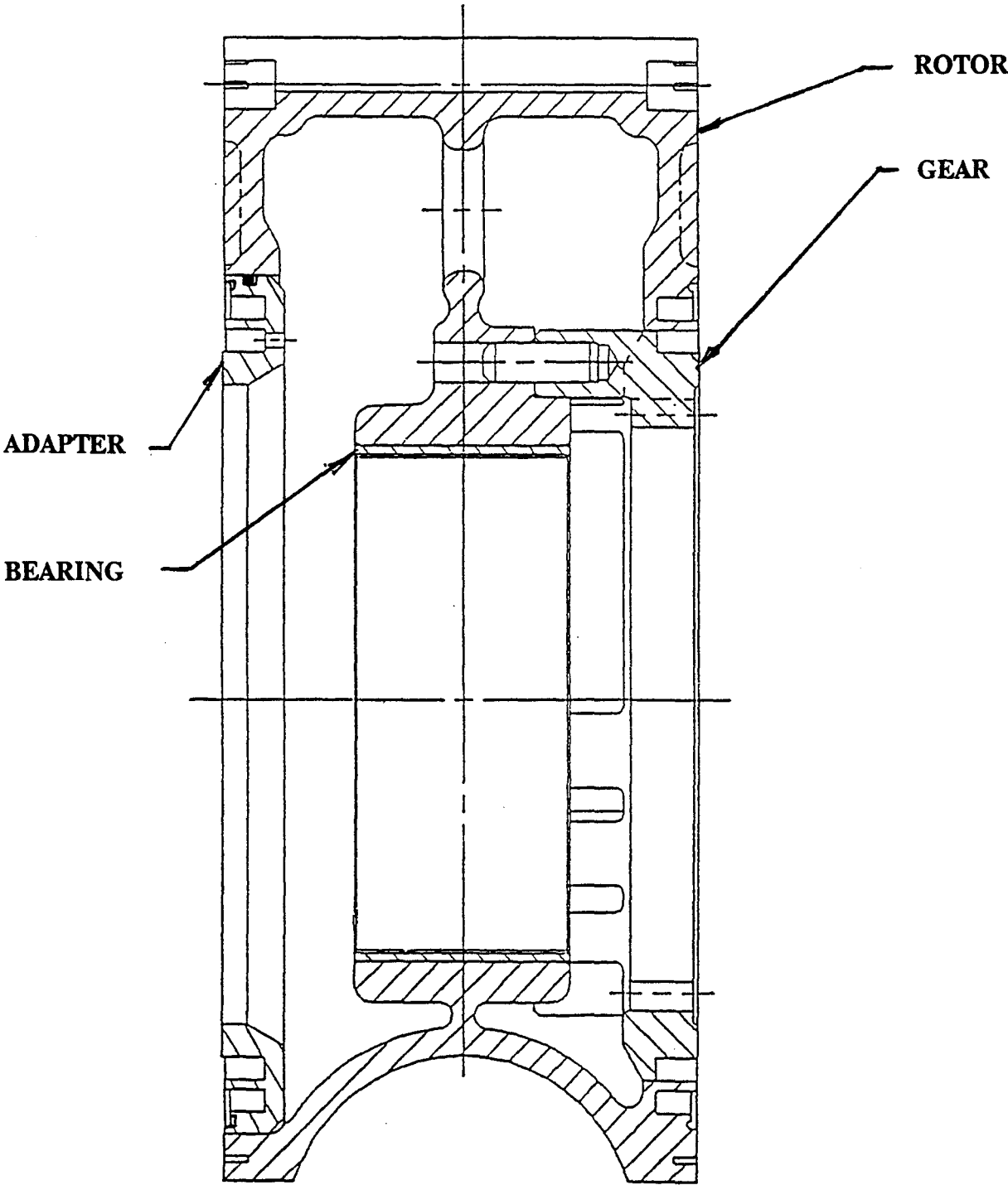


Figure No. 3

ADVANTAGES OF LIGHTWEIGHT ROTORS

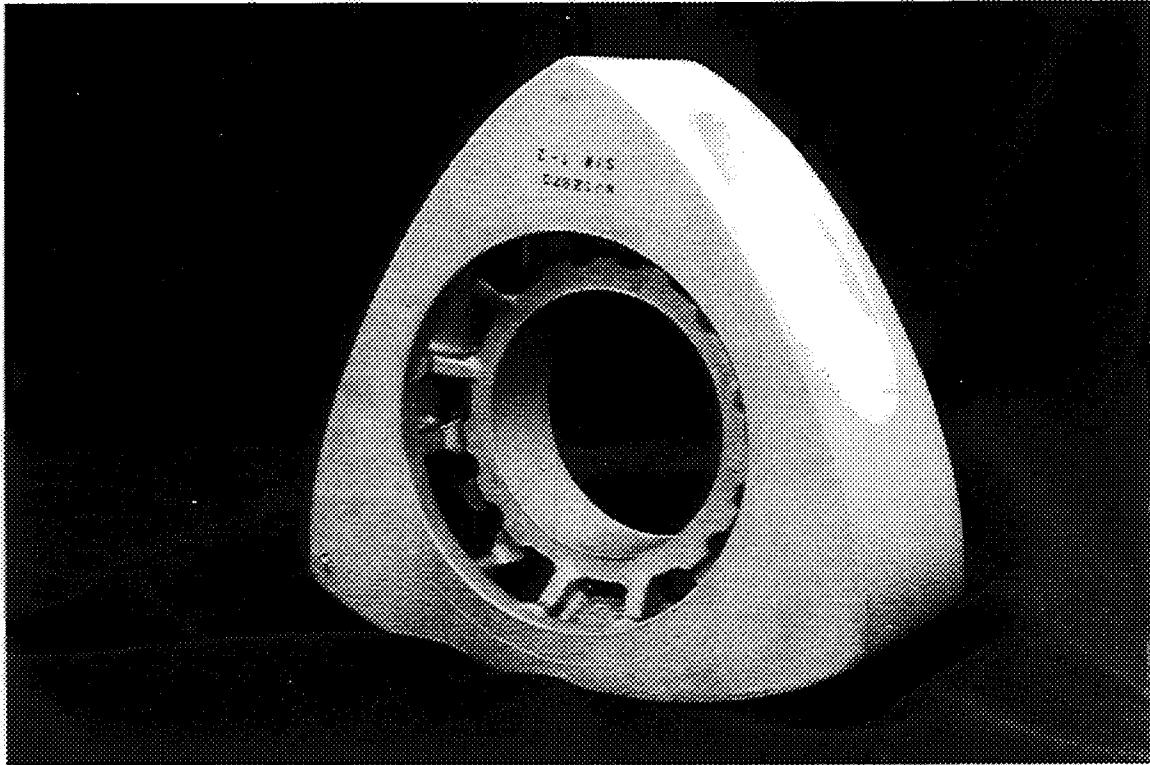
CRANKSHAFT ASSEMBLY WEIGHT SAVINGS

REDUCED CRANKSHAFT SLOPES

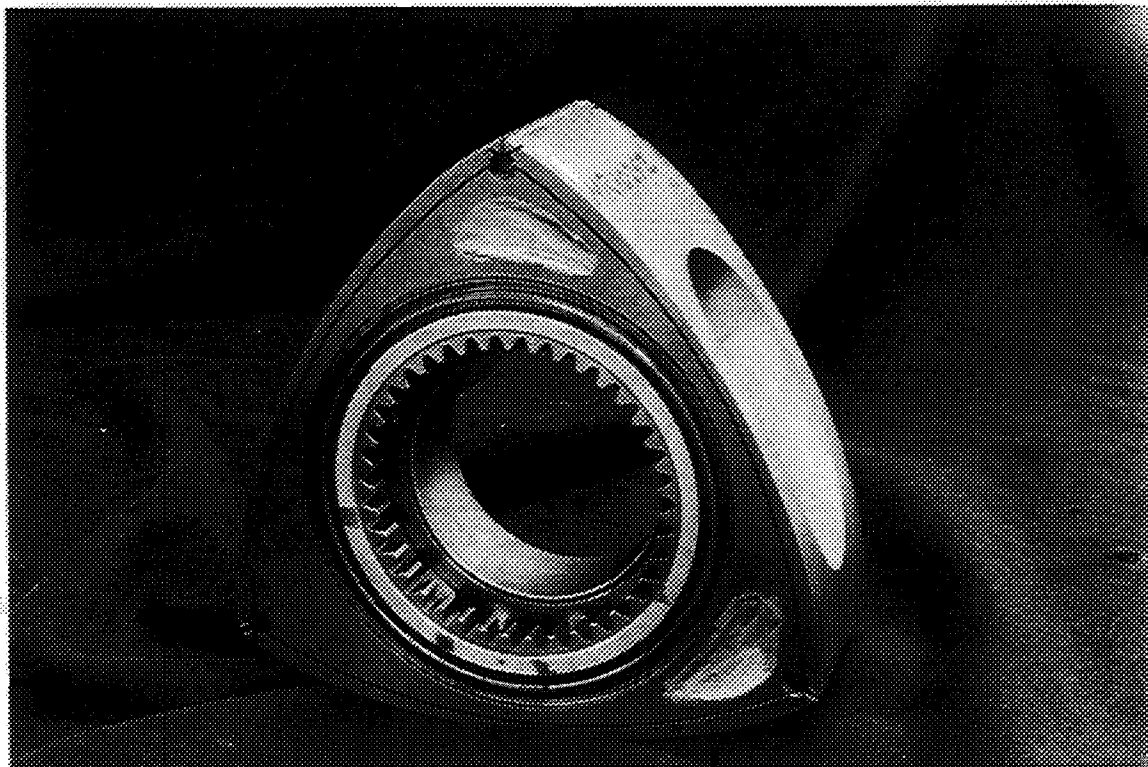
REDUCED ROTOR & MAIN BEARING LOADS

IMPROVED ENGINE ACCELERATION

Figure No. 4



TITANIUM ROTOR CASTING



ROTOR, GEAR, AND BEARING ASSEMBLY
DRAWING NUMBER NR10252
TITANIUM 6-2-4-2 ROTOR
FIGURE 5

COMPOSITE DRIVE END HOUSING

PRESENT WT. 14.4 Lbs. (6.53kg)

COMPOSITE WT. 10.5 Lbs. (4.76kg)

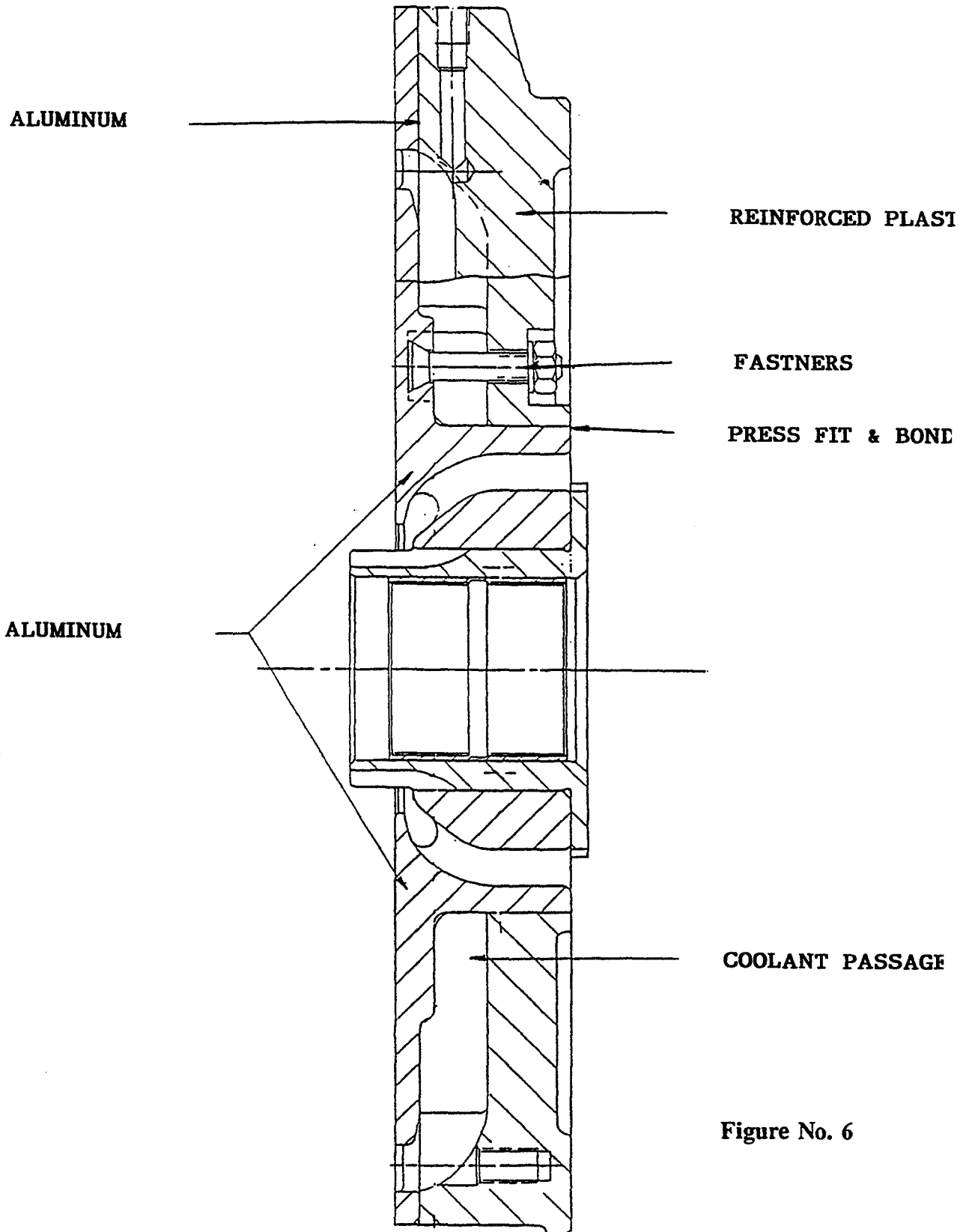


Figure No. 6

ALUMINUM - PLASTIC MATERIAL COMPARISON

MATERIAL	TENSILE STRENGTH 10³ psi(kPa)	ELONGATION %	TENSILE MODULUS 10⁶ psi(kPa)	DENSITY #/in.³ (kg/cm³)
ALUMINUM A356 - T6	38(262kPa)	5	10.3(71kPa)	0.097 (.0027kg/cm³)
REINFORCED PLASTIC TORLON 5030	32.1(221kPa)	2.3	2.1(14.47kPa)	0.058 (.0016kg/cm³)

Figure No. 7

4.4 CATALYTIC SURFACES

CATALYTIC SURFACE COMPONENT DEVELOPMENT

INTRODUCTION

One goal of the NASA Technology Enablement program is to develop new materials for major components and heat barrier coatings to reduce rotary engine heat rejection rates. A numerical goal of a 40% reduction in heat rejection from the baseline 1988 Series 70 engine was set forth in the NASA Phase III Technical Proposal. A related goal was investigating a catalytic surface coating on various combustion chamber components to enhance combustion efficiency and turn-down capability.

Engine testing of the thermal barrier coated rotor had been conducted in the NASA Phase II contract. The test used a 17-4PH stainless steel rotor coated with a .005 inch (0.127mm) thick bond coat and .025 inch (0.635mm) thick zirconia coating. Figure 1 shows the detail of the ceramic thermal barrier coating as applied by Adiabatics, Inc. The barrier was intended to reduce heat transfer through the rotor to the engine oil, and to increase rotor surface temperatures for increased engine operating efficiency.

Engine performance data comparing the thermal barrier rotor installed in Engine 0704 -3, and a conventional 17-4PH uninsulated rotor installed in Engine 0704-1, are provided in Figures 2 and 3. Figure 2 shows that less than a 2% difference in observed Brake Specific Fuel Consumption (BSFC) was noted between the two builds of the engine. The BSFC performance data was taken at 5500 RPM using the N41 (4x0.009 inch (0.229mm) orifice) main nozzle. Figure 3 compares the heat rejection to the oil of the same two engines at 4400 RPM. At loads up to 133 psi (916 kPa) BMEP the oil heat rejection for Engine 0704-1 (standard rotor) was higher than for Engine 0704-3 (thermal barrier rotor). However, at high load (approximately 148 psi (1019 kPa) BMEP) the oil heat rejection of Engine 0704-3 was 5% higher than for 0704-1. This reversal in trend is not well understood, but is attributed to factors other than the thermal barrier coating. The increased oil flow is attributed to the increased bearing clearance of Engine 0704-3.

No reduction in engine BSFC or heat rejection to the engine oil was believed to be attributable to the thermal barrier coating applied to the rotor. Further testing of the thermal barrier coating was pursued in the Phase III Contract in conjunction with evaluation of the catalytic surface rotor.

OBJECTIVE

To establish the potential for catalytic surfaces to improve combustion rates and to improve engine operating efficiencies. The investigation will test the effect of introducing a catalytic surface into the combustion chamber. The investigation is a cooperative effort with Precision Combustion, Inc. (PCI).

TECHNICAL APPROACH

Testing of the catalytic surface concept consisted of engine testing catalyst coated components and examining changes in engine fuel consumption performance and exhaust emissions.

To determine the effect of catalytic surfaces the thermal barrier coated rotor from Engine 0704-3 was coated with a catalyst and rebuilt as engine 0705-2. The catalytic coating was applied to the rotor flank and rotor pocket surfaces over the thermal barrier coating.

The catalytic coating is intended to promote combustion of fuel in close proximity to the rotor face and pocket. The catalytic coating, by promoting the oxidation process, is intended to reduce fuel ignition delay and to promote combustion stability at lower temperatures than would be required for non-catalytic surfaces. The catalytic coating is a proprietary coating developed and applied by Precision Combustion (reference SAE paper 890326).

RESULTS

Engine performance testing of the catalytic coated, thermal barrier rotor was conducted in the NASA enablement single rotor rig engine 0705-2. Comparison to the performance of engine 0704-3, which tested the thermal barrier rotor previously, revealed no significant change to the engine fuel consumption. Comparisons of the fuel flow versus the engine load for the two engines are provided in Figures 4 and 5. The fuel consumption of the two engines was nearly identical throughout the load range tested at engine speeds of 4000 and 6000 RPM.

Differences in turbine inlet and turbine outlet temperatures and exhaust energy were apparent for the two engines 0704-3 and 0705-2, as shown in Figure 6. The catalytic surface rotor engine 0705-2 featured an exhaust port enlarged by 18% relative to engine 0704-3. The differences in turbine inlet temperature observed are believed to be attributable to this engine configuration change. No effect on engine BSFC is attributed to the enlarged exhaust port.

Overall, no significant change in engine fuel consumption performance is believed to be attributable to the catalytic rotor surfaces.

Exhaust emissions were measured for Engine 0705-2 with the catalytic surface rotor. However, due to problems with the exhaust gas sampling system, the emission data obtained are believed to be invalid. The emissions-based calculations for air-to-fuel ratios were twice the observed values. The exhaust sampling probe was found to be plugged with carbon which suggests that the exhaust sample was diluted with air.

CONCLUSIONS

Application of the catalytic coating to the rotor flank and pocket did not measurably change the fuel efficiency of the rotary engine. No conclusion regarding the catalytic coatings' effect on exhaust emissions can be reached due to the test difficulties encountered.

RECOMMENDATIONS

Consider applying the catalyst coating to a rotor which would provide a higher surface temperature. Candidate designs for providing higher surface temperatures include the titanium rotor and/or a thicker thermal barrier on the rotor surfaces.

ROTOR WITH THERMAL BARRIER COATING

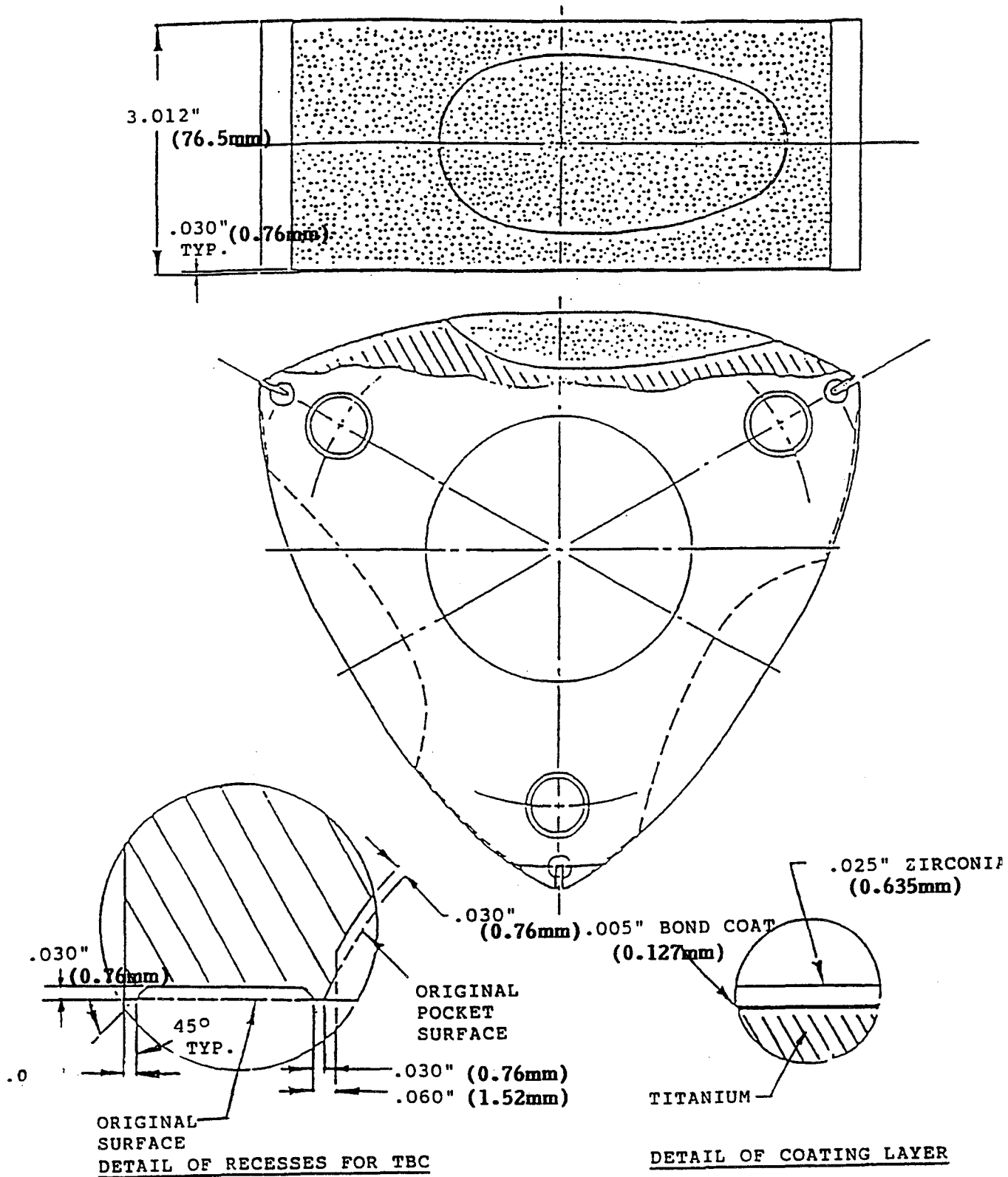


Figure No. 1

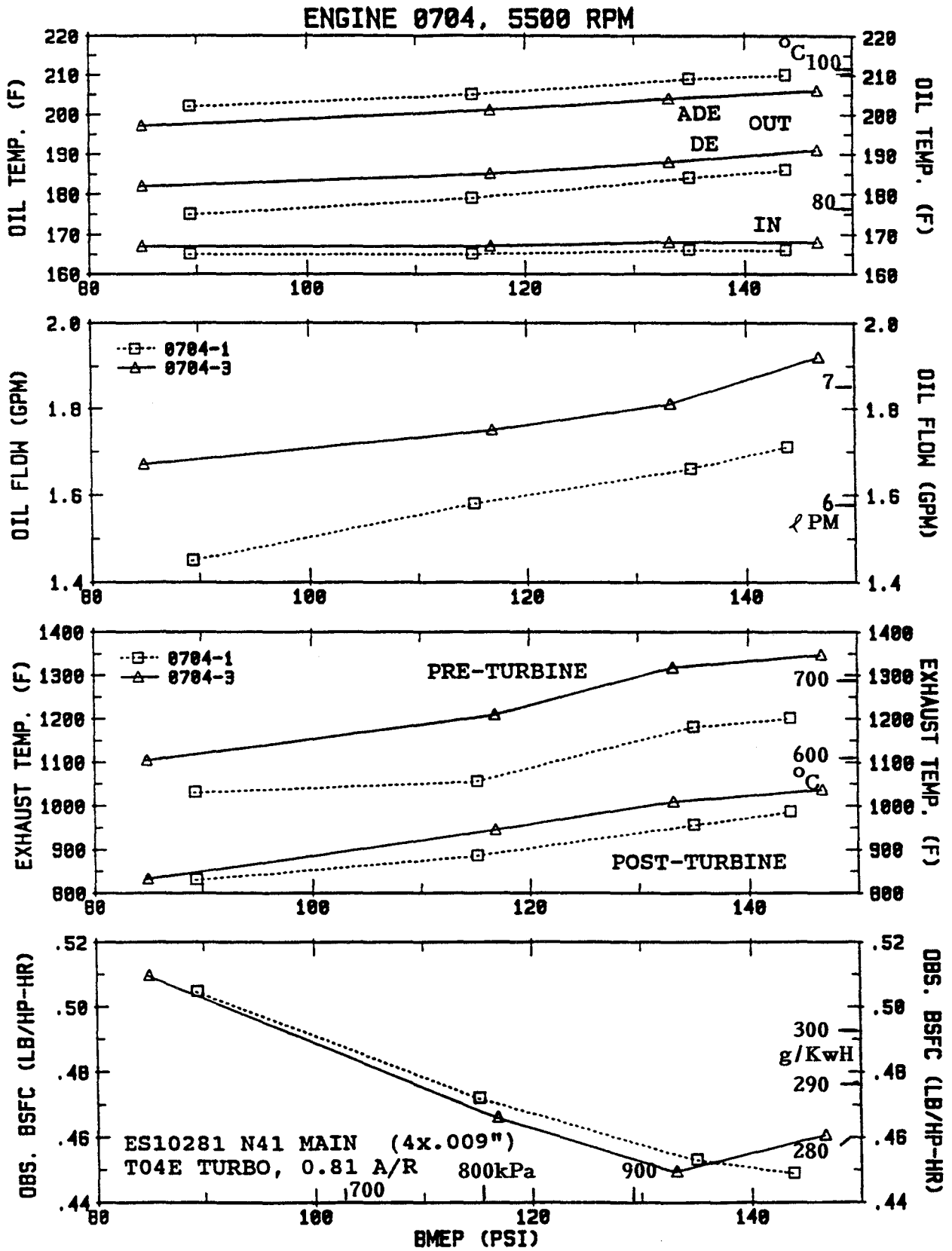


Figure No. 2

ENGINE PERFORMANCE

ENGINE 0704, 4400 RPM
ES10281N41 MAIN (4x.009")

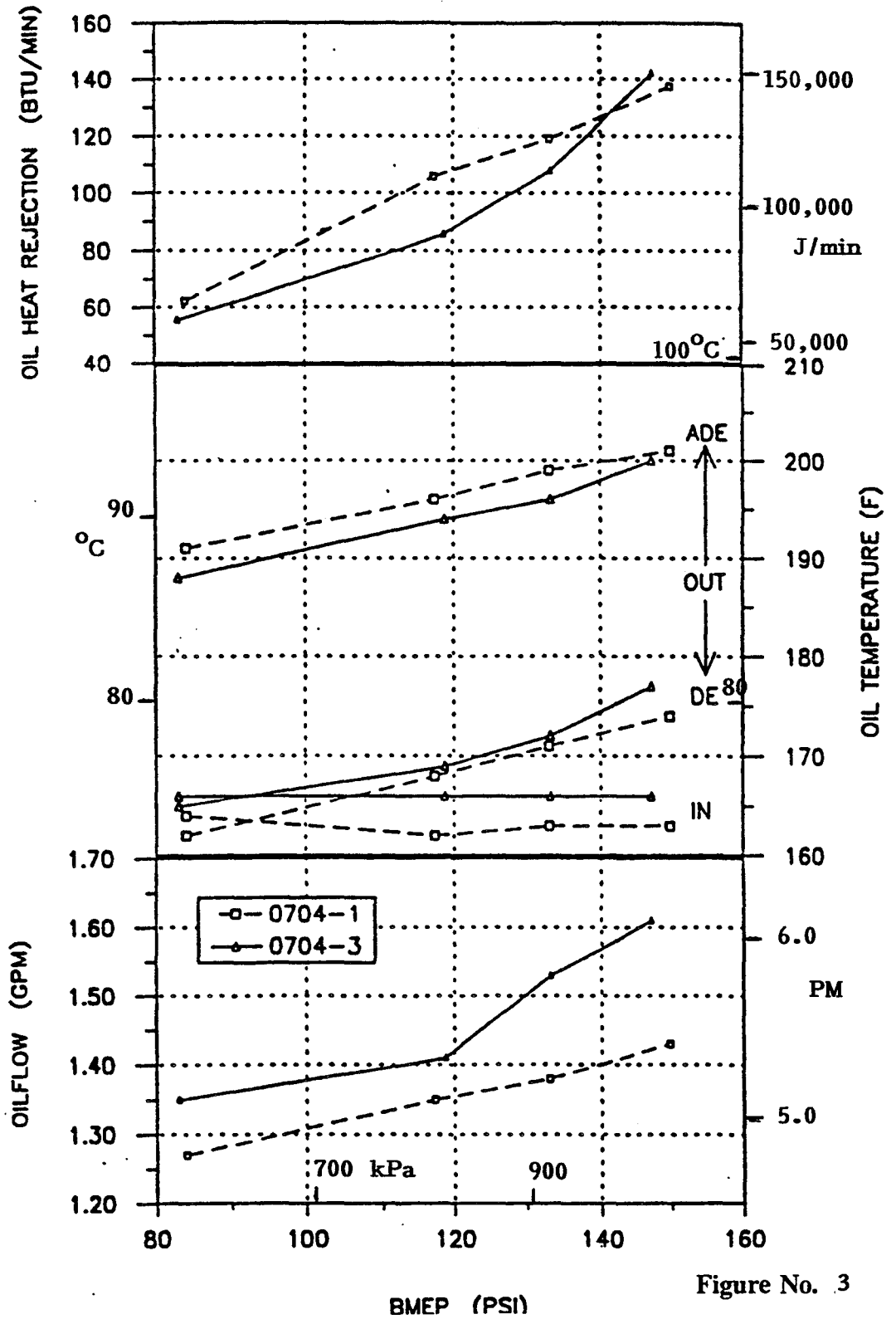


Figure No. 3

Fuel Flow Comparison

4000RPM

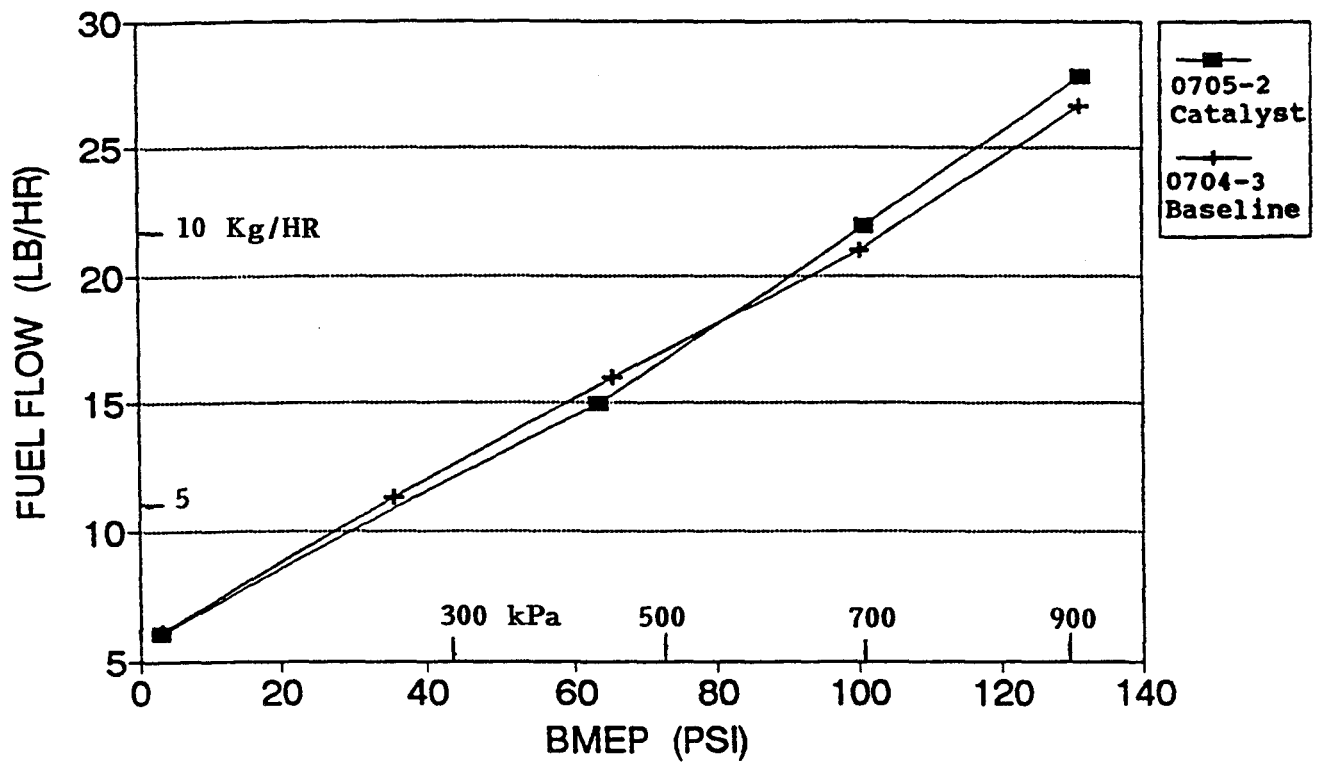


Figure No. 4

Fuel Flow Comparison

6000 RPM

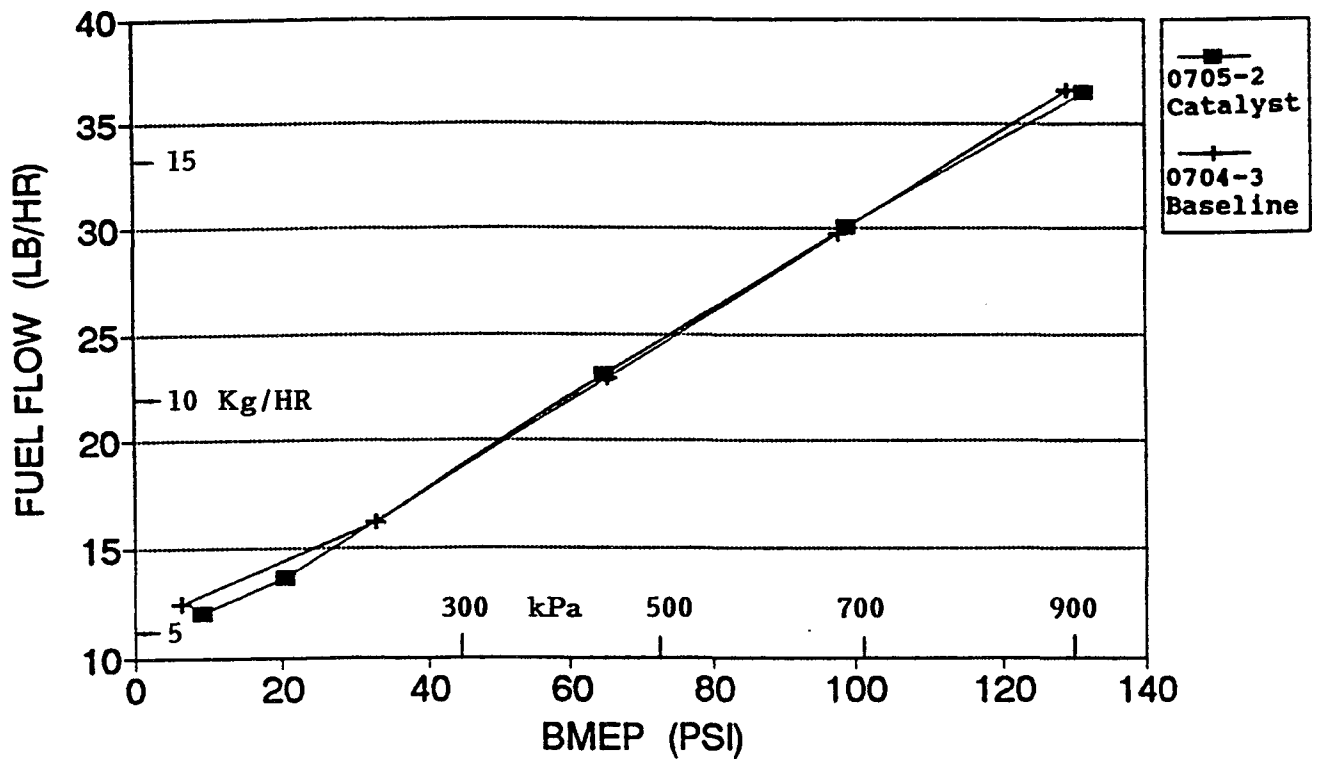


Figure No. 5

ENGINES 704-3 AND 705-2

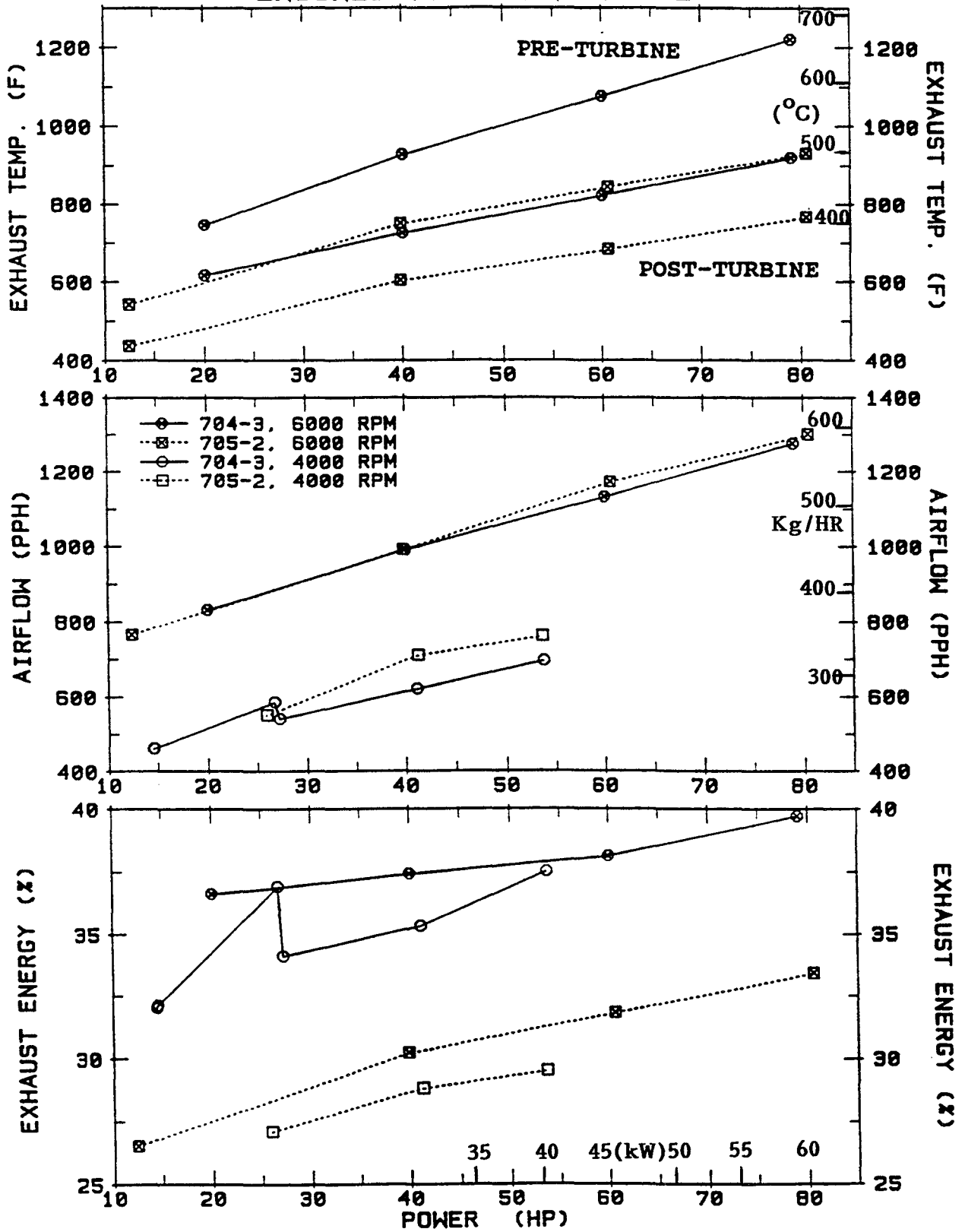


Figure No. 6

4.5 REFERENCE ENGINE DESIGN

PRECEDING PAGE BLANK NOT FILMED

PAGE 212 INTENTIONALLY BLANK

INTRODUCTION

The purpose of the 2013R Reference Engine Design is to define a Stratified Charge Rotary Engine (SCRE) configuration as a baseline aircraft engine. The design is intended to reflect the advanced technologies, engine components, design analyses and assessments established in the performance of the NASA Phase III contract. The Reference Engine Design was initiated in June 1990 and completed by September 1990. The continued Reference Engine Design update effort was curtailed with program re-direction as discussed in Section 2.0 Executive Summary.

OBJECTIVE

Conduct a SCRE aircraft Reference Engine Design for an engine with the capability of 400 horsepower at takeoff with a 40% brake thermal efficiency at best cruise power, and a 2,000 hour TBO (time between overhaul) service life. The Reference Engine Design shall address components, subsystems and technologies considered in the technology enablement program and critical to meeting the objectives. The Reference Engine Design shall also consider where appropriate current and anticipated light aircraft design practices and utilize general aviation type accessories suitable for light aircraft use.

TECHNICAL APPROACH

Design of the Reference Engine was based upon a twin rotor, 70 Series core power section, 40 cu. in. (0.7ℓ /rotor displacement) and integrated into a complete general aviation engine configuration. Component sections of the core rotary power plant were defined on the basis of overall rotary engine expertise, consultations with accessory suppliers, major air framer's, turbomachinery and control suppliers and consideration of advanced technologies anticipated as a result of the critical technology enablement effort.

The basic design parameters considered were:

- 400 BHP (300 kw) at Take-Off
- 300 BHP (225 kw) at Maximum Cruise
- 2000 Hr. Time Between Overhauls (TBO)
- Jet-A Fuel (Primary); DF-2, AVGAS (Alternate)
- Planetary Reduction Gear
- Clockwise and Counterclockwise Prop Rotation
- Crankshaft Speed 8500 RPM
- Propeller Speed 2500 RPM (approx.)
- Cruise Altitude Capability 33,000 Ft. (10km)
- Lightweight components deriving from the technology enablement program.
- Consideration of a high commonality family of engines having 1-6 rotors.
- Manufacturing technologies for cost, quality and durability/performance considerations.

- Integration of core stratified charge rotary engine power section and accessory components into a complete aircraft engine package for single and twin aircraft installation.
- Providing a baseline configuration for reference wherein critical component technology enablement items can be integrated and evaluated as the component technologies are advanced.
- Torsional damping provisions, propeller shaft and reduction gearing for adaptability of conventional light aircraft propellers.

The design effort included layout of the internal power section components including rotors, rotor housings, side and intermediate housings, crankshaft and counterweights. To this core power unit, provisions for the propeller shaft, reduction gear and torsional damper were added. Accessory drives for the required-to-run engine accessory components (fuel injection, ignition, coolant and oil) were integrated. Also, drives for accessories related to aircraft installation were provided. Coolant and oil coolers, turbomachinery and mounting considerations were addressed. Weight calculations for detailed components and the overall package (dry) were completed and the center-of-gravity defined. Performance characteristics were estimated at Take-off, 75% cruise, 65% cruise, 55% cruise, approach, taxi and idle conditions. These projections defined anticipated performance capabilities that could be achieved (if a full-up aircraft engine package was prepared and tested) utilizing technologies to be derived from re-directed technology enablement program as discussed in Section 2.0, Executive Summary.

RESULTS

Reference Engine Design

A Reference Engine Design, which includes a propeller reduction gear assembly, power section, and engine accessories was completed. The Reference Engine Design provides a Stratified Charge Rotary Engine configuration for aircraft application representative of the requirements for aircraft application and includes consideration of the advanced technologies pursued in the technology enablement program.

The Reference Engine is designed and packaged as an aircraft engine which will fit within a tapered nacelle inside diameter of 21.0 to 26.0 inches (533 to 660mm) from behind the propeller to the rear accessory end respectively. The Reference Engine will have an overall length of 57.6 inches (1463 mm) and a total weight of 480 pounds (dry) (218 kg).

The general construction and layout of the Reference Engine Design is shown in Figure 1, Basic Arrangement; Figure 2, Accessory End View; and Figure 3, Propeller End View. The aircraft nacelle diameters are superimposed on the End Views for reference.

The complete engine installation and location of the engine accessories is shown in Figure 4, Preliminary Installation Drawing, Left Side; Figure 5, Preliminary Installation Drawing, Right Side; and Figure 6, Preliminary Installation Drawing, Accessory End View.

A description and illustration of some of the major Reference Engine Design components are provided in the following paragraphs.

PROPELLER REDUCTION GEAR ASSEMBLY

The Propeller Reduction Gear Assembly is shown in Figure 7. The Assembly includes the Reduction Gear Housing and Nose Cone, the Propeller Shaft Assembly, Torsional Coupling, Planetary Reduction Gearing, and Vacuum and Propeller Governor Drives. The Reduction Gear Assembly serves the following functions:

- a. Enclosure of the reduction and accessory drive gear trains, and torsional coupling.
- b. Lubrication supply for the gearing and attendant bearings, and propeller thrust bearing.
- c. Structural support for the propeller shaft, torsional coupling, reduction gear and pinion, and loads imposed by propeller thrust and aircraft maneuver conditions.
- d. Oil supply through the propeller shaft from the prop governor to control propeller pitch.

The propeller shaft torsional coupling is shown in Figure 8. The planetary reduction gear propeller drive provides the capability for clockwise or counterclockwise rotation as required for twin engine aircraft installation. Figure 9 shows the clockwise prop reduction gearing. Figure 10 shows the counterclockwise reduction gearing. Both mechanisms provide a gear ratio of 3:39 to 1.0, for a resulting propeller speed of 2511 rpm at take-off conditions.

TURBOMACHINERY

A major installation concern of the Reference Engine Design is location, configuration, and support of the turbomachinery. To maintain the minimum nacelle diameter of 26 inches the turbocharger must be mounted on a truss support system bolted to the Accessory Housing. The truss support is shown in Figure 11. The turbocharger is mounted to the support plates and connected to the intercooler as shown in figure 12.

ENGINE COOLANT SYSTEM

The engine coolant system features a dual path coolant flow through the engine and a four pass coolant system through each set of paired end and rotor housings. The dual path coolant flow independently cools the Anti-Prop End and Prop End Rotor Housings by splitting the coolant flow at the coolant manifold integrally cast into the Anti-Prop End Housing. Both coolant paths then utilize a four pass cooling system through the End and Rotor housings as shown in Figures 13 and 14. The arrangement of the four pass system was developed to enhance cooling at regions of maximum heat flux, where the cooling mechanism is primarily nucleate boiling. The coolant flow circuitry is designed to locate the regions of maximum heat flux near the end of an axial series flow where coolant static pressure is lower. The lower coolant static pressure enhances the formation of nucleate boiling.

ENGINE LUBRICATION SYSTEM

The Reference Engine Lubrication System schematic is shown in Figure 15. The Lubrication System shows the oil cooler incorporated into the engine oil pressure system. The following advantages are attributed to the pressurized oil cooler:

- a. The oil cooler core size is reduced.
- b. The risk of cooler blockage due to air entrainment is reduced.
- c. The scavenge system is simplified. Generally the oil scavenge system is the most temperamental and altitude sensitive section of the lubrication system.
- d. Oil de-aeration in the oil tank is generally expected to be improved due to the increased temperature of oil in the tank.

FUEL PUMP TIMING

The Reference Engine Design includes a Fuel Pump Advance/Retard Mechanism. The pressure activated mechanism, activated by engine oil pressure, is shown in Figure 16.

ENGINE ENVELOPE

The Reference Engine total weight and center of gravity is shown in Figure 17. The engine total weight includes the Reduction Gear Assembly (but no propeller), the Engine Power Section, and the engine accessories. The present estimated engine weight is 480 lbs. dry (218

kg). A moderate weight reduction program is believed to be capable of providing an engine dry weight of just below 400 lbs (181 kg).

ENGINE PERFORMANCE

The estimated Performance Data for the aircraft Reference Engine Design are provided in Figures 18 and 19. Figure 18 provides an engine operation summary. Figure 19 provides estimated engine fuel consumption at typical aircraft mission duty cycle operating points.

CONCLUSIONS

The Reference Engine Design provides a realistic baseline definition of an advanced SCRE suitable for light aircraft usage.

RECOMMENDATIONS

- 1) Critical technology enablement advancements occurring during the latter stages of the NASA Phase III contract should be integrated into the Reference Engine Design. As noted previously, the design update activities originally planned were curtailed upon program re-direction. Some items which should be considered are:
 - The Dual Orifice Pilot Nozzle
 - The Titanium Rotor
 - Rotor Combustion Pocket configurations which provide lower cruise BSFC
- 2) A weight reduction program should be initiated to markedly lower the overall engine weight. This program should include a search for the lowest weight applicable engine accessories.

LIST OF FIGURES

<u>FIGURE</u>	<u>TITLE</u>
1.	BASIC ARRANGEMENT
2.	ACCESSORY END VIEW
3.	PROPELLER END VIEW
4.	PRELIMINARY INSTALLATION DRAWING: LEFT SIDE
5.	PRELIMINARY INSTALLATION DRAWING: RIGHT SIDE
6.	PRELIMINARY INSTALLATION DRAWING: ACCESSORY END VIEW
7.	REDUCTION GEAR HOUSING AND NOSE CONE
8.	PROPELLER SHAFT TORSIONAL COUPLING
9.	CLOCKWISE PROPELLER REDUCTION GEARING
10.	COUNTERCLOCKWISE PROPELLER REDUCTION GEARING
11.	TURBOCHARGER SUPPORT
12.	TURBOCHARGER/INTERCOOLER INSTALLATION
13.	COOLANT FLOW SCHEMATIC THROUGH ENGINE
14.	COOLANT FLOW THROUGH ROTOR HOUSING
15.	LUBRICATION SYSTEM
16.	FUEL PUMP ADVANCE/RETARD MECHANISM
17.	ENGINE WEIGHT AND CENTER OF GRAVITY LOCATION
18.	OPERATING DATA SUMMARY
19.	ESTIMATED FUEL CONSUMPTION

2013R NASA REFERENCE ENGINE

BASIC ARRANGEMENT

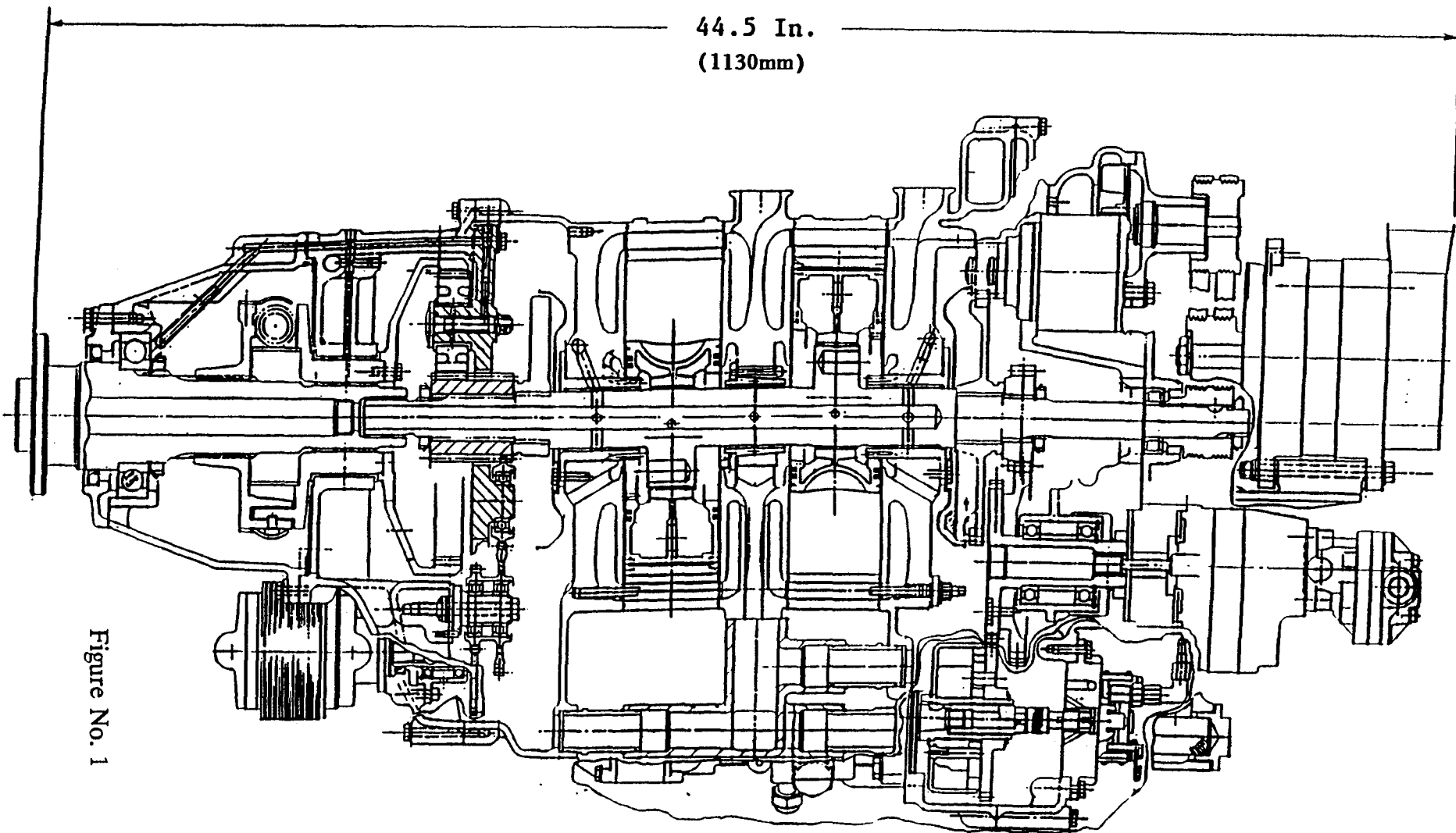


Figure No. 1

2013R NASA REFERENCE ENGINE

ACCESSORY END VIEW

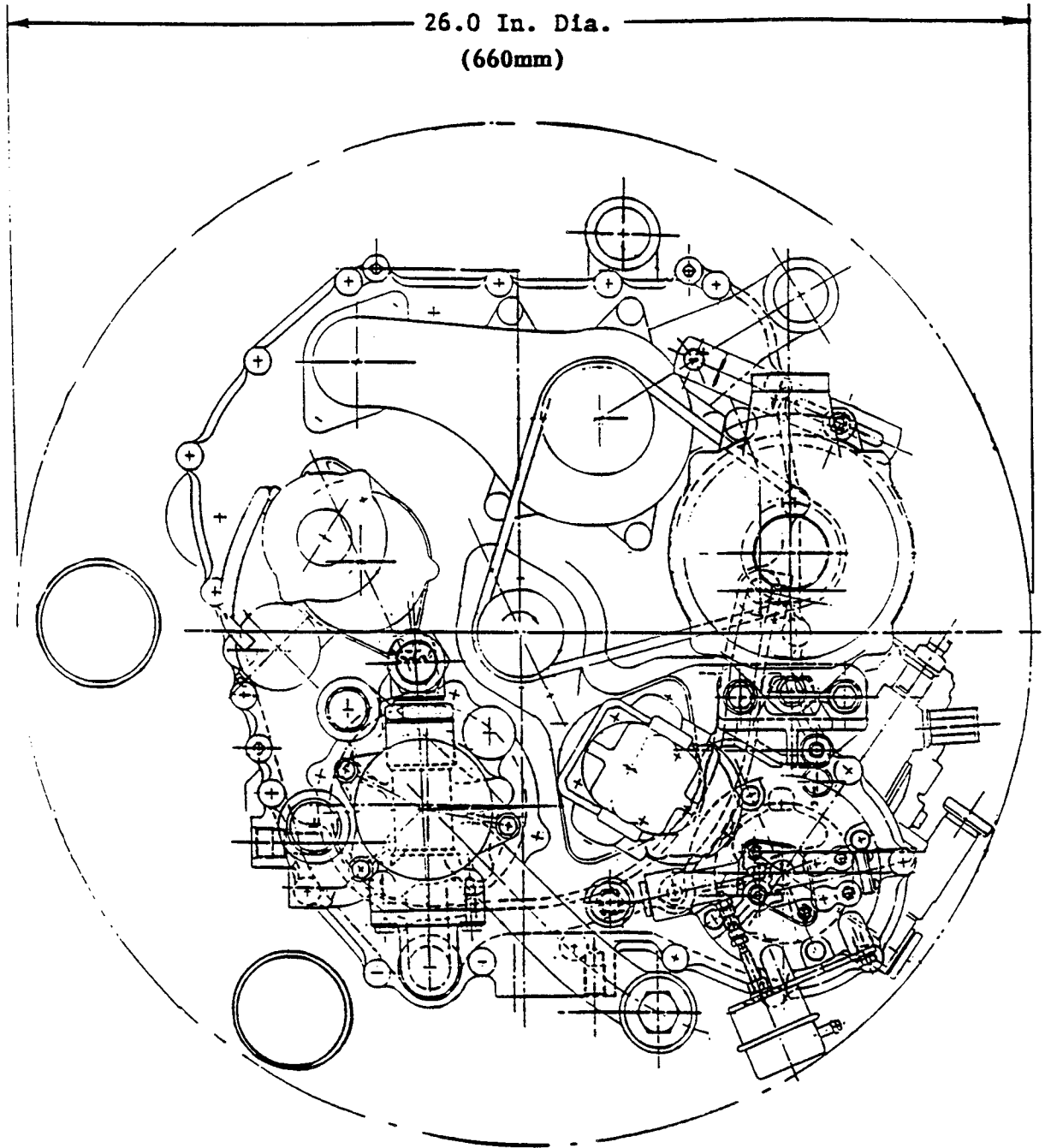
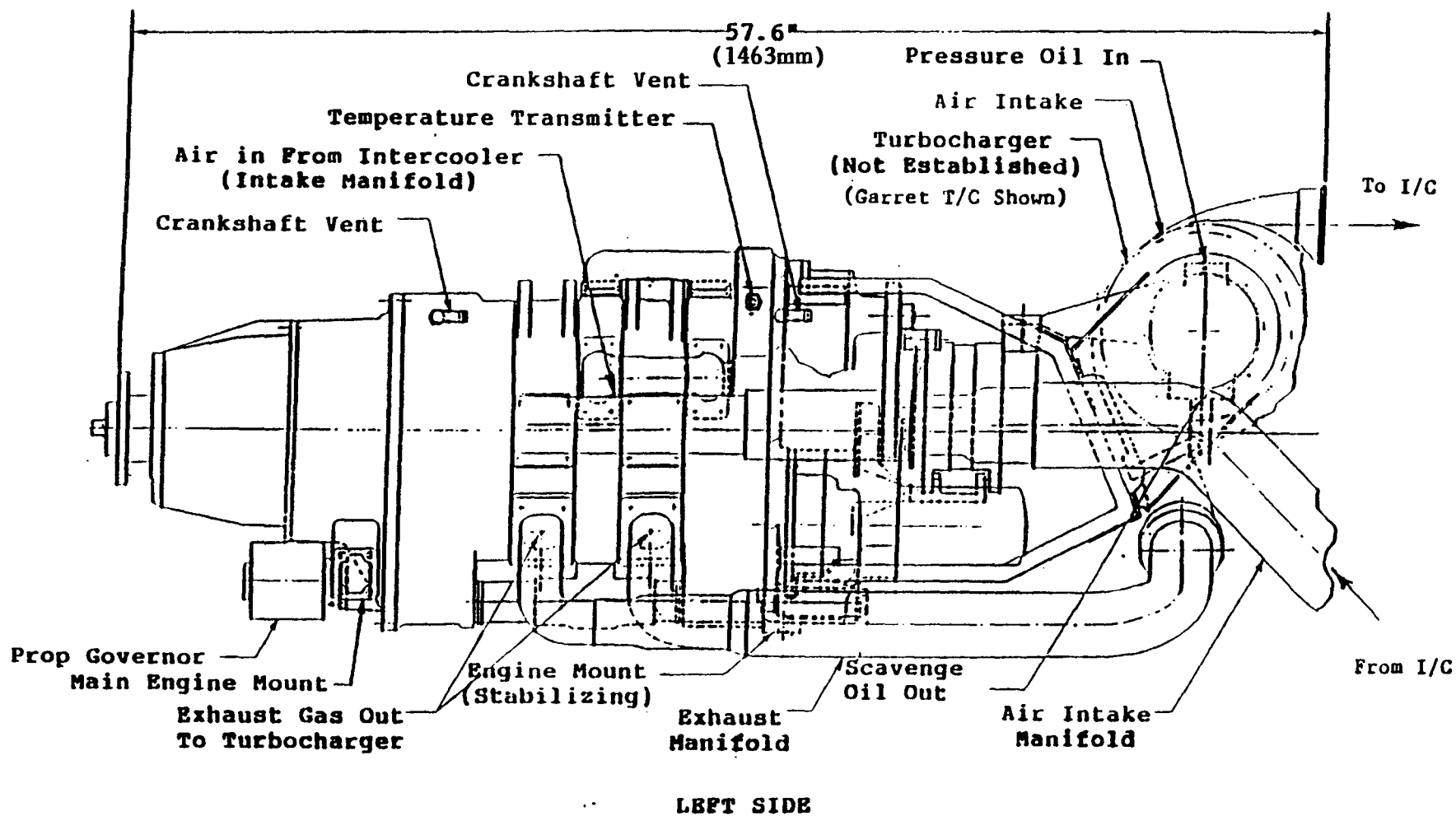


Figure No. 2

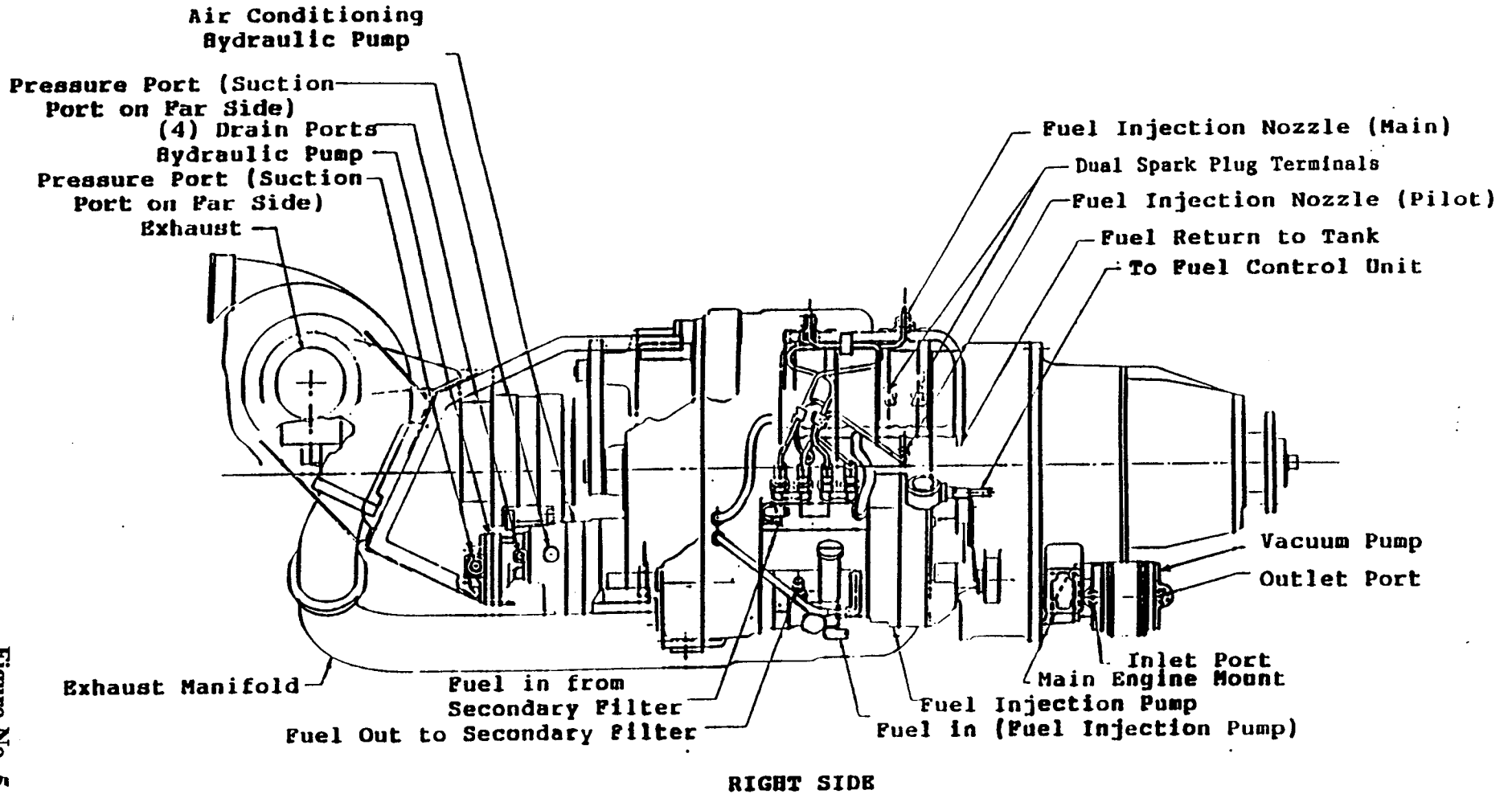
**2013R NASA REFERENCE ENGINE
PRELIMINARY INSTALLATION DRAWING**



224

Figure No. 4

**2013R NASA REFERENCE ENGINE
PRELIMINARY INSTALLATION DRAWING**



225

Figure No. 5

**2013R NASA REFERENCE ENGINE
PRELIMINARY INSTALLATION DRAWING**

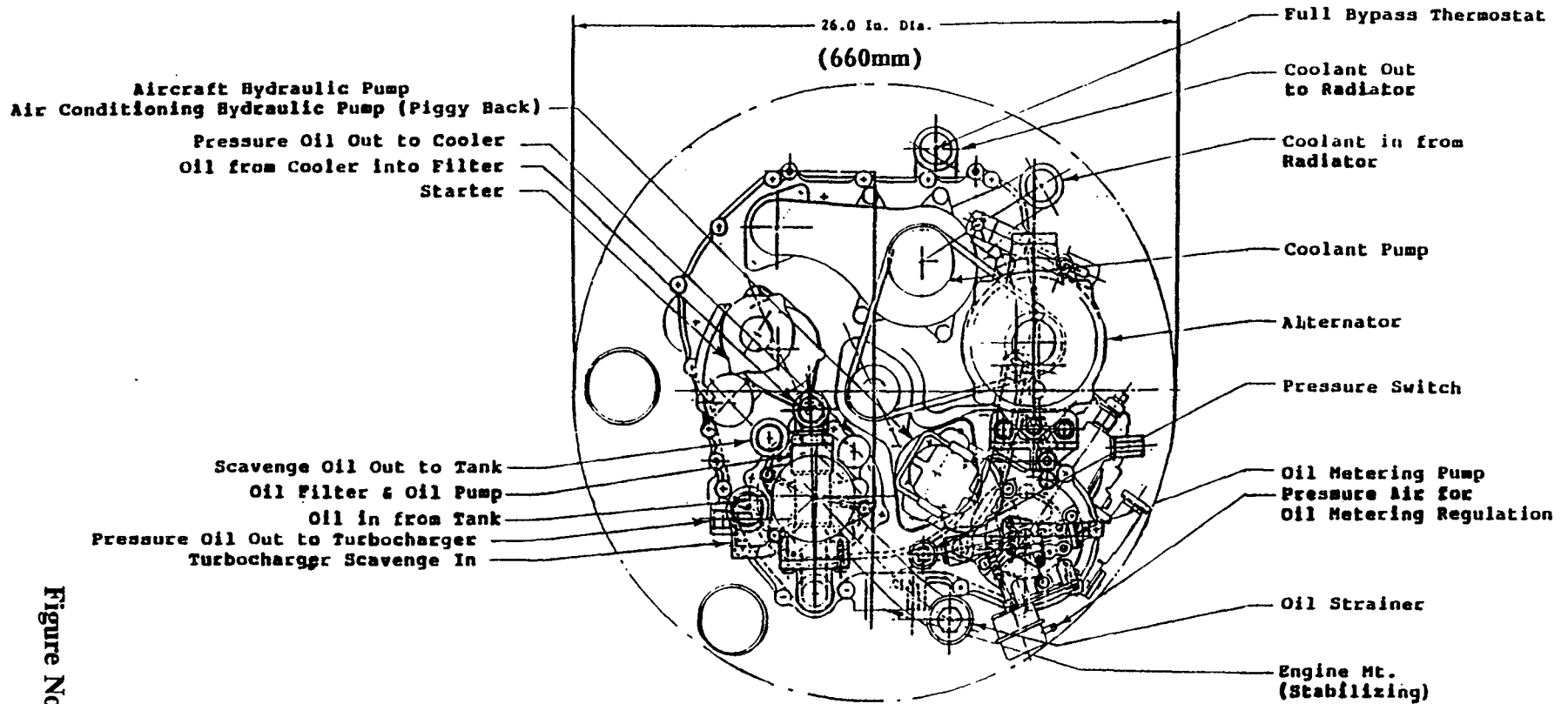


Figure No. 6

2013R NASA REFERENCE ENGINE
REDUCTION GEAR HOUSING AND NOSE CONE

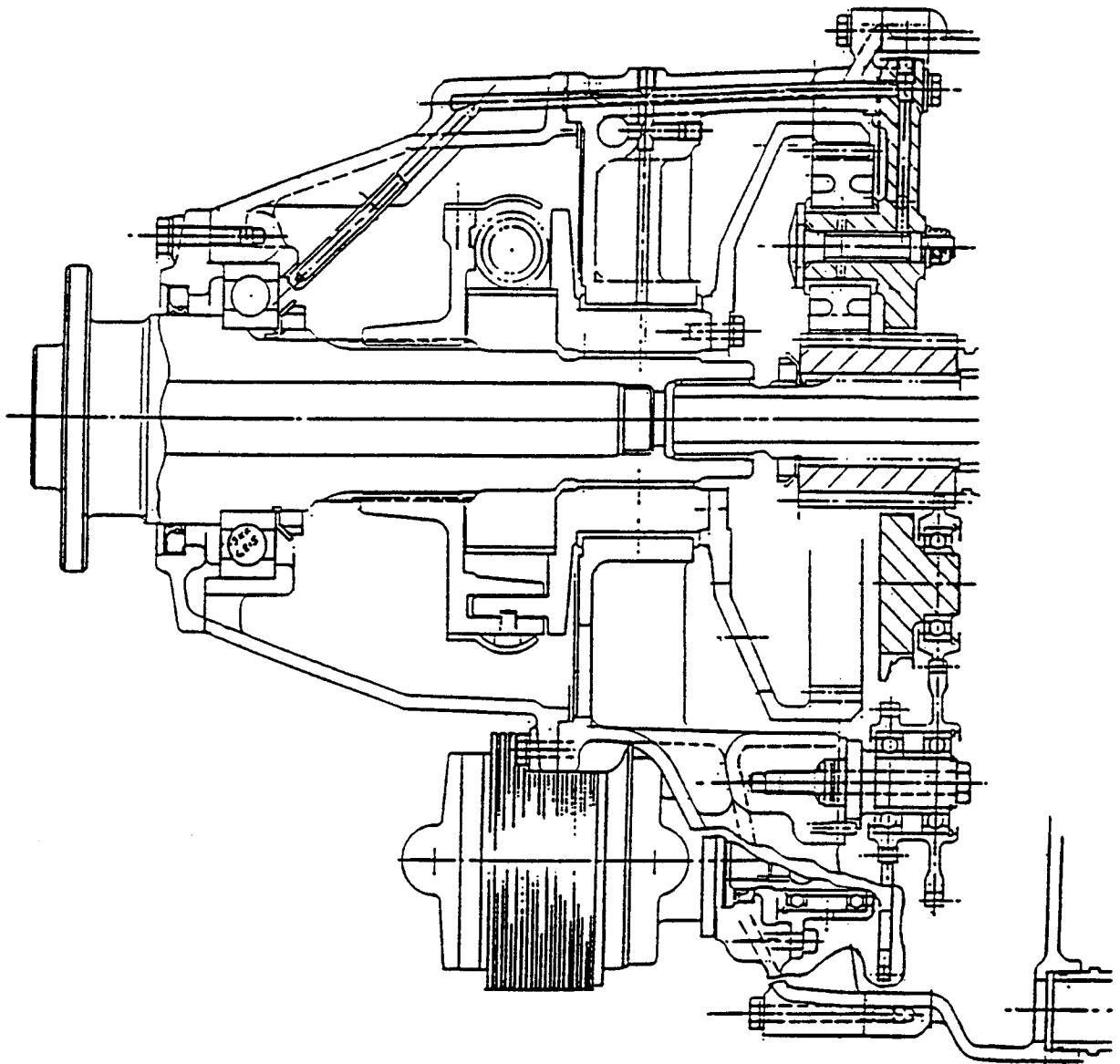
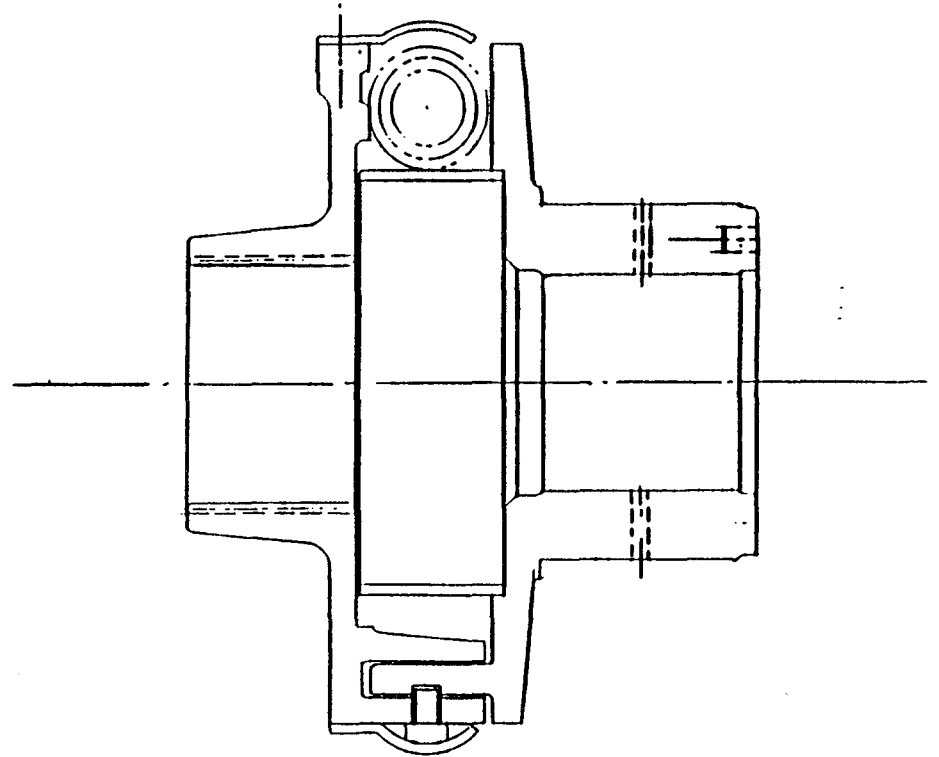
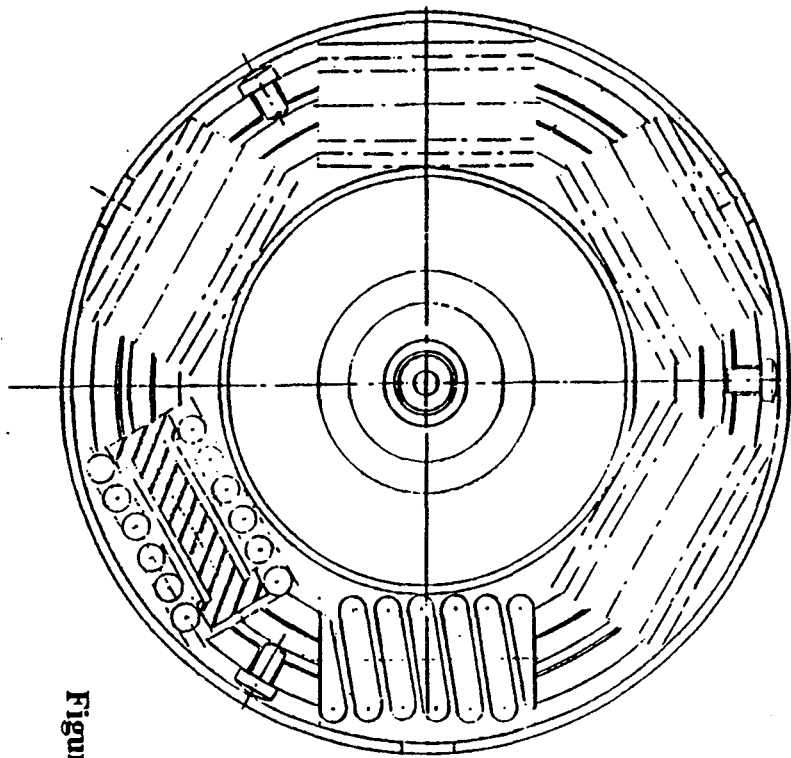


Figure No. 7

2013R NASA REFERENCE ENGINE
PROP SHAFT TORSIONAL COUPLING



228

Figure No. 8

**2013R NASA REFERENCE ENGINE
CLOCKWISE PROP REDUCTION GEARING**

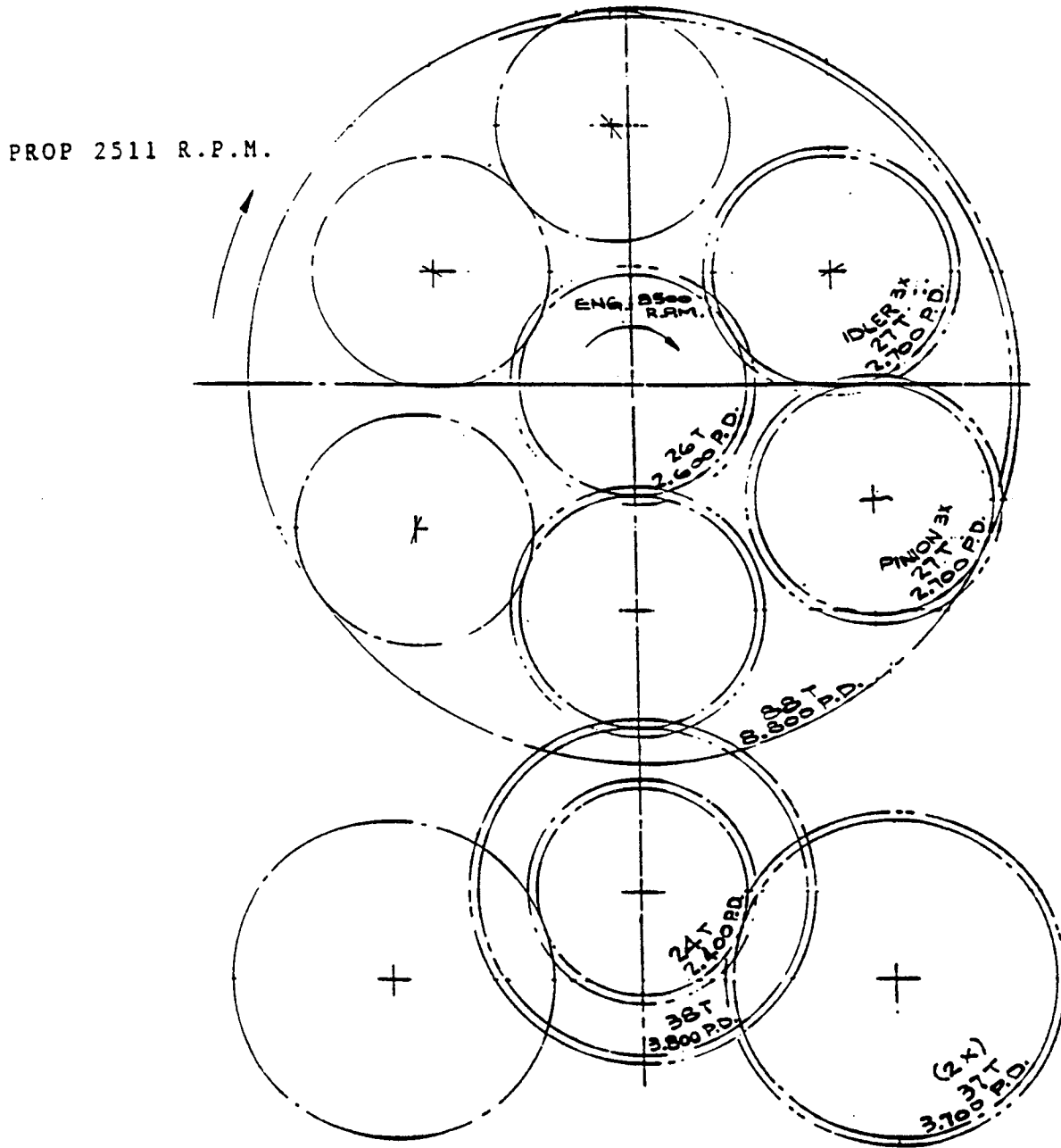


Figure No. 9

2013R NASA REFERENCE ENGINE
COUNTERCLOCKWISE PROP REDUCTION GEARING

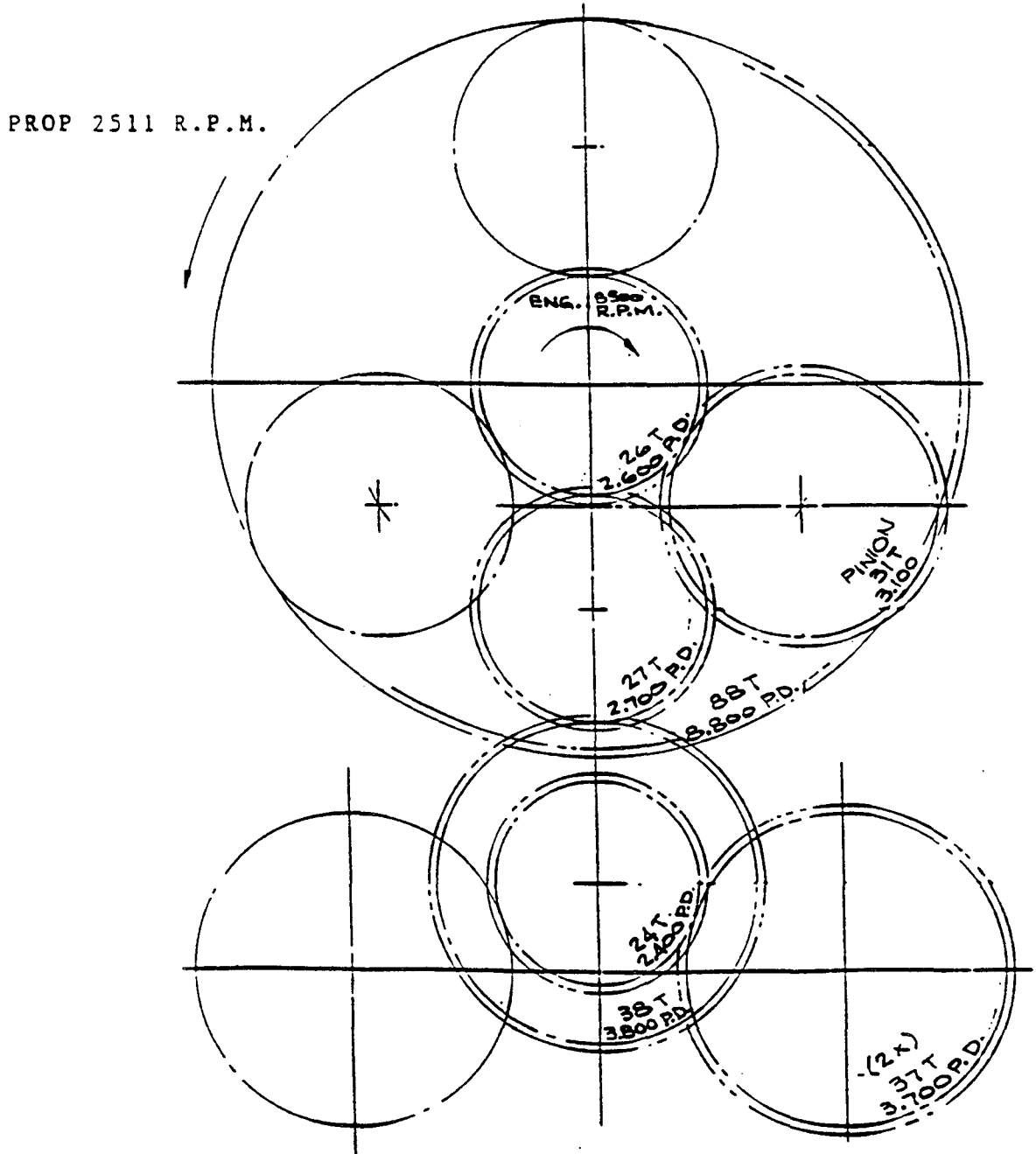


Figure No. 10

2013R NASA REFERENCE ENGINE

TURBOCHARGER SUPPORT

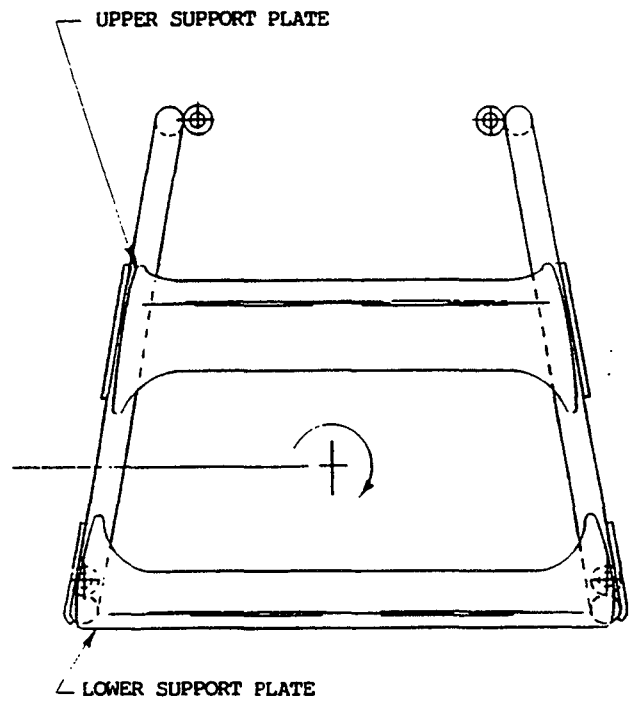
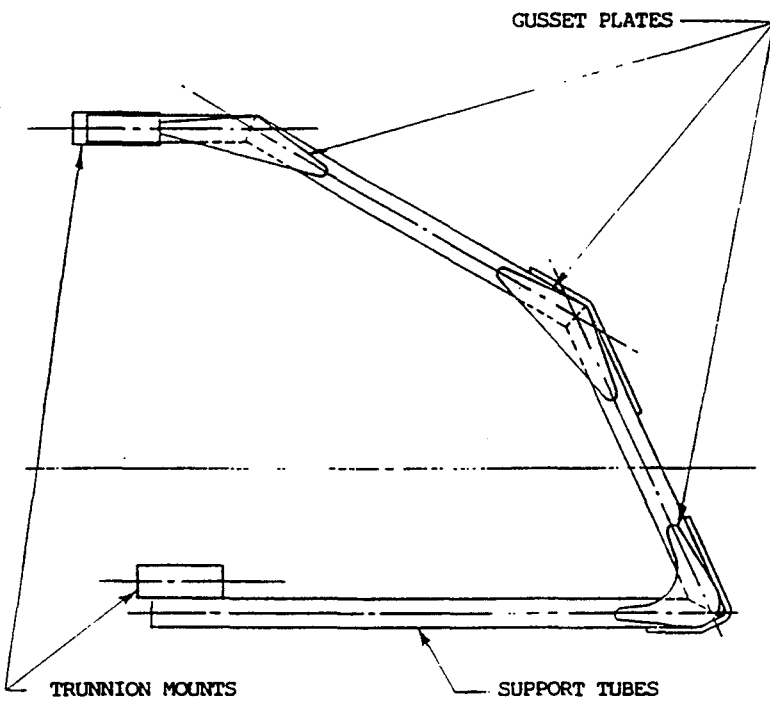
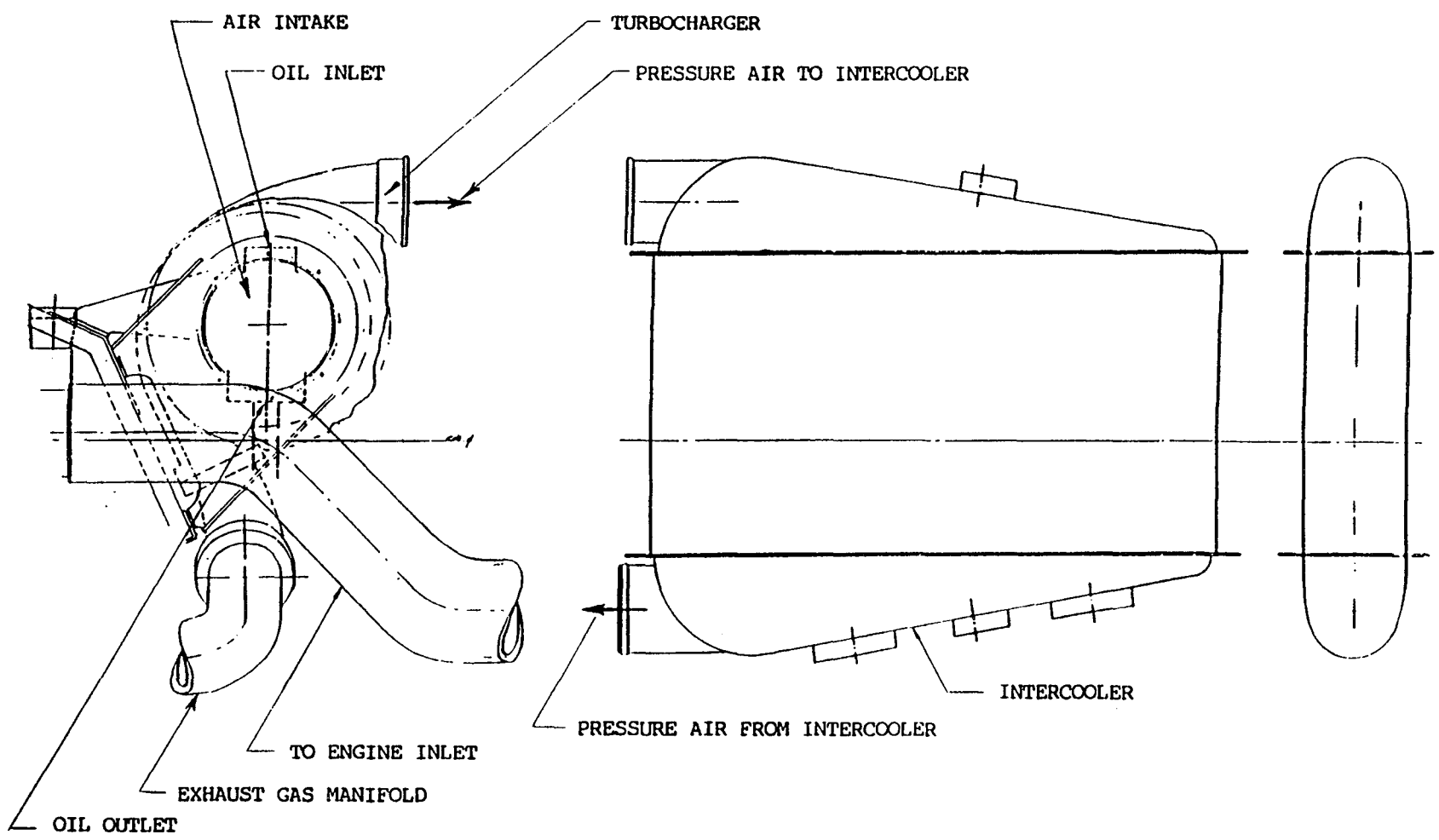


Figure No. 11

2013R NASA REFERENCE ENGINE
TURBOCHARGER/INTERCOOLER INSTALLATION



232

Figure No. 12

2013R NASA REFERENCE ENGINE

COOLANT FLOW SCHEMATIC THRU ENGINE

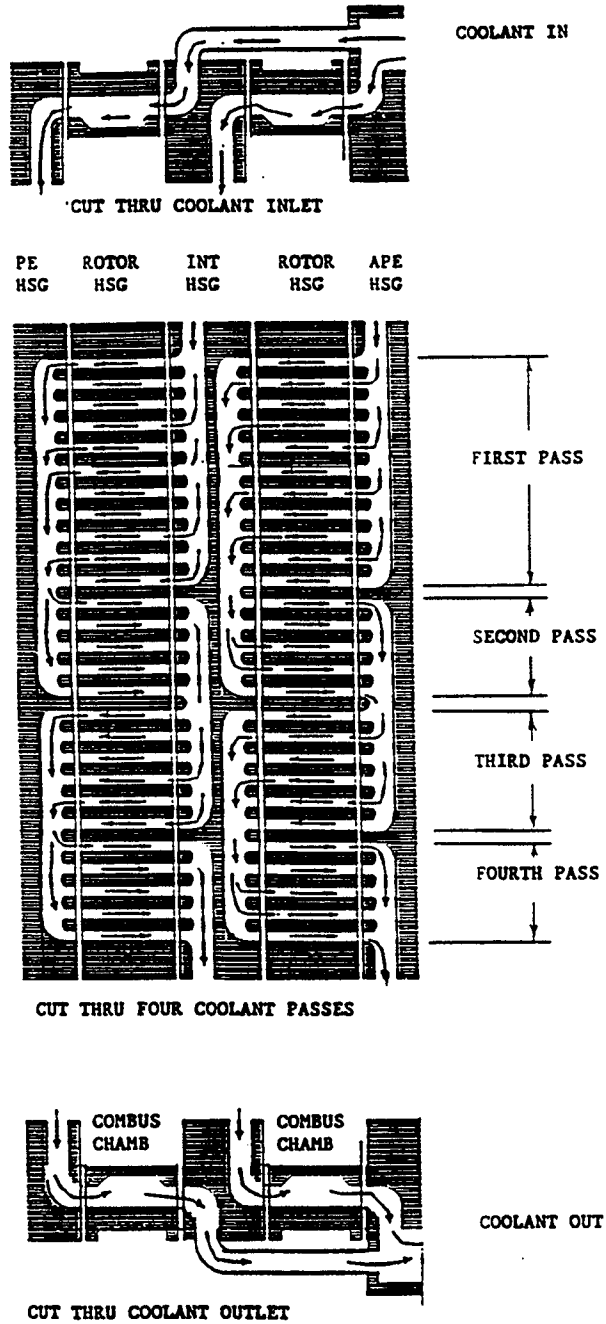


Figure No. 13

2013R NASA REFERENCE ENGINE
COOLANT FLOW THRU ROTOR HOUSING

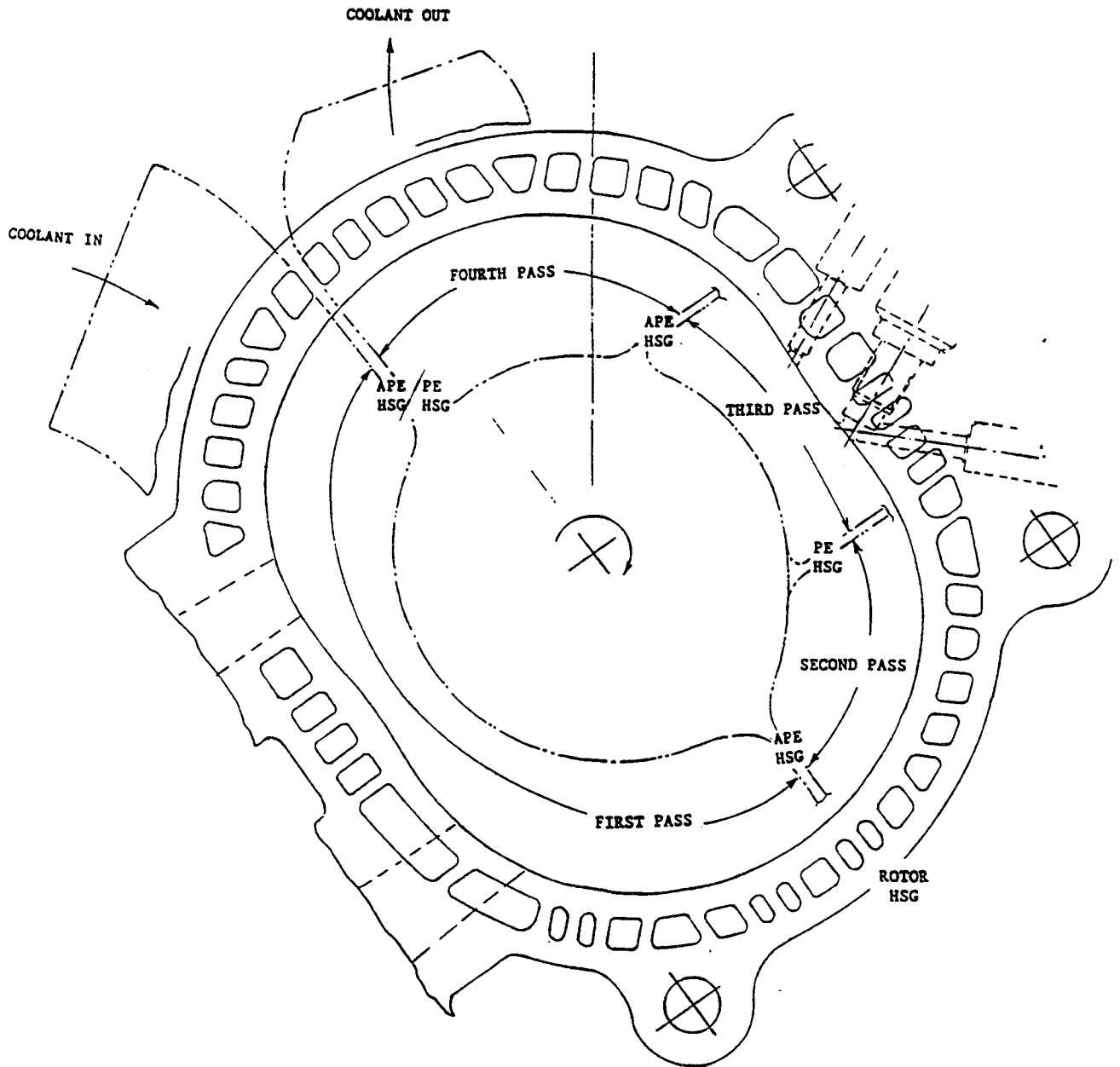


Figure No. 14

2013R NASA REFERENCE ENGINE

LUBRICATION SYSTEM

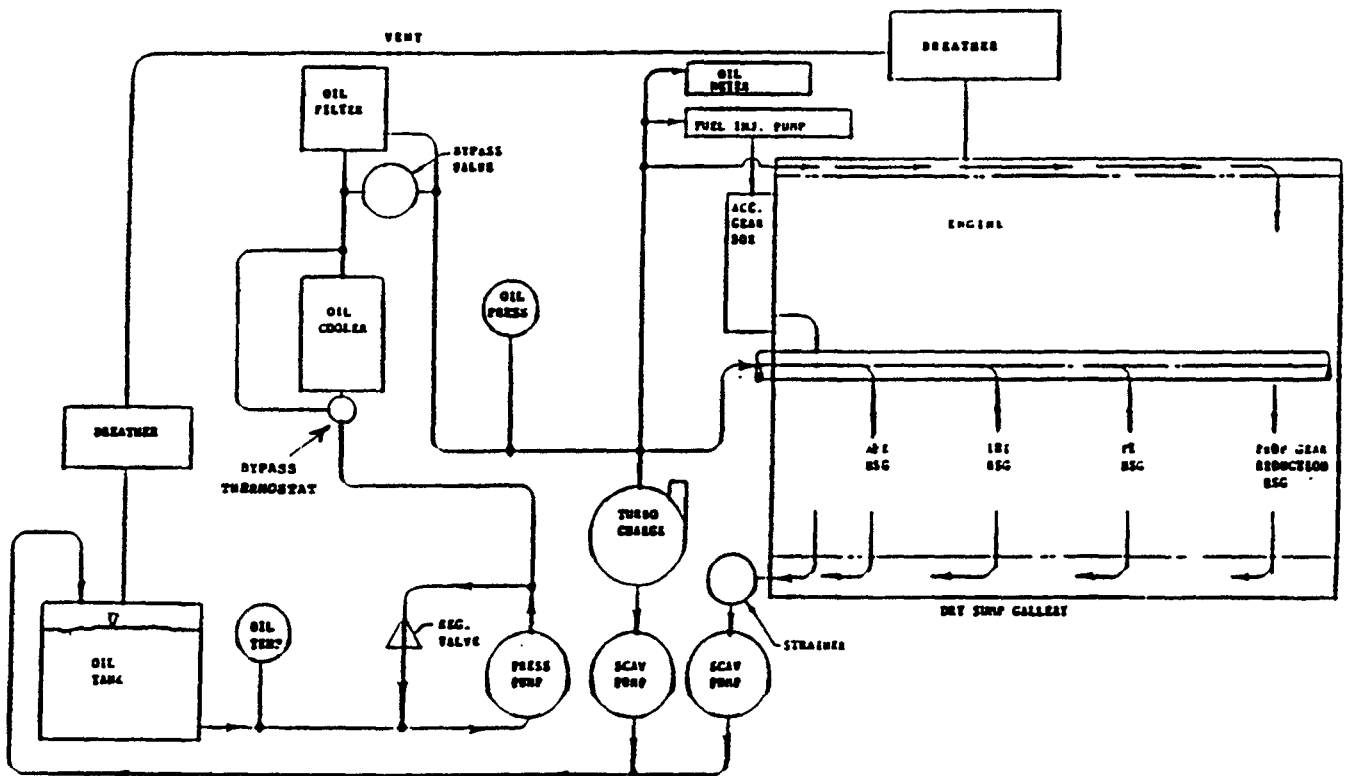
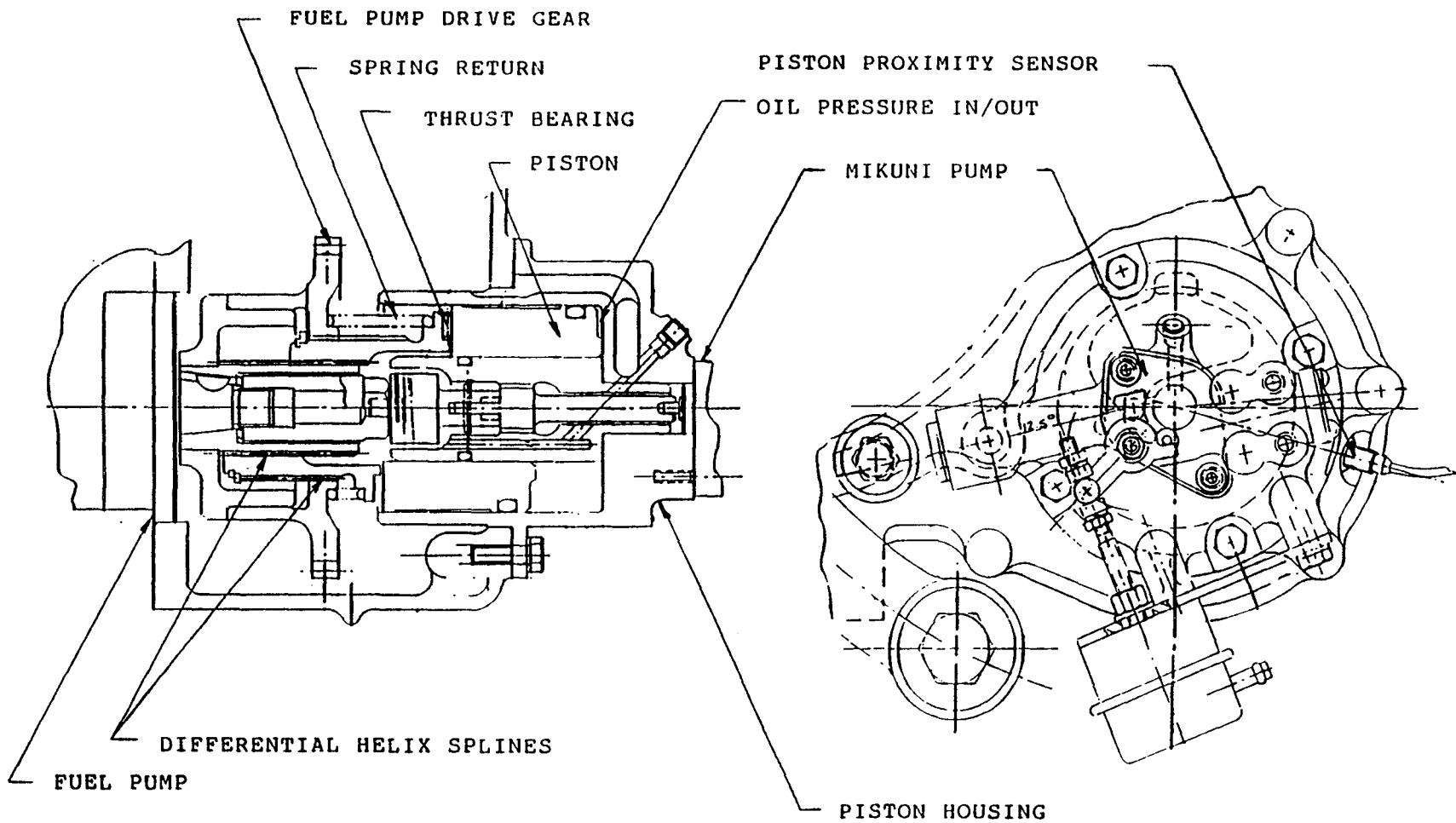


Figure No. 15

2013R NASA REFERENCE ENGINE

FUEL PUMP ADVANCE/RETARD MECHANISM



2013R NASA REFERENCE ENGINE

ENGINE WEIGHT AND C.G.

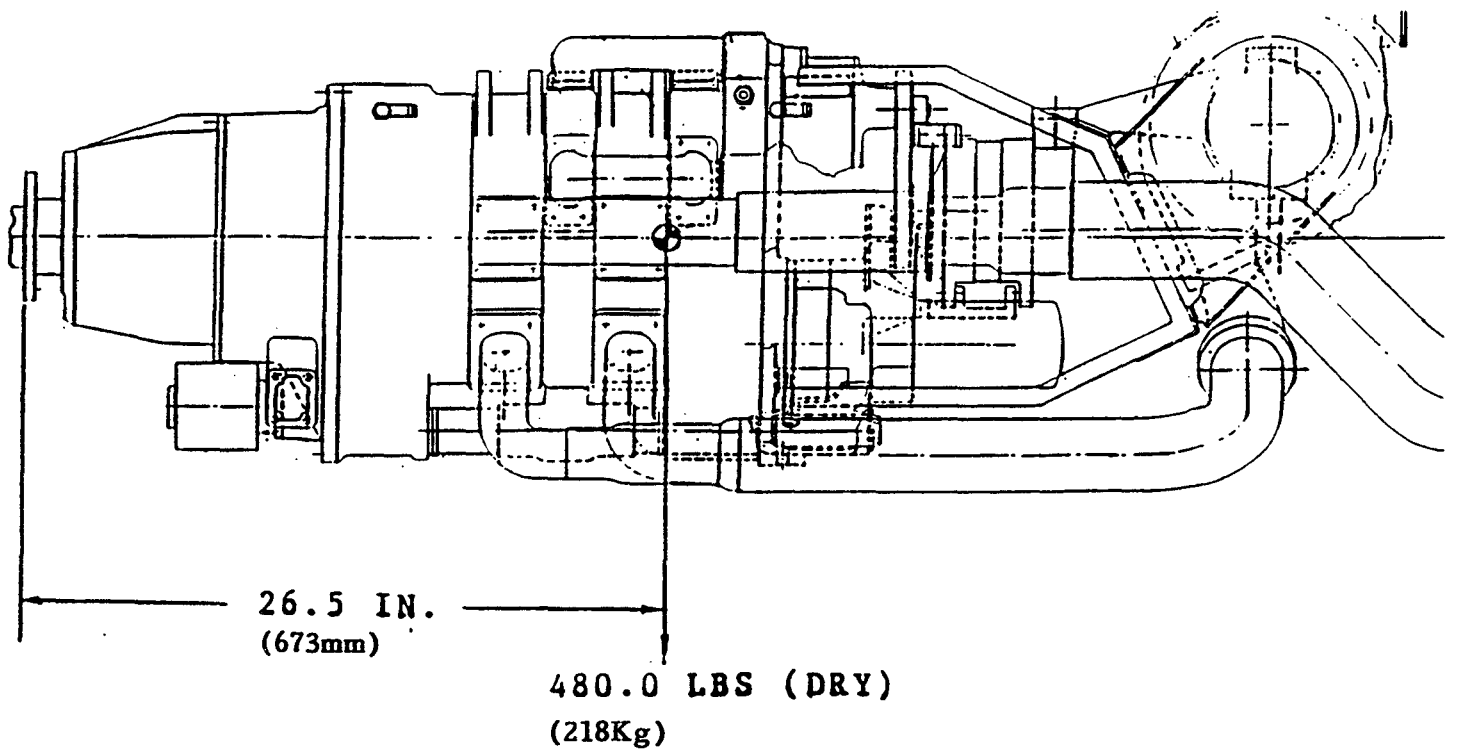


Figure No. 17

2013 NASA REFERENCE ENGINE

OPERATING DATA SUMMARY

	TAKE-OFF		75% CRUISE		
	S.L.	25,000'	S.L.	25,000'	33,000'
BHP (KW)	400 (300)	-	300 (225)	-	-
RPM	8500	-	7500	-	-
IMEP-PSI (kPa)	277.3 (1910)	-	237.2 (1634)	-	-
IHP (KW)	481 (361)	-	363 (272)	-	-
FMEP-PSI (kPa)	46.7 (322)	-	41.2 (284)	-	-
FHP (kw)	81 (61)	-	63 (47)	-	-
BMEP-PSI (kPa)	230.6 (1589)	-	196 (1350)	-	-
F/A	.0374	-	.0360	-	-
BSFC-LB/HP-HR (g/kwr)	.421 (256)	-	.424 (258)	-	-
AIRFLOW-LB/HR (KG/H)	4495 (2039)	-	3530 (1601)	-	-
P ² /P ¹	2.5	6.84	2.16	5.89	8.5
P ³ -IN. HG (KPA)	69.0 (233)	75.9 (257)	60.7 (205)	60.7 (205)	60.7 (205)
T ³ -°F (°C)	140.3 (60.1)	-	140.3 (60.1)	-	-
FUEL FLOW-LB/HR (KG/H)	168.32 (76.3)	-	127.08 (57.6)	-	-
AMBIENT TEMP.-°F (°C)	59.0 (15)	-30.2 (-34)	59.0 (15)	-30.2 (-34)	-58.7 (-50)
AMBIENT PRESS-INHG (kPa)	29.92 (101.2)	11.10 (37.5)	29.92 (101.2)	11.10 (37.5)	7.732 (26.1)

FIGURE 18

2013R NASA REFERENCE ENGINE

ESTIMATED FUEL CONSUMPTION

<u>RATING</u>	<u>HP (KW)</u>	<u>RPM</u>	<u>BSFC LB/HP-HR</u>	<u>GRS/KW-HR</u>
Take-Off	400 (300)	8500	.421	256
75% Cruise	300 (225)	7500	.424	258
65% Cruise	260 (195)	7150	.429	261
55% Cruise	260 (195)	6765	.434	264
Approach	160 (120)	7150	.482	293
Taxi	40 (30)	3830	.644	392
Idle	4 (3)	1780	1.10	669
Idle	0 (0)	1780	3 lb/hr.	1.36 Kg/hr.

FIGURE 19

5.0 AIRFRAME/MISSION MODEL

PRECEDING PAGE BLANK NOT FILMED

PAGE 240 INTENTIONALLY BLANK

INTRODUCTION

The Airframe/Mission Model Technology assessment of this contract was intended to identify and evaluate the general aviation application best suited to the advanced Stratified Charge Rotary Engine.

The best suited application would utilize the unique characteristics of the Stratified Charge Rotary Engine in shaping the airframe configuration and airplane mission. Further, the technology assessment would provide a method for evaluating the performance of the rotary engine in the proposed application. The Airframe/Mission Technology model assessment was subcontracted to the Beech Aircraft Corporation. Beech Aircraft has extensive experience in the development and application of new aircraft technology.

OBJECTIVE

The first objective was to define a representative airframe and airframe mission model. The airframe selected would be intended to best demonstrate the advantages and characteristics of the stratified charge rotary engine. The second objective was to define an airframe mission and mission simulation model. The simulation model would describe and evaluate the selected aircrafts' mission performance with the stratified charge rotary engine.

TECHNICAL APPROACH

The development effort to define the airframe, airframe mission, and mission simulation model was divided by the Beech Aircraft Corporation (Beech) into four discrete tasks. These tasks were:

1. Definition of a representative general aviation airplane configuration and performance characteristics.
2. Definition of general aviation type mission profiles from taxi and takeoff through climb and cruise and back to landing and taxi.
3. Definition of appropriate criteria of merit.
4. Production of a complete airplane/mission system simulation model which will evaluate the criteria of merit when used with a Deere furnished engine model.

Beech provided the rationale framework required to establish airplane characteristics and mission profiles appropriate to the advantages and characteristics of the stratified charge rotary engine.

RESULTS

Each task which defined the airframe mission and mission simulation model will be addressed separately in the following sections. Complete details of the Beech analysis effort are provided in Reference 1.

1. Definition of Airplane Configuration and Performance

Definition of a representative airplane configuration and performance characteristics entailed consideration of numerous factors. Factors of primary consideration included the rotary engine lapse rate, take off field length, airplane drag coefficients, cruise speed and engine and airframe weights.

Consideration of the above factors provided an initial aircraft configuration and an initial set of design goals. The multi-engine executive transport was selected to provide the most advantageous application of the stratified charge rotary engine. The airplane configuration was then sized for the rotary engine to make the most favorable comparison to current turboprop airplanes which dominate the executive transport market.

The stratified charge rotary engine, as specified in the contract, has a significantly different power lapse rate with altitude than a turboprop. Comparisons of lapse rate with altitude for the stratified charge rotary and for a turboprop are shown in Figures 1 and 2. Figure 1 shows power versus altitude for a turboprop with the same take-off rating as the rotary engine, while Figure 2 compares the turbine and rotary engines with cruise power matched. Normally the case is considered where cruise power is comparable. This comparison indicates the turboprop provides more takeoff power for the same cruise power than the rotary engine. Thus the airplane sizing for the rotary engine tends to lead to a smaller airplane.

Take off field length is proportional to wing loading times power loading divided by maximum lift co-efficient. A maximum lift coefficient of 2.0 in the take-off configuration is considered feasible without imposing excessive drag. Figure 3 shows the allowable gross weight as a function of wing area and field length for two engines at 392 HP (294kw) each (400 hp, 300kw- 8hp, 6kw mechanical loads). A balanced field length of 4000 feet (1219m) or less was used as a design goal.

The wetted area drag coefficients of current airplanes in this class range from about .005 to .006. Advances in airfoils and construction techniques should allow a drag coefficient of .0045 and some modern airplanes approach this value. Figure 4 illustrates the total airplane wetted area versus design speed and altitude for the cruise power available from the rotary

engine. Current airplanes in this class have wetted areas in the 1100 to 1300 square feet (102-121 square meters) range. An initial cruise speed of 300 knots was selected which leads to a wetted area of 1055 square feet (98 square meters) at the engine cruise critical altitude of 33,000 feet (10 km).

The initial cruise speed selection was based on a data correlation of aircraft maximum speeds. Implied in those data was that induced drag was on the order of 10% of parasite drag. Induced drag is closer to 20% of parasite drag for the cruise at 33,000 feet (10 km). As shown in figure 5, the 300 knot goal led to an unacceptably small airplane. A goal of 280 knots gives a more practical size as shown in Figure 6. Both figures show results from a simplified synthesis program using Breguet's range equation and a weight correlation equation.

Airframe weights were approximated from a correlation of empty weight minus installed engine weight per unit wetted area. The resulting estimated weights were somewhat higher than indicated by the weight correlation equation used in the synthesis routine which had been based on turboprop airplanes. The result was some adjustment of weight goals from those shown on Figures 5 and 6.

The following design goals were selected based on the results of the above analysis.

Wetted Area	1100 Sq. Ft. (102 sq. M)
Wing Area	195 Sq. Ft. (18.1 Sq. M)
Fuel Weight	1400 lbs. (635 kg.)
Empty Weight	5100 lbs. (2313 kg.)
Take Off Gross Weight	8000 lbs. (3629 kg.)
Aspect Ratio - selected	10

An engine installation layout was made based on the heat exchanger sizes received from Sundstrand. The best arrangement was to mount the heat exchangers between the engine mount rails with cooling air entering below the exchangers and flowing upward to exits in the top of the cowl as shown in Figure 7. The heat exchangers were re-sized to better fit the available space.

Heat exchanger weights were originally based upon a liquid cooled, turbocharged engine of comparable power. The coolant radiator is approximately two times and the intercooler approximately five times the weight of comparable items for a reciprocating engine. The comparison is based upon the split intercooler for the single compression stage. Weights cited are for the core only and do not include manifolds and plumbing which will reduce further the engine weight advantage of the rotary. The engine weight savings over comparable reciprocating engines was estimated to be 100 pounds (45.4 kg). The increased weights of the heat exchangers will reduce the advantage to less than 50 pounds (22.7 kg).

Propeller sizing for the rotary engine application was strongly influenced by noise limits. Noise limits in Europe have now been reduced to 72 DBA flyover. New airplanes should be designed to be marketable worldwide.

Figure 8 shows the maximum diameter allowed as a function of RPM for 72 DBA. Figures 9 to 11 then show the resulting efficiencies for the corresponding points with the cruise RPM reduced by the engine RPM ratio of cruise to maximum RPM (7500/8500). From these curves it can be seen that a four bladed prop of 92 inches diameter (2337mm) with takeoff RPM of 1950 is near peak efficiency for all calculated flight points (gear ratio-0.229).

The initial aircraft design layouts had used a smaller propeller and the layout has been modified to accommodate the larger propeller size. Nacelles had to be moved outboard, the landing gear lengthened and the engine moved slightly forward to maintain clearance of the crew and flight controls from the 5 degree propeller cone as shown in Figure 12.

Final aircraft specifications and performances are as follows.

Wetted area,	1100 Sq. Ft. (102 Sq. M)
Wing area,	195 Sq. Ft. (18.1 Sq. M)
Fuel weight,	1300 lbs. (590 kg.)
Empty weight,	5200 lbs. (2359 kg.)
Gross weight,	8000 lbs. (3629 kg.)
Aspect ratio	10
Cruise speed (33000 ft/10 km), knots	277
Range (33000 ft/10 km) nm @	
Max cruise speed	1550 nm
Max range	1803 nm
Time to climb (33000 ft/10km), min	24

Performance estimates have been based on the expected attainable wetted area drag coefficient of 0.0045.

2. Definition of Mission Profiles

Two mission profiles were selected and are shown below. These missions are for standard day temperature conditions (ISA).

Mission 1 includes segments for taxi and take off, climb to cruise altitude, and descent to sea level. Allowances were made for a 45 minute reserve flown at long range power at cruise altitude. Cruise altitude is 25,000 feet (7.62 km) and maximum cruise power is used for the cruise segment. The climb, cruise and descent legs have a total range of 600 nautical miles.

Mission 2 is the same as Mission 1 except the climb, cruise and descent legs have a total duration of six hours and the cruise is accomplished with maximum range power.

Data set listings for these missions are included in Appendix D of Reference 1.

3. Definition of Criteria of Merit

The criteria of merit is the product of range and payload. This parameter results in a large number for a high payload carried a long distance. The larger the number the better the capability of the airplane. This parameter reflects the most common evaluation of an airplane's performance.

4. Production of Mission Analysis Simulation Model

A mission analysis simulation model was developed to allow operational evaluation of the basic aircraft configuration performance. The simulation program accounts for all phases of a flight from ground operation to cruise reserves.

The mission analysis program includes numerical representations of the engine, propeller and airframe performance. An engine model furnished by John Deere simulates engine performance. The propeller performance is predicted using a general propeller chart presented in Reference 2. The basic propeller chart was extrapolated for the low engine power operating region of some mission segments. Airplane drag is represented by a basic drag polar with skin friction and form factor drag as well as lift dependent drag.

The mission segments available in the program are ground, climb, cruise, descent and climb-cruise descent. The climb-cruise-descent segment combines the three mission flight segments to allow a time, fuel or distance constraint to be applied to the sum of the flight segment. Program output data sets to illustrate program utilization are provided in Reference 1. Complete program user input variable lists are included in Appendix A of Reference 1.

CONCLUSIONS

1. A representative, general aviation type airframe was sized and characterized. A multi-engine executive transport was selected to best demonstrate the advantages of the stratified-charge rotary engine. The airplane has a gross weight of 8000 pounds (3629 kg), a cruise speed of 277 knots at 33,000 feet (10 km), and a maximum range of 1803 nautical miles. The airplane was sized to make the most favorable comparison to current turboprop airplanes.
2. Two mission profiles were selected. Both mission include segments for taxi and take off, climb to cruise altitude of 25,000 feet (7.62km), and descent to sea level. In addition, there is a 45 minute fuel reserve. The first mission has a total range of 600 nautical miles, with maximum cruise power at cruise. The second mission has a total duration of six hours, with cruise at maximum range power.
3. The criterion of merit selected is the product of range and payload. This product reflects the most common evaluation of an airplane's performance. The larger the "product" the better the capability of the airplane.
4. A mission analysis program was written which will accept an engine performance subroutine and will provide aircraft mission performance. The program accounts for all phases of a flight from ground operation to cruise reserves. The program calculates the criterion of merit for the selected mission.

RECOMMENDATIONS

1. The analytical mission analysis program should be used concurrently in evaluating engine design alternatives. Design changes which impact engine envelope, gross weight, power output, or bsfc can be examined with the mission analysis program for effects of the changes on airplane configuration and or mission capability.

REFERENCES

1. Bernstorf, D., Zickhur, T., "Summary Report: Airplane Configuration and Analysis for the Stratified Charge Rotary Engine Study", Report #E24734, 16 Sept 1991, Beech Aircraft Corporation
2. Perkins, C.D., and Hage, R.E, "Airplane Performance, Stability and Control, "Wiley and Sons, Inc. New York, 1949

ENGINE LAPSE RATE

TYPICAL TURBOPROP VS DEERE ROTARY

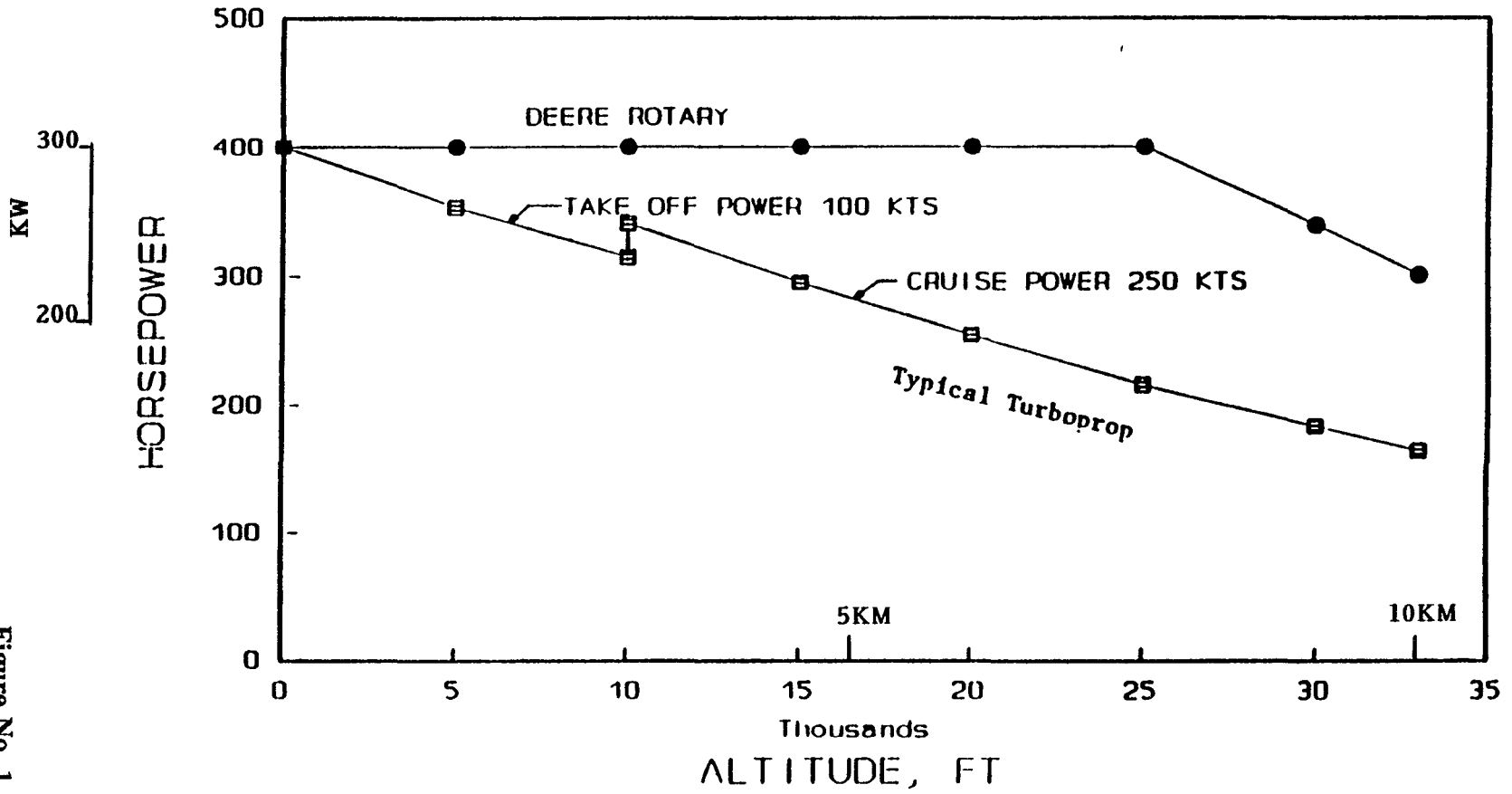
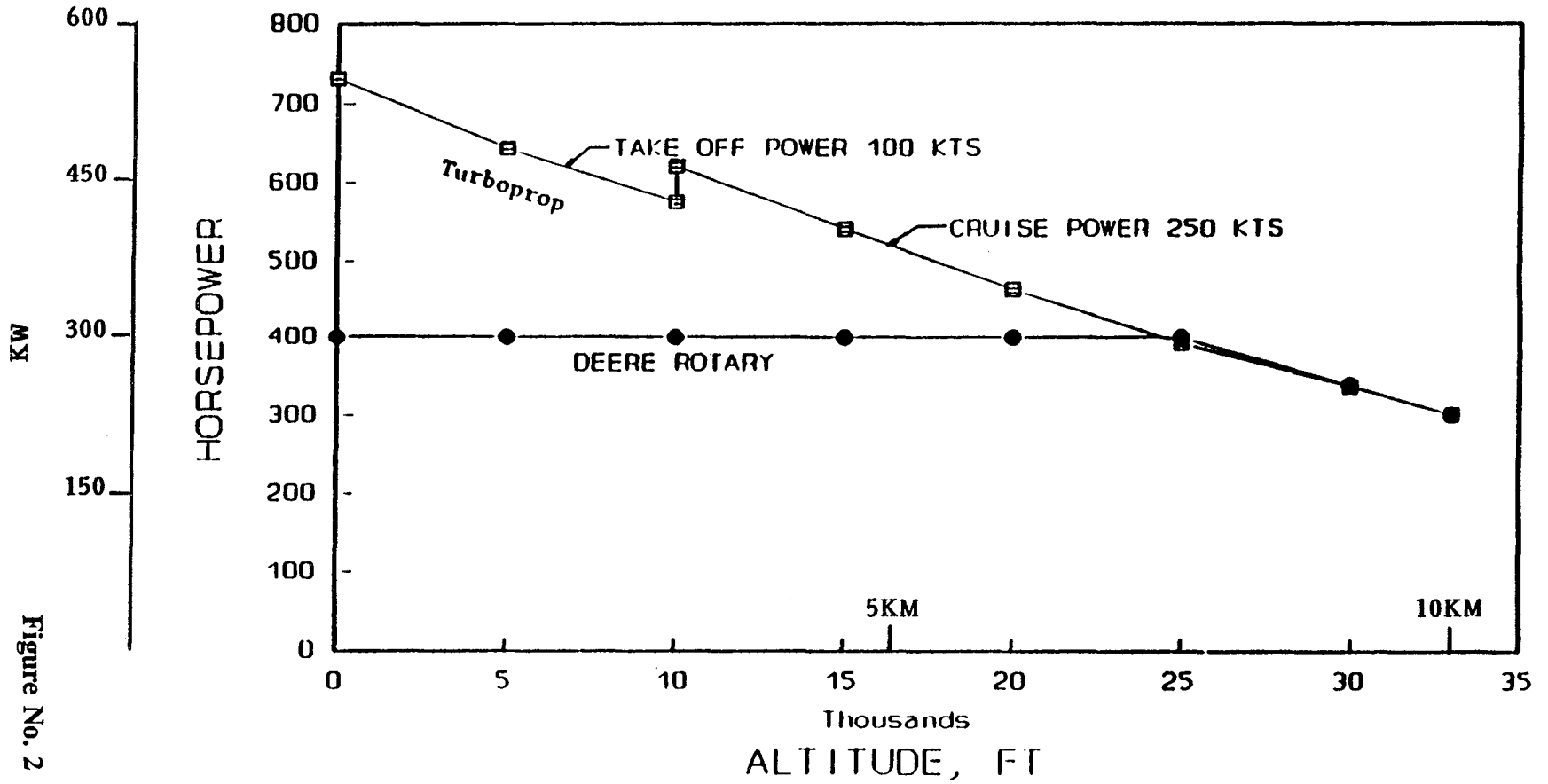


Figure No. 1

ENGINE LAPSE RATE

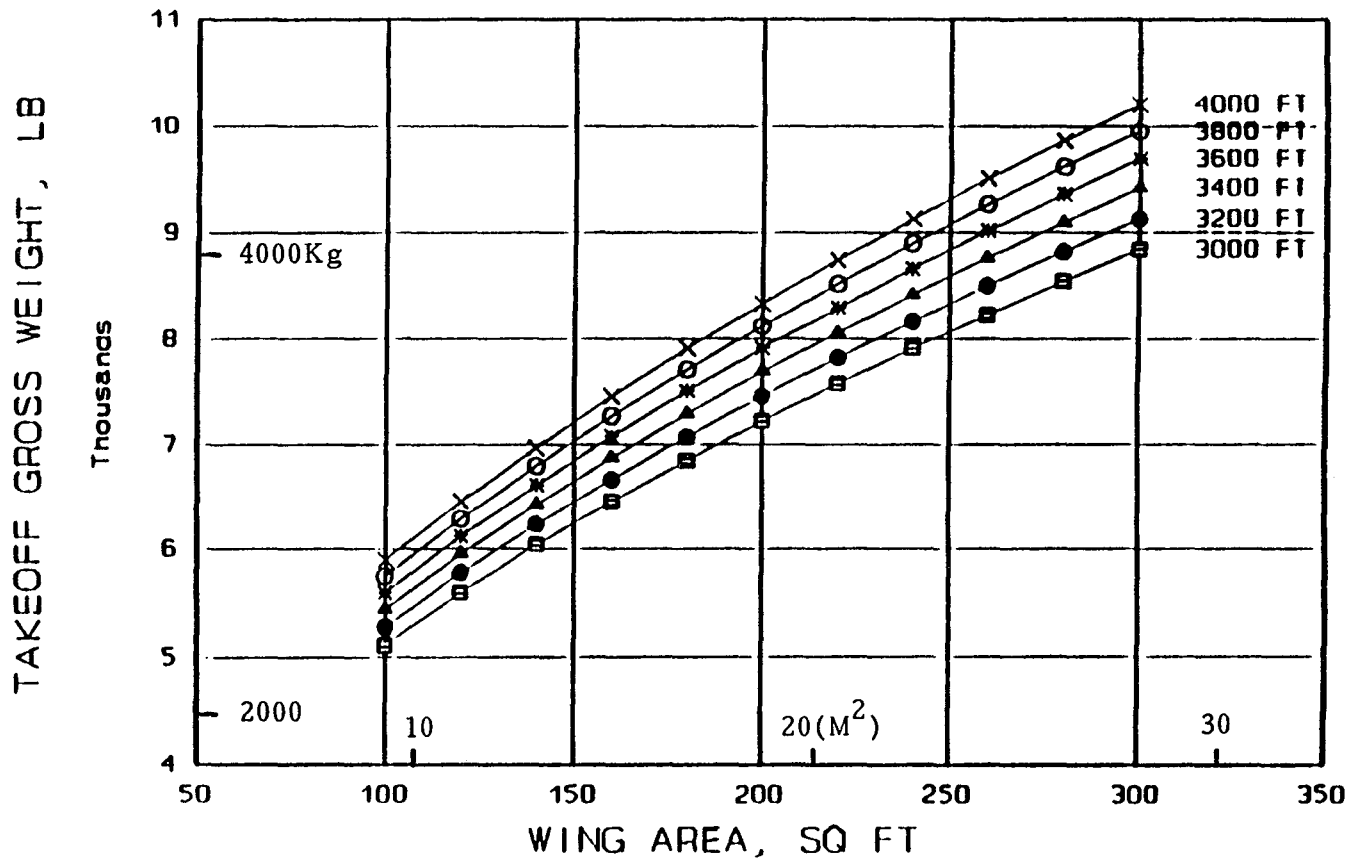
TYPICAL TURBOPROP VS DEERE ROTARY



250

Figure No. 2

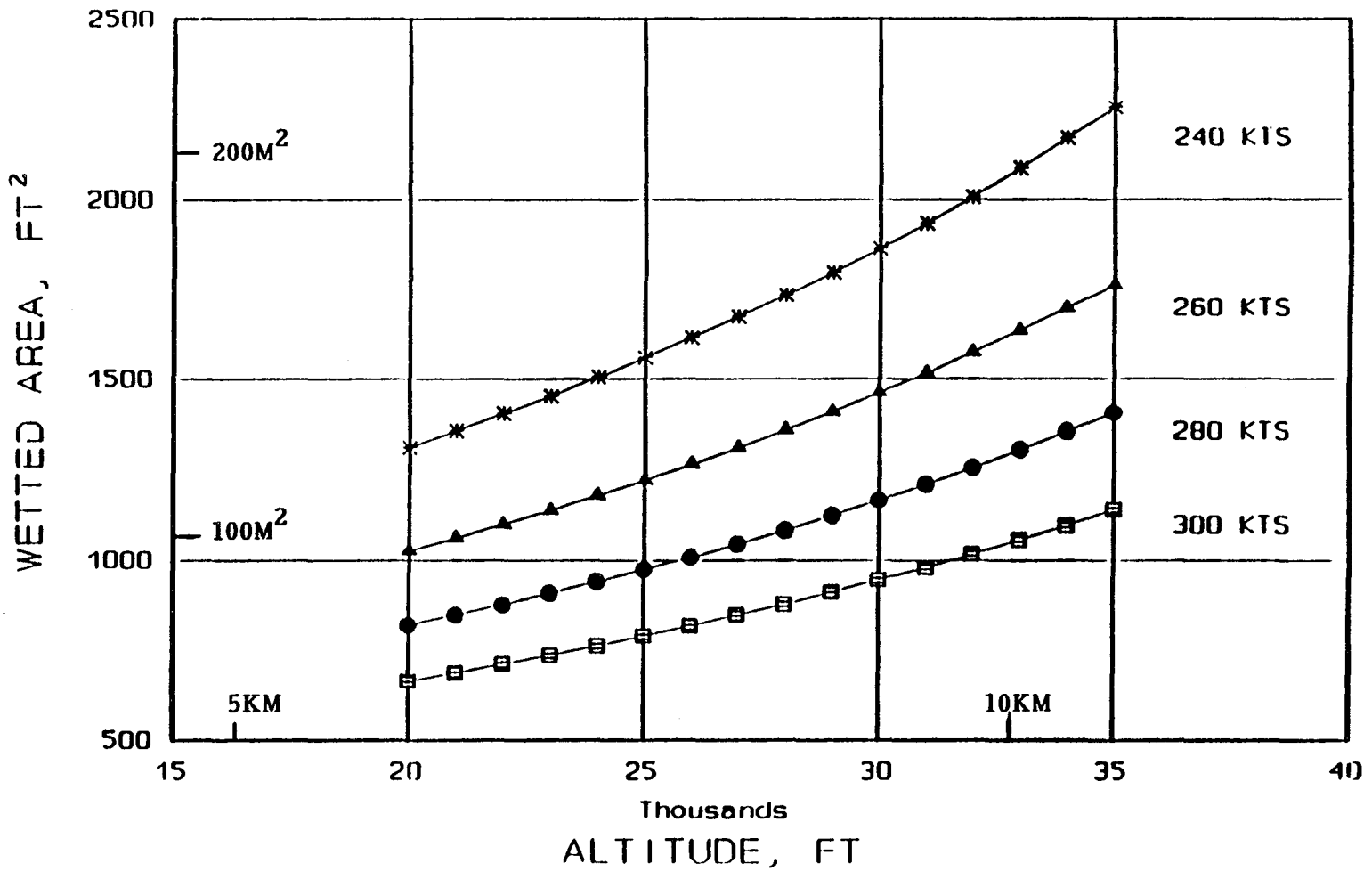
WEIGHT LIMITS FOR BALANCED FIELD LENGTH



$C_{lmax}=2.0$ $HP=392(2)$
 $K_w=294(2)$

Figure No. 3

WETTED AREA SIZING



Cfe = .0045

HP(INSTALLED) = 292(2)
 KM " 219(2)

Figure No. 4

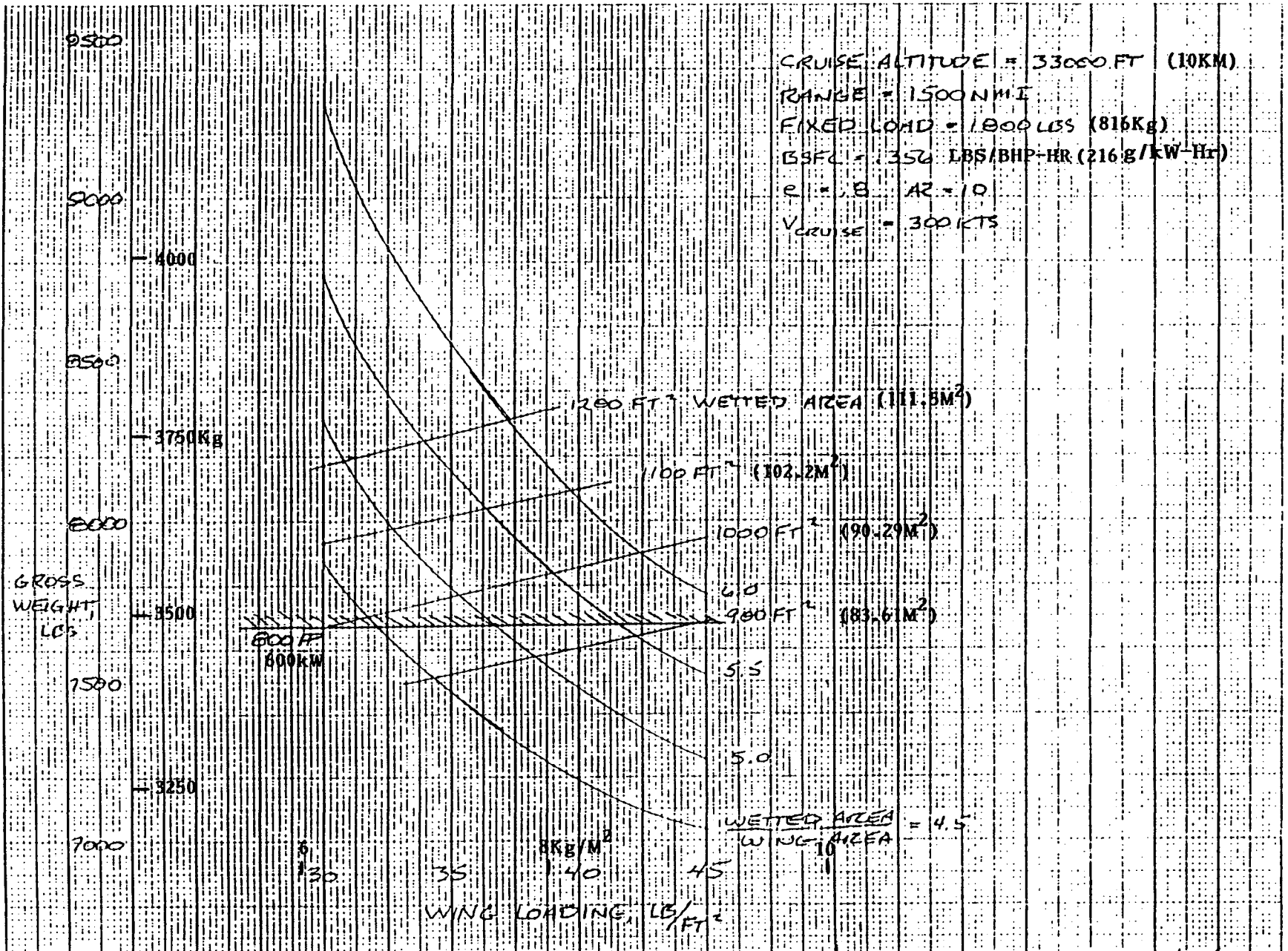


Figure No. 5

7/29/90

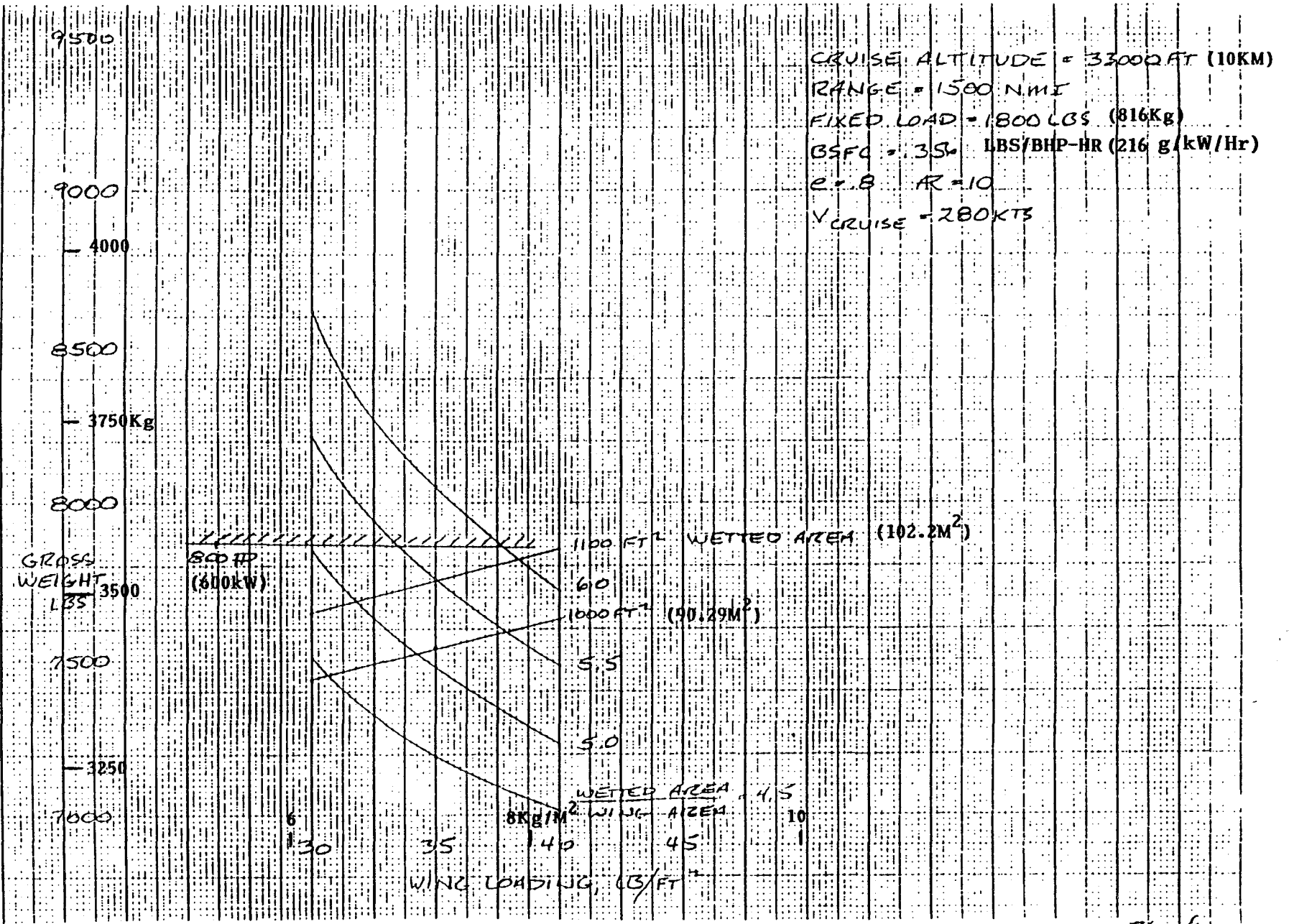
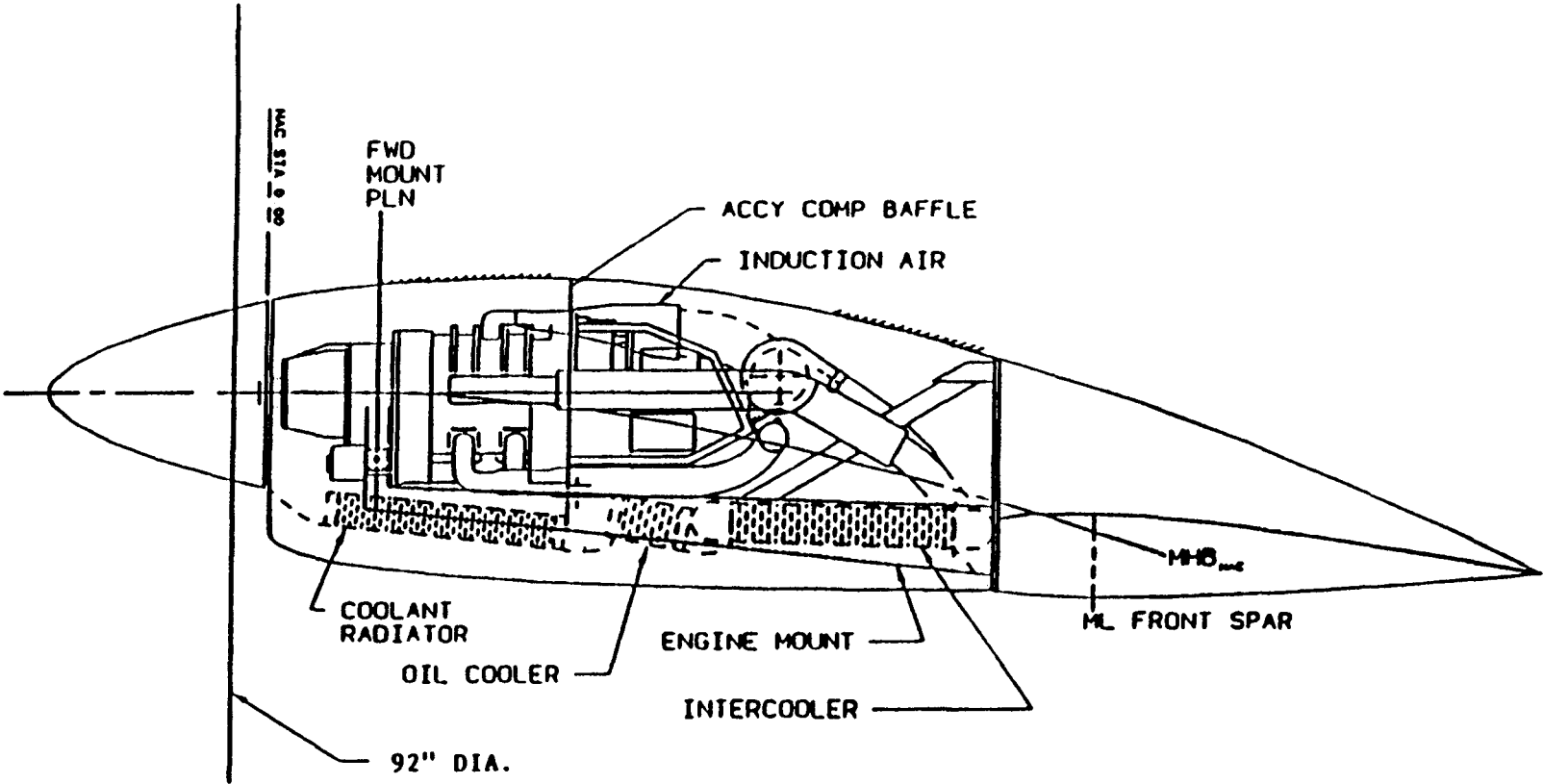


Figure No. 6

7/20/90

Rotary-Powered Twin Study



255

Figure No. 7



JOHN DEERE/NASA PROPELLER OPTIMIZATION
 PROPELLER SIZED FOR 72 DBA FLY-OVER NOISE
 AT 400BHP (300KW) 1000 FT. (304M) 119 KTAS

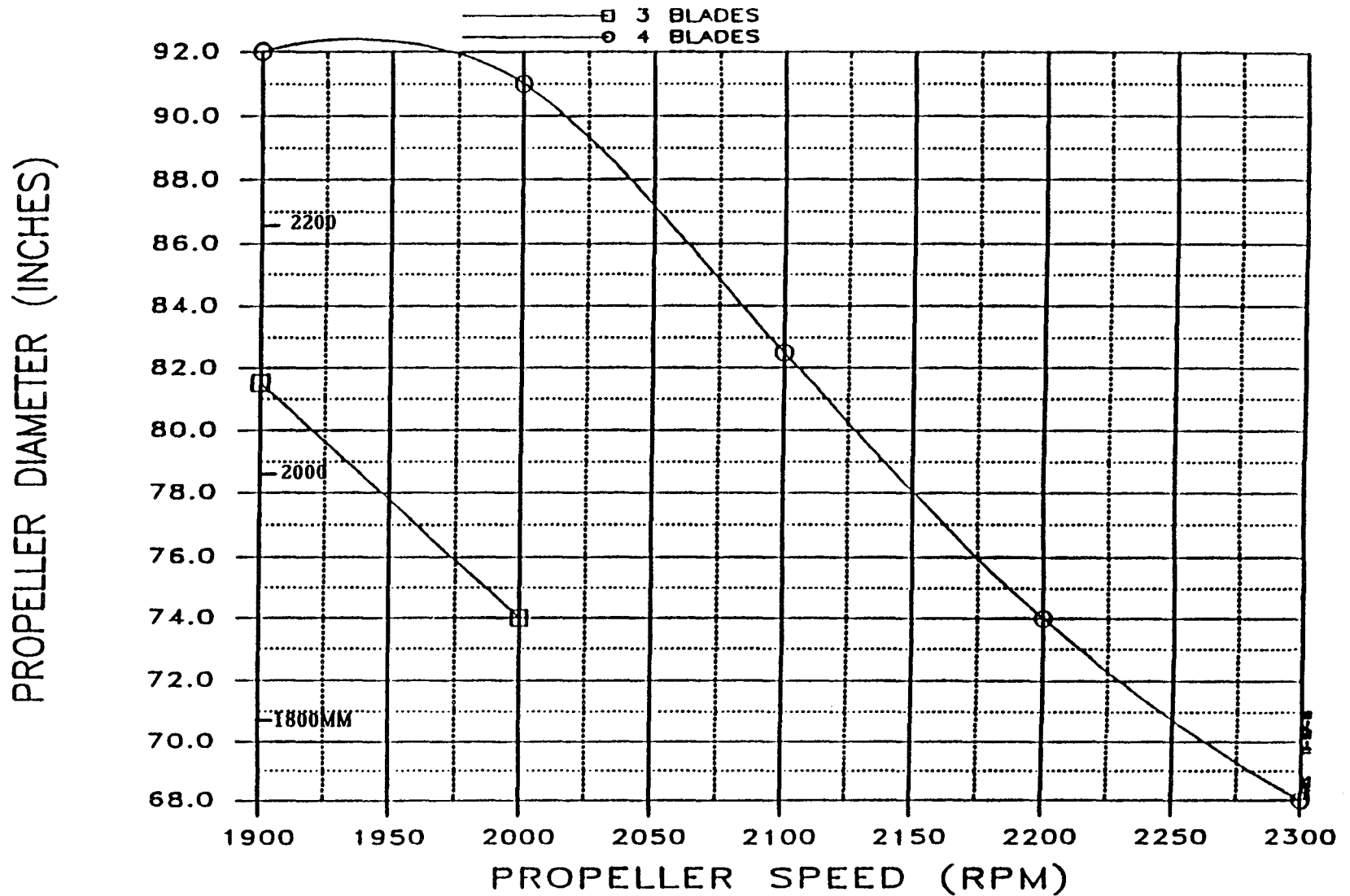


Figure No. 8

JOHN DEERE/NASA PROPELLER OPTIMIZATION
PROPELLER SIZED FOR 72 DBA FLY-OVER NOISE
TAKE-OFF, SEA LEVEL, ISA, 400SHP (300KW)

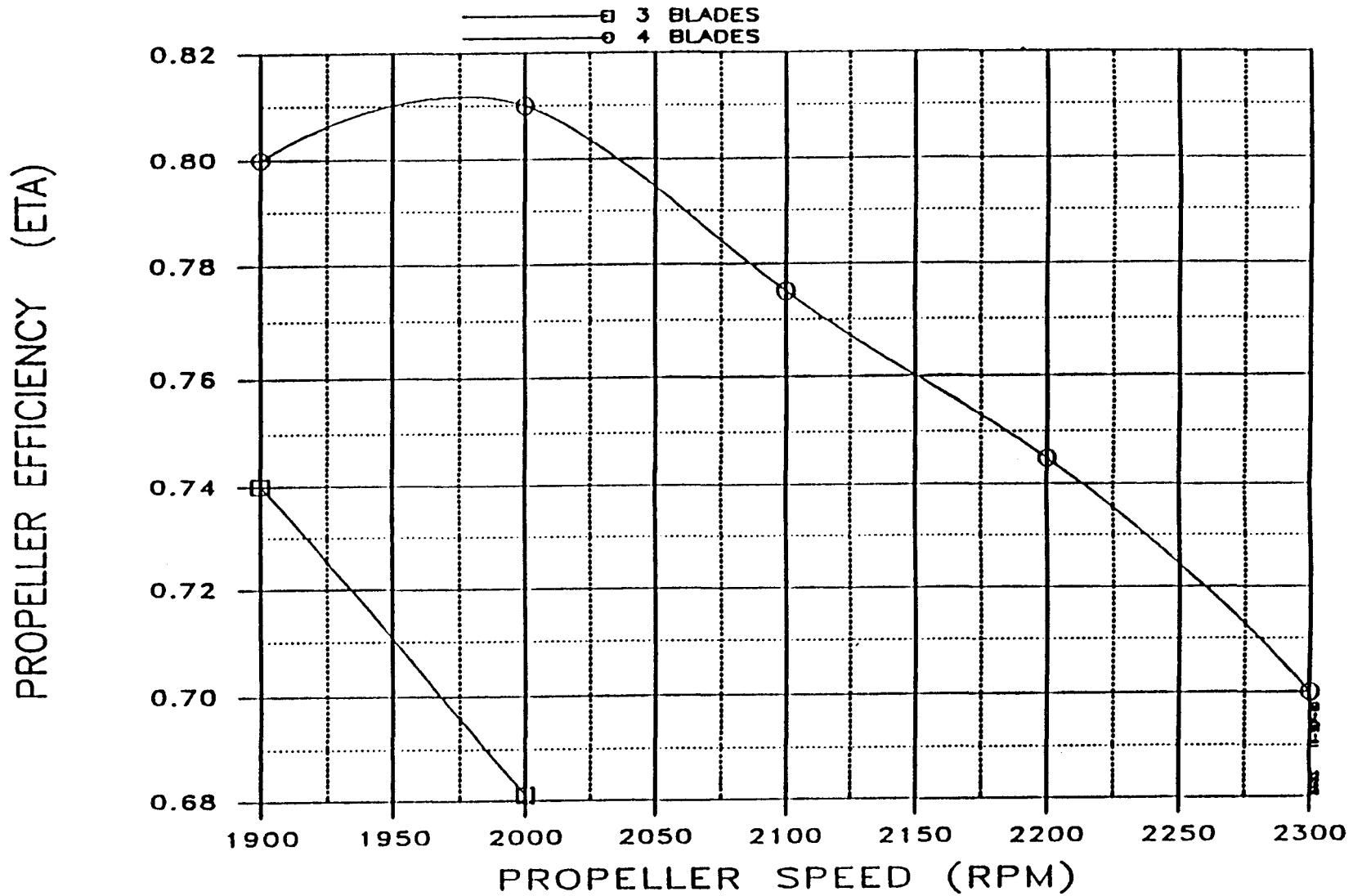


Figure No. 9

JOHN DEERE/NASA PROPELLER OPTIMIZATION
PROPELLER SIZED FOR 72 DBA FLY-OVER NOISE
CLIMB, 25,000 FT. (7.62KM) ISA, 400SHP (300KW)

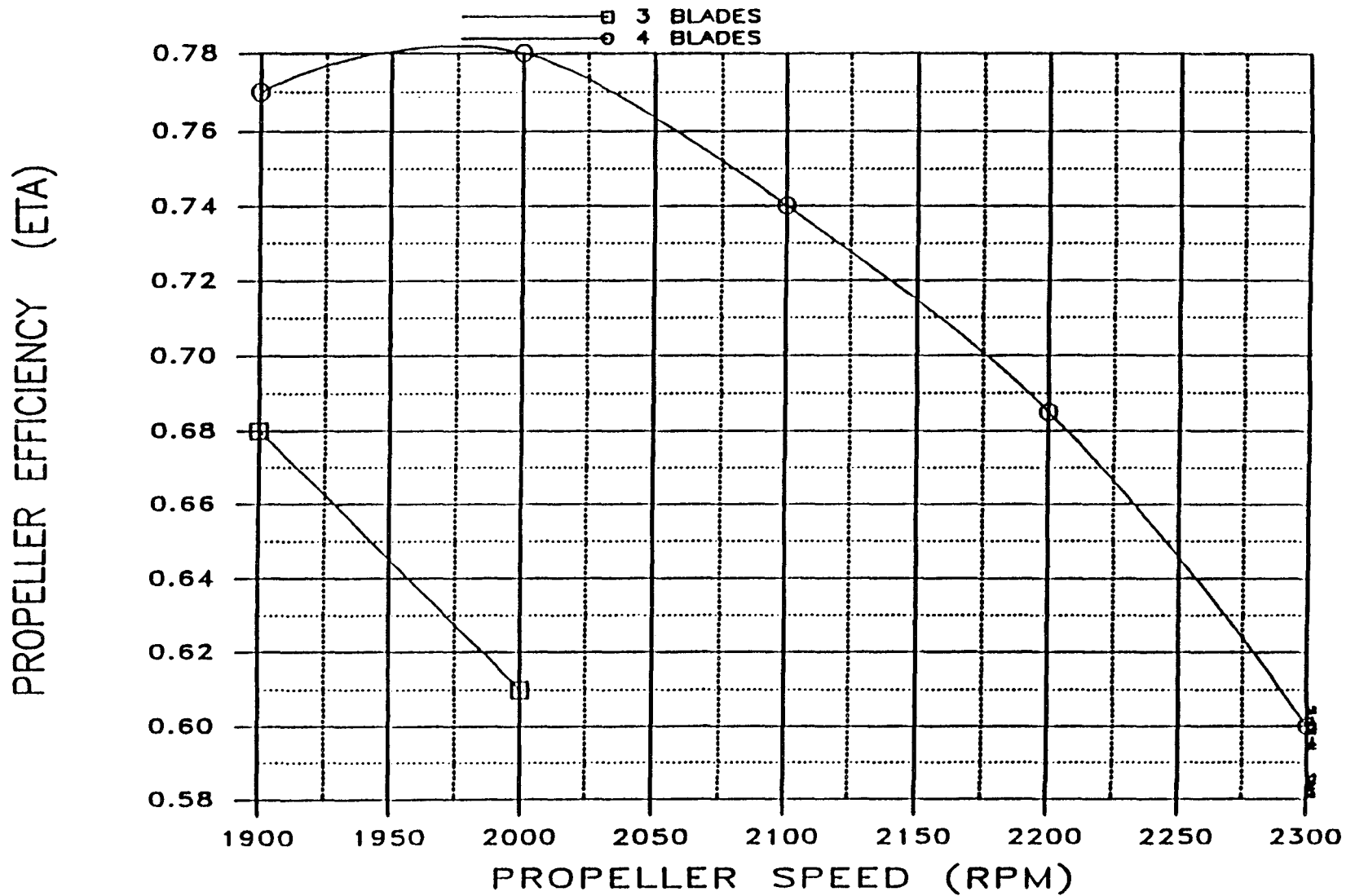


Figure No. 10

JOHN DEERE/NASA PROPELLER OPTIMIZATION
PROPELLER SIZED FOR 72 DBA FLY-OVER NOISE
CRUISE, 33,000 FT. (10KM) ISA, 300SHP (225KW)

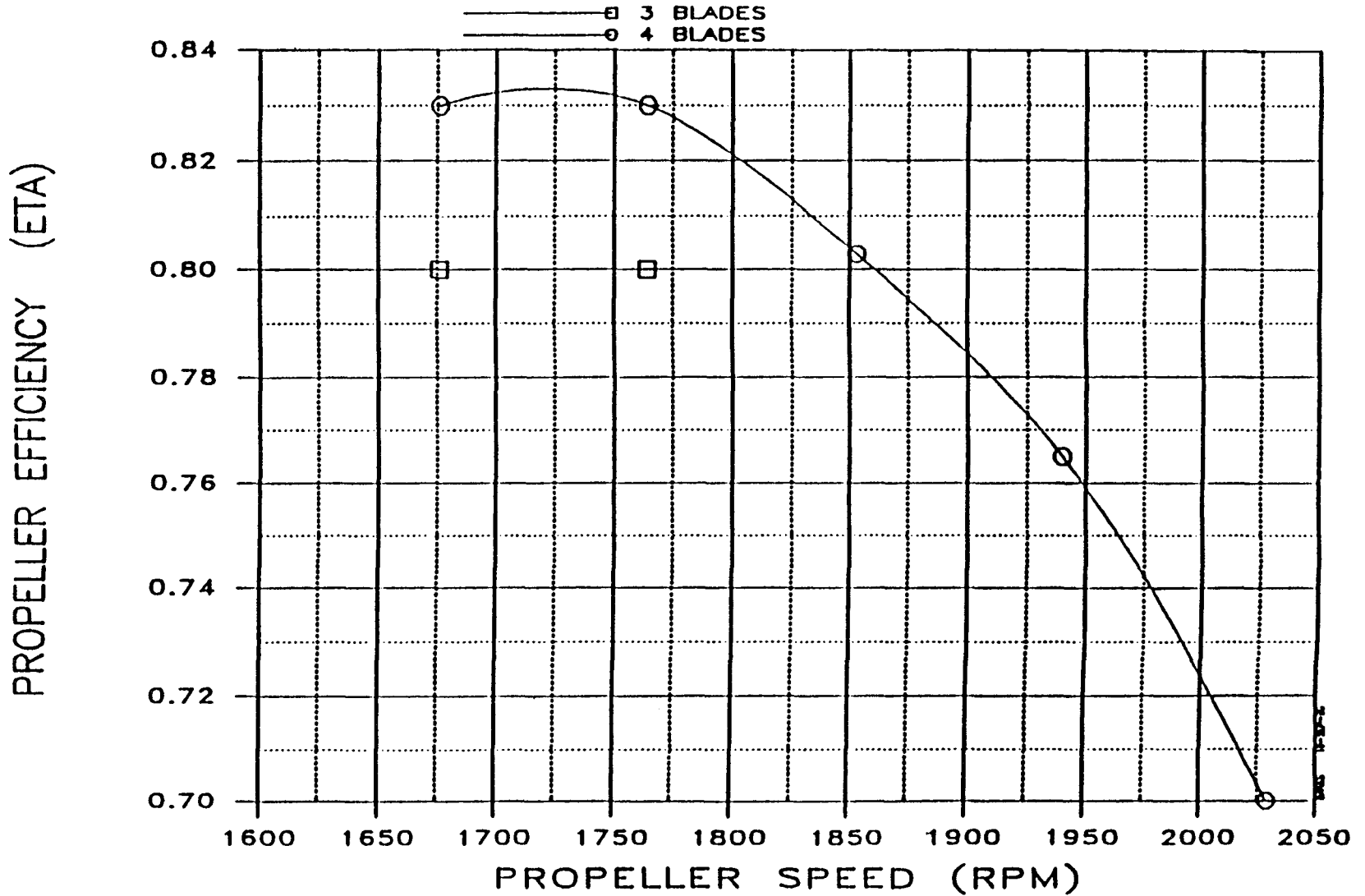


Figure No. 11

6.0 CONTROLS SYSTEM MODEL

PRECEDING PAGE BLANK NOT FILMED

PAGE 260 INTENTIONALLY BLANK

6.0 Controls System Model

INTRODUCTION

A subcontract was placed with Douglas Aircraft Company for purposes of investigating an advanced technology automatic control system for the overall basic engine system (including management of combustion, air, coolant, lube, fuel injection, propeller and accessory systems). The activity was terminated in the initial phase, "Technology Assessment" with re-direction of the overall technology enablement program as discussed in Section 2.0 Executive Summary.

Objectives

1. Minimize fuel consumption by:
 - Integrating the control of the entire system to take advantage of coupling effects that are neglected otherwise.
 - Designing a control system that gives minimum energy performance under disturbances such as gusts, torque load or altitude changes.
2. System monitoring and protection from overspeeding or overheating.
3. Providing diagnostics and maintenance assistance by logging occurrences of operation in critical performance areas; storing the information and taking action for safe operation.

Technical Approach

The workplan defined for this task consisted of four major tasks with appropriate subtasks.

1. Technology Assessment
2. Model Development
3. control System Development
4. Reporting

The schedule and identification of subtasks is presented in Figure 1. As noted in the schedule, activity was terminated shortly after the program start.

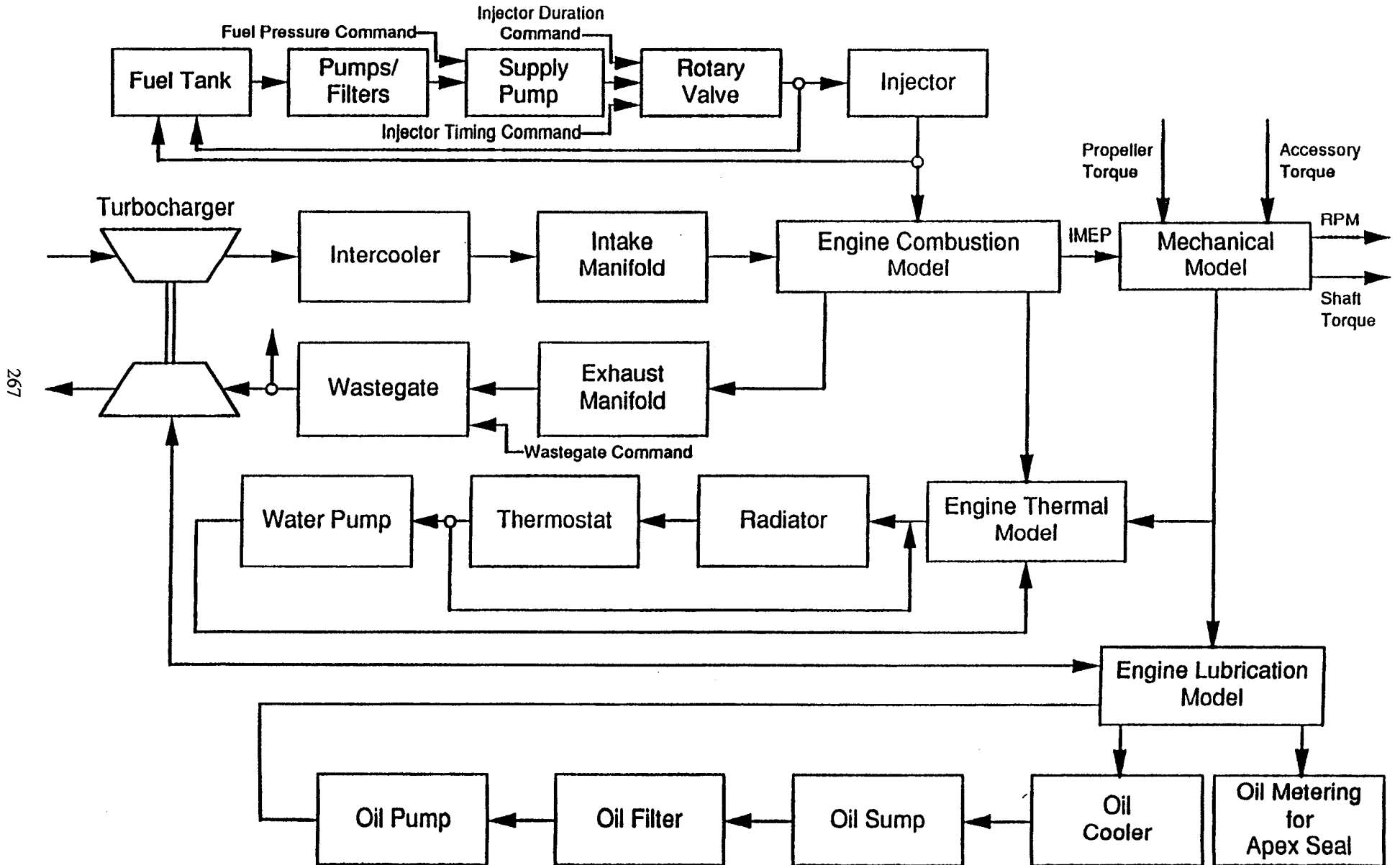
Results

1. The literature search was essentially completed in terms of identifying literature sources on rotary engine control, intermittent combustion and rotary engine modeling, multivariable control, fuel injection, ignition systems, apex seal lubrication systems, oil, coolant and fuel management systems and turbocharger control.
 - Acquired 150 Publications and Papers
 - Built Database
 - Entered Literature into Database
 - Reviewed and Documented 50% of Literature
 - Developed List of Additional Publications from References
 - Researchers Contacted
 - John Moska - University of Wisconsin
 - Engine Modelling for Real-Time Control
 - Nonlinear Control Theory Applied to Engines
 - Jeffrey Runde - General Motors, Allison Division
 - Automatic Transmission Modelling
 - Control of Automatic Transmissions
2. Discussions were held with the airframer (Beech Aircraft), the turbomachinery supplier (Sundstrand Aerospace) and the engine prime contractor (JDTI, Inc.) to acquire models and data related to the control analysis.
3. An engine system block diagram was established, Figure 2.
4. A list of controllable and measurable variables was jointly prepared with JDTI, Inc.
5. The MIT/Bartrand model was acquired and executed with only minor editing.
6. Simulation development was initiated.

Recommendations

1. Continue to developed a simulation to describe the dynamic behavior of the Stratified Charge Rotary Engine and its subsystems. The simulation can support the development and evaluation of control laws and logic and can encompass all expected control variables, significant sensed variable and operating parameters.

Engine System Block Diagram



7.0 TURBOMACHINERY

INTRODUCTION

Analytical studies of turbomachinery systems were conducted to determine the optimum overall system configuration appropriate to the critical technology enablement objectives. Primary requirements were 400 BHP (300kw) at take-off, maintained to 25,000 feet (7.57 km) and maximum cruise power (75%) maintained to 33,000 feet (10 km) altitude combined with the improved efficiency and reduced heat rejection requirements.

The task was subcontracted to Sundstrand Corporation and included assembly of component sizing and performance prediction models into a system analysis model for evaluation of candidate systems. Evaluation criteria were developed, and an optimization routine used to find the preferred configuration. The best turbomachinery configuration included a compounding turbine, which converts some of the exhaust energy to shaft power, as well as a turbocharger having two compressor stages driven by a single-stage turbine. The intake charge was intercooled between compressor stages and between the second compressor and the engine intake port. Intake manifold pressure control was effected by exhaust wastegate operations.

The System and Turbomachinery Development Task was divided into the following four subtasks:

Subtask 1 - System Analysis and Optimization.

Subtask 2 - Component and Subsystem Design

Subtask 3 - Subsystem Design

Subtask 4 - Component Verification

Subtask 1 involved analysis of various turbocharging and turbocompounding concepts and the selection of an optimum configuration.

The effort was terminated upon the completion of Subtask 1 due to redirection of the program as discussed in Section 2.0 Executive Summary.

OBJECTIVE

To identify an engine turbomachinery system capable of providing sufficient inlet air pressure boost for the Stratified Charge Rotary Engine to allow full power operation to a 25,000 foot (7.57 km) altitude, and 75 percent power for cruise up to 33,000 (10 km) feet altitude. The turbomachinery should provide the required altitude capability with minimum adverse effects upon the engine brake specific fuel consumption.

TECHNICAL APPROACH

The design and sizing analysis of the turbomachinery system was divided into three phases.

1. Identify the Candidate Systems
2. Develop an Analytical Model
3. System Evaluation and Selection

The technical approach for each phase is summarized herein.

1. Identify the Candidate Systems

Models of candidate turbomachinery systems were constructed to estimate and optimize characteristics of components. These system configurations were combined into a thermodynamic analysis computer program which balances component functions and computes system parameters. A typical turbomachinery system for a rotary engine is shown in Figure 1. This system, like all systems evaluated, employs various turbine and compressor stages, heat exchangers, charge air lines, and ram air ducts. A gearbox is employed for the power turbine options. Each component type is modeled by unique component computer subroutines which predict component size and weight. Most of the routines perform heat transfer and thermodynamic analysis for the individual components.

Several types and arrangements of turbomachinery equipment were considered for the stratified charge rotary engine. The system shown in Figure 1 is an example of a simple, thermodynamically complete turbomachinery system for a turbocompounded, turbocharged engine system.

Different candidate system arrangements can be devised from this system by varying the number of compression stages, the number of turbine stages, the order in which the exhaust gases pass through the turbines, and the presence or absence of the power turbine which provides the turbocompounding.

A number of candidate system configurations were identified. Three configurations were deemed appropriate for further evaluation. These were:

- 1) Multiple Spool System - Composed of two conventional turbochargers, each having a single compressor stage and a single turbine stage, with intercooling after each compressor stage.

- 2) Multiple Stage System - Similar to the Multiple Spool System, but combines the two compressors on a single shaft driven by a single turbine.
- 3) Single Stage System - is similar to the above, but uses only a single stage of compression.

The three configurations were evaluated by themselves and combined with a power recovery turbine placed in the exhaust stream between the engine exhaust port and the turbocharger turbines. The power recovery turbine provides the turbocompounding effect by extracting excess power from the exhaust and adding it to the engine output shaft through a gearbox. Preliminary analysis indicates that there is significant gas power available for turbocompounding, and that this function may be necessary to achieve the engine BSFC goal. The three candidate systems selected are shown in Figure 2.

In Figure 3 are shown four other schematics which were proposed but discarded for various reasons. The first configuration is like the basic multiple spool configuration, but uses an additional valve to control the compressor flow split. This causes additional compressor matching problems without adding any performance to the system. The second schematic, REDIV Alternate 2, suggests using a variable geometry turbine instead of wastegate control and an axial/centrifugal compressor. This is thermodynamically equivalent to the multistage turbocharger at design operation, which is the only operating condition analyzed to date. Some operational (off-design) advantages may accrue from using variable geometry instead of wastegate control. Controls would be more complex, and development would be necessary. The three equal turbocharger schematic was proposed as a potential approach for constructing a ground test article to demonstrate thermodynamic performance. The additional pieces of hardware and plumbing would make it impractical for aircraft installation. The alternate turbocompound schematic illustrates the potential for positioning the power turbine last in the exhaust, instead of first. This is suggested in the literature as a technique for improving engine throttle response, because it tends to maintain turbocharger turbine pressure ratios at a more constant level. However, it also eliminates the increase in turbocharger output with increasing altitude, which is an absolute must for the aircraft engine.

2. Develop the Analytical Model

A turbomachinery system model was developed to predict the performance characteristics of each of the candidate systems. Each element within each candidate system was characterized in terms of weight, volume and performance. The system elements modeled include the turbines and compressors, heat exchangers, air ducts, exhaust pulses and gearbox. A separate system model was prepared for each of the three candidate systems.

The system analysis modeling program calculates candidate system operating conditions and provides an optimization routine. A system schematic with various configuration options is shown in Figure 4. The analysis program calculates system state points (temperature, pressure, and flow rate) at the numbered locations shown in Figure 4. The calculated state points are based on the input design conditions, design constraints, and the current values of optimization parameters. The system model then calls the various component sizing models to size the components based on the calculated state points.

An equivalent power function is calculated for each candidate system. The equivalent power function is evaluated from the resultant values (from the system analysis) of engine exit pressure, power turbine power, incurred drag and fixed weight. The equivalent power predicts the usable power (net power) supplied to the airframe.

An optimization routine is included in the system analysis computer program. The optimization routine varies the system optimization parameters until the equivalent power is maximized. A flow chart of the system model analysis program is provided in Figure 5. The system model thus maximizes equivalent power for each candidate system. Comparison of equivalent power calculated for each candidate system enables selection of a "best" turbomachinery system configuration.

3. System Evaluation and Selection

The final system evaluation and selection process encompassed the following three steps:

- a. Identify the design conditions
- b. Establish the optimization criteria
- c. Establish parametric factors affecting system optimization criteria.

A synopsis of the above three steps is provided in the following paragraphs.

a. Identify the design conditions

Evaluation of the turbomachinery candidate systems requires establishing design conditions which constrain the system operation. The basis for the system evaluation selected is the specified full power output operation capability at 25,000 foot (7.57 km) altitude (25,000 feet (7.57km) climb). The design conditions established for the 25,000 foot (7.57 km) climb are listed in Table 1. A secondary set of assumed physical design constraints were established for the air handling ducts. These assumed design constraints are listed in Table 2. Further discussion of development of the design

condition (especially conditions downstream of the propeller wash) are provided in reference 1.

b. Establish the Optimization Criteria

Optimization of the turbomachinery system by the selected mathematical system analysis requires an objective function which varies smoothly with the independent system parameters. The turbocharger system imposes three penalties on the airframe and engine. These penalties are the system's fixed weight, the drag incurred by the ram air cooled heat exchangers, and the back pressure imposed at the engine exhaust. An optimization algorithm must balance the benefits of increased propulsive power or efficiency provided by the turbomachinery against the penalties incurred. The ram drag of the system, drag due to lift incurred by system weights, engine power changes due to exhaust pressure changes, and power turbine power contributions can all be combined into a single expression for net output power due to the turbomachinery system.

The NASA contract for development of the stratified charge rotary engine set goals for power, weight, and fuel consumption of the entire system. However, allotments for the turbomachinery were not specified, nor was any guidance provided in evaluating system tradeoffs. The "best" turbomachinery for the purposes of this contract will therefore be the one which maximizes installed thrust minus drag.

The net effect of the turbomachinery system on engine shaft power available for propulsion is obtained by converting net drag to a (negative) thrust power and adding this value to the net power. The final expression of equivalent power provides the numerical basis for evaluation of the candidate systems.

Table 1
Design Conditions
25,000 ft. (7.57km) climb

Ambient	
Pressure	5.46 psia (37.62 kPa)
Temperature	6.71° F (-14° C)
Mach number	0.267
Downstream of Propeller	
Pressure (Psia)	5.84 psia (40.2 kPa)
Total Temperature	16.14 ° F (-8.8° C)
Mach number	0.311
Engine air requirements	
Inlet temperature	140.00 ° F (60° C)
Inlet flow rate	70.55 lbm/min (32 Kg/Min)
Inlet Pressure	34.90 psia (240 kPa)
Exit temperature	1154.00 ° F (623° C)
Exit flow rate	72.84 lbm/min (35 Kg/min)
Engine parameters	
Propeller efficiency	0.83
Displaced volume	0.046 ft ³ (.0013m ³)
Engine Speed (rpm)	8500.00
Exit pressure for 400 HP (300kw)	30.60 psia (211 kPa)
Aircraft lift over drag	11.20

Table 2
Assumed Design Constraints

Charge Air Ducts	
Compression side	
Length	5.00 ft (1.52m)
Material	Al
Wall thickness	0.03125 in. (.794mm)
Density	172.80 lbm/ft ³ (2.19 kg/m ³)
conductivity (Btu/hr ft ° F)	110.00
Expansion side	
Length	3.00 ft (0.91m)
Material	Steel
Wall thickness	0.03125 in (0.79mm)
Density	499.50 lbm/ft ³ (6.34 kg/m ³)
Conductivity (Btu/hr ft ° F)	8.67
Insulation	
Density	11.90
Conductivity (BTU/hr ft ° F)	0.10
Inlet and Exit	
Inlet diffuser half angle (deg)	10.00
Exit nozzle half angle (deg)	10.00
Ratio of nozzle exit to freestream momentum	1.0
Heat loss to surroundings	
Heat transfer coefficient (Btu/hr ft ² ° F)	2.0
Ram air heat exchanger cooling duct	
Inlet diffuser half angle (deg)	10.00
Angle of exit flow relative to free stream	0.00

c. Establish Parametric Evaluation Factors

Nine parameters have been identified which affect the optimization function, as well as penalty factors of weight, drag, and engine exhaust pressure. Some parameters affect one or two of these penalty factors. The optimization parameters are listed below along a description of the penalty factors they affect.

1. First stage compression ration	affects system weight and engine exit pressure (net power); affects heat exchanger size which has only slight effect on incurred drag
2. Intercooler charge air exit temperature	same effects as above
3. Inter/aftercooler charge air side pressure drop	trades heat exchanger weight against engine exit pressure (net power); affects heat exchanger size which has only slight effect on incurred drag
4. Duct mach number	trades duct weight against engine exit pressure (net power); no effect on incurred drag
5. Power supplied to prop shaft from power turbine	affects power turbine weight (and system weight slightly) and engine exit pressure (net power); no effect on incurred drag
6. Expansion side duct insulation thickness	trades weight of insulation against engine exit pressure (net power); no effect on incurred drag
7. Inter/aftercooler air side pressure drop	trades weight of heat exchangers against ram air drag; no effect on engine exit pressure (net power)
8. Intercooler air flow rate	trades weight of heat exchangers against ram air drag; no effect on engine exit pressure (net power)
9. Aftercooler air flow rate	trades weight of heat exchangers against ram air drag; no effect on engine exit pressure (net power)

ORIGINAL PAGE IS
OF POOR QUALITY

The effects of each of the optimization parameters was examined individually. Several were found to have optima which fell into narrow ranges and could be fixed for system optimization studies.

The dual stage turbocharger system (two compressor stages driven by one turbine stage) was used for evaluating the effects of insulation thickness, pressure ratio split, intercooler charge air exit temperature, and air side pressure drop and flow rate through the intercooler and aftercooler on net drag, net power and equivalent power. Turbocompounding was not included, inter/aftercooler charge air side pressure drop was set to 0.125 psid, and duct Mach number was set to 0.175 for this set of optimization studies.

Insulation Thickness:

As insulation is added to the exhaust ducts, less thermal energy is lost and lower engine back pressure is required to drive the turbines, resulting in a net power increase. However, duct weight and net drag increase. The net effect is for equivalent power to drop as insulation thickness is increased. Therefore, insulation thickness is set to zero since this leads to maximum equivalent power.

Compressor Pressure Ratio Split:

Over a wide range of the other optimization parameters, the first stage compression ratio (Pr) is optimal between 3.6 and 3.8 for maximum equivalent power. Pressure ratio was, therefore, fixed at 3.7.

Ram Air Heat Exchanger Pressure Drop:

As intercooler and aftercooler air side pressure drop (ΔP_c) increases, heat exchanger weight decreases but ram air drag increases. Only net drag is effected. A value of ΔP_c of 0.1 psid was found to be optimal for minimum net drag.

Intercooling:

The intercooler charge air exit temperature was examined for its effect on net power, net drag, and equivalent power. For each exit temperature the inter/aftercooler ram air flow rates are optimized for minimum net drag. Over an exit temperature range from 140.0° F to 210.0° F (60 to 99° C), the resultant equivalent power is constant within 0.7%. The charge air exit temperature is set to 150.0° F (66° C) since it yields high net power. The intercooler and aftercooler flow rates for which net drag is minimized for the 150.0° F (66° C) exit temperature are 53.3 and 54.7 lbm/min (24.2 and 24.8 kg/min) respectively.

Charge Air Heat Exchanger/Duct Pressure Drop:

The optimal values of intercooler/aftercooler charge air pressure drop, duct mach number, and turbocompounding power remain to be determined. The previously discussed optimization parameters will remain fixed for this analysis. The power turbine is placed upstream of the turbocharger as this minimizes power turbine weight with little effect on the turbocharger. Normalized parameters for heat exchanger pressure drop and Mach number were utilized to allow varying the two parameters together systematically. Normalized pressure drops from 0.05 to 0.25 psid (0.34 to 1.72 kPa) and normalized Mach numbers from 0.10 to 0.30 were examined. As the pressure drop and Mach number increase the heat exchangers and duct weights decrease, which result in a net drag decrease. However, power must be expended to overcome the increased charge air pressure drops, and thus net power is decreased. The resultant equivalent power curves, shown with net power and net drag curves in Figure 6, are nearly flat with a slight maximum between 25 and 50% of the pressure drop range. The equivalent power decreases at higher pressure drops. thus values of 0.125 psid (0.86 kPa) and 0.175 Mach number are chosen for charge air pressure drop and duct Mach number respectively.

Power Turbine Power:

Power turbine power is indicated by the coding numbers on the curves, in tens of horsepower (e.g., the curve having the numeral "4" embedded in it indicates a fixed power turbine power of 40 horsepower). With increasing power turbine power, net power increases. Net drag at first increases; there is a jump in weight, and thus in net drag from zero power (no turbine or gearbox) to finite power output. Then net drag decreases as increasing power turbine pressure ratios (at fixed flow) result in faster, smaller turbines. Equivalent power decreases with the initial addition of hardware between zero and non-zero turbine power, then increases. Net and equivalent power increase monotonically with increasing power turbine power, seemingly indicating very large power availability. However, there is probably a practical limit at back pressures sufficiently high (exhaust pressures near engine inlet pressure) to cause engine scavenging difficulties. The inlet and exhaust pressures specified by REDIV (34.9 and 30.6 psia (240 and 211 kPa), respectively) are shown on the net power plot. they show a practical power turbine maximum design power to be in the 50-60 horsepower (37.5-45 kw) range (with NO pulse effects), with resulting equivalent power of 35-40 horsepower (26.2-30kw).

Figure 7 shows the effect of ΔP_{hx} and M_d , again using the parameter k , at various levels of turbocompounding power, on net drag, net power, and equivalent power with initial estimates of pressure pulse effects included. The trends are the same as those with pressure pulse effects neglected, however the levels of available power turbine power are increased to 65-80 horsepower (48.7-60kw). Both net power and equivalent power are increased by 15-20 horsepower (11.25-15 kw) by pulse effects. (Although incomplete, the pressure pulse analysis indicated that even higher turbine powers should be available with pulse recovery.)

In summary, the power turbine analysis shows equivalent power gains of 35 horsepower (26.2 kw) (minimum, steady flow) to 60 horsepower (45 kw) (maximum, initial pulse analysis), or more. These gains represent recovery of 12-20 percent of the rotary engine shaft power from its wasted exhaust energy; inclusion of the power turbine in the optimum system would seem to be mandatory. Some further pulse analysis, in conjunction with installation design, is needed to quantify the achievable turbocompounding benefit.

RESULTS

The system analysis program was used to characterize the three candidate systems previously shown in Figure 2. These systems are the multiple spool, multistage, and single stage turbochargers, each in a system utilizing a power turbine upstream of the turbocharger(s) for turbocompounding. The calculated equivalent powers for the three optimized systems are shown in Figure 8.

The dual stage configuration leads to the highest value of equivalent power by a modest amount (16 percent higher than that of the dual spool). The single stage system, expected to be potentially the best, falls midway between the others. Relative to the dual stage configuration, the single stage system suffers from somewhat poorer thermodynamic performance (no intercooling) as well as high aftercooler weight resulting from the need to use steel materials at the high compressor outlet temperature.

Since the equivalent power does not indicate a clear advantage for one of the configurations, others factors, such as reliability, cost, off design performance, should be considered. Table 3 lists some of the other advantages and disadvantages of the three configurations.

Table 3

System Configuration Tradeoffs

Dual spool	-	Largest regions of shaft speed where speed match is possible. Allows each turbine and compressor to be run at near optimal speed for best efficiency.
	-	Lowest engine back pressure
	-	Good performance range for off-design operation
	-	Most complex, highest weight
Dual stage	-	Smaller region of shaft speed where speed match is possible. More difficult to get all turbomachinery elements to optimal speed for best efficiency
	-	Good performance range for off-design operation
	-	Low engine back pressure
	-	Simple and low weight
Single stage	-	Simple and low weight
	-	High engine back pressure
	-	Narrower performance range for off-design operation
	-	Very narrow region of shaft speed where speed match is possible. May not be possible to get both wheels to optimal speed for best efficiency
	-	High compressor and turbine tip speeds (high stress)

CONCLUSIONS

1. The dual stage turbocharging configuration with an upstream turbocompounding (power) turbine is preferred for its high equivalent power, good off-design operating performance range, and reasonable simplicity. The recovery of pulse power leads to substantial increases in power turbine output, so the system should be designed to fully utilize this power. The power turbine can provide at least 60 to 80 hp (45 to 60 kw), while keeping the engine back pressure between 30.6 psia and 34.9 psia (211 and 240 kPa).
2. The selected turbomachinery system configuration incorporates a turbocharger consisting of two compressor stages and one turbine stage on a single shaft, intercooling after each compressor stage, and a compounding turbine upstream of the turbocharger (at the engine exhaust). The system is estimated to weigh 206.50 lbm (93.66 Kg), to impose a net ram drag of 5.05 lbf (22.46N) on the aircraft, and to produce 49.4 hp (37 kw) of shaft power through turbocompounding (increasing engine output).
3. The contract for development of the SCRE turbomachinery system set goals for power output, weight and fuel consumption of the entire engine system. Allotments for the turbomachinery system were not known, nor was any guidance provided for establishing priorities among available design tradeoffs. Re-evaluation of the engine total system and turbomachinery priorities may result in selection of a different configuration for the turbomachinery system.

RECOMMENDATIONS

Additional analytical efforts are needed to better quantify exhaust pulse effects, which apparently will significantly affect turbomachinery sizing and power output. Additionally, an off-design system analysis should be performed to learn how the proposed system configuration(s) perform at lower altitudes and lower throttle settings. These conditions will determine control schedules and may have an impact on proper turbomachinery matching.

REFERENCE

Volume II, Appendix C

Engineering Report, "Turbomachinery System Analysis For Stratified Charge Rotary Engine Critical Technology Enablement", R.O. Brennan, Sundstrand Aerospace Corporation, 4 October 91.

LIST OF FIGURES

- FIGURE 1 TURBOCOMPOUND ENGINE
- FIGURE 2 TURBOCOMPOUND CANDIDATE SYSTEMS
- FIGURE 3 ALTERNATE CANDIDATE SYSTEMS
- FIGURE 4 TURBOMACHINERY SYSTEM STATE POINTS
- FIGURE 5 SYSTEM ANALYSIS PROGRAM FLOW CHART
- FIGURE 6 EFFECT OF CHARGE AIR PRESSURE DROP (NO PULSE EFFECTS)
- FIGURE 7 EFFECT OF CHARGE AIR PRESSURE DROP (WITH PULSE EFFECTS)
- FIGURE 8 SYSTEM COMPARISON

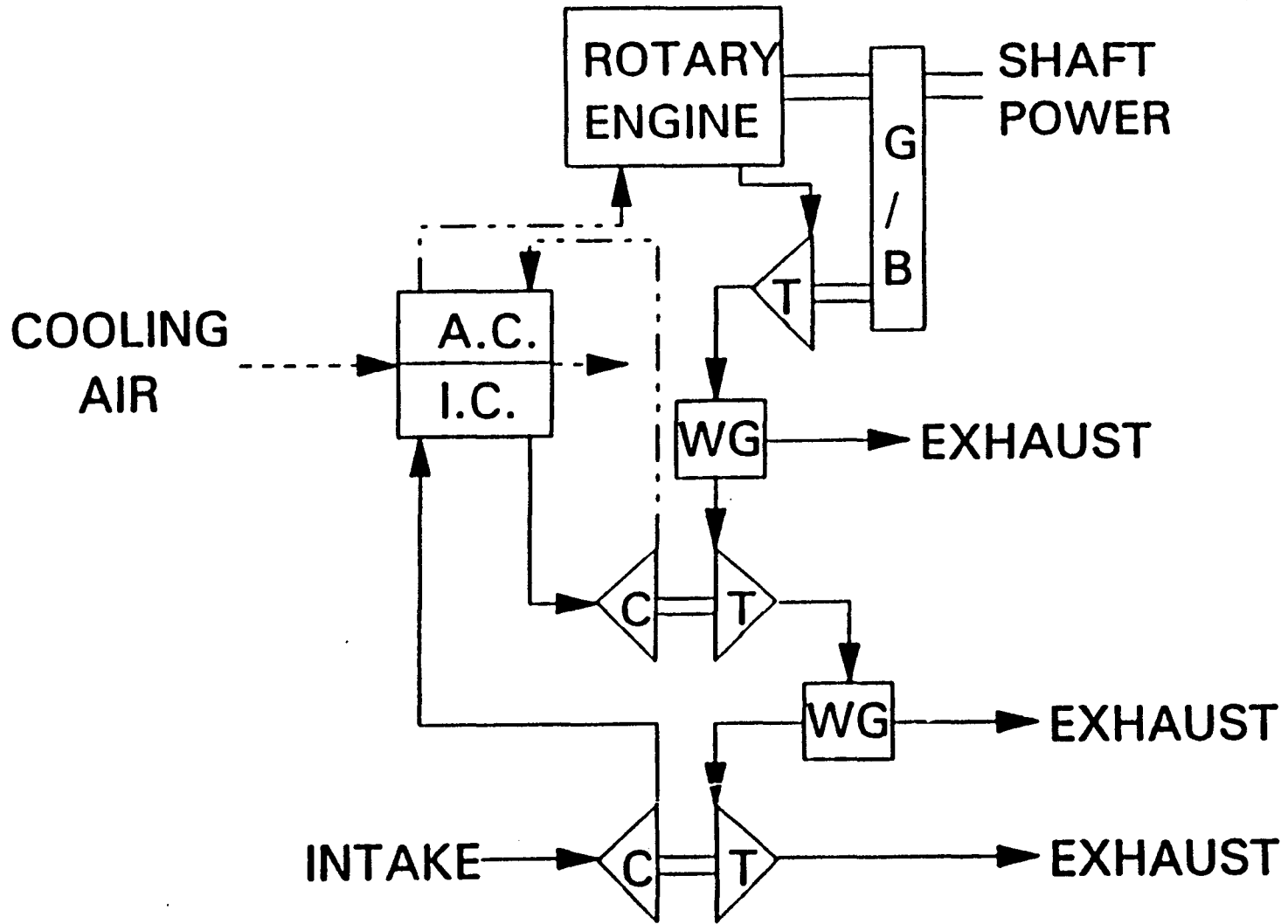
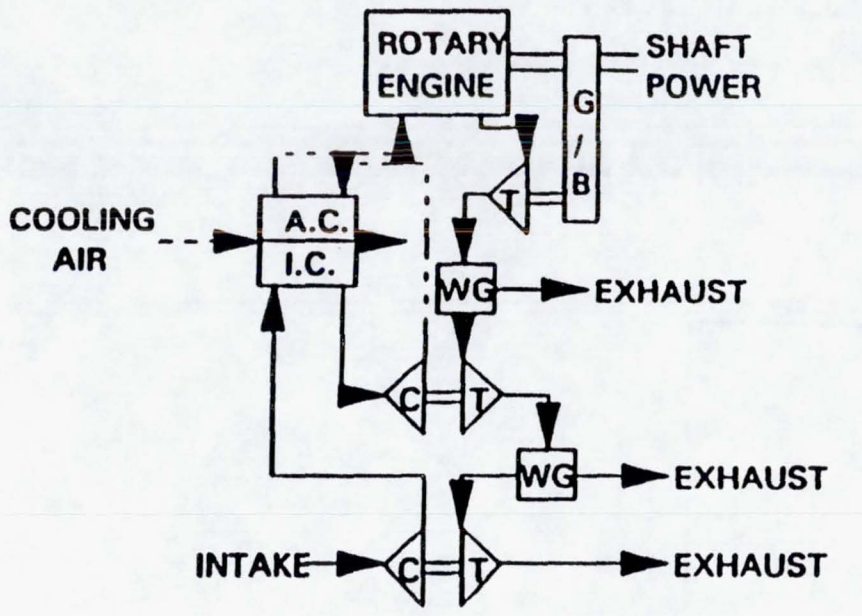
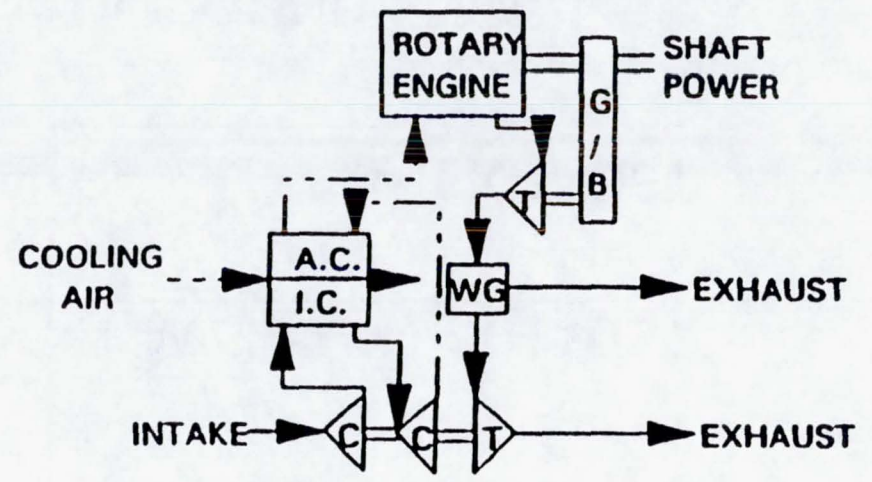


Figure No. 1

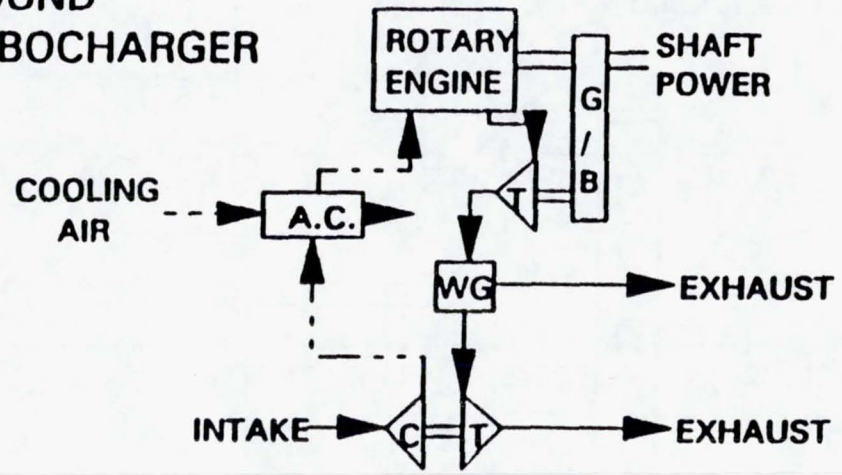
FIGURE 1. TURBOCOMPOUND ENGINE



**TURBOCOMPOUND
MULTIPLE SPOOL TURBOCHARGER**

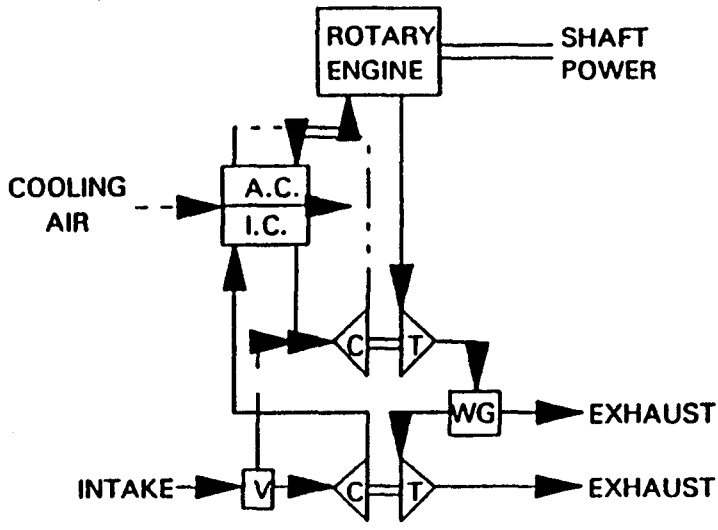


**TURBOCOMPOUND
MULTIPLE STAGE TURBOCHARGER**

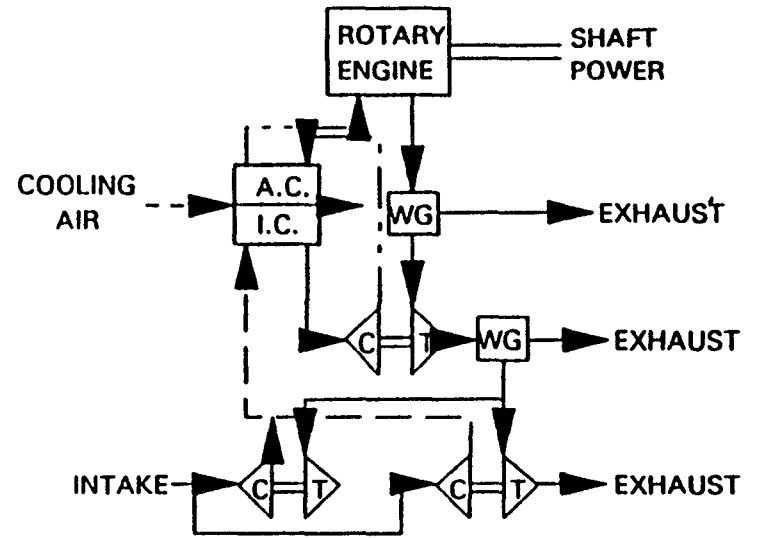


**TURBOCOMPOUND
SINGLE STAGE TURBOCHARGER**

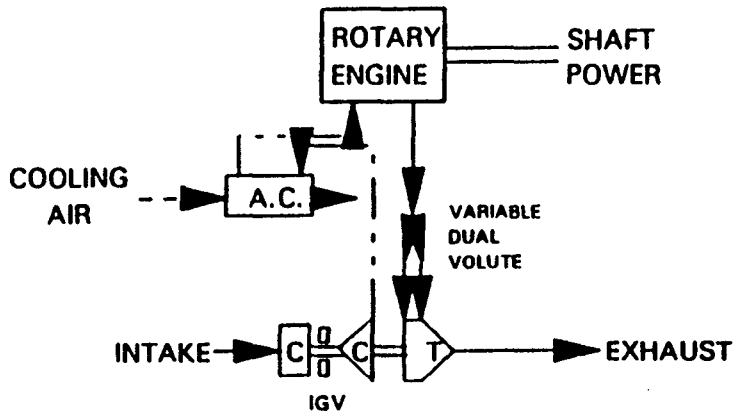
TURBOCOMPOUND CANDIDATE SYSTEMS



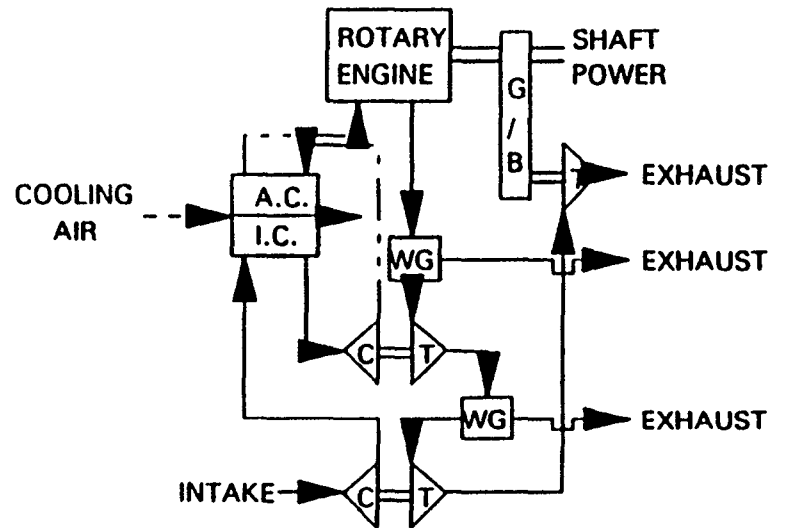
REDIV ALTERNATE 1



3 EQUAL TURBOCHARGERS



REDIV ALTERNATE 2



ALTERNATE TURBOCOMPOUND ENGINE

ALTERNATE CANDIDATE SYSTEMS

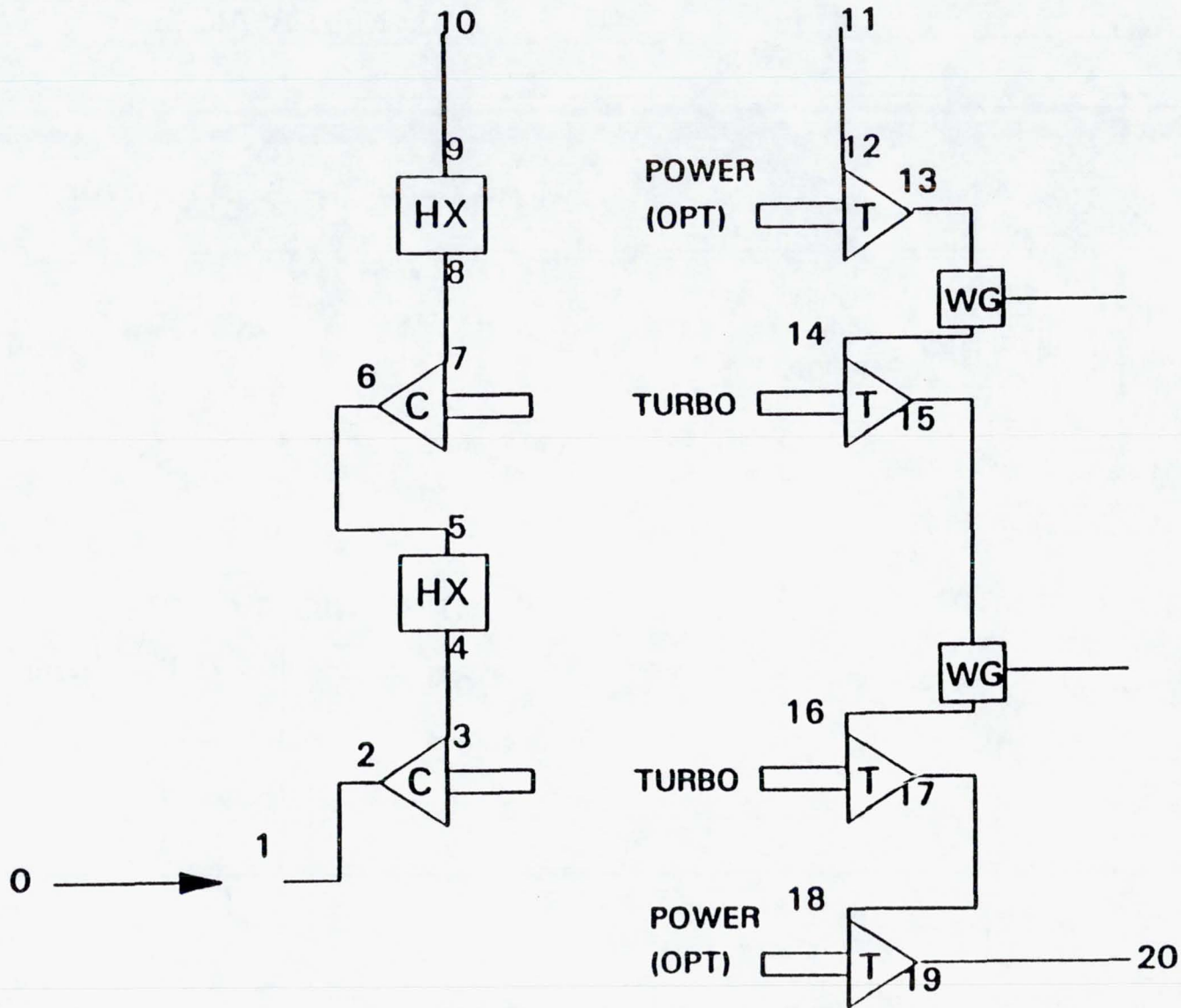
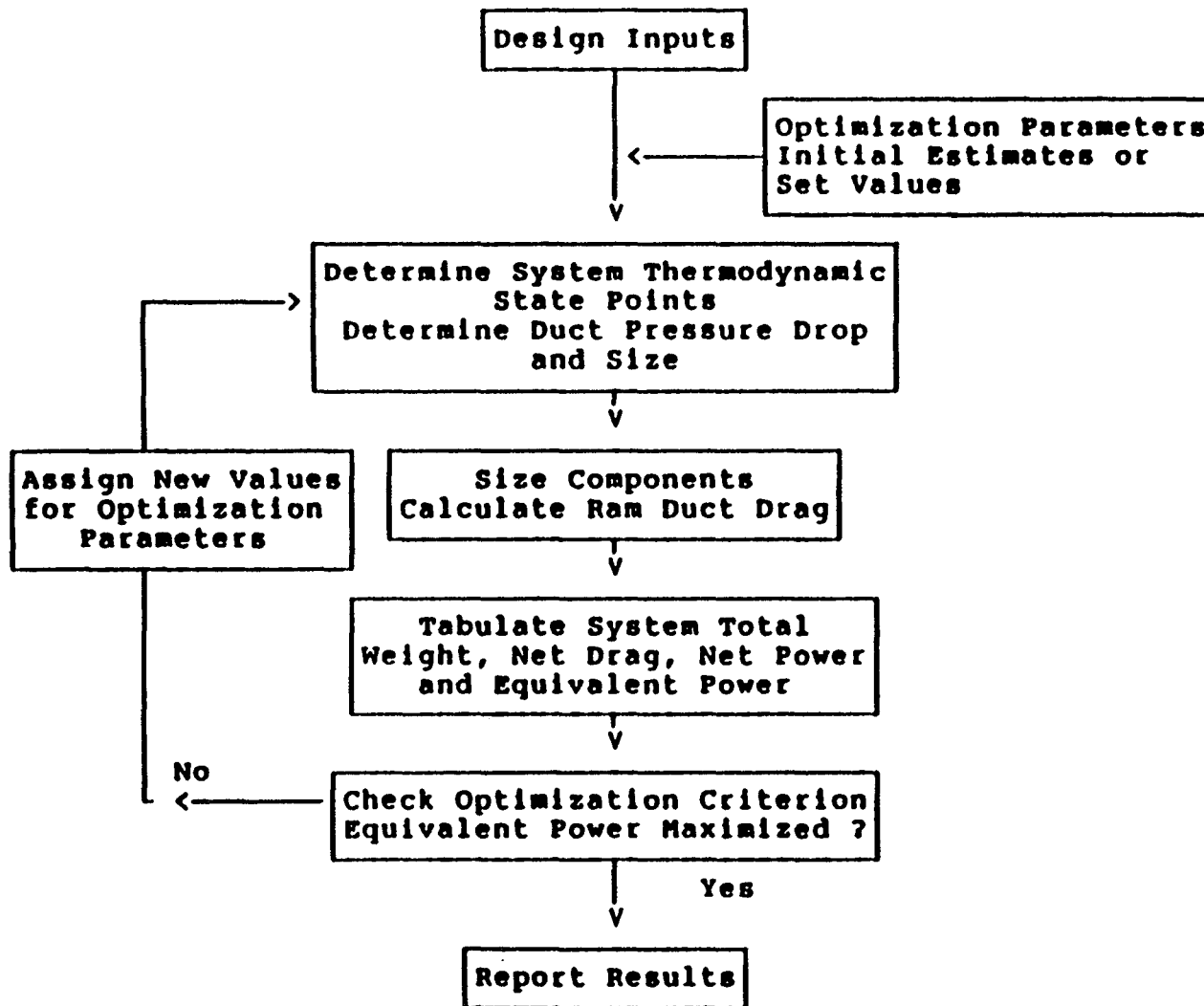


Figure No. 4

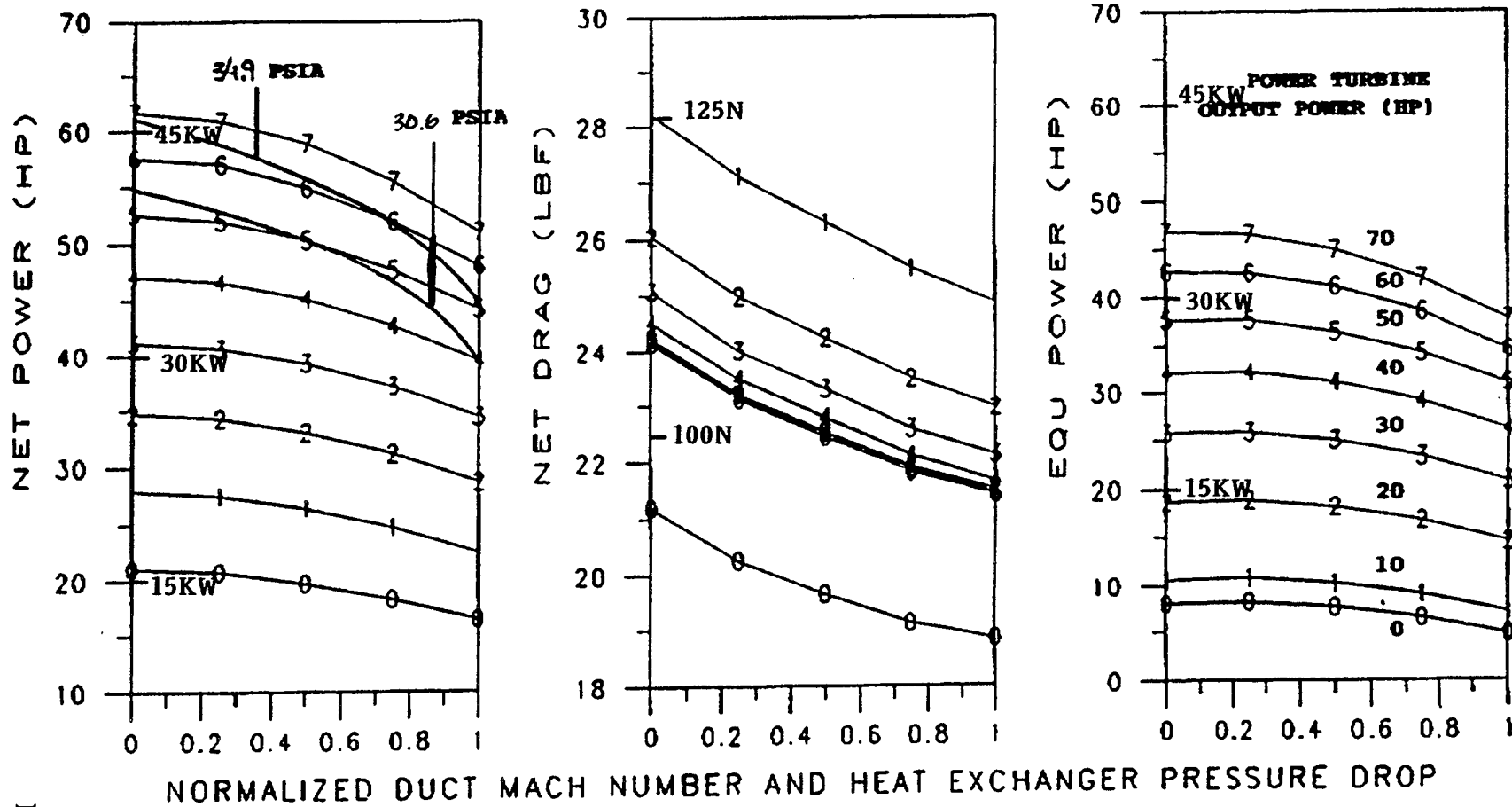
TURBOMACHINERY SYSTEM STATE POINTS



289

Figure No. 5

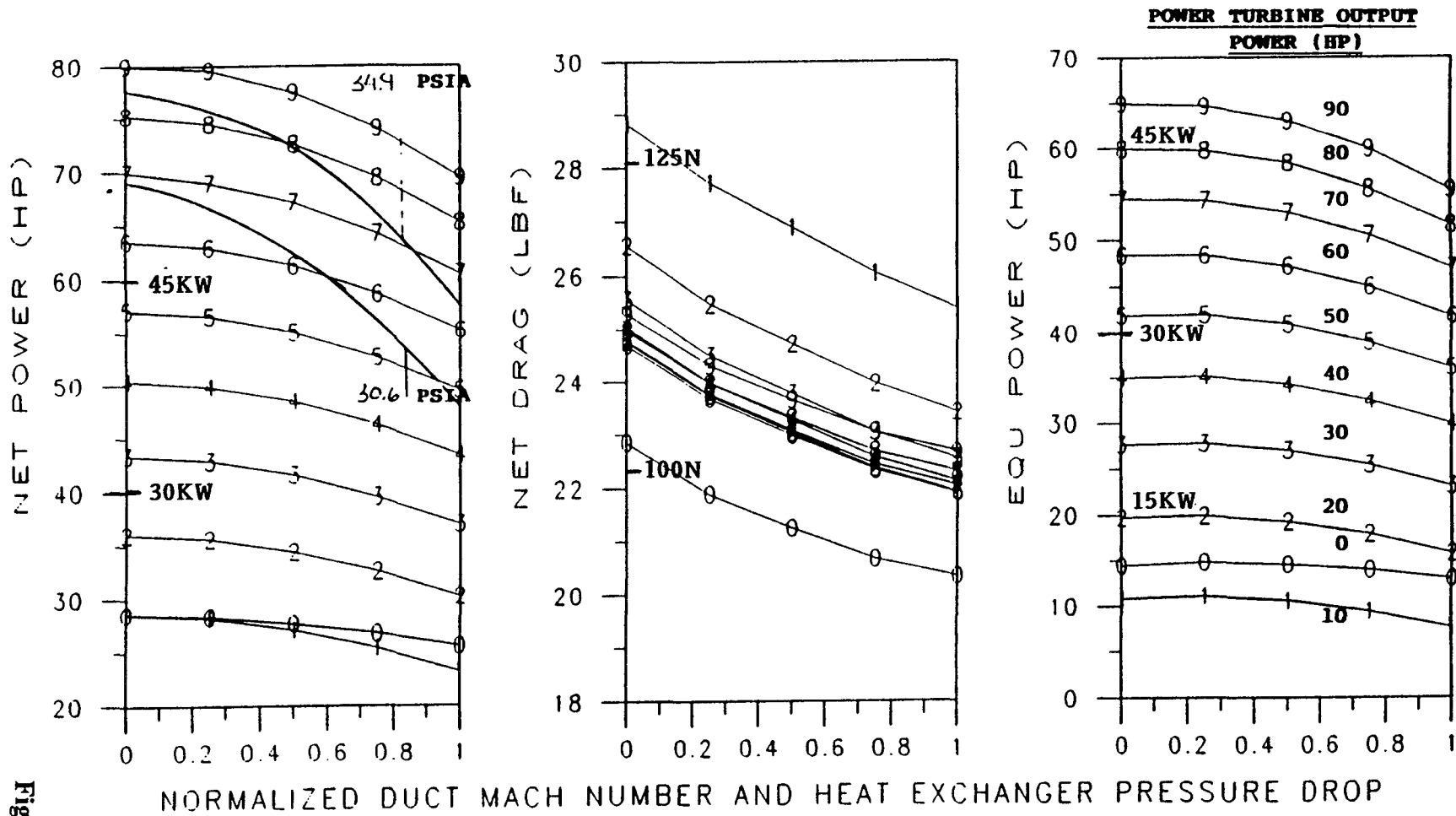
SYSTEM ANALYSIS PROGRAM FLOW CHART



$$\frac{\Delta P - \Delta P_{\min}}{\Delta P_{\max} - \Delta P_{\min}} \text{ and } \frac{M_d - M_{d\min}}{M_{d\max} - M_{d\min}}$$

Figure No. 6

EFFECT OF CHARGE AIR PRESSURE DROP (NO PULSE EFFECTS)



$$\frac{\Delta P - \Delta P_{\min}}{\Delta P_{\max} - \Delta P_{\min}} \quad \text{and} \quad \frac{M_d - M_{d\min}}{M_{d\max} - M_{d\min}}$$

EFFECT OF CHARGE AIR PRESSURE DROP (WITH PULSE EFFECT)

Figure No. 7

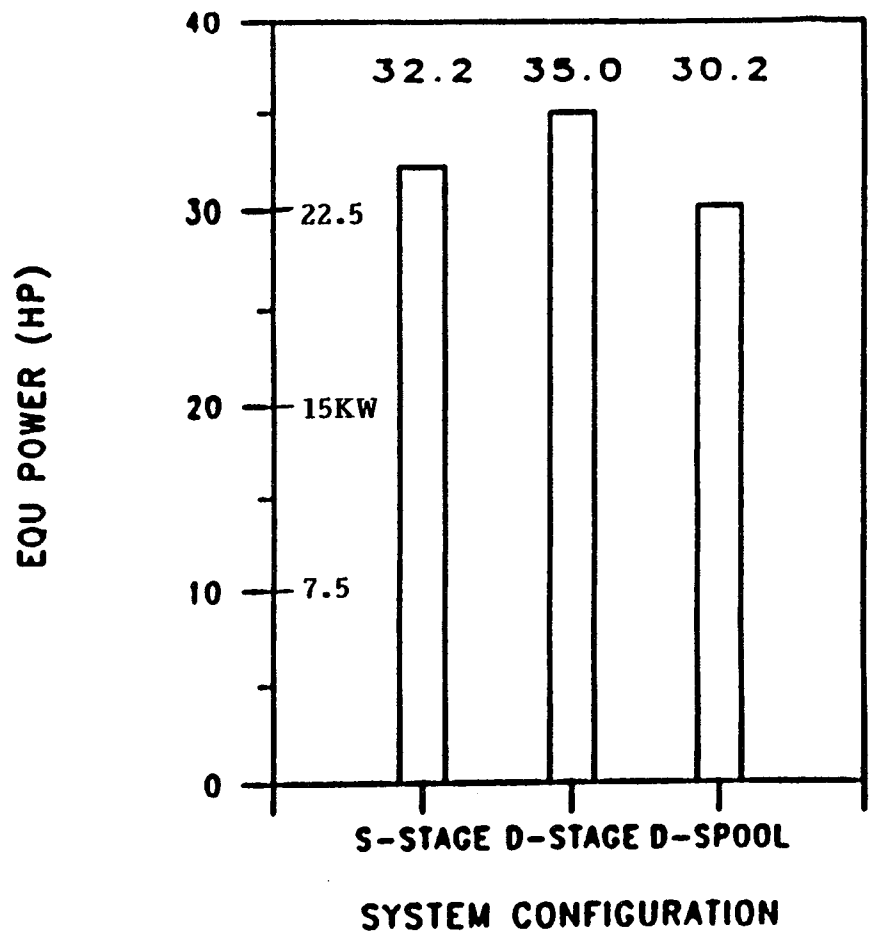


Figure No. 8

8.0 UNIVERSITY COORDINATION

~~ATTACHING PAGE BLANK NOT FILLED~~

INTRODUCTION

During the time period of this program basic research o rotary engines were being carried out at Carnegie-Mellon University, Michigan State University, Princeton University and at Sverdrup Technologies. This work complemented the development work at John Deere Technologies International. The basic work was analytical (at Carnegie-Mellon, Princeton and Sverdrup) and experimental (at Michigan State University). References 1-9 are publications which illustrate the nature of the work at these places. The work at Princeton is covered separately in Section 3.2 and Appendix A of this report.

OBJECTIVES

The objectives of this task were:

1. Coordinate the work at these different centers so that analytical and experimental studies would complement each other; and
2. Transfer information when applicable to more applied critical technology enablement efforts including research rig engine testing for confirmation and correlation.

TECHNICAL APPROACH

A 'Rotary Engine Research Coordinating Committee' which had been established during phase II of the NASA program was the main forum for exchange of technical information. Meetings were held bi-annually in different locations. Two meetings were held in 1990 (the first at NASA and the second at Michigan State University). A third meeting was held in May 1992 at John Deere Technologies International. At these meetings the latest analytical and experimental results were presented and discussed. The experimental program was set up so that in addition to obtaining fundamental information regarding rotary engine flow-fields, results could be used to validate the computer codes. Results from the use of the computer codes are presented in Section 3.2, and in the references listed herein..

RESULTS

The University coordination conducted during this program permitted an open exchange of ideas and directions in analytical and experimental efforts. These exchanges resulted in a more focused multi-pronged thrust toward improving combustion and airflow condition contributing to higher efficiencies.

CONCLUSIONS

The university coordination was complementary to the experimental research conducted in this program and permitted the utilization of advanced theoretical and experimental technologies.

REFERENCES

1. Hamady, F., Stuecken, T. and Schock, H., "Airflow Visualization and LDV Measurements in a Motored Rotary Engine Assembly part 1: Flow Visualization," SAE Paper No. 900030.
2. Chouinard, E., Hamady, F. and Schock, H., "Airflow Visualization and LDV Measurements in a Motored Rotary Engine Assembly Part 2: LDV Measurements," SAE Paper No. 900031
3. Bartrand, T.A., And Willis, E.A., "Performance of a Supercharged Direct-Injection Stratified-Charge Rotary Combustion Engine," paper presented at the Joint Symposium on General Aviation Systems co-sponsored by the AIAA and FAA at Ocean City, NJ, April 1990.
4. Raju, M.S. and Willis, E.A., "Computational Experience with a 3-D Rotary Engine Combustion Model," paper presented at the Joint Symposium on General Aviation systems co-sponsored by the AIAA and FAA at Ocean City, NJ, 1990.
5. Morita, T., Hamady, F., Stuecken, T., Somerton, C. and Schock, H., "Fuel-Air Mixing Visualization in a Motored Rotary Engine Assembly," SAE Paper No. 910704.
6. Hamady, F., DeFilippis, M., Stuecken, T. and Schock, H., "Experimental Analysis of Blowby and Flow Field Interaction in a Motored Rotary Engine," SAE Paper NO. 910893.
7. Li, Z., Shih, T.I-P, Schock, H. and Willis, E., "A Numerical Study on the Effects of Apex Seal Leakage on Wankel Engine Flow Fields," SAE Paper No. 910703.
8. Raju, M.S. and Willis, E., "Three-Dimensional Analysis and Modeling of a Wankel Engine," SAE Paper No. 910701.
9. Li, Z., Steinthorsson, E., Shih, T.i-P. and Nguyen, H.l., "Modeling and Simulation of Wankel Engine Flowfields," SAE Paper No. 900029.

9.0 CONCLUSIONS AND RECOMMENDATIONS

9.0 CONCLUSIONS AND RECOMMENDATIONS

Conclusions

Significant progress was made in key critical technology areas.

- Advanced, higher speed CFD capability was achieved.
- Correlation between 3-d combustion modeling and experimental hardware performance results was achieved.
- Power density equivalent to 400 BHP (300kw) in a twin rotor 0.7ℓ /rotor displacement engine was demonstrated.
- Fuel consumption reduction equivalent to 0.375 lbs/BHP-hr (228 gr/kw-hr) referred to a twin rotor 0.7ℓ /rotor displacement engine was demonstrated.
- Major system understanding and directions for future improved systems were established including
 - fuel injection systems
 - turbocharging systems
 - control systems
 - airframe and missions
- Directions were established for lightweight, improved rotor designs
- An overall aircraft engine reference design was completed, suitable for a baseline reference configuration

Recommendations

- Continue experimental testing and analysis to evaluate items designed and procured but not tested as a result of curtailment of this program
 - leading pocket rotor
 - re-entrant pocket rotor
 - intake and exhaust port variations
- Continue the technology enablement effort to permit preparation of and evaluation of several iterations of the twin rotor configuration over the full operational range of start, idle, taxi, climb, cruise and take-off power and speed conditions.

10.0 LISTING OF APPENDICES (VOLUME II)

PREVIOUS PAGE BLANK NOT FILMED

PAGE 300 INTENTIONALLY BLANK

10.0 LISTING OF APPENDICES (SEPARATE VOLUME)

- APPENDIX A: NEW IMPROVED COMPUTATIONAL FLUID DYNAMICS (CFD) CODES/DETAILED ILLUSTRATIONS
- APPENDIX B: FEASIBILITY ANALYSIS-ROTATING VALVE HIGH PRESSURE COMMON RAIL SYSTEM
- APPENDIX C: TURBOMACHINERY SYSTEM ANALYSIS FOR STRATIFIED CHARGE ROTARY ENGINE CRITICAL TECHNOLOGY ENABLEMENT; REPORT NO. AER 3485, SUNDSTRAND AEROSPACE CORPORATION, 4 OCTOBER 91

REPORT DOCUMENTATION PAGE			Form Approved OMB No. 0704-0188	
Public reporting burden for this collection of information is estimated to average 1 hour per response, including the time for reviewing instructions, searching existing data sources, gathering and maintaining the data needed, and completing and reviewing the collection of information. Send comments regarding this burden estimate or any other aspect of this collection of information, including suggestions for reducing this burden, to Washington Headquarters Services, Directorate for Information Operations and Reports, 1215 Jefferson Davis Highway, Suite 1204, Arlington, VA 22202-4302, and to the Office of Management and Budget, Paperwork Reduction Project (0704-0188), Washington, DC 20503.				
1. AGENCY USE ONLY (Leave blank)	2. REPORT DATE August 1992	3. REPORT TYPE AND DATES COVERED Final Contractor Report		
4. TITLE AND SUBTITLE Stratified Charge Rotary Engine Critical Technology Enablement Volume I			5. FUNDING NUMBERS WU-505-62-1 C-NAS3-25945	
6. AUTHOR(S) C.E. Irion and R.E. Mount			8. PERFORMING ORGANIZATION REPORT NUMBER E-8831	
7. PERFORMING ORGANIZATION NAME(S) AND ADDRESS(ES) Rotary Power International, Inc. P.O. Box 128 Wood-Ridge, New Jersey 07075			10. SPONSORING/MONITORING AGENCY REPORT NUMBER NASA CR-189106	
9. SPONSORING/MONITORING AGENCY NAME(S) AND ADDRESS(ES) National Aeronautics and Space Administration Lewis Research Center Cleveland, Ohio 44135-3191			11. SUPPLEMENTARY NOTES Project Manager, Paul T. Kerwin, Propulsion Systems Division, NASA Lewis Research Center, organization code 2703, (216) 433-3409.	
12a. DISTRIBUTION/AVAILABILITY STATEMENT Unclassified - Unlimited Subject Category 07			12b. DISTRIBUTION CODE	
13. ABSTRACT (Maximum 200 words) This report summarizes results of a critical technology enablement effort with the stratified charge rotary engine (SCRE) focusing on a power section of 0.67 liters (40 cu. in.) per rotor in single and two rotor versions. The work is a continuation of prior NASA Contracts NAS3-23056 and NAS3-24628. Technical objectives are multi-fuel capability, including civil and military jet fuel and DF-2, fuel efficiency of 0.355 Lbs/BHP-Hr. at best cruise condition above 50% power, altitude capability of up to 10Km (33,000 ft.) cruise, 2000 hour TBO and reduced coolant heat rejection. Critical technologies for SCREs that have the potential for competitive performance and cost in a representative light-aircraft environment were examined. Objectives were: the development and utilization of advanced analytical tools, i.e. higher speed and enhanced three dimensional combustion modeling; identification of critical technologies; development of improved instrumentation, and to isolate and quantitatively identify the contribution to performance and efficiency of critical components or subsystems.				
14. SUBJECT TERMS Stratified charge; Rotary; Engine; Aircraft; Fuel injection; CFD computer codes; Flow visualization; Multi-fuel			15. NUMBER OF PAGES 305	
			16. PRICE CODE A14	
17. SECURITY CLASSIFICATION OF REPORT Unclassified	18. SECURITY CLASSIFICATION OF THIS PAGE Unclassified	19. SECURITY CLASSIFICATION OF ABSTRACT Unclassified	20. LIMITATION OF ABSTRACT	